Isolated switchable polyoxometalates onto nanostructured HOPG surfaces

Juba Salhi

To cite this version:

Juba Salhi. Isolated switchable polyoxometalates onto nanostructured HOPG surfaces. Material chemistry. Sorbonne Université, 2023. English. NNT : 2023SORUS549 . tel-04466409

HAL Id: tel-04466409
https://theses.hal.science/tel-04466409

Submitted on 19 Feb 2024

Sorbonne Université

Ecole doctorale de Chimie Moléculaire de Paris Centre – ED 406

Institut Parisien de Chimie Moléculaire / Equipe Edifices polymétalliques

Isolated switchable polyoxometalates onto nanostructured HOPG surfaces

By Juba Salhi

PhD thesis in Chemistry

Directed by Florence Volatron and David Kreher

Presented and publicly defended on November 20, 2023

Dr. Frédéric Cherioux	Université de Besançon	Rapporteur
Dr. Alicia Forment Aliaga	Université de Valece	Rapportrice
Dr. Lara Perrin	Université Savoie Mont-Blanc	Examinatrice
Pr. Bernold Hasenknopf (Président du jury)	Sorbonne Université	Examinateur
Dr. Florence Volatron	Sorbonne Université	Directrice de thèse
Pr. David Kreher	Université Versailles St-Quentin	Co-directeur de thèse
Dr. Imad Arfaoui	Sorbonne Université	Invité

Acknowledgements

First, I want to thank the members of the jury: Dr. Alicia Forment Aliaga and RD. Frederic Cherioux for accepting the role of reviewers, and Dr. Lara Perrin and Pr. Bernold Hasenknopf for participating as examiners.

This thesis was carried out at the IPCM laboratory (Institut Parisien de Chimie Moléculaire) at Sorbonne University, within the E-POM team (Polymeric Metallacycles). I am immensely grateful to Dr. Florence Volatron, who hired me for this thesis and perfectly fulfilled her role as my supervisor during these three years. I appreciate her patience, kindness, and encouragement, as well as her availability and responsiveness. Her teachings and scientific rigor have been invaluable and allowed me to acquire priceless knowledge, it was truly a privilege for me to work under your supervision. I thank Imad Arfaoui, who taught me all what I know about STM and AFM. His knowledge and teaching skills have proven to be precious, allowing me to understand and master these microscopy techniques, which were one of the cornerstones of this thesis. I also appreciate him for the time he spent reviewing and correcting my manuscript. I am also very grateful to Professor David Kreher, my co-supervisor, who recommended me for this thesis. He has always been there during the most crucial moments, and I also thank him for the assistance he provided in correcting my thesis manuscript.

I thank Dr. Guilhem Simon, who helped me with the analysis of all the infrared spectra obtained during my thesis. His contribution to this work and his expertise proved to be invaluable. Additionally, I would like to express my gratitude to Professor Alexandre Dazzi, who allowed conducting AFM-IR analyses, a highly interesting technique that yielded priceless results.

I would like to express my sincere thanks to Dr. Guillaume Izzet, whose teachings and advices on synthesis have proven to be crucial and have allowed me to acquire vast knowledge in organometallic synthesis, NMR and UV-visible spectroscopy.

I also extend my thanks to Professor Anna Proust, our team leader, for her warm welcome within the team and the laboratory.

I express my gratitude more broadly to all the members of the E-POM team, including the permanent members I haven't mentioned yet: Dr. Sébastien Blanchard, Dr. Richard Villanneau, Séverine Renaudineau, Dr. Geoffroi Guillemeau, and Dr. Valérie Marvaud, for the serene atmosphere they create in the laboratory. I also thank all my fellow doctoral and postdoctoral colleagues, especially Patrick for his assistance with the final experiments of my thesis, Ludivine and Kevin who arrived at the laboratory at the same time as me, and Kelly my lab mate who has already defended her thesis, and everyone else for the positive atmosphere they brought daily during these three years. I also want to thank the ERMMES team for their contribution to the good atmosphere in the laboratory.

Content table

CHAPTER I: Data storage devices, molecular electronics and state of the art

This chapter will present modern data storage devices and the principle of their functioning, the fabrication techniques of their components, which are nanometric semiconductors, and the limitations of the fabrication that are being reached for these devices based on miniaturization.

The alternative ways for the conception of more cost, energy and capacity effective devices will be then presented, with a particular focus on the potential of molecular based electronic materials. Their advantages and the challenges these materials oppose will be discussed, and we will make an analogy between molecular and semiconductor based electronic devices functioning.

A presentation of the molecules exhibiting the required properties for molecular electronic will be made, with an accent about these properties, their interests and fields of application. Polyoxometalates (POMs) will then be presented generally, and in particular, Keggin POMs characteristics will be discussed.

We will make an overview of the different strategies used by research teams to organize POMs into thin films, monolayers and isolated periodic units on surface, particularly relying on functionalized substrates as template to induce the organization with the different favorable and unfavorable molecular interactions.

Finally, we will present self-assembling molecules used to functionalize substrates into templates helping for the individualized organization of molecules on the surface, we will especially present tris-styrylbene based 2D self-assemblies on HOPG substrates, and its use for this purpose. I will end this chapter by presenting the expected ins and outs of my work as well as the various strategies considered.

I - Data storage devices overview

Nowadays, electronic devices such as solid state drives (SSDs) and RAM memory are widely used for data storage, and they have undergone rapid evolution over the past few decades[1] (Figure 1). The core of these devices is based on silicon nanoscaled semiconductors packed in chips with billions of integrated circuits that are fabricated using lithographic techniques[2–4]. In modern electronic, a type of transistor called a metal-oxide-semiconductor field-effect transistor (MOSFET) is widely used for all memory components. MOSFETs are considered to be one of the most important materials in modern electronics and are among the most manufactured items in human history.

Figure 1 : Random access memory devices (RAM), left: 128 Mo memory capacity produced in 2002 year right: 16 Go memory capacity produced in 2018 (128 times memory capacity in the same device size)[5]

MOSFETs are made of doped silicon, which consists of single-crystal silicone molded into thin layers called wafers.[6] Their structure is divided into four terminals, the body (B) consist of p-type doped semi-conductor silicon (hole carrier), the source (S) and the drain (D) which are both made of n-doped semi-conductor silicon (electron carrier), the gate (G) made of metal or conductive silicon and separated by an isolating oxide layer.[7] The contact area between the n-type and p-type semiconductor is the depletion region, where the free electrons from the n-type layer fill-up the holes in the p-type layer. When the equilibrium is reached, the depletion zone become positively charged in the n-side and negatively charged in the p-side, and an electronic field is created preventing further electrons exchange acting like an insulator.[8] Due to this isolative depletion region, when positive and negative electrical charges are applied to the source (S) and drain (D) terminals, electricity cannot flow. However, when a positive electric charge is added on the gate terminal, the holes beneath the oxide layer undergo a repulsive force and are pushed downwards, and at the same time, electrons from the n-doped source and drain regions are attracted, creating an electron rich channel (an n-channel) between (S) and (D), allowing an electric current to flow (Figure 2). This ability allows MOSFETs to be switched on and off by controlling the current flow, this simple operation is the basis of electronic devices where every switch on or off is interpreted as 0 or 1 and which is the binary code of computer systems.[9] These on/off states are needed to be enough stable in order to avoid loss of information during the writing and reading process.

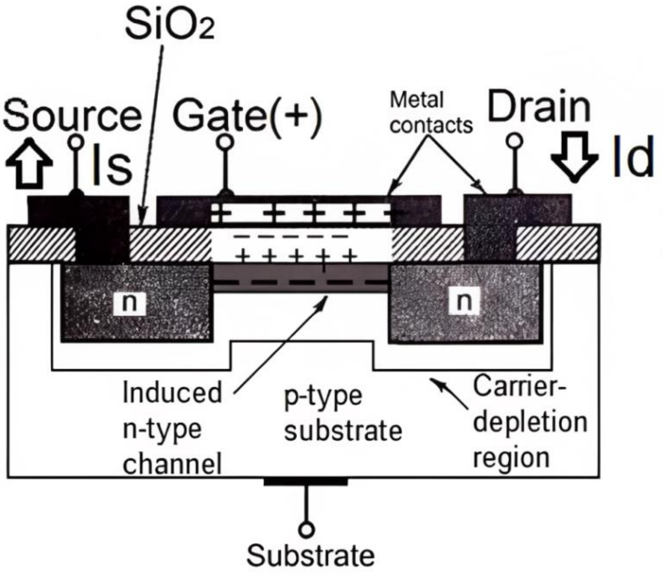

Figure 2 : Schema of MOSFET with the formation of the electron rich channel between the source and the drain after application of a current on the gate (G)[10]

For data storage devices, MOSFETs are integrated into electronic chips, and the more transistors the chip contains, the greater the data storage capacity. Thus, one of the key points to improve the performance of these devices is to reduce the size of the transistors to increase data storage density.[11] Manufacturing techniques of electronic chips have known a considerable progress, passing from a size of 0.18 micron per transistor in 2000 to 5 nanometer nowadays. The production of chips with 3 nm size transistors have recently started according to TSMC company.[12] However, the miniaturization of these transistors is reaching its physical limits, indeed, the number of transistors in dense integrated circuits evolves according to Moor's law,[13] which states that speed and capability of computers can be expected to double every two years as a result of increases in the number of transistors a microchip can contain, but a slowdown in the evolution of chip's transistors density has recently been observed[13] due to the complex process involved for the miniaturization of these components,[14] as shown in Figure 3.

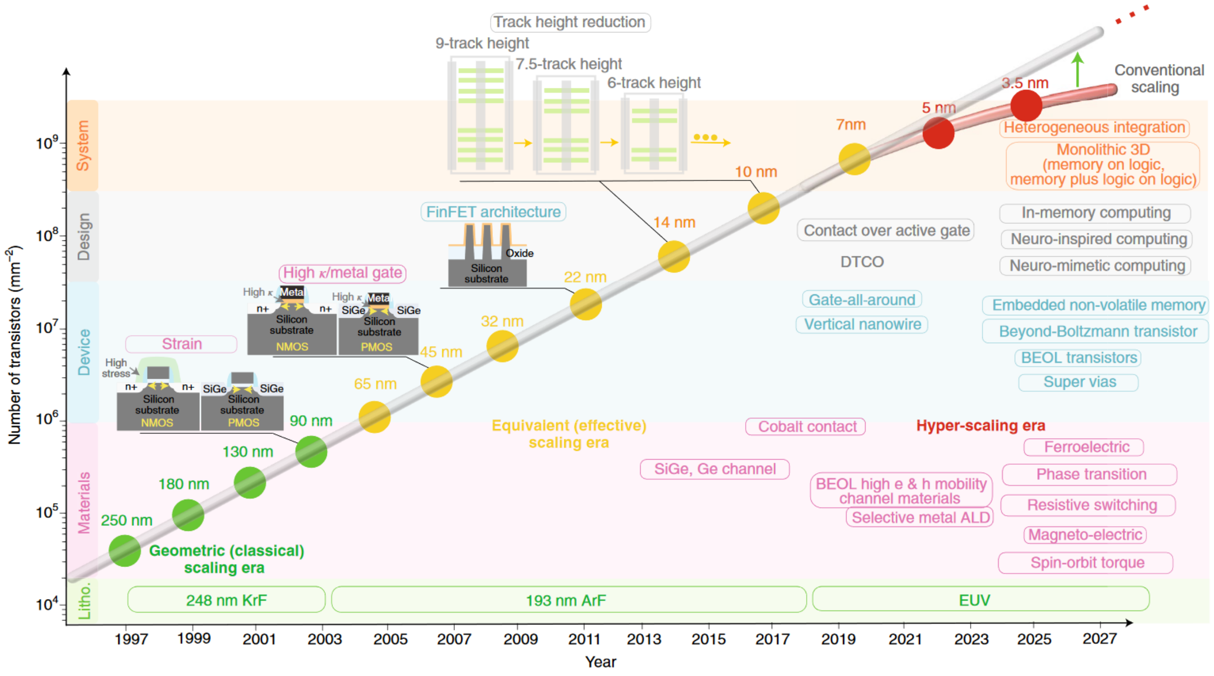

Figure 3 : Size and number of transistors per mm2 since 1997 and expected evolution for 2027, illustrating the slowdown of Moore's law[15]

The needs for data storage worldwide increase constantly[16] due to factors such as human population growth and a rapid spreading of numeric technologies in many fields of daily life. Another critical point is the reduction of power consumption of these memory devices[17], indeed, the increase of data centers requiring to be powered constantly pauses serious energy and environmental problems.[18]

Several alternatives are envisaged to overcome these limitations, such as a change in the architecture,[19] and the use of nanoparticles or DNA fragments to replace MOSFETs and/or increase data storage density with a reduction of power consumption.[20–23] One of the most promising alternatives consists of packed individual molecules as data storage units.[24] This approach allows in theory to increase the storage density due to the small size of molecules and to make more energy efficient devices to provide a viable solution for these problems.[25] Also, due to their versatility, molecules can offer novel functionalities. The leveraging of their electronic, optical, and magnetic properties would allow the development of novel functionalities and promising devices in fields such as multi-level memories,[26] and quantum computing.[27] Another advantage that molecular memory materials can potentially offer is a cost-effective production,[28] due to the fabrication methods and the cost of molecules.[29,30]

However, the design of these materials requires several challenges, and one of the most important is to be able to precisely control the organization of the molecules on surface, to have packed and periodical distribution in order to optimize the storage density, but at the same time separated molecules from each other to allow the individual addressing. Also, scalability is an important point for the fabrication of enough large substrates. Thus a reliable and repeatable method of fabrication is crucial, and if these points are reached, an analogue material to the MOSFETs-based ones will be obtained with a writing/reading process being able to be performed on single molecules.

II - Molecular electronics

Molecular electronics is a branch of nanotechnology that focuses on the design, fabrication, and study of electronic components and devices at the molecular scale. It involves the use of individual molecules or molecular systems as functional building blocks for constructing electronic circuits and devices that range from simple components like molecular wires[31] and switches,[32] to more complex structures like molecular transistors.[33]

Molecular wires, which consists of a single or a few molecules capable of conducting electrical current, can be synthesized with different conductive properties such as metallic, semiconducting, or insulating behavior, depending on the molecular structure and arrangement.[34] Molecular wires can be used to connect various electronic components and create functional circuits. One example of the study of molecular wires is reported by Sukegawa *et al.* where they studied the photo induced electron transfer between donor (zinc porphyrin) and acceptor (C60) molecules connected by a pi-conjugated rigid molecular bridge made of oligo-p-phenylenevinylene.[35]

Another element in molecular electronics is the molecular switch. These are molecules capable of changing their states in response to external stimuli such as light, electric fields, or temperature. Amongst the molecules that exhibit such property we can cite the dithienylethenes[36] that are reversible molecular switches consisting of conjugated parts connected by a switching element (Figure 4), and azobenzenes[37] that can undergo light-driven trans/cis isomerization. Switching between different states allows the realization of logic operations and memory functions using unique molecules[32] in the same way as it’s done with transistors in modern electronic circuits.

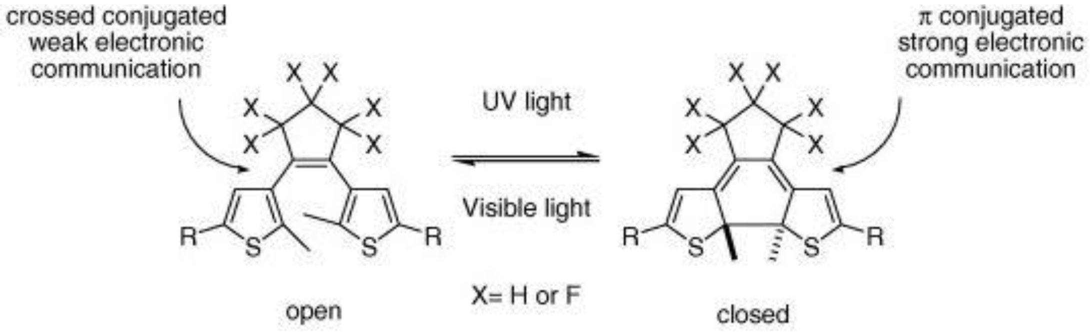

Figure 4 : Reversible photocyclisation of 1,2-dithienylethene moieties upon UV–Vis light irradiation[32]

Data storage devices based on molecules, although still at the fundamental research level, are drawing much interest, indeed, researchers have demonstrated the use of individual molecules, such as rotaxane, as storage elements for binary datas[38]. However, one of the major challenges in molecular electronics is the precise arrangement and integration of individual molecules into functional devices. While the semi-conductor-based electronic materials have already reliable and scalable fabrication methods based on top down approach[39], the conception of molecular electronic devices for data storage is still at a research stage, and rely most commonly on a bottom-up approach.[40] These two approaches are one of the principal differences between the conception of classic semi-conductor-based electronic components and the emerging molecular based electronic materials. Top-down approach being the most widely used in semiconductor industry, it has undergone a rapid evolution during the past decades, and many top-down approaches techniques have been developed based mainly on lithography.[41]

II.1 – Top-down approach

Top-down approach in the semiconductor industry can be divided into several techniques (Figure 5). Basically, it is a subtractive process where the starting material is composed by a bulk silicon substrate which is treated with various processes in order to remove material layer by layer to create complex patterns on silicon wafers. An example of a top-down approach method consist of applying a mask or resist layer on the surface of the substrate which is then patterned by exposing it to light or chemicals. The exposed areas are then removed to leave a patterned layer that acts as a template for the subsequent etching process.[42]

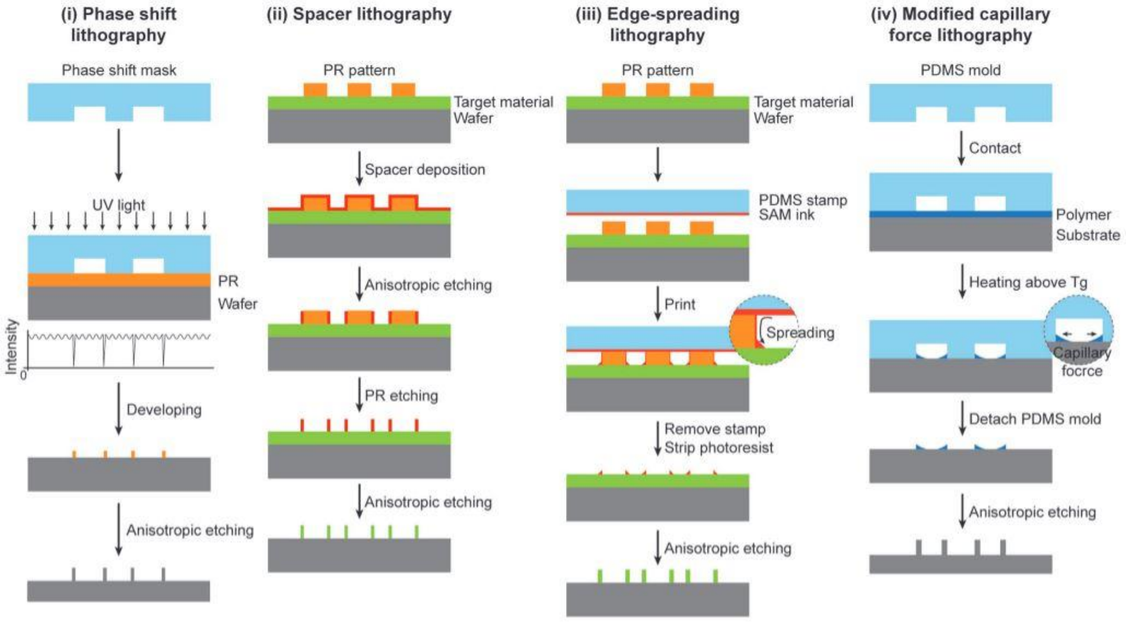

Figure 5 : Schema of four diffrent top-down lithography etching processes[41]

The top-down approach is a highly precise and repeatable process that allows for the fabrication of complex patterns and structures at a nanoscale level. However, this approach has its limitations, as it is difficult to achieve high aspect ratios and precise control over the size and shape of the features, which is due to factors such as the diffraction limit of light (Rayleigh Criterion) used in photolithography and the limitations of chemical etching techniques[43]. Also, the technique is not suitable for creating three-dimensional structures[44], and the cost of the equipment and facilities is expensive (Figure 6).

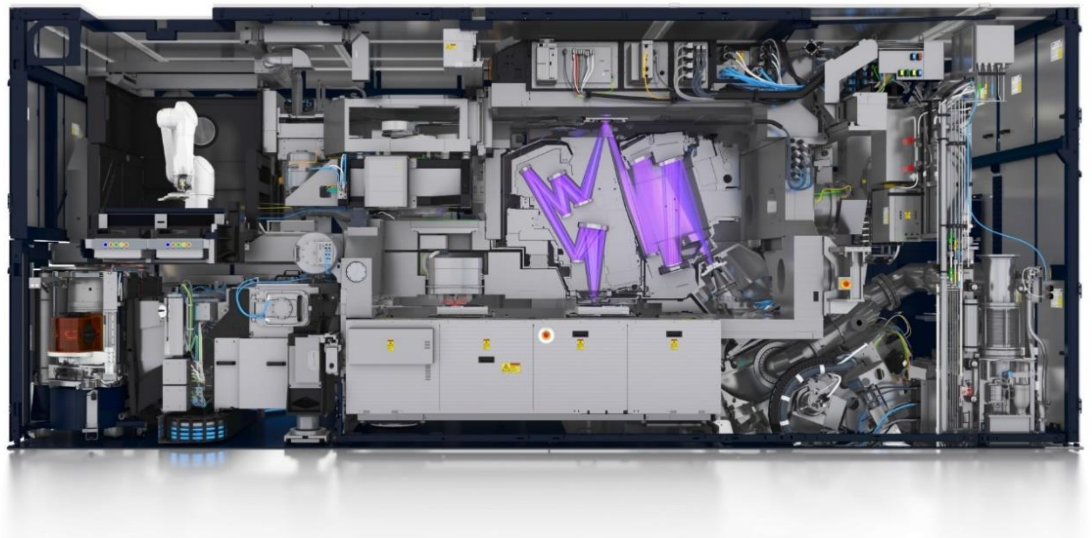

Figure 6 : Extrem ultraviolet lithography system by ASML company[45] *(size of a double-decker bus and weigh around 180 tonnes ~150 million euros)*

II.2 – Bottom up approach

The bottom-up approach in molecular electronics involves the assembly of individual molecules or nanoscale building blocks to create functional devices. This approach relies mainly on self-assembly processes, where the molecules or building blocks interact with each other through various chemical and physical forces to form ordered structures[46] (Figure 7).

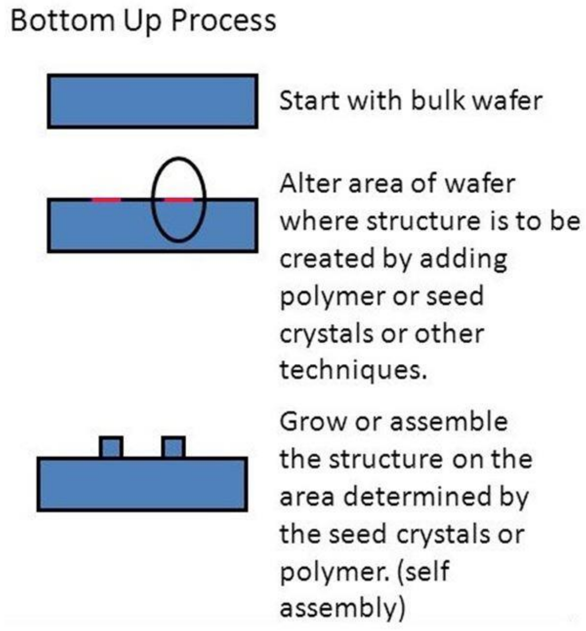

Figure 7 : Bottom-up material fabrication approach[47]

One advantage of the bottom-up approach is that it allows for the creation of highly ordered and precise structures at the molecular scale taking advantage of properties such as self-assembling. It also has the potential to be more cost-effective compared to the top-down approach, as it does not require expensive equipment and facilities.[48]

However, the bottom-up approach has its own set of limitations, and one of the key challenges in molecular electronic field is to reliably and reproducibly fabricate molecular-based devices at a large scale. This requires the development of methods for precisely positioning and attaching molecules to surfaces, as well as for controlling their electronic properties. Several techniques are used for the fabrication and characterization of molecular-based devices, including self-assembly, molecular beam epitaxy, and scanning probe microscopy-based techniques such as scanning tunneling microscopy (STM) and atomic force microscopy (AFM).[49]

II.3 - Molecules for data storage devices

Molecules that have potential use in molecular electronics, particularly for memory applications, should have specific properties, amongst them, stable electronic states, magnetic properties such as anisotropy, single molecule magnet and optical properties[50]. Some common molecular systems investigated for data storage include metal complexes, organic compounds, and various cluster molecules.[51]

II.3.1 Optical properties

Optical properties are studied in the field of data storage, by using in particular the photoswitchable characteristic exhibited by several types of molecules[52] to simulate the on/off states of transistors. Metal complexes attracted a lot of interest as molecular switches, due to their ability to change their electronic state by using light. For example, Aminoazobenzene-substituted ruthenium complex has been studied as molecular switch by Amar *et al.* for its potential applications in molecular photonic memory devices, due to its reversible photoisomerization properties (Figure 8).[53]

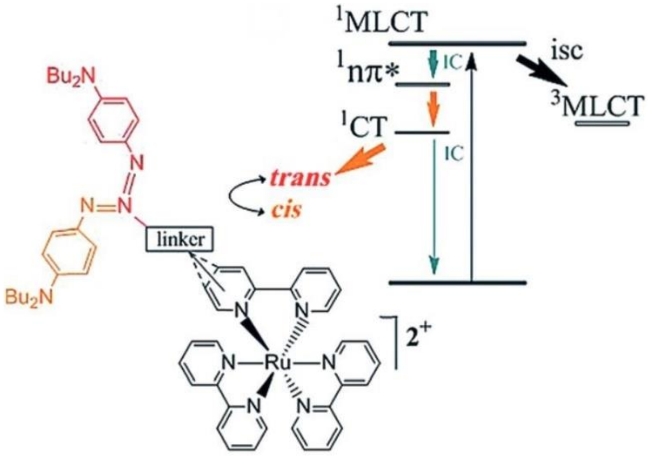

Figure 8 : (a) Aminoazobenzene-substituted ruthenium complexes with reversible photoisomerization properties[53]

II.3.2 Magnetic properties

For data storage and particularly in the field of quantum computing[54], specific magnetic properties are required to allow manipulation and storage of quantum information. One important property is the ability to maintain magnetic coherence, which is the preservation of the orientation of electron spins over a certain period of time. This is essential for maintaining the stability of quantum information[55,56]. Several transition metal complexes have been studied for this property.[57,58]

Quantum computing is a type of computing that uses quantum-mechanical phenomena to perform operations on data. In quantum computing, a qubit (short for quantum bit) is the basic unit of quantum information. Unlike classical bits, which can only have a value of either 0 or 1, qubits can exist in a superposition of both states simultaneously. This means that a qubit can represent both 0 and 1 at the same time, with a probability of each state that is determined by the state of the qubit. The behavior of qubits is governed by the principles of quantum mechanics, which allows for phenomena such as entanglement and interference, where the state of one qubit can affect the state of another qubit, even if they are separated by a large distance[59,60]. Because of their ability to exist in superposition and their potential for entanglement, qubits are the fundamental building blocks of quantum computers, which have the potential to solve certain problems exponentially faster than classical computers[61,62]. However, building and maintaining stable qubits is a major challenge in the development of quantum computers[63]. Thus, one of the key advantages of using molecular electronics in quantum computing is the ability to achieve extremely high levels of control over individual molecular components. This level of control is essential for achieving the precise quantum state manipulation required for quantum computing[64]. Indeed, molecular electronics offers the potential for constructing stable and controllable qubits[65]. This is because molecules can offer a wide range of unique electronic properties, including the ability to act as spin qubits[66], which can be manipulated using external magnetic fields.[67]

Molecules with large magnetic moments, such as rare earth ions and also transition metal complexes, are often used for this purpose[68,69]. Also, these molecules should have a long relaxation time, which is the time it takes for the system to return to its equilibrium state after being perturbed. This allows for stable storage of quantum information[70]. Figure 9 shows a reported polyoxometalate with the general formula $[V^{IV}_{15}As^{III}_{6}\ O_{42}(H_2O)]_{62}$ named V15 with an interesting relaxation time for a potential use as qubit.

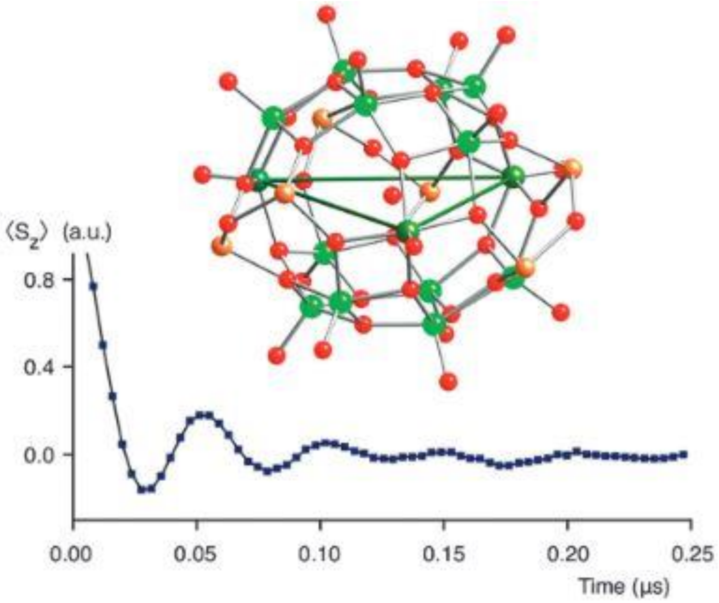

Figure 9 : Structure of V15 POM as spin qubit candidate and time evolution of the average spin after spin echo sequence (green, V; orange, As; red, O)[71]

Other important magnetic properties include anisotropy, which is the dependence of magnetic properties on direction, and coherence length, which is the distance over which the magnetic coherence is maintained[72].

II.3.3 Red/Ox properties

Redox properties of molecules could potentially allow the manipulation and storage of information[73]. It refers to the ability of molecules to undergo reversible oxidation and reduction processes, which can be used to store and manipulate electronic charge and spin states[74,75]. This property is typically exhibited by molecules that have a high degree of electron delocalization, such as conjugated organic molecules or transition metal complexes[76,77]. These molecules can undergo reversible oxidation and reduction reactions (Figure 10), which can be used to switch between different electronic states and store information.

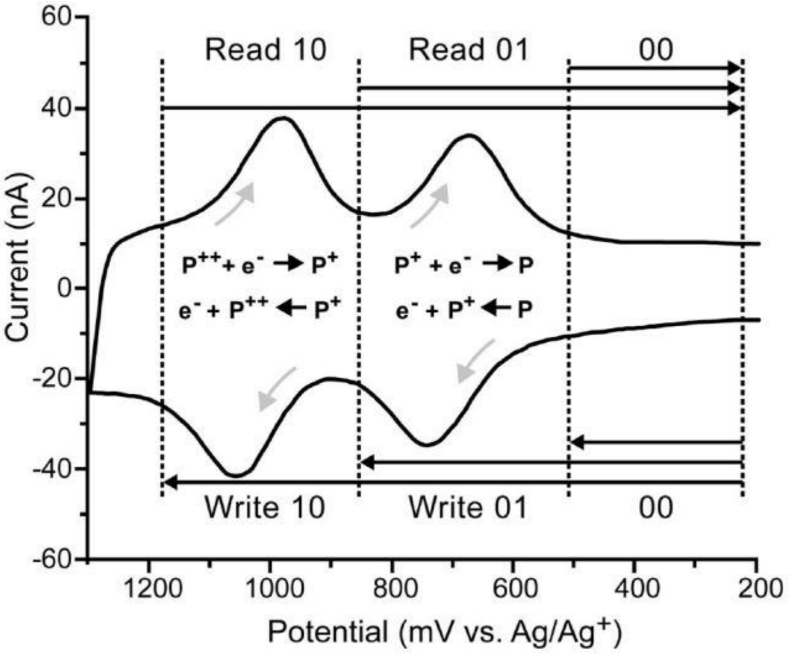

Figure 10 : Reversible redox cycles of of porphyrin for read/write process[78]

Also, the ability to maintain redox stability, which is the ability to resist irreversible oxidation or reduction, is essential for maintaining the stability of the system and avoiding degradation or loss of information[79]. Molecules with stable redox states, such as metal complexes or organic radicals, generally present interesting redox stability[80,81]. These molecules should have a high redox potential as well, which is the energy required to transfer an electron from one state to another. This allows for efficient and controlled manipulation of electronic states and the storage of information[82].

Polyoxometalates (POMs) are a class of inorganic compounds that have recently gained attention as promising candidates for molecular electronics due to their unique electronic, magnetic and redox properties[83]. POMs are composed of metal oxide clusters linked by oxygen atoms, and their properties can be tuned by changing the metal and oxidation state of the clusters. Recent studies have shown that POMs can be used as charge storage materials and in data storage applications due to their high stability and large dipole moment[84–86].

III - Polyoxometalates for molecular electronics

Polyoxometalates (POMs) are a class of inorganic metal-oxo clusters with a wide range of applications in catalysis, energy storage, medicine, and electronics and spintronics[87,88]. POMs consist of a core of transition metal cations, usually tungsten or molybdenum, generally at their highest oxidation state, linked together by bridging oxygen atoms to form a three-dimensional structure. They have been extensively studied due to their unique structural and electronic properties.

III.1 – General overview

POMs were first discovered by the D´Elhuyar brothers, Juan José D´Elhuyar and Fausto D´Elhuyar back to 1783 when they obtained the $(NH_4)_3[PMo_{12}O_{40}]$ POM from the reaction of ammonium molybdate with phosphoric acid and described it as a yellow spicy/bitter tasting salt[89]. Although, Berzelius is the one that first reported the system in 1826[90], and Keggin solved the structure in 1933 using powder X-ray diffraction[91,92]. Since then, hundreds of POMs with varying sizes, shapes, and compositions have been synthesized and characterized. POMs can have high symmetry, such as the Keggin structure, a spherical structure composed of 12 tetrahedral units, or low symmetry, such as the Lindqvist structure, a hexanuclear cluster with a trigonal prismatic shape. POMs can range from small clusters with a few metal atoms that have a molecular weight of hundreds daltons and around one nanometer size, to large aggregates of hundreds of metal atoms with a molecular weight of thousands daltons and a size of several nanometers.

The general formulas of POMs are written as $[M_mO_y]^{n-}$ for isopolyanion POMs and $[X_xM_mO_y]^{n-}$ for heteropolyanion POMs. The X atoms are usually cations such as phosphorus, gallium, aluminum…etc. The metal M is most commonly group 6 (molybdenum or tungsten), and less commonly group 5 (vanadium, niobium or tantalum); x, m and y are stoichiometry coefficients and n is the charge of the POM. They can be associated to a large variety of counter-cations: organic cations (alkyl ammonium or phosphonium…), and inorganic cations (alkalines, protons…). The choice of counter ion can have a significant influence on their physical and chemical properties[93], and one of the main effects is the solubility of POMs which is a critical factor in many applications, such as catalysis and energy storage and material science. For example, ammonium and alkali metal counter ions are known to enhance the solubility of POMs in water, while organic counter ions are known to enhance their solubility in organic solvents. The main types of POMs can be classified based on their structure, which includes Keggin, Anderson, Lindqvist, and Wells-Dawson POMs, that are certainly the most studied ones.

Anderson type POMs have the general formula $[XM_6O_{24}]^{n-}$, their planar structure was proposed by J. S. Anderson in 1937[94] and confirmed by H. T. Evans in 1948 with the determination of the cristal structure of a single $[TeMo_6O_{24}]^{6-}$ molecule[95]. The structure consists of a central XO_6 ion forming an octahedron and surrounded by six octahedral edge sharing MO_6 units (Figure 11).

Lindqvist are a category of POMs that do not have heteroatoms, the general formula of lindqvist POMs is $[M_6O_{19}]^{n-}$ and their structure form a hexanuclear cluster with a trigonal prismatic shape, composed by 6 MO_6 octahedrons, it provides a set of eight identical triangular faces (Figure 11).

Wells-Dawson POMs structure is composed by eighteen metal atoms, each of them in a pseudo-octahedral MO_6 environment, these octahedrons are organized into parallel rings of 3, 6, 6 and 3 metal ions, the two rings of the polar regions with 3M each are called caps while the two rings with 6M each in the equatorial region are called belt, the center of each belt ring is occupied by a XO_4 tetrahedron. The general formula for Wells-Dawson POMs is $[X_2M_{18}O_{62}]^{n-}$ (Figure 11).

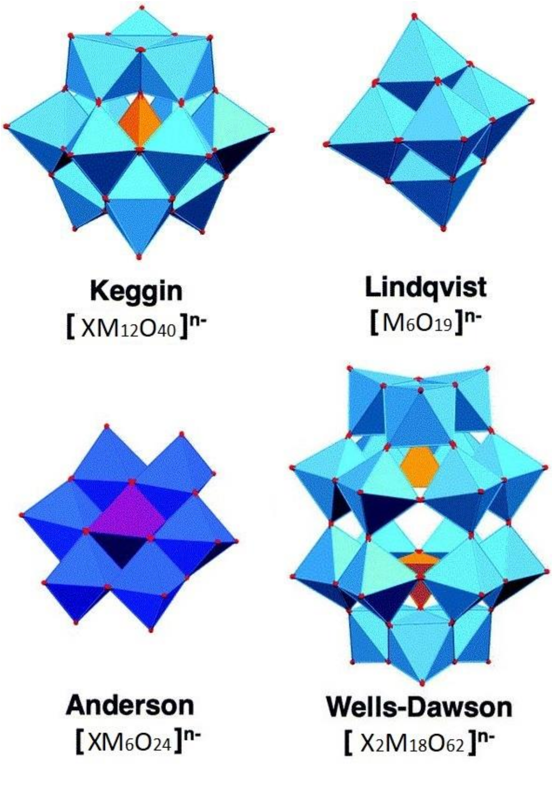

Figure 11 : Sturctures and formulas of common polyoxometalates, top-left : Keggin, top-right : Lindqvist, down-left : Anderson and down-right : Wells-Dawson

III.2 – Keggin POMs

Lastly, as this work focus particularly on Keggin POMs, a more detailed description of its structure and properties will be given. These POMs are named after the British chemist Peter Keggin, who first described their structure in 1933, their general formula is $[XM_{12}O_{40}]^{n-}$ and they are widely studied due to their structural and electronic properties. Additionally, Keggin POMs are relatively easy to synthesize and modify, making them attractive for researchers interested in exploring their properties and applications.

III.2.1 Structure of Keggin POMs

Keggin POMs have a spherical structure composed of 12 tetrahedral units, each tetrahedron contains a metal center most commonly a molybdenum or tungsten, surrounded by four oxygen atoms. The tetrahedra are linked by sharing oxygen atoms to form the larger spherical structure. The center of the structure is occupied by a heteroatom, typically phosphorus, silicon or boron in a center of tetrahedron as shown in Figure 12.

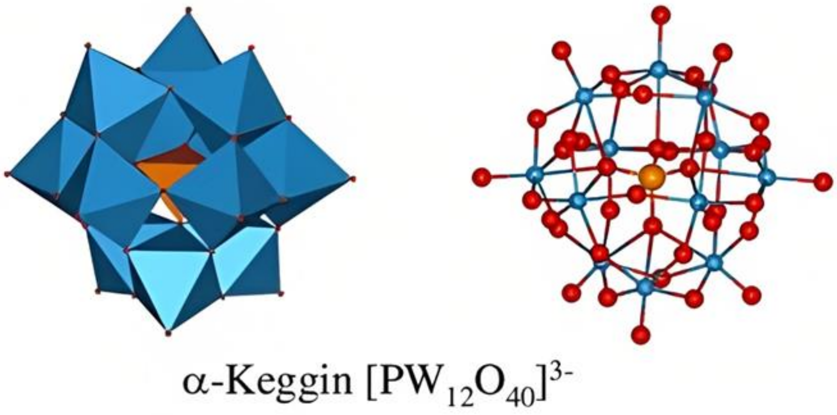

Figure 12 : Keggin POM structure with polyhedra (left) and ball and stick (right) representations with in red balls the oxygen atoms, in blue balls the tungsten atoms and in orange ball the central phosphorus atom

The physical size of Keggin POMs is around 1 to 2 nanometers, however, it can vary depending especially on the counter ion, for example, the $H_3[PMo_{12}O_{40}]$ has a reported structure of 1.3-1.4 nm[96] and the free anion $[PW_{12}O_{40}]^{3-}$ has a diameter of approximately 1.06 nm.[97]

III.2.2 Synthesis

The synthesis of Keggin polyoxometalates, as well as for other species, involves the reaction of metal salts such as MoO_4^{2-}, WO_4^{2-} and VO_4^{-3} in water using acidic reagents such as HCl. The reaction is carried out through a condensation reaction between two metal centers coordinated to OH ligands which are formed by the addition of the acid. The condensation reaction continues adding metal-oxygen to the structure until the highly stable electronic structure of the POM is reached. The presence of the desired heteroatom in stoichiometric amount in the starting material leads to the Keggin structure, and due to the electrostatic interactions, the cationic heteroatom occupy the center of the MO_6 anions (Figure 13).[98,99]

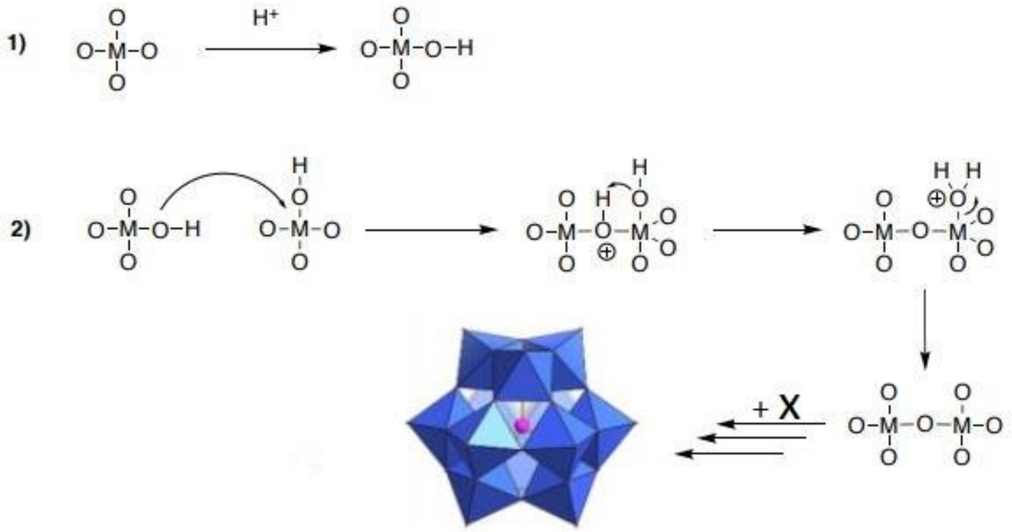

Figure 13 : Synthesis steps of keggin POMs (general formula $[XM_{12}O_{40}]^{n-}$)

Lacunar and functionalized hybrid Keggin POMs can also be synthesized, in order to modify their properties and increase their applicability in various fields.

LK-POMs consist of a Keggin-type polyoxometalate anion with one or more missing metal atoms, resulting in a "lacuna" or vacancy in the cluster structure, entire and lacunar Keggin POMs are shown in Figure 14. Their synthesis is a process that require a careful increase of the pH, and basically, it consists of treating the pristine Keggin POM with a base such as carbonate or hydroxide in water to reach a pH range of stability of the desired lacunar species[100]. The lacunar POMs possesses much more nucleophilic oxygen atoms at the edges of the vacancies, as well as higher negative charge compare to the pristine Keggin POM.

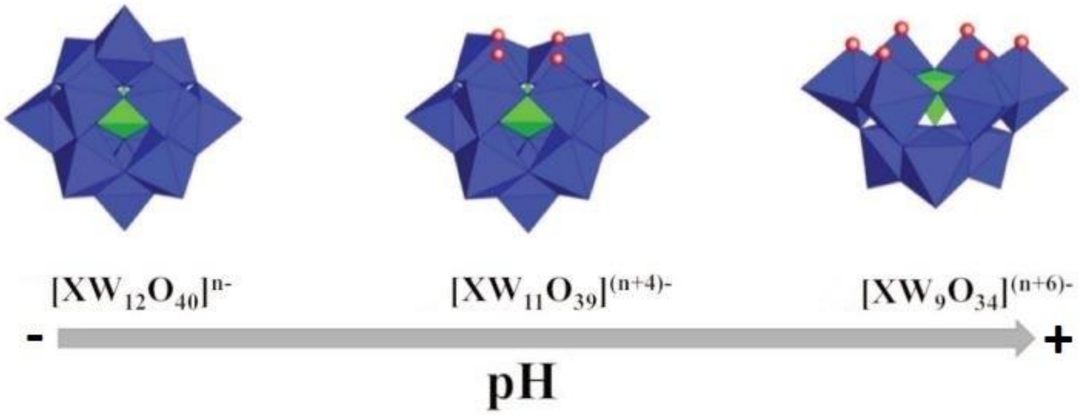

Figure 14 : Formation of lacunar Keggin POMs by increasing the pH in solution

These lacunar species, $[XM_{11}O_{39}]^{(n+4)-}$ or $[XM_9O_{34}]^{(n+6)-}$, are particularly interesting because they allow the incorporation of an organic tail to the POM structure, to form a functionalized hybrid Keggin POM. Their nucleophilic oxygen atoms form bonds with an electrophilic organometallic compound (Figure 15).[101,102]

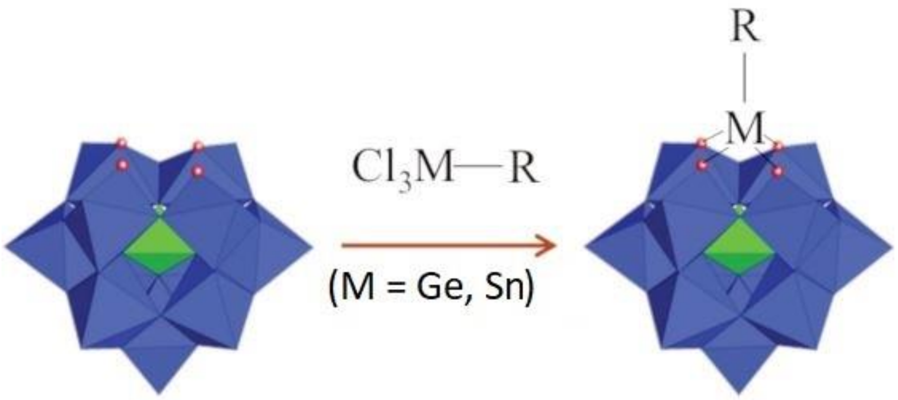

Figure 15 : Synthesis of functionalized hybrid Keggin POM (General formula $[XM_{11}O_{39}\{M(R)\}]^{n-}$) (M≠M)

III.2.3 Properties of Keggin POMs

Keggin POMs exhibit a great variety of interesting properties that makes them attractive for several applications. One of their most notable properties is their redox activity. They can undergo reversible redox reactions (Figure 16), which makes them useful as electrocatalysts[103] or a variety of reactions, including the oxygen evolution reaction (OER) and hydrogen evolution reaction (HER), redox properties are also useful in the domain of molecular electronics[104]. Their redox properties can be tuned by substituting one or more metal center in the structure, as reported by Laurans *et al.*[105] for the Keggin hybrid POM $(TBA)_4[PW_9Mo_2O_{39}\{Sn(C_6H_4I)\}]$. Some POMs exhibit photoredox activities which allows them to be used in the field of photochromic materials, as shown for the substituted POMs $K_{3+n}[PW_{12-n}V_nO_{40}]$ (n = 1, 2, 3) in the work conducted by Wang *et al.*[106]. Finally, their interesting reversible redox states addition allows them to act as charge storage materials in electrochemical devices[107].

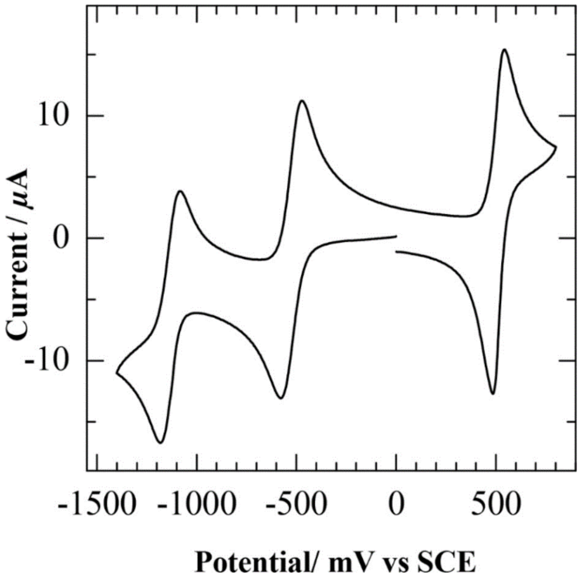

Figure 16: Cyclic voltammogram showing the multiple reversible redox states of functionalized Keggin POM $(TBA)_4[PW_9Mo_2O_{39}\{Sn(C_6H_4I)\}]$[105]

Keggin POMs that carries an H^+ counter-cations are also known for having high acidity, which makes them useful in acid-catalyzed reactions[108–110]. They can act as solid acid catalysts for heterogeneous catalysts for a variety of organic reactions such as C-C bond formation.[111]

Concerning the magnetic properties of Keggin POMs, it arises from the presence of paramagnetic metal centers, such as molybdenum or tungsten (when the POMs are reduced), in the Keggin structure. The paramagnetic centers have unpaired electrons, which give rise to a magnetic moment and can interact with each other, leading to magnetic ordering or spin-dependent interactions. The magnetic behavior of the POM depends on the metal center and its oxidation states, the number and arrangement of paramagnetic centers in the structure, and the presence of counterions and their nature.[112]

Some Keggin POMs show paramagnetic behavior due to isolated transition metals in the structure, as shown by Rong *et al.*[113] for the $[PW_{11}O_{39}Ru(L)]^{4-}$ (with L = H_2O, pyridine, dimethyl sulfoxide), while others exhibit antiferromagnetic or ferromagnetic interactions between paramagnetic centers resulting in magnetic ordering, we can cite for example the reported Keggin POM $\{[Cu(phen)]_2[SiMo_{12}O_{40}(VO)_2]\}^{2-}$ (Figure 17)[114,115]. In addition, some Keggin POMs can display spin-crossover behavior, where a change in temperature or pressure induces a transition between low- and high-spin states of the paramagnetic centers (such as iron).[116]

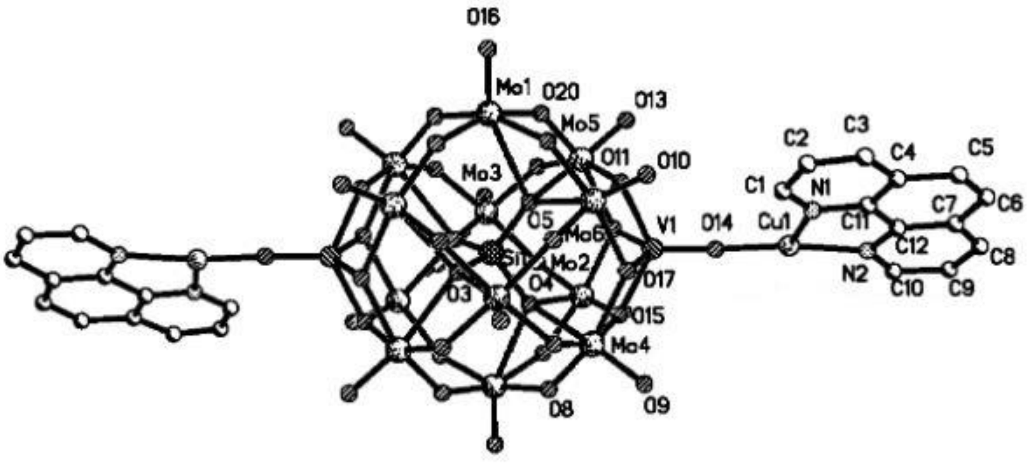

Figure 17: Structure of the $\{[Cu(phen)]_2[SiMo_{12}O_{40}(VO)_2]\}^{2-}$ Keggin POM[115]

Thus, magnetic properties of Keggin POMs can be tuned by modifying the composition and structure of the compounds. This versatility makes Keggin POMs attractive for a range of applications, including as magnetic materials, catalysts, and sensors.

III.3 – 2D organization of POMs at molecular scale on surface

Many attempts to organize polyoxometalates into thin films, monolayers and organized sub-monolayer for various applications such as data and energy storage were conducted during these past two decades[117–119]. Based on the bottom-up approach and using POMs and several types of other molecules as building blocks, this approach is the most commonly attempted and gave generally positive results concerning the obtainment of thin films or monolayers on surface. Sub-monolayers of POMs on surfaces however are less commonly reported, and even in the rare articles were such systems are described, POMs are not enough organized on the surface or not individualized, indeed, most of the works in this field report POMs forming small clusters of several molecules randomly deposited on the surface, or individual POMs trapped in the defects of the substrate without any periodicity or even organization. To this day, no work has reported a sub-monolayer of POMs, individualized being isolated from each other, and at the same time organized periodically on a surface.

One method to obtain a monolayer or multilayer film of POMs is to deposit them using the Langmuir-Blodgett technique. Langmuir-Blodgett films was reported several times in the literature, one example is the work done by Clemente-León *et al.*[120–122] they made and characterized those films using techniques such as surface pressure-area isotherm, infrared spectroscopy, X-ray diffraction and cyclic voltammetry.

The use of layer by layer deposition is also a viable approach to make monolayer or multilayer film of POMs on surface. The method is reported by Li *et al.*[123] were they succeeded to make a monolayer of POMs on a substrate as well as GO (graphite oxide)-POM multilayers. Basically, they deposited first a PEI (Polyethylenimine) film on different substrates (quartz glass, silicon and PET) by dip-coating in a 2.5 mg/mL PEI solution for 15 min, the substrate is then rinsed and dried and dip-coated again in a soltion of $H_3[PW_{12}O_{40}]$ at 1 mg/ml during 15 min to form the monolayer of POMs. To make the POM-GO multilayers, they dip-coated the previous substrate containing the monolayer of POMs in a solution of 2 mg/ml PAH (Polyhydroxyalcanoate) followed by a subsequent 20 min immersion in a 0.3 mg/mL GO water solution, they repeated this dip-coating depositions of polymer and POMs to obtain a thin film (Figure 18). It’s interesting to notice that the structure obtained by this layer by layer dip-coating deposition rely on electrostatic interactions for the self-assembly. They fabricated then field effect transistors based on this composite film and characterized them.

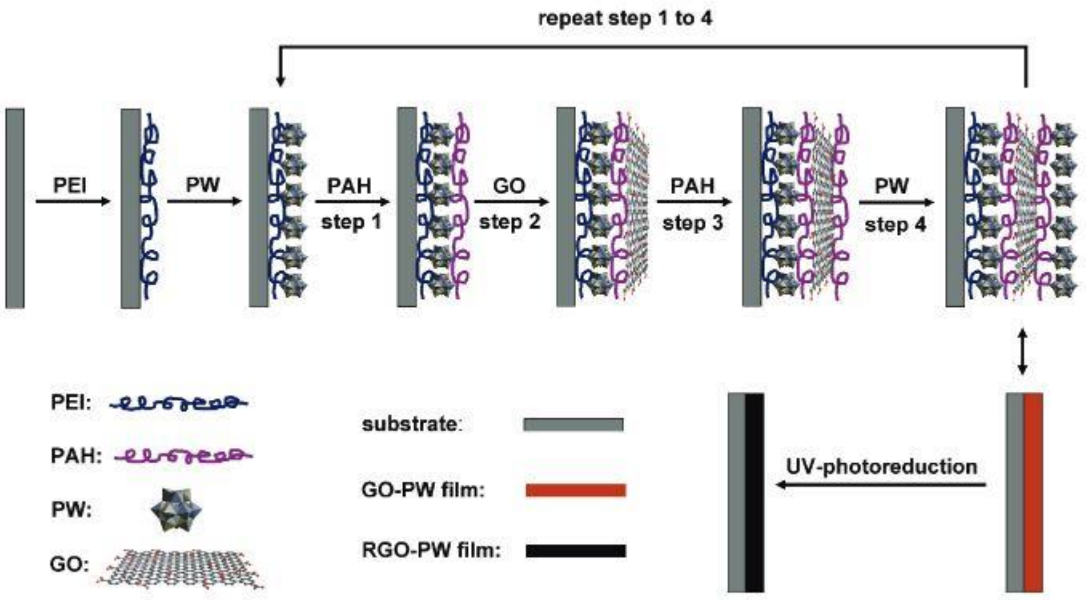

Figure 18 : Layer by layer dip-coating deposition of GO-POMs to form composite thin film[123]

A different reported method for shaping POMs into a monolayer is to use a covalent grafting of POMs on the substrate, this method requires several synthesis steps on the POM to functionalize it with the desired terminal functions for the grafting, as it involves hybrid functionalized POMs. An example of this technique is shown in the work of Laurans *et al*. The method is based on functionalizing the POM itself with a carboxylic acid terminal function to graft it onto Si/SiO_2 flat substrate to form homogeneous and flat monolayer[117] (Figure 19), other works using different types of terminal functions on the POMs to graft them covalently on different substrates validate the use of this approach.[124–126]

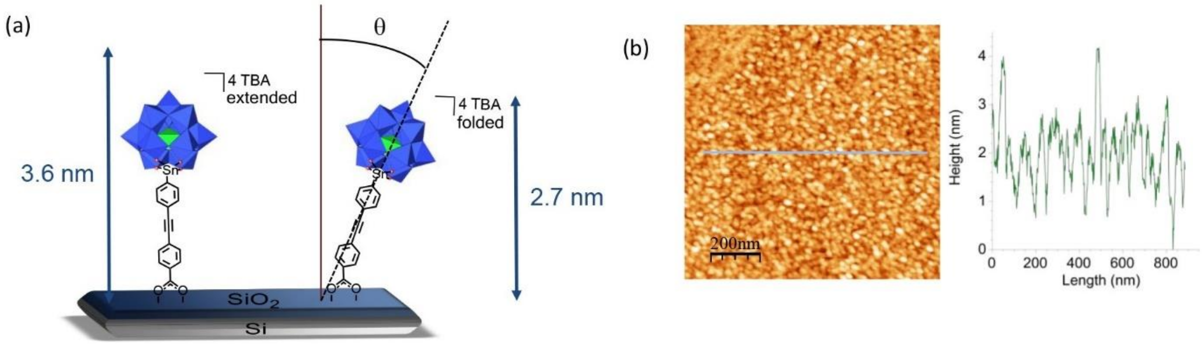

Figure 19 : (a) Schema of the different angles of grafting of the POM on Si/SiO_2 substrate and theoritical hights (b) AFM image of the grafted substrate and hight profile of the surface[117]

Another approach using electrostatic interactions on substrate modified by grafting molecules is reported[127–129]. The differences with the previous grafting method is that herein, the functionalization is operated on the substrate by grafting molecules at its surface which present a function able to be protonated to generate positive charges. POMs are then attached using electrostatic interactions. Two ways to attach POMs electrostatically are possible, first, a ion exchange between a POM and the surface can be done[130,131] second, as many of them can also be obtained as an acid salt, they can be used directly to protonate the surface. An example of well controlled monolayer using electrostatic interactions provided by a functionalized substrate is reported by Dalla Francesca *et al.* A substrate of Au(111) is prepared by grafting ammonium alkane chains, 6-Amino-1-hexanethiol hydrochloride, on the surface using the thiol function, the substrate is then treated to adjust the ratio NH_2/NH_3^+ and POMs are deposited by deep coating the substrate in a solution of 1 mM POMs in acetonitrile[132] (Figure 20).

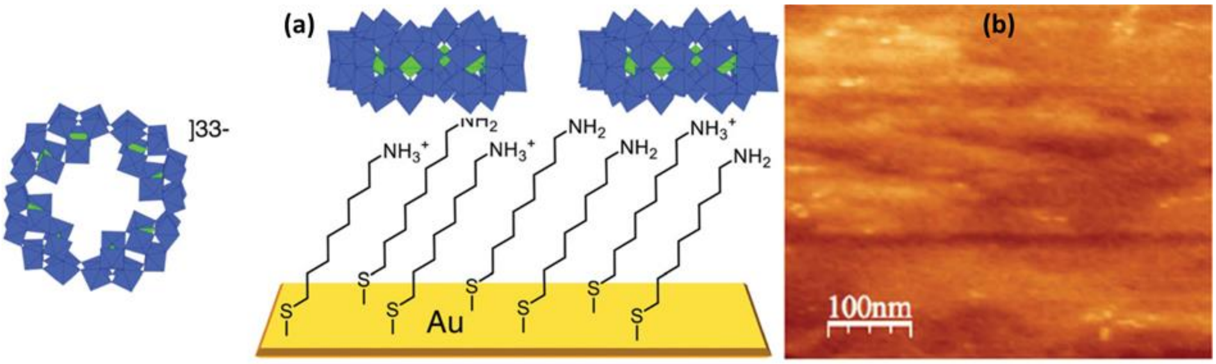

Figure 20 : Polyhedral representation $[H_7P_8W_{48}O_{184}]^{33-}$(color code:$WO_6$ octahedra blue, PO_4 tetrahedra green) and schematization (not atscale) of its electrostatic deposition onto a 8-amino-1-octanethiol (AOT)SAM. The POM has a wheel-shaped structure with a diameter of~2.0 nm and a thickness of ~1.0 nm. (b) AFM image of deposited layer of the POMs on functionalized surface of Au(111) with the 8-amino-1-octanethiol[132]

As it was shown by the different characterization techniques, these approaches give a thin film or a monolayer of POMs on the surface without reaching the molecular individually organized system, in the other hand, it is known that the design for single molecular memory devices have to respect some very specific conditions, such as individualized addressable molecules avoiding collective effect with neighbors[133,134], densely packed system in order to optimize the data storage density.[135]

Other works were carried out to isolate POMs individually on a surface in order to probe the properties of a single molecule, however it consisted to trap them randomly in the surface defects or in the break-junction set-ups[136–138]. An example we can cite is reported by Linnenberg *et al.*[139] were they managed to isolate Lindqvist functionalized POM $(nBu_4N)_2[V_6O_{13}\{(OCH_2)_3CCH_2SC_6H_5\}_2]$ on a surface of Au(111), taking advantage of its low charge to avoid the highly relevant problem of agglomeration shown for example for the $[V^{IV}_{10}V^{V}_{8}O_{42}(I)]^{5-}$ Dawson POM[136] by reducing the POM to POM electrostatic interactions. However, even if they succeeded to individualise POMs on the substrate, no organisation was reached and the POMs were randomly distributed, forming small clusters located in different areas of the surface (Figure 21).

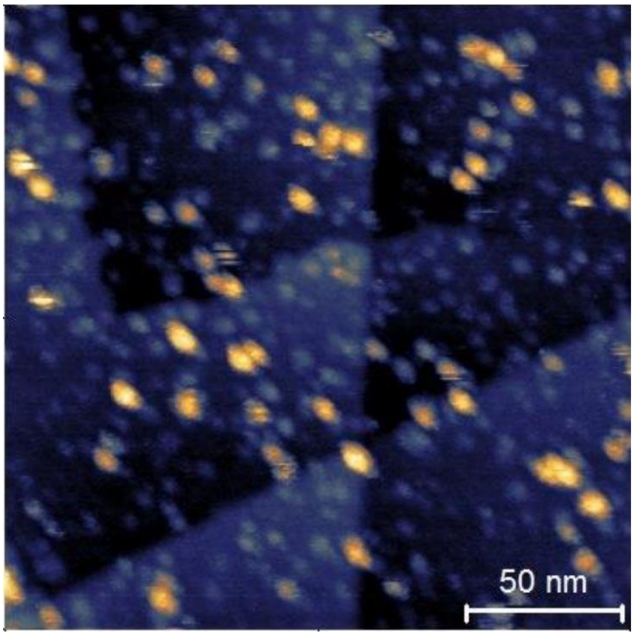

Figure 21 : STM image of $(nBu_4N)_2[V_6O_{13}\{(OCH_2)_3CCH_2SC_6H_5\}_2]$ *on Au(111) (SI ref. 139)*[139]

The rare attempts made in order to periodically organize POMs at a molecular scale and individually isolated from each other on surface have failed[140]. Indeed, POMs tend to form aggregates because of POM to POM electrostatic interaction in solution[141] which make them difficult to assemble into ordered structures, particularly at a molecular scale on a surface. One of the closest attempts to build such material is the work reported by Lombana *et al.*[140] using a nanoporous template of self-assembled organic molecules to help for the separation and individualization of the POMs, it resulted by having two or three molecules per pore but it demonstrated the encouraging results and the great potential of this method to reach this type of organization (Figure 22).

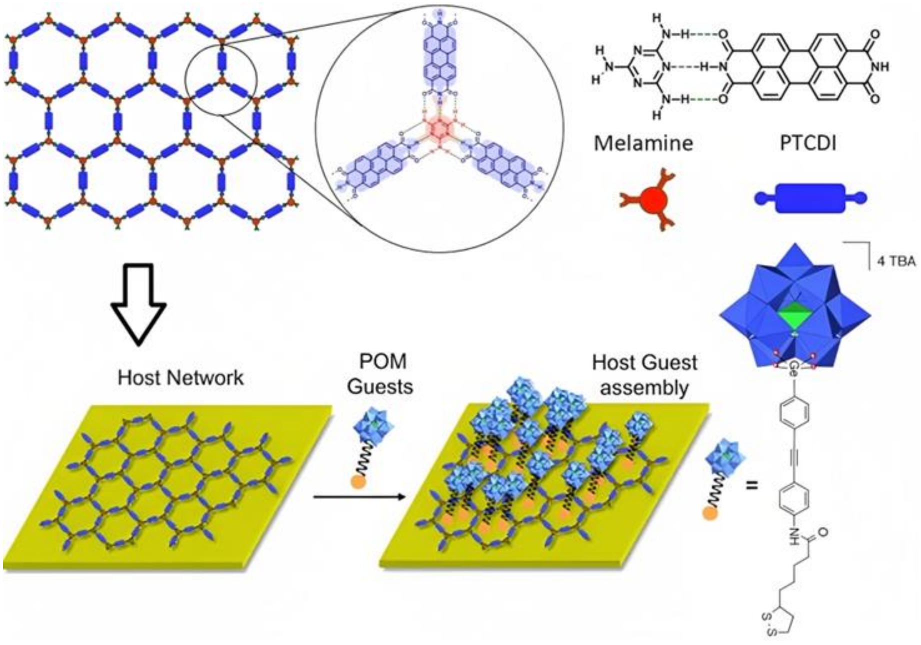

Figure 22 : Controled grafting of functionalized POM on Au(111) using a template of self-assembled organic molecules layer[140]

Another work reported by Zhang *et al.*[142] likely show the organization of $K_{12}Na_2H_2[Ir_2C_{l8}P_2W_{20}O_{72}]$ and $Na_8[HPW_9O_{34}]$ POMs on HOPG through the use of a 2D network of self-assembled molecules on its surface. However, in this article, the authors rely solely on STM images without analyzing the apparent height of the two POMs to compare it between them or to the corresponding heights that can be expected from each POM. Furthermore, they did not provide any chemical characterization of the surface that could tend to show that these observed molecules are indeed the POMs. Taking in account that one of the main limitations of STM is the chemical analysis, the self-assembly of POMs reported in this study can only remain at the level of hypothesis. However, these promising results show once more the interest of using a 2D template to induce the organization of POMs on surface.

Thus, during this project we will use the same method of functionalized substrates with templates directing the organization of polyoxometalates.

IV – Surface patterning of self-assembled molecules into 2D networks

Self-assembly is a process where molecules spontaneously assemble into ordered structures without external intervention[143], it is a key point for the design and fabrication of molecular electronic devices, indeed, this process enables the creation of highly ordered and well-defined structures at the nanoscale level, which is crucial for the development of high-density data storage devices[144,145]. One important property of self-assembling molecules is the ability to form stable and well-defined monolayers on surfaces which can act as templates for the deposition of additional layers or for the incorporation of other molecules[146]. Self-assembling molecules with specific functional groups can also bind selectively to certain substrates, allowing for precise control over the assembly process.[147,148]

Another important property is the ability to form multilayer structures with a high degree of order, through layer by layer deposition methods such as drop-casting and dip coating. This allows for the creation of complex architectures with precise control over the positioning and orientation of the molecules, an interesting example of such self-assembled systems were reported by Brisse *et al.*[149] using first a conjugated self-assembly molecule 1,3,5-tris((E)-3,5-bis(dodecyloxy)styryl)benzene to functionalize HOPG substrate forming a periodic nanoporous 2D network on its surface, then secondly, adding a zinc phtalocyanine coordinated to a ligand (1-(pyridin-4-ylmethyl)pyrrole-2,5-dione named L) with pyridine terminal function that occupy these nanopores, leading to a molecules organized periodically on the surface (Figure 23). This example illustrates well the layer by layer self-assembly process, involving different types of non-covalent interactions and allowing the fabrication of complex structures on surface. These structures can be used to create well-defined pathways for charge or spin transport, as well as the positioning and distribution of functions of interest on the surface, which is essential for the development of molecular materials.[150]

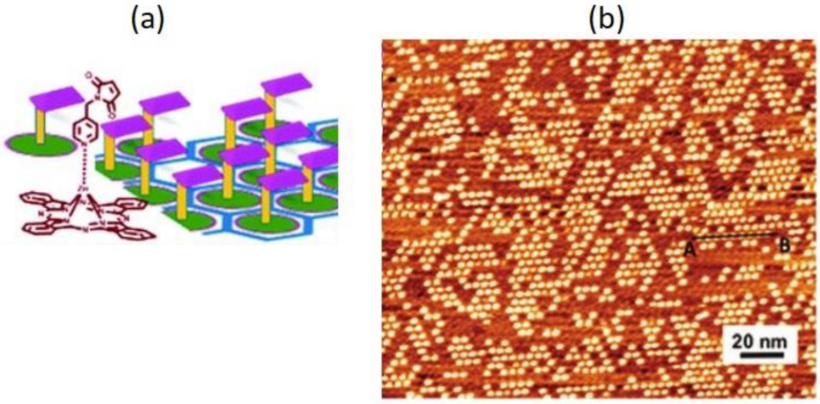

Figure 23 : Nanoporous monolayer of TSB3,5-C12 molecules after the addition, by drop-casting, of ZnPc-L complex molecules, 200 nm 200 nm STM image at the air/HOPG interface in the current mode with 1.3 V and 12 pA as the sample bias and tunneling current, respectively[149]

The self-assembly of molecules into 2D networks for surface patterning has been of great interest in recent years due to its potential applications in fields such as electronics, optoelectronics, and sensing.[151–153] The recent advances in experimental techniques such as scanning tunneling microscopy and atomic force microscopy have also enabled researchers to observe the self-assembly of molecules into 2D networks at the atomic scale[154–156]. This has allowed for a deeper understanding of the intermolecular interactions that drive the self-assembly process and has opened up new possibilities for the design of functional materials.

IV.1 – Molecular interactions of self-assembled systems

The mechanism of self-assembly is governed by a variety of intermolecular interactions, including hydrogen bonding, van der Waals interactions, electrostatic interactions, and π-π stacking interactions[157]. Each of these interactions can play a different role in determining the structure and properties of the resulting structure shape. For example, van der Waals interactions can be used to promote the packing of molecules into a dense ordered structure, while hydrogen bonding between complementary functional groups can be used to direct the assembly of molecules into specific patterns.[158,159] The interactions involved in the self-assembly process are basically non-covalent, the main ones can are hydrogen bonding, van der Waals forces, coordination bonding and electrostatic interactions. They can be classed according to their strength (Figure 24), and they occur between the same type and/or different molecules to give a large panel of shapes. In addition to the interactions between the molecules, the molecule/substrate interactions are crucial as well for the self-assembly process as it is a fine equilibrium between molecule-molecule interaction and molecule-substrate interaction that leads to highly ordered molecular systems.

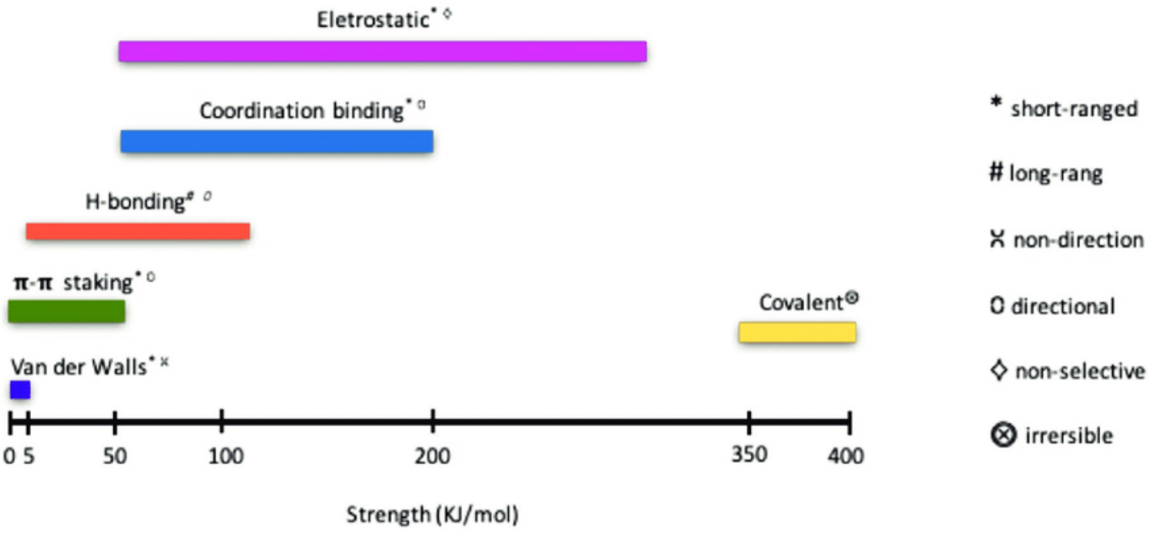

Figure 24 : Average range of strength of non-covalent interactions and their properties[160]

More complex structures can also be obtained relying particularly on host-guest interactions, as shown by several teams using molecules such as coronene, porphyrins, phtalocyanines…etc. as guests, on host substrates composed of 2D self-assembled conjugated molecules leading to nanopores on its surface[161–163]. The deposition of these molecules is made generally layer by layer, on the clean virgin substrate a first self-assembling molecule is deposited to form the 2D network with the nanopores, and then the desired molecule to trap inside the pores is deposited. The deposition is generally done by drop-casting a highly diluted solution of these molecules in an organic solvent.[164,165] This principle of host/guest molecules can be used at every stage of material design, allowing the bottom-up fabrication of high complex structure with a controlled molecular arrangement. For instance, the porphyrin and phtalocyanine molecules previously used as guests can then be used as host molecules using their metal center, such as zinc, to attach a new guest molecule thanks to the formation of a coordination bond.[149,150,166]

Understanding molecular interactions is crucial in designing and building self-assembling 2D molecular systems. These interactions determine the shape and orientation of the individual molecules in the system. The comprehension of these interactions will allow the design of molecules that will assemble in specific ways to create a desired structure or pattern.

IV.1.1 Hydrogen bonds

Hydrogen bonding is a fundamental chemical interaction that plays a crucial role in self-assembling processes. It occurs between hydrogen bonded to an electronegative atom such as oxygen or nitrogen and another electronegative atom carrying a free pair of electrons. They are generally represented by dotted lines and are weak bonds relatively to covalent ones, the energy required to break the OH covalent bond (the bond dissociation energy) is about 464 kJ/mol, while comparatively, the energy required to break an O---H hydrogen bond is about 21 kJ/mol, so less than 5% of the energy of a real covalent bond.

Hydrogen bonds are directional;[167,168] it means that it is aligned in the axis of the valence bond that is associated with it. For example, in water, the three atoms O, H and O forming the hydrogen bond are aligned. This property allows to have very well defined molecular architectures, as in ice or in water at short distance, or in biological molecules such as proteins, or DNA whose two strands are linked together by hydrogen bonds (Figure 25). This property is also involved during self-assembling processes and participates into the orientation and shape of the final structure.

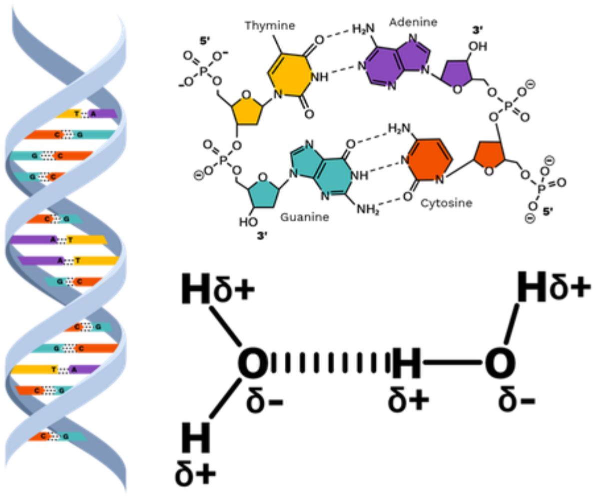

Figure 25 : Diractional hydrogen bonds between proteins contributing to give its shape to DNA[169]

IV.1.2 π-π stacking

For the self-assemblies of conjugated molecules on surface, π-π stacking is the preponderant interaction. It is non-covalent attractive interaction involving π bonds of aromatic rings and allowing them to stack together. Typically, the separation between the two stacked molecules is 0.34 nm. The π-stacking can occur in either eclipsed or displaced arrangement, in the case of a dimer stacking a slight displacement between the two molecules is generally preferred to avoid electron repulsions, as shown in Figure 26, the attraction occur between the sigma framework of one molecule and the π electrons of the other.[170]

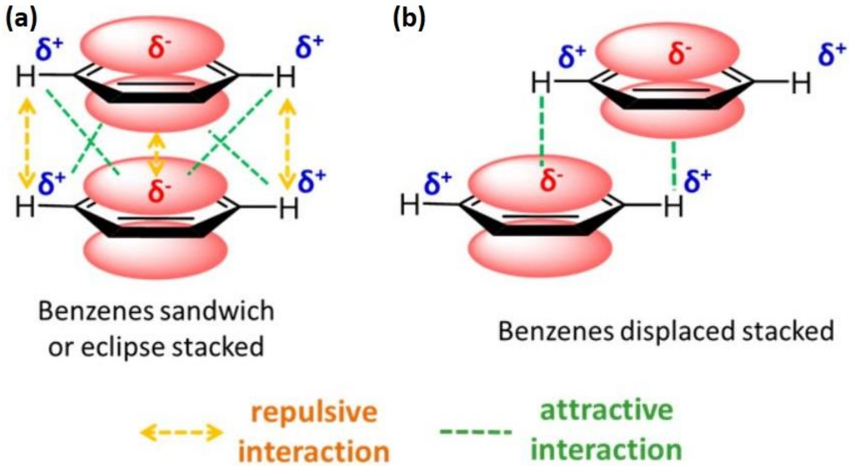

Figure 26 : Schema attractive and repulsive interactions in stacking of two benzene molecules (a) eclipsed stacking (b) displaced stacking[171]

In the case of the stacking between two different molecules, the eclipsed stacking could be preferred, for instance, for a benzene ring substituted with electronegative atoms such as fluorine the polarity of the ring is reversed and the eclipsed stacking is favored as shown in Figure 27.[172]

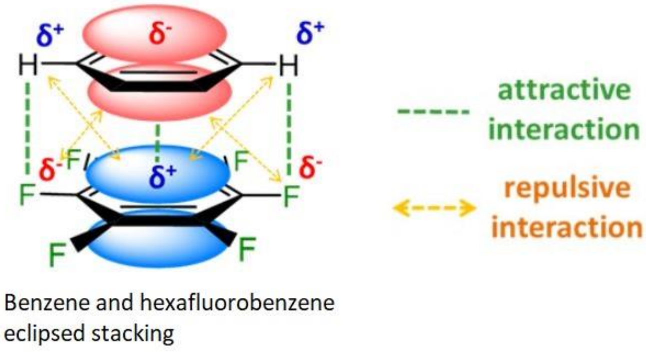

Figure 27 : Schema of the favored eclipsed stacking interactions between benzene and hexafluorobenzene[171]

As the interaction relies on overlapping of p orbitals in π-conjugated systems, its strength increase as the number of π-electrons increases, thus, highly conjugated flat polycyclic aromatic hydrocarbons such as pentacene, coronene or phtalocyanines exhibit strong π-stacking effect. This property plays a crucial role in various parts of supramolecular chemistry, allowing molecules to form organized mono or multilayers by π-stacking on the surface of substrates such as graphene or gold, rather than to be randomly distributed on the surface. However, the orientation of the molecules ones they are π-stacked depend mostly on the intermolecular interactions, such as hydrogen bonding as we it was described previously, or Van-der-Waals interactions, that gives these highly organized and periodic distribution.

IV.1.3 Van-der-Waals forces (VdW)

Van-der-Walls forces are attractive interactions and the weakest among non-covalent ones. They are from electrostatic origin and are a combination of three forces resulting from different effects, Debaye, Keesom and London forces, the resulting VdW force operate at very short range[160]. Their strength varies proportionally to the equation $1/R^7$ while it's $1/R^2$ for electrostatic forces, with R the distance between the two atoms. Typically, the energy range of VdW forces vary between less than 1 $kj.mol^{-1}$ to 4 $kj.mol^{-1}$, making the dissociation of the molecules easy and giving flexibility to the system.

The main role of VdW forces in the self-assembly process is the ordering and cohesion of alkyl chains[173], for instance, in 2D assemblies they control the structure and phase transitions in the system as shown by Gao *et al.*[174].

IV.1.4 Electrostatic interactions

Electrostatic interactions, also referred to as ionic bonding, are short-ranged, non-selective and the strongest non-covalent interactions (see Figure 24). They occur between two oppositely charged molecules. The strength of the ionic interaction depends on the charges of the molecules, and it can be determined by a measure of the lattice energy of the compound. In general, the energy of electrostatic interactions varies from hundreds to thousands $kj.mol^{-1}$, though, as these interactions are not directional, even with this remarkably high energy and strong stability in solid state, the ionic bond can be easily interrupted or broken in some solvents such as water or ionic liquids. This versatility makes electrostatic interactions interesting for the conception of mechanically robust and chemically reversible supramolecular materials.

Electrostatic interactions are widely used in self-assembling processes, in a specific branch of supramolecular chemistry called ionic self-assembly (ISA), for the conception of structures such as self-complementary peptides[175], self-assembling surfactant[176] and polyelectrolytes[177]. In 2D self-assemblies on surfaces, these interactions are mostly used to attach inorganic molecules and form thin films or monolayers, in particular for POMs deposition on the surface.[178]

IV.1.5 Coordination bonding

For coordination bond, the electrons are provided entirely by one of the two involved atoms, in contrast, for a covalent bond, the pair of electrons is equally shared between the two involved atoms. Coordination bonds are formed between a Lewis acid such as a transition metal and a Lewis base, a molecule able to donate at least one pair of electrons and called ligand. The Lewis acid, metal or ion, occupy a central position and the ligands surround it. Several ligands can be coordinated to the same metal or ion to create a coordination sphere and form complexes with various geometries.

Coordination bonds are generally weaker than covalent or ionic ones, their bonding energy varies between 60 to 300 $kJ.mol^{-1}$, making them stronger than other non-covalent interactions[173].

In self-assembly, coordination is used in several reported works to synthesize supramolecular materials, mostly for metal organic frameworks[179,180], but also to attach molecules on functionalized surfaces with highly organized and periodic disposition[149,181]. One example of the use of coordination for self-assembly on surface is reported by Li *et al.*[166] where they studied the coordination of 1, 3-di (4-pyridyl) propane to a zinc phtalocyanine pi-stacked on surface. They made an organized self-assembled structure through a layer by layer drop casting process, starting by the deposition of 2, 6, 11-tricarboxydecyloxy-3, 7, 10-triundecyloxy triphenylene (asym-TTT) on HOPG to have a first 2D patterned substrate. They added by drop-casting zinc phtalocyanine (ZnPc) in toluene to have dimers adsorbed in the anisotropic rearrangement of the asym-TTT supramolecular network, then they drop-casted the 1, 3-di (4-pyridyl) propane to coordinate it to the ZnPc on surface as shown in Figure 28.

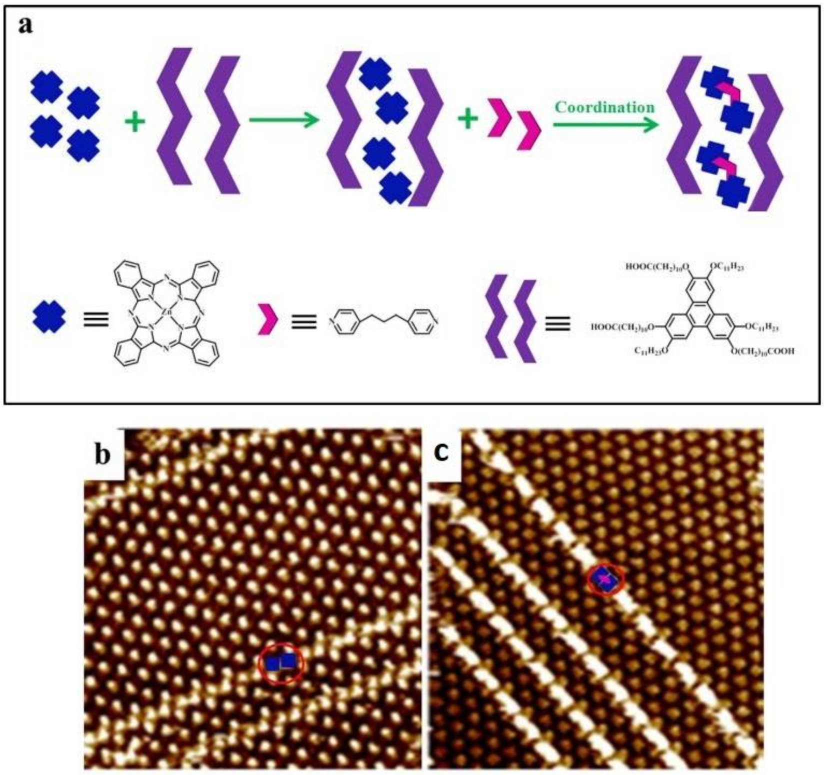

Figure 28 : (a) Schematic illustration of the formation of ZnPc/dipy-pra coordination (b) STM image showing assembled structure of asym-TTT/Zn-Pc (42.2 nm × 42.2 nm, Iset = 198.4 pA, Vbias = 600.0 mV) .(c) STM image showing entirely assembled structure of asym-TTT /Zn-Pc/dipy-pra system after the dipy-pra molecule was added (37.9 nm × 37.9 nm, Iset = 247.1 pA, Vbias = 1037 mV)[166]

Thus, coordination bonding has already demonstrated a great potential to self-assemble and organize molecules even in the particularly tricky field of surface chemistry.

IV.1.6 Host-guest approach

Host-guest systems stand apart from molecular interactions as described earlier. Yet, their existence hinges precisely upon these interactions. These systems hold immense significance in the realm of supramolecular 2D assemblies, offering the capability for meticulous, highly ordered, and periodic molecular-level organization on surfaces.[182]

Basically for 2D assemblies, the surface confined host-guest systems have drawn much attention, they are built by patterning substrates using self-assembling molecules that leads to periodically distributed nanopores, amongst them we can cite the porous networks made of the triangular phenylene-ethynylene macrocycles (DBA)[183], the hydrogen-bonded porous hexagonal network formed by benzene-1,3,5-tricarboxylic acid (TMA)[184], and the honeycomb network formed by the 1,3,5-tris((E)-3,5-bis(alkoxy)styryl)benzene (TSB).[185]

These systems were used to trap several types of molecules with this host-guest interaction in their nanopores to organize them periodically on the surface. Indeed, inside of these pores the substrate is exposed, acting as a host and allowing some specific molecules to pi-stack on it acting as guests. Amongst these guest molecules we can cite planar molecules such as polycyclic aromatic hydrocarbons compounds (coronene, pentacene…etc.), porphyrins, phtalocyanines and their derivatives and 3D molecules such as fullerene and its derivatives.

One example of this host-guest system is reported by Plas *et al.*[186] in this work they have first patterned an HOPG substrate using a boroxine-based covalent organic framework to have a 2D nanoporous network on the surface. Fullerene is then added on the surface of this substrate and act as a guest molecule spontaneously occupying the nanopores as shown in Figure 29.

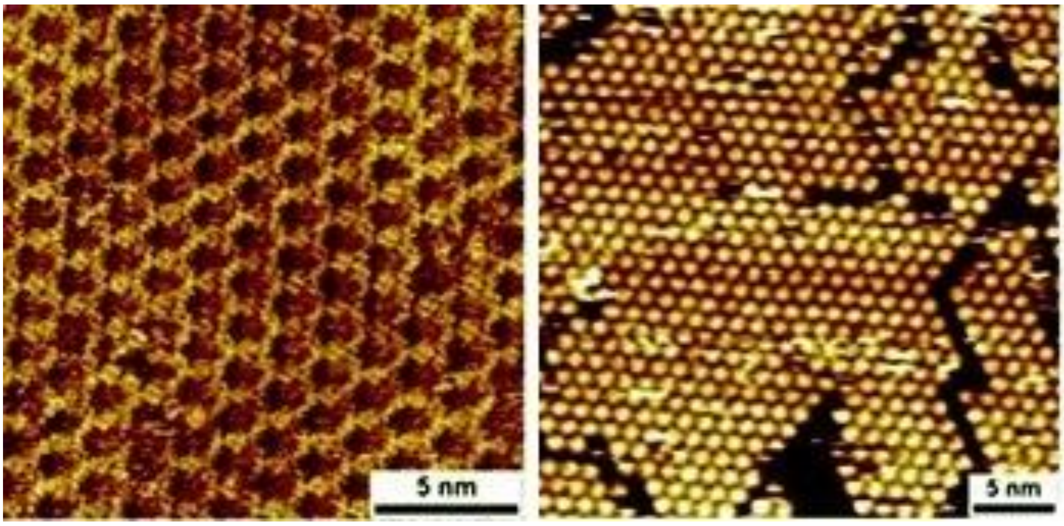

Figure 29 : STM image of the boroxine based covalent network exhibiting nanopores on the surface of the substrate (left) (Vbias = -0.600 V , Iset = 0.06 nA) and STM image of the substrate after deposition of C_{60} molecules that occupy the nanopores (right) (Vbias = -0.900 V, Iset = 0.02 nA)[186]

IV.2 – HOPG for bottom-up molecular patterning

One of the most widely used substrates for 2D self-assemblies is HOPG (highly oriented pyrolytic graphite)[187–190]. It is a carbon substrate produced by the pyrolysis of a highly ordered graphite crystal under controlled conditions. The resulting material has a highly ordered surface structure, with a flat surface and regularly spaced graphite layers oriented perpendicular to the surface[191]. The ordered surface structure of HOPG arises from the anisotropic growth of the graphite crystal during pyrolysis, which results in the alignment of the graphene layers in a particular direction (Figure 30).

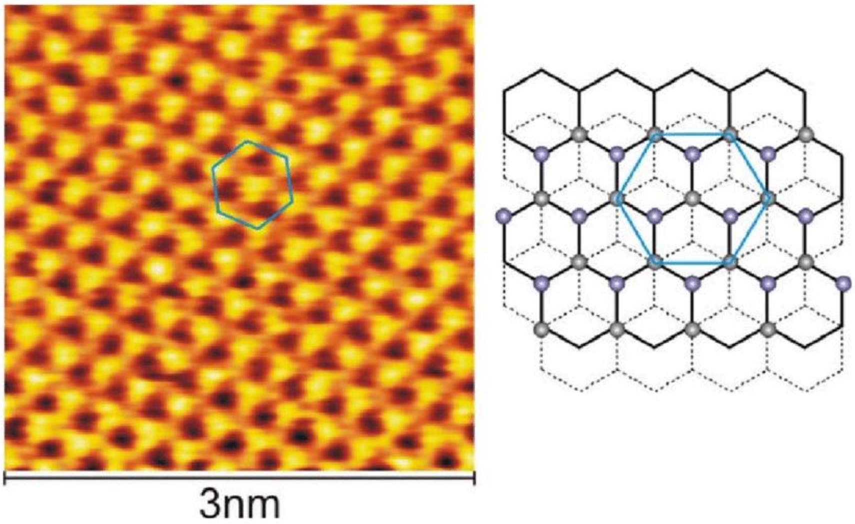

Figure 30 : STM image of the surface of HOPG (left), and scheme of its structure (right)[192]

The surface of HOPG is characterized by a high degree of structural perfection, with a low density of defects and a high degree of atomic flatness. The flatness of the HOPG surface make it an ideal substrate for the self-assembly of molecules, as it allows for precise positioning and alignment of the molecules on the surface. It also presents a good chemical stability, meaning that it does not react with most chemicals or biological molecules. This stability allows for long-term experiments, and makes it a privileged substrate for use under ambient conditions. In addition to its structural properties, HOPG is also characterized by its electrical conductivity[193], which makes it an ideal substrate for electronic applications. The conductivity of HOPG arises from the highly ordered nature of its surface structure, which allows for efficient charge transport across the surface.

Basically, the 2D self-assemblies of aromatic compounds on HOPG relies mainly on π-stacking interactions, then to induce an organization or orientation for the molecules on the surface, long alkyne chains can be incorporated to increase the distance from a molecule to another and VdW forces act to stabilize and organize them. Functions such as carboxylic acid, alcohol and amines can also be incorporated to the molecules to bind them to each other through hydrogen bonds and induce a specific arrangement.[159,194] This remarkable versatility can produce in theory infinite number of nanopatterns on HOPG by tuning the molecular building blocks.[195–198]

IV.3 – Self-assembly of tris-styrylbenzene (TSB) molecules and its derivatives on HOPG

Aromatic compounds are a widely studied class of molecules for self-assemblies, notably on HOPG substrates, to form 2D networks[164,165,199]. They present many interesting properties for surface functionalization, amongst them, their high surface area organization, pore size and shape selectivity, various 2D patterns networks, and electronic and optical properties. Particularly, tris-styrylbenzene (TSB) molecules and its derivatives have attracted a lot of attention for these reasons[200–203]. TSB are a class of aromatic symmetrical molecules composed of three phenyl rings attached through a double carbon-carbon bond to a central benzene in the positions 1,3,5 (Figure 31 (a)). The molecule can be tailored with many functions either on the central benzene and/or on the terminal phenyl groups to modify its electronic, structural and self-assembling properties.[204] Herein, we will particularly focus on the 1,3,5-tris((E)-3,5-bis(alkoxy)styryl)benzene derivatives of TSB molecule, noted TSB-3,5 with n = 8, 10, 12 (Figure 31 (b)).

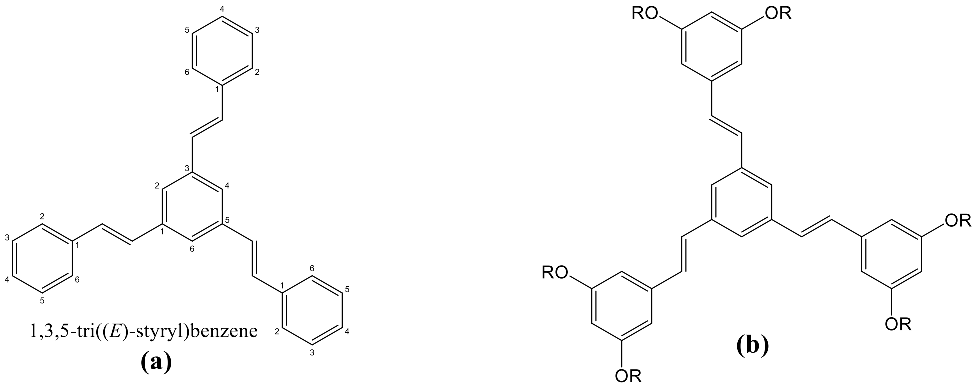

Figure 31 : (a) Schema of tris-styrylbenzene molecule (b) schelma of 1,3,5-tris((E)-3,5-bis(alkoxy)styryl)benzene with R = C_8H_{17}, $C_{10}H_{21}$, $C_{12}H_{25}$

The method of deposition consists of drop casting a highly diluted solution of TSB in toluene on a freshly cleaved HOPG substrate, the solvent is then allowed to evaporate at ambient conditions. The STM images are then either made directly on air, or a solution of phenyloctane is dropped on the sample surface and STM images are made at the liquid/solid interface. STM images made in these conditions (liqid/solid) exhibit a better quality. Indeed, the solvent used (phenyloctane in this case) should have a high boiling point (262 °C for 1-phenyloctane) to remain on the surface during the entire experiment and ensure to perfectly insulate the STM tip and the surface from any molecules present in air that could disturb the imaging process by interacting with the STM tip. However, the deposition of such solvent that has high boiling point could be problematic for the sample, in the case for example where another layer of molecules needs to be added after the imaging. The method is reported in several works using TSB self-assemblies.[165,205] Another original technique to form a monolayer of self-assembled TSB molecules on HOPG was reported by Bléger *et al.* consisting in immersing the STM tip in a droplet (10 µl) of 10^{-4} mol.L^{-1} solution of TSB in toluene and to approach the tip to a substrate of HOPG wetted with phenyloctane, imaging is then carried at the liquid/solid interface.[185]

The supramolecular arrangement of TSB-3,5 molecules on HOPG shown by STM forms large areas of highly organized 2D network, the molecule appear on the surface as a small triangle forming two different structures, honeycomb (or hexagonal), and herringbone structure (Figure 32). The arrangement of the molecule depends on several parameters including the temperature, concentration of the deposited solution. An example of the parameters driving the arrangement of TSB-C3,5 is reported by Bellec *et al.* They have shown that a deposition of TSB-C3,5-C12 on a cooled substrate (12°C) leads to poor organized network, then after heating this substrate for 30 min at 60 °C, a herringbone network is formed. But, when the same TSB-C3,5-C12 (same concentration) is deposited directly on HOPG at 60 °C, honeycomb arrangement is obtained. These results show that temperature certainly play a role in the organization of tht TSB-3,5-C12, but the final arrangement depend on growth history as well.[200] The length of the alkoxy chains is also important for the arrangement of the TSB-C3,5. Indeed, it is reported that for 8 and 10 carbons, the molecules forms mostly honeycomb network. At 12 carbons or at 14 carbons the self-assembling tends to form herringbone networks much more easily.[204]

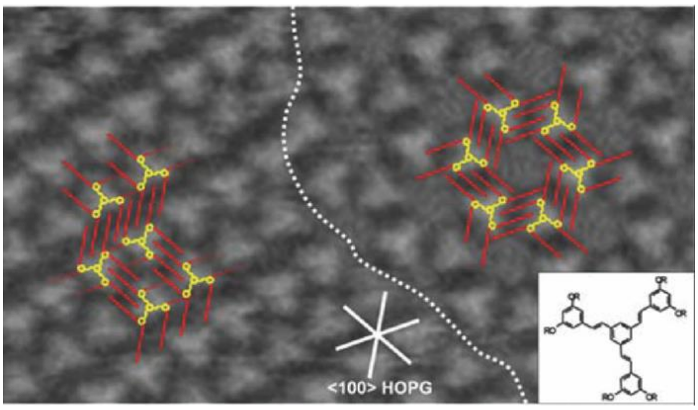

Figure 32 : STM image of the two different organizations of TCB-3,5 on HOPG, left herringbones and right hexagons (or honeycomb) (Vbias = –970 mV, Iset = 14 pA)[200]

The length of the alkoxy chains can be modified. As mentioned, TSB molecules for self-assemblies are synthesized with chains of 8 up to 14 carbons, allowing shaping the size of the nanopores of the 2D network by increasing or decreasing the distance between 2 molecules in function of carbon chains length as shown in Figure 33 and table 1. This ability to control the sizes of the pores makes the substrate functionalized with this molecule tunable to selectively trap and organize molecules of various sizes. Nevertheless, it's important to observe that the network's stability is influenced by the length of these alkoxy chains. Specifically, the stability ranges from 8 to 14 carbons; beyond or below this range, the network's stability is impacted, resulting in significantly less organized areas.[204]

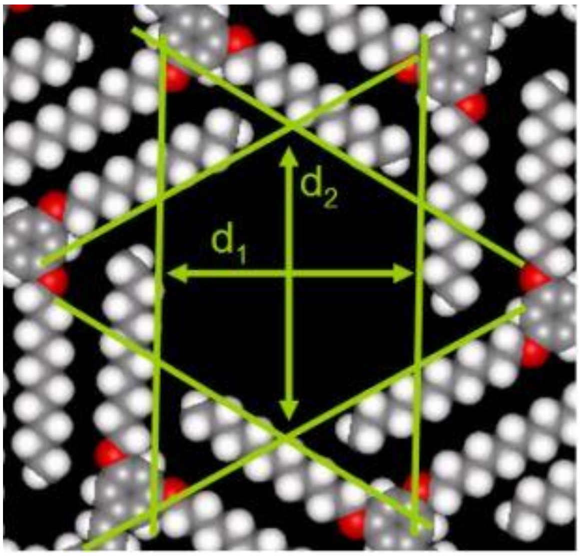

Figure 33 : Scheme of the pore formed by self-assembled TSB network showing the two sizes d1 and d2 of its hexagonal shape[204]

Table 1 : Dimensions of the pores in function of the number of carbons in the alkoxy chains (length of the chains)[204]

	8C/chain	10C/chain	12C/chain	14C/chain
d1(nm)	1.05	1.47	1.89	2.32
d2(nm)	1.39	1.88	2.37	2.86

Different domains of orientation are also noticed (Figure 34). These domains depend for example on the disposition of the molecule on the surface, that is induced by the nucleation and growth of the of the network on the surface after the deposition by drop casting.[204] Indeed, the number of domains observed right after the deposition reflects the number of nuclei formed before the substrate is fully covered. Therefore, after some time ripening effect tend to homogenize these domains reducing their number.[200]

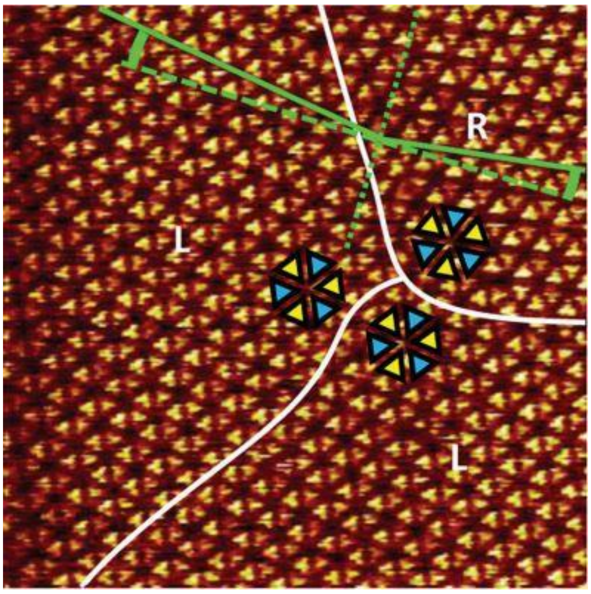

Figure 34 : Different domains of self-assembled TSB-3,5 induced by the orientation of the molecule on HOPG (Vbias = 1.1 V, Iset = 20 pA)[203]

TSB-3,5 was used as functionalizing molecule for HOPG substrate for the conception of supramolecular materials. Its interesting properties and its versatility allowed this molecule to be used to organize several molecules with various (coronene, phtalocyanines…) sizes on the surface of patterned HOPG substrate.[149,150,165,181,185]

V – Purpose of this thesis

Herein, our objective is to organize polyoxometalates on a surface, as a monolayer of molecules separated from each other with a periodic distribution. Our goal is to reach a system where POMs are disconnected from each other and from the substrate, and at the same time densely packed on the surface, in order to be able to address them individually without disturbing the other neighboring molecules on the network. To do so, we will have to overcome many challenges, starting with the POM to POM interactions that tend to form aggregates.[141]

Another critical point is the characterization of our samples at the molecular scale, indeed, the detection of the presence of POMs on the surface of a substrate alone do not allow affirming that the molecules are highly organized. To be able to prove it, many characterization techniques will be needed, and it will be the combined results of all these techniques that will definitely give an answer about the organization of POMs.

To achieve our objective, we will use different approaches based on a substrate functionalized with organic molecules to form a 2D network on its surface. This template will help to induce the periodic organization of POMs. Thus, different strategies will be investigated, using coordination and electrostatic bonding, as well as π-stacking interactions to attach POMs on our substrate.

During this work, we will use two different approaches to try to organize POMs periodically on functionalized HOPG substrate. In chapter II, we will try to drive POMs into the nanopores formed by the self-assembly of TSB, and to do so, functionalized hybrid Keggin POMs will be synthesized and anchored to molecules that will serve to drive them into the nanopores. In chapter III, we will synthesize a new molecule that self-assemble on HOPG based on the model of TSB-3,5 to try to attach pristine Keggin POMs periodically on the fuctionalized HOPG substrate patterned with this new molecule using electrostatic interactions. Various and original characterization techniques will be used to probe our samples at different scales.

CHAPTER II: Organization of hybrid POMs with the help of anchor molecules

In this chapter, the method attempted to arrange POMs is by linking them to planar molecules (through a coordination or a covalent bond), which would act as anchors to position them precisely on the surface. A modified substrate consisting of HOPG is employed, featuring a self-assembled molecule known as 1,3,5-tris((E)-3,5-bis(dodecyloxy)styryl)benzene, referred to here as TSB-Cn, where 'n' is the number of carbon atoms in the alkoxy chains. This molecule is a derivative of TSB and has previously been documented in literature for its ability to form 2D networks with pores on HOPG surface, as shown in chapter I. The goal is to utilize these periodic pores as hosts for the polyoxometalates. To achieve this, functionalized hybrid Keggin POMs are synthesized and linked to a phtalocyanine or a pyrene by coordination or covalent bond respectively, that will play the role of anchor to guide the POMs into the pores on the surface of the substrate.

I – Hybrid POMs with a phtalocyanine anchoring group

Due to its ability to form a coordination bond, and to occupy the pores formed on the surface of HOPG by the self-assembled TSB molecule, zinc phtalocyanine (ZnPc) is selected to fulfill the role of an anchor molecule[149], and as such, the TSB-C12 derivative is employed to functionalize HOPG. The diameter of the hexagonal pores created by this derivative on the surface, estimated at 2.37 nm[204] (cf. chapter I), offers enough space to host the ZnPc molecule with the anchored Keggin POM, and ensure a good separation between the molecules to obtain isolated POMs from each other. This template should enable a periodic arrangement and the desired separation between individual POMs on the surface.

I.1 – Preparation of the functionalized TSB-C12/HOPG substrate and organization of ZnPc

To functionalize HOPG substrate, TSB-C12, synthesized in the polymer team of our laboratory by Dr. Lydia Sosa-Vargas, is solubilized in toluene with a concentration of 10^{-4} mol.L^{-1} and 10 µl of this solution are drop-casted on the surface of freshly cleaved HOPG to obtain a full coverage of the substrate. Indeed, theoretical calculations give a concentration of $3.4*10^{-5}$ mol.L^{-1} for the formation of a full monolayer on 1x1 cm^2 of the substrate (the area approximately covered by 10 µL of solution), but experimental studies show that rather, a concentration of 10^{-4} mol.L^{-1} is needed for a full coverage, and this due to the formation of multilayers and some aggregates. Details about theoretical and experimental concentrations for a full coverage rate can be found in the appendix. To prevent rapid solvent evaporation and to facilitate the self-assembly of molecules, the sample is covered for approximately 5 minutes. Following this, images of the surface are made using STM under ambient conditions, showing the formation of the expected nanoporous 2D network (Figure 35). This modified substrate will henceforth be referred to as TSB-C12/HOPG. STM images obtained during this thesis are made at the From Molecules to Nano-objects: Reactivity, Interactions and Spectroscopies (MONARIS) laboratory of Sorbonne University in collaboration with Dr. Imad Arfaoui.

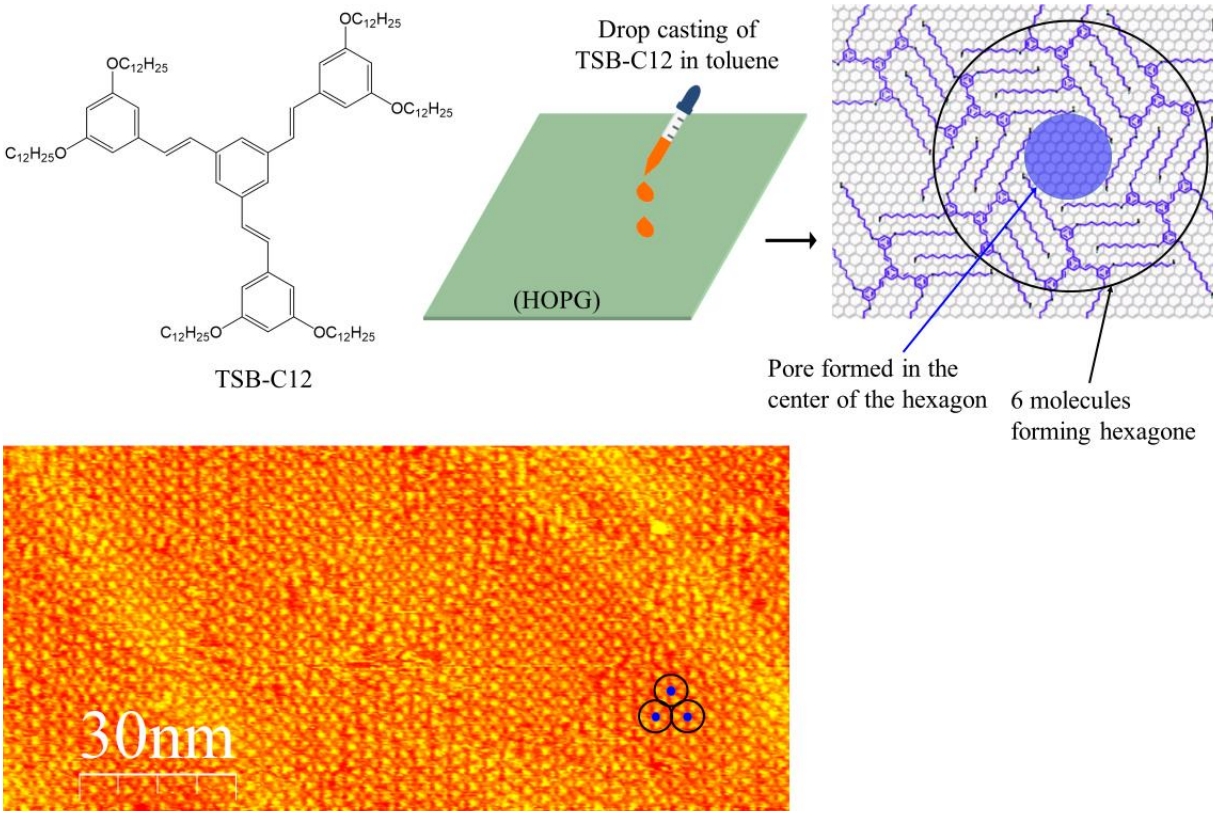

Figure 35 : (top) Scheme of the deposition and self-assembling of TSB-C12 on HOPG, (down) STM image (150 nm x 80 nm^2) of the self-assembled TSB-C12 on HOPG with 3 groups of 6 molecules surrounded by a black circle and the pores on their center shown by a blue dot (Vbias = 1 V, Iset = 20 pA)

The deposition of the ZnPc is made in a second step. First, 2 mg of the molecule are solubilized in 2 mL of chloroform, and the resulting solution is stirred overnight. Afterward, the solution is centrifuged and filtrated using a 0.2 µm porosity filter, and the ZnPc saturated solution is obtained, named here after ZnPc.sat. The ZnPc.sat solution is then diluted 500 times and 15 µL are drop casted on the surface of the TSB-C12/HOPG substrate. The theoretical calculations for a full coverage of ZnPc molecule in the pores (appendix) have shown an amount of 15 µL of a solution with a concentration of 1.96*10^{-6} mol.L^{-1}. Given the concentration of the ZnPc.sat solution in chloroform calculated at 7.35*10^{-4} mol.L^{-1} (see part I.2.2), the concentration of the 500 times diluted solution deposited on HOPG substrate is 1.47*10^{-6} mol.L^{-1}, which is slightly close to the theoretical results. This sample will be referred to as the ZnPc-TSB-C12/HOPG substrate. Typical STM image is reported in Figure 36 (down).

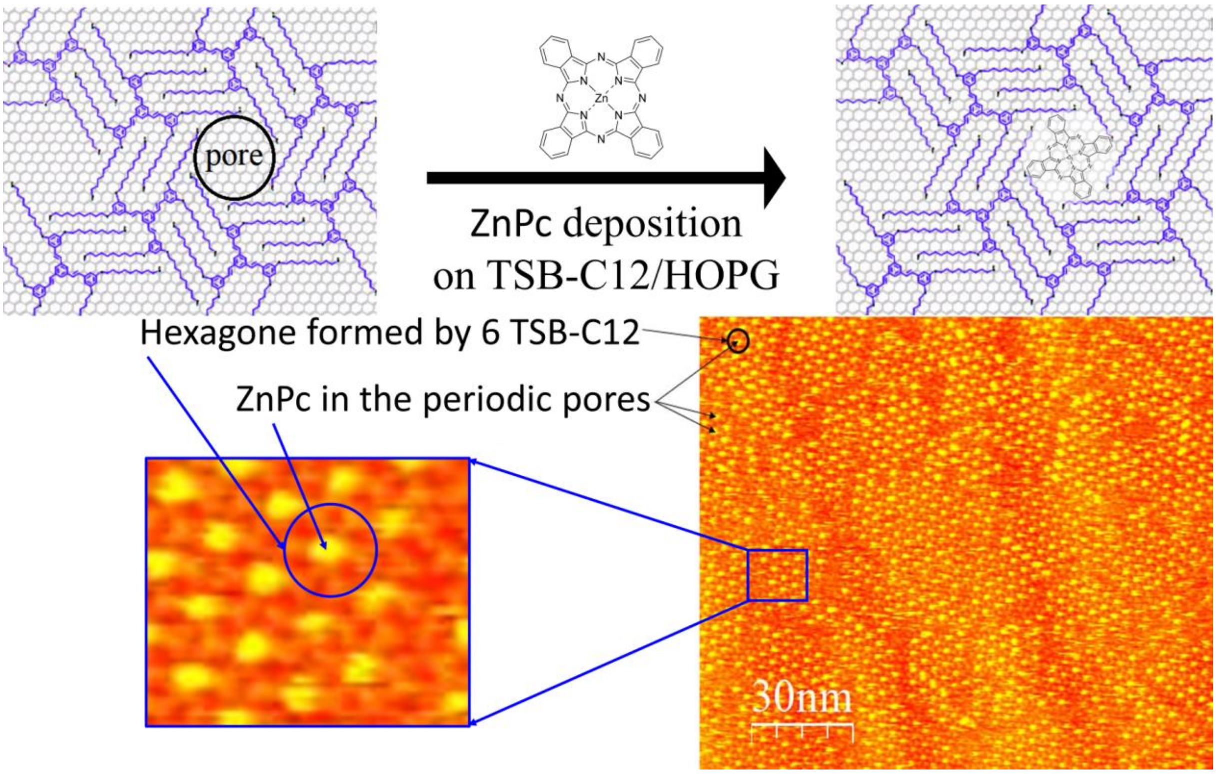

Figure 36 : (top) Scheme of the ZnPc occupying the pores on the surface of the TSB-C12/HOPG, (down) STM image (150 nm x 125 nm) of the self-assembled TSB-C12 on HOPG (Vbias = 1.3 V, Iset = 18 pA)

It shows that ZnPc spontaneously occupy the pores of the 2D network formed by TSB-C12 on HOPG, thanks to host/guest interactions driven by the pi-stacking of the ZnPc on the HOPG surface exhibited inside the pores, as it is illustrated by the scheme in the same Figure 36 (top) describing the assembly of the molecules on the surface of HOPG.

The aim of this approach is to take advantage of this spontaneous periodical arrangement of the ZnPc, by making it an anchor to a POM to guide it into the pores of the TSB-C12/HOPG substrate. To do so, a functionalized Keggin POM will be linked to the ZnPc molecule through a coordination bond.

I.2 – Preparation of the TBA[K^{Mo}(pyr)]-ZnPc complex in solution

The first step consists of the synthesis of the functionalized POM that will be anchored to the ZnPc through a pyridine terminal function. Keggin POM is chosen due to its size that allows fitting one POM per pore and ensuring them to be separated on the surface, as explained in the beginning of chapter II. Furthermore, this POM and its derivatives are widely used in our team[117,206,207] and its synthesis and characterizations are well mastered. Keggin POMs are also widely studied by several other teams around the world, providing well documented data available in the literature. The molybdate Keggin POM is used in particular, due to its more accessible reduction potential[208] that makes it more attractive for redox characterizations on surface.

The functional group incorporated to the POM consists of a linear organic tail composed of two aromatic rings. A phenyl ring linked to the POM through a tin atom, and a pyridine terminal ring. These two aromatic rings are tied by a triple carbon-carbon bond that ensures a strait and rigid shape, and the nitrogen of the pyridine group is positioned on para position of the C≡C triple bond. The counter ions of the POM consist of four tetrabutylammonium cations (TBA). Its general formula is $TBA_4[PMo_{11}O_{39}\{Sn(C_{13}H_8N)\}]$ and its schema is shown in Figure 37.

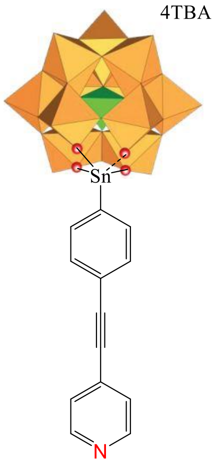

Figure 37: Scheme *of the functionalized hybrid molybdate Keggin POM* $TBA_4[PMo_{11}O_{39}\{Sn(C_{13}H_8N)\}]$

I.2.1 – Synthesis of the pyridine terminated hybrid POM TBA[K^{Mo}(pyr)]

The first step of the synthesis of the $TBA_4[PMo_{11}O_{39}\{Sn(C_{13}H_8N)\}]$ POM, named here after TBA[K^{Mo}(pyr)], consist of the preparation of the lacunar species $TBA_4[PMo_{12}O_{40}]$. The pristine 12-phosphomolybdic acid $H_3PMo_{12}O_{40}$ is solubilized in water, treated with lithium carbonate to adjust the pH and form the lacunar derivative. An excess of tetrabutylammonium bromide (TBABr) is then added and the $TBA_4[PMo_{11}O_{39}]$ precipitate. The product is purified by a slow recrystallization in acetonitrile to obtain a sufficiently pure product for the following steps. The functionalization of this lacunar molybdate POM is done under argon atmosphere using $Cl_3Sn(C_6H_4)I$ and freshly distilled triethylamine in dry acetonitrile, to obtain the $TBA_4[PMo_{11}O_{39}\{Sn(C_6H_4)I\}]$ intermediate. The final step consists of a Sonogashira coupling reaction of the functionalized $TBA_4[PMo_{11}O_{39}\{Sn(C_6H_4)I\}]$ POM with 4-ethynylpyridine under argon atmosphere in dry DMF, and in the presence of triethylamine. The schema of the synthesis is shown in Figure 38.

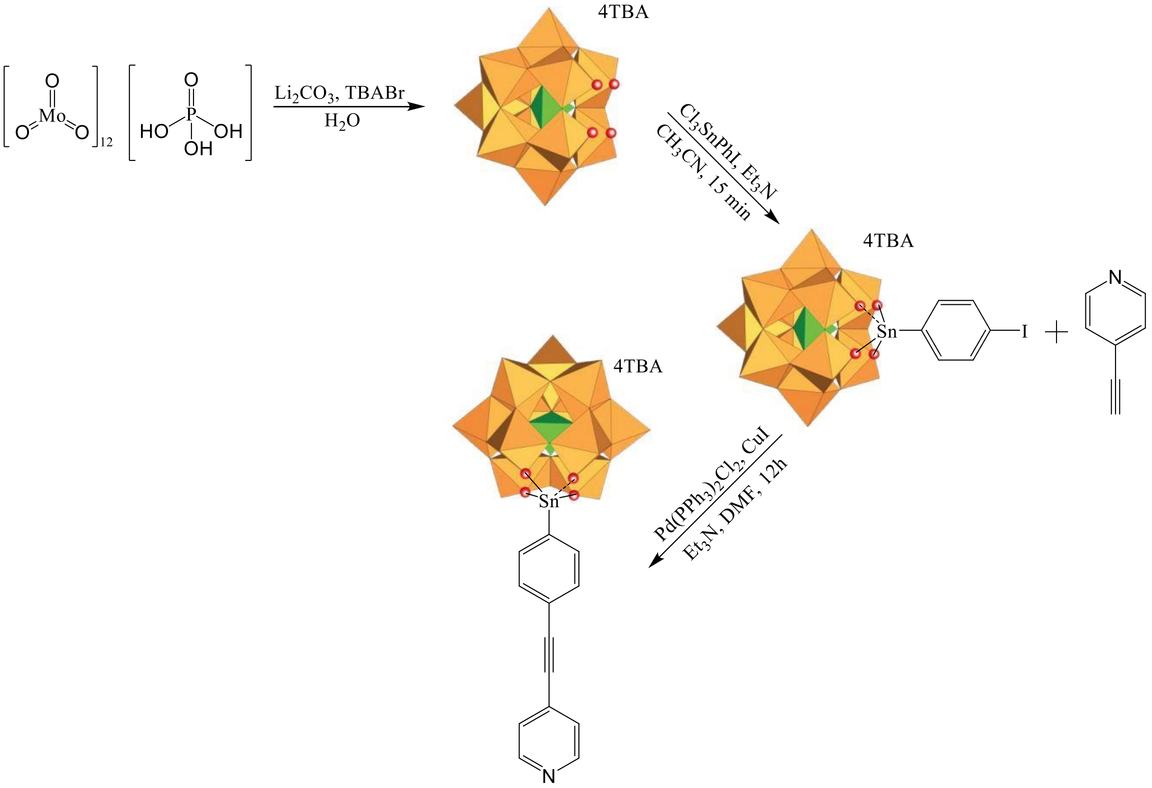

Figure 38 : Scheme of the synthesis of the functionalized Keggin POM with pyridine terminal function

The final product is analyzed by NMR ^1H and ^{31}P in CD_3CN, and it appeared on NMR ^1H that a part of the POMs charges is compensated by triethylammonium (about 0.5 eq of Et_3NH^+ and 3.5 eq of TBA) leading to the $Et_3NH_{0.5}TBA_{3.5}[PMo_{11}O_{39}\{Sn(C_{13}H_8N)\}]$ POM (Figure 39).

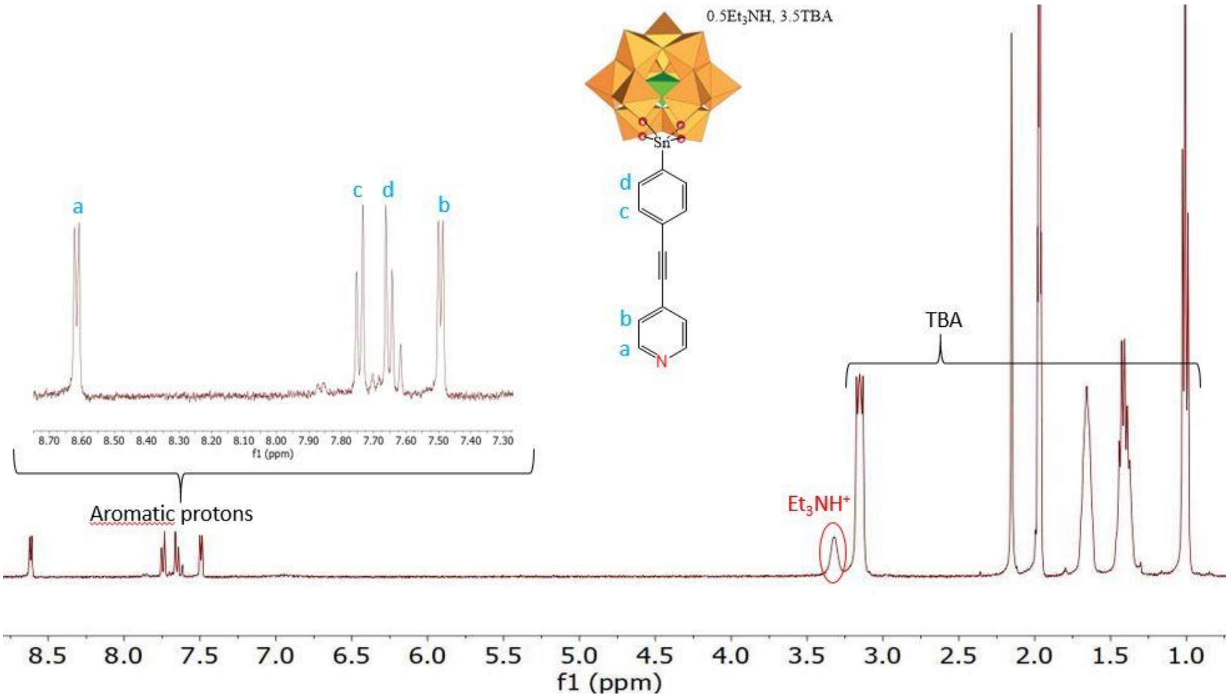

Figure 39 : Scheme of the $Et_3NH_{0.5}TBA_{3.5}[PMo_{11}O_{39}\{Sn(C_{13}H_8N)\}]$ POM and NMR ^1H spectra obtained after the first purification steps showing the prensence of the triethylammonium (red circle)

In order to eliminate the Et_3NH^+ and to replace it by TBA counter ions, the use of an ion exchange Amberlite^{TM} resin enriched with TBA cations is first attempted. The POM was solubilized in acetonitrile and treated over the resin during 30 min. The NMR ^1H shown a successful elimination of the triethylammonium counter ions, but also a protonation of the pyridine function through a modification of the shape of the doublet at 8.63 ppm, attributed to the protons on alpha of the nitrogen atom, becoming wider with an overlap between the two peaks. This protonation is problematic as the aim is to coordinate this pyridine function to the ZnPc through the free doublet of its nitrogen atom. Also, the NMR ^{31}P shows a degradation of the POM (apparition of a second peak) (Figure 40).

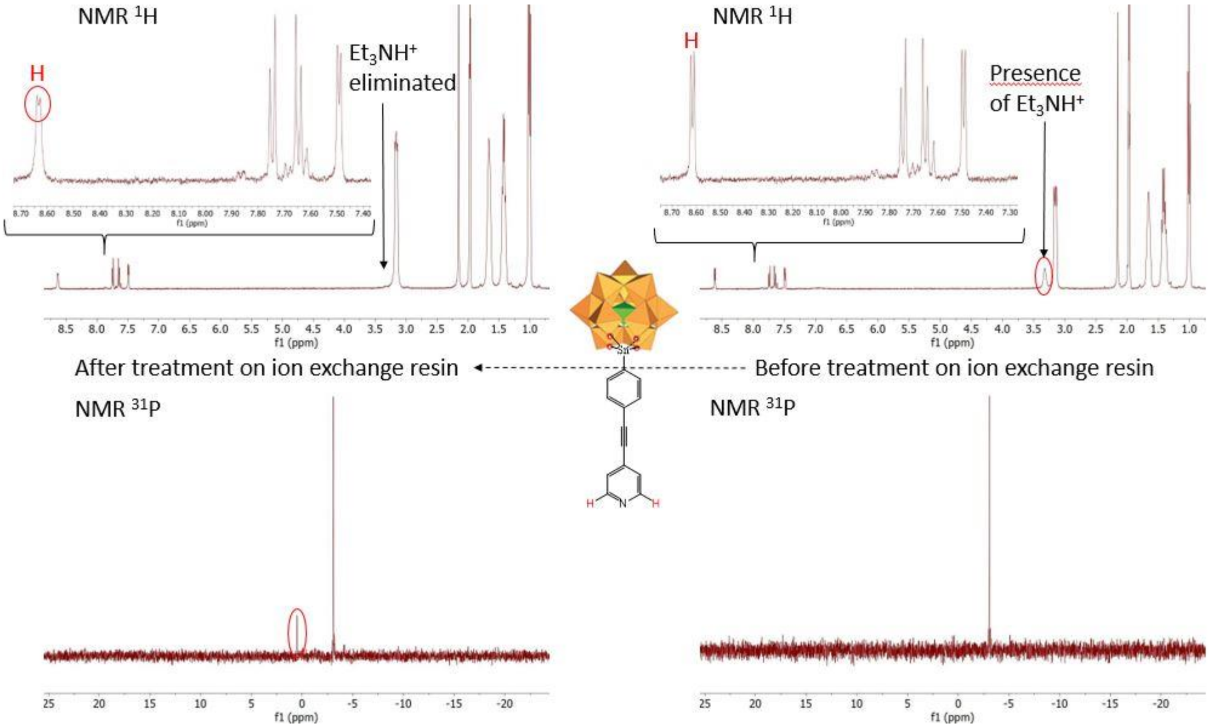

Figure 40 : NMR ^{1}H (top) and ^{31}P (down) before (right) and after (left) treatement of the $Et_3NH_{0.5}TBA_{3.5}[PMo_{11}O_{39}\{Sn(C_{13}H_8N)\}]$ POM on the ion exchange resin with the scheme of the POM showing the affected protons by the protonation of the pyridine group

Another way is then used to eliminate the Et_3NH^+ and avoid the protonation of the pyridine. The TBA[K^{Mo}(pyr)] was solubilized in acetonitrile and 0.25 equivalent of tetrabutylammonium hydroxide (TBAOH) are added to the solution. The mixture is stirred during 5 minutes and a large excess of diethyl ether is added to precipitate the POM. The product is dried and checked by NMR ^{1}H and ^{31}P in CD_3CN (Figure 41).

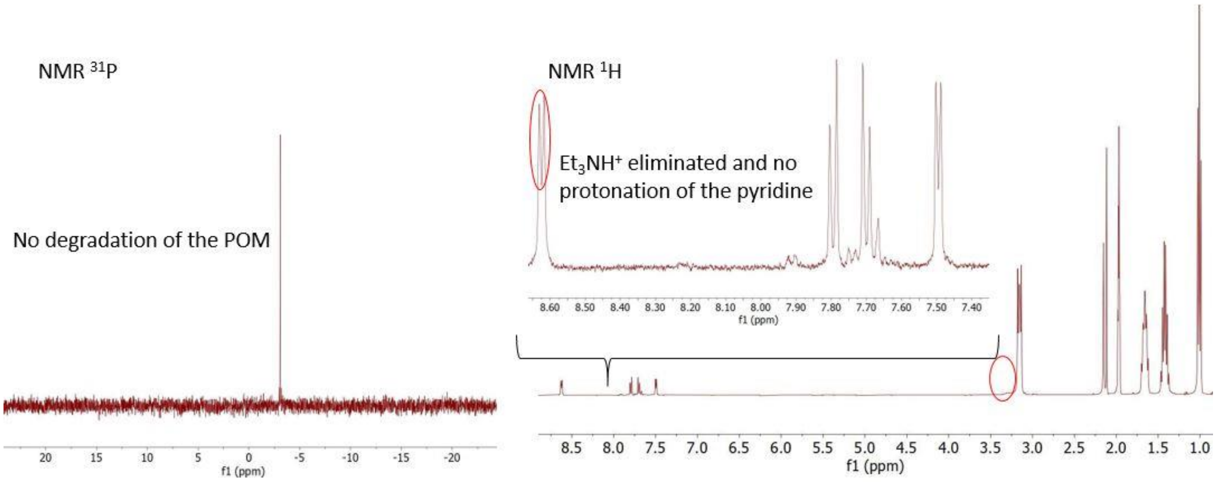

Figure 41 : NMR ^1H (right) and ^{31}P (left) of the TBA[K^{Mo}(pyr)] after treatment with TBAOH, the red circles shows the elimination of Et_3NH^+ and the clear doublet of the protons on alpha of the nitrogen atom, showing the absence of protonation

The NMR shows the removal of Et_3NH^+ by the TBAOH, the hydroxide deprotonated the triethylammonium forming triethylamine and water, and the TBA cations replaced the Et_3NH^+ as counterions. The NMR ^{31}P shows also the presence of one single peak meaning that the POMs were not degraded. All details of the synthesis can be found in the appendix.

I.2.2 – Complexation of the TBA[K^{Mo}(pyr)] to the zinc phtalocyanine

To form the TBA[K^{Mo}(pyr)]-ZnPc complex, both molecules have to be solubilized in the same solution. Moreover, coordinating solvents such as DMF have to be avoided in order to allow the pyridine of TBA[K^{Mo}(pyr)] to coordinate the ZnPc without being in competition with the solvent.

ZnPc molecule is soluble in non-polar and low polarity solvents. Measurements of its solubility have been done in non-coordinating solvents such as toluene, chloroform and dichloromethane, using UV-visible and Beer Lambert law.

Saturated solutions were prepared by putting 2 mg of ZnPc in 2 ml of each one of the three solvents, and the solutions are stirred overnight. The mixtures are then centrifuged and filtrated using a 0.2 µm filter, and diluted 150 times. UV-visible measurements are done on each one of the solutions (Figure 42).

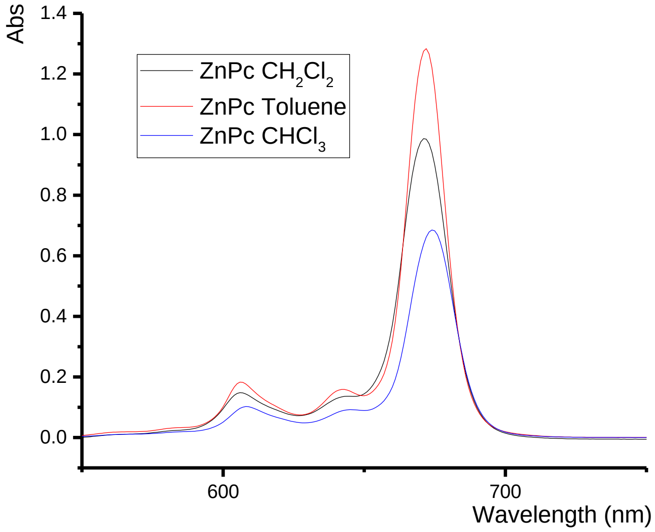

Figure 42 : UV-visible of ZnPc in dichloromethane (black) toluene (red) and chloroform (blue)

The concentration of the three solutions was estimated as following

$$A = \varepsilon * l * C$$

$$C = \frac{A}{\varepsilon * l}$$

With A: the absorbance, ε: the molar absorption coefficient, l: the optical path length and C: the concentration.

With l = 0.5 cm and ε (ZnPc) being arround 281800 L.mol^{-1}.cm^{-1},[209] the concentration in the cuvette (C_{cuv}) is then estimated and the concentration of the saturated solution (C_{sat}) can also be approximated by multiplying C_{cuv} by 150.

The results are reported in table 2.

Table 2 : absorbance, concentration of ZnPc in the cuvette and saturated concentration of ZnPc for each toluene, dichloromethane and chloroform

solvent	A	C_{cuv}(mol.L^{-1})	C_{sat}(mol.L^{-1})
Toluene	1.28	$9.08*10^{-6}$	$1.36*10^{-3}$
Dichloromethane	0.99	$7.03*10^{-6}$	$1.05*10^{-3}$
Chloroform	0.69	$4.90*10^{-6}$	$7.35*10^{-4}$

These results show that ZnPc molecule has higher solubility in toluene, followed by dichloromethane and the weakest one in chloroform. The preparation of a ZnPc solution in chloroform according to the procedure described in I.1 give an amount of ZnPc in 15µL in accordance with the theoretical calculations for a full coverage.

In contrary to the ZnPc, the hybrid POM TBA[K^{Mo}(pyr)] is soluble in polar organic solvents only, such as acetonitrile, DMSO, DMF...etc. but not soluble in either toluene, dichloromethane or chloroform. Thus a binary solvent will be necessary in order to solubilize both the POM and the ZnPc. Besides, another important parameter for the choice of the solvent is the ebullition point. Indeed, to allow the molecules to self-assemble on the surface the evaporation time of the solvent must be controlled and not excessively quick.

Given these parameters, a binary solvent composed of acetonitrile, that poorly or don't coordinate the ZnPc; and chloroform, that has higher ebullition point than dichloromethane and allow to solubilize a sufficient quantity of ZnPc is used. The rate of this binary solvent is fixed at 30/70 for acetonitrile and chloroform respectively, to afford a good solubility to the POM. Toluene could not be used as the solubility of the POM in a solvent containing toluene is really low, and by increasing the amount of acetonitrile to improve it, the solubility of ZnPc is impacted. Note that a binary solvent made of dichloromethane and acetonitrile 70/30 respectively can be used for certain characterizations in solution, but for depositions on surface chloroform is preferred due to its lower volatility.

A UV-visible spectrum of the ZnPc in a binary solvent is performed to determine its saturated concentration and compare it with its maximum concentration in pure chloroform (Figure 44).

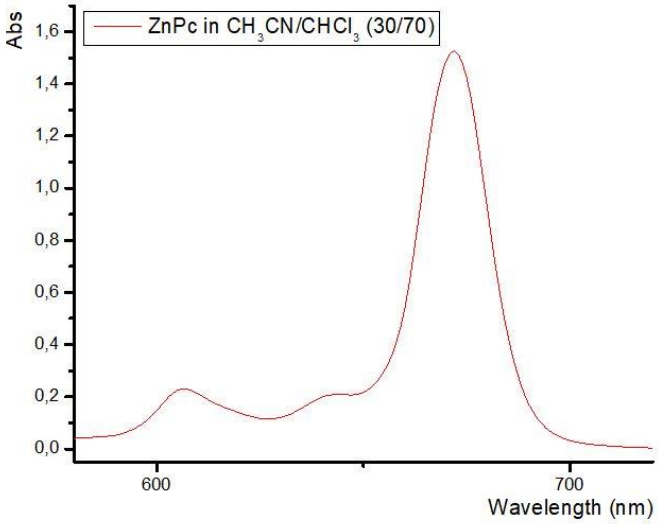

Figure 43 : UV-visible spectroscopy of ZnPc in binary solvent composed of acetonitrile/chloroform (30/70)

A saturated solution of ZnPc is prepared in the binary solvent acetonitrile/chloroform (30/70) and diluted 25 times before using for UV-visible measurements. The concentration of the saturated solution is calculated as previously, with a cuvette of 1 cm length rather than 0.5 and the maximum absorbance at 1.53. The concentration obtained is C = $1.4*10^{-4}$ mol.L^{-1}, wich is sufficient for the solutions that will be used for NMR characterizations, and for deposition on surface.

Before the deposition of the coordinated POM to the ZnPc on the functionalized substrate, it is necessary to probe the formation of this compound in solution, in conditions as similar as possible to the ones used for the deposition. To do so, NMR and UV-visible are used.

I.2.2.1 – NMR ^{1}H characterizations

To probe the formation of the coordination bound between the POM and the ZnPc, NMR tubes are prepared in the binary solvent composed of deuterated acetonitrile/chloroform 30/70. In the first tube, 2 mg of TBA[K^{Mo}(pyr)] ($0.67*10^{-3}$ mmol) are solubilized in 150 µL of CD_3CN and 350 µL of $CDCl_3$ are added. The NMR ^{1}H spectrum is done with a 600 MHz apparatus.

0.6 mg ($1.04*10^{-3}$ mmol, 1.55 equivalents) of ZnPc are then partially solubilized in 30 µL of $CDCl_3$ and added to the previous NMR tube containing the TBA[K^{Mo}(pyr)] then NMR ^{1}H is performed.

A last NMR tube is prepared with 0.6 mg of ZnPc firstly solubilized in 350 µL, and secondly 150 µL of CD_3CN are added. The tube is passed to the 600 MHz apparatus to perform the NMR ^{1}H and serves as a blank tube containing the ZnPc alone in the binary solvent.

The three NMR ^{1}H spectra are shown in Figure 44.

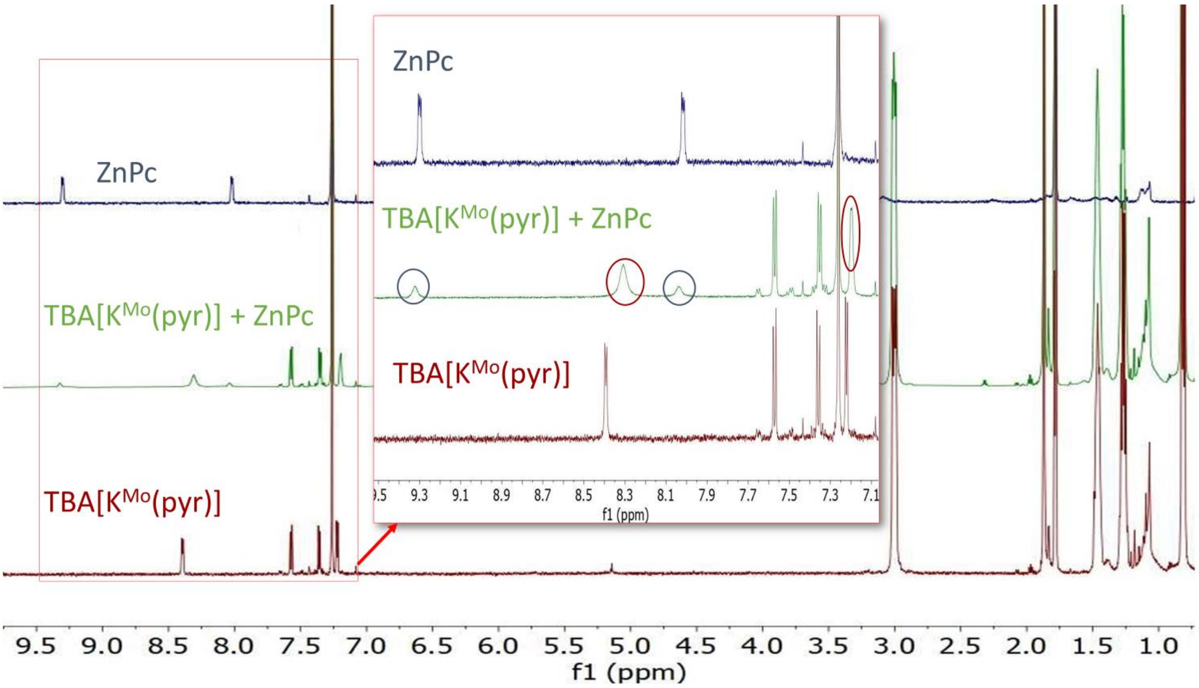

Figure 44 : NMR ^{1}H of TBA[K^{Mo}(pyr)] (red), ZnPc-TBA[K^{Mo}(pyr)] complex (green) and ZnPc (blue) in $CD_3CN/CDCl_3$ (30/70 in volume). Magnified peaks on the green spectrum show the differences on the spectrum of the ZnPc-TBA[K^{Mo}(pyr)] complex compare to the spectrum of the ZnPc alone (blue circles), to the spectrum of TBA[K^{Mo}(pyr)] alone (red circles)

The proton NMR of the ZnPc, TBA[K^{Mo}(pyr)], and both molecules in the binary solvent show interesting results. An effect on the two multiplets of the ZnPc (9.32 ppm and 8.04 ppm, blue spectrum in Figure 44) is noticed when it is in presence of the TBA[K^{Mo}(pyr)] (blue circles in Figure 44). A decrease in the intensity of the ZnPc peaks and an overlap of their signal is noticed (green spectrum in Figure 44), while the signal of these peaks in the tube containing only ZnPc molecules (blue spectra in Figure 44) is more intense and the multiplets clearly visible with four peaks each. Moreover, a shift is noticed for these peaks passing from 9.30 to 9.32 ppm for the more deshielded peak, and from 8.02 to 8.04 for the less deshielded.

For the signal of TBA[K^{Mo}(pyr)], a more important effect is noticed in the presence of ZnPc. An important overlap accompanied with a collapse of the doublet attributed to the protons on alpha position of the nitrogen atom (cf. Figure 39) is shown, with a significant shift of its position from 8.39

ppm for TBA[K^{Mo}(pyr)] alone in the binary solvent (red spectrum in Figure 44) to 8.31 ppm for TBA[K^{Mo}(pyr)] + ZnPc (green spectrum in Figure 44). The doublet attributed to the protons on beta position to the nitrogen atom of TBA[K^{Mo}(pyr)] (cf. Figure 39) is also affected with an overlap, a little collapse, and a shift of its position from 7.22 ppm (Figure 44 red spectrum) for TBA[K^{Mo}(pyr)] to 7.20 ppm (Figure 44 green spectrum) for ZnPc + TBA[K^{Mo}(pyr)].

These results tend to demonstrate qualitatively the formation of the complex in solution, by an effect noticed on both TBA[K^{Mo}(pyr)] and ZnPc while the molecules are solubilized in the same solvent, with the closest protons to the nitrogen atom (cf. Figure 39) of TBA[K^{Mo}(pyr)] being the ones particularly affected.

This NMR characterizations allowed to demonstrate qualitatively the formation of the TBA[K^{Mo}(pyr)]-ZnPc complex, showing particularly that the functionalized POM coordinate the ZnPc through the nitrogen atom of its pyridine function.

I.2.2.2 – UV-visible characterizations

For UV-visible characterizations, a saturated solution of ZnPc in dichloromethane is prepared, and its concentration calculated using Beer Lambert law. Dichloromethane is used because of the POM that exhibit a slightly better solubility in this solvent compared to chloroform. A solution of 2 mg of TBA[K^{Mo}(pyr)] in 1 ml of acetonitrile is prepared and used to add equivalents of POM to the ZnPc solution. The formation of the complex is then followed by UV-visible spectroscopy (Figure 45).

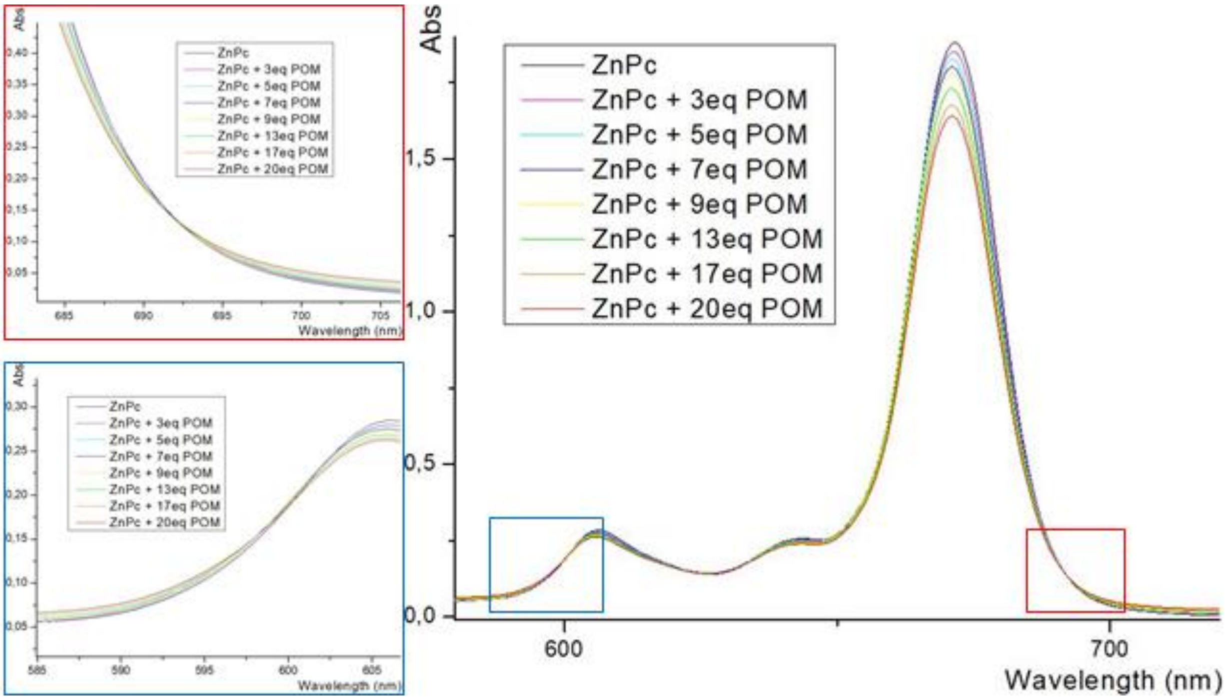

Figure 45 : UV-visible spectroscopy of ZnPc in dichloromethane with addition of equivalents of TBA[K^{Mo}(pyr)] in acetonitrile (up to 20 eq) showing the apparition of two isobestic points at around 600 nm and 692 nm

The UV-visible spectrum obtained in Figure 45 shows two isobestic points at 600 nm and 692 nm, after the addition of TBA[K^{Mo}(pyr)] into the ZnPc solution. The presence of these isobestic points demonstrate the existence of an equilibrium in solution involving two species, the POM TBA[K^{Mo}(pyr)] and the ZnPc. We have shown by NMR ^{1}H that the bond formed between these two molecules involve the nitrogen atom of the pyridine function of TBA[K^{Mo}(pyr)], that coordinate the zinc of ZnPc.

To ensure that these isobestic points are due to the coordination of the TBA[K^{Mo}(pyr)] and not to the acetonitrile, a blank is made by adding volumes of pure acetonitrile to a ZnPc solution equivalent to the previously added volumes containing the TBA[K^{Mo}(pyr)]. The UV-visible spectra are shown in Figure 46.

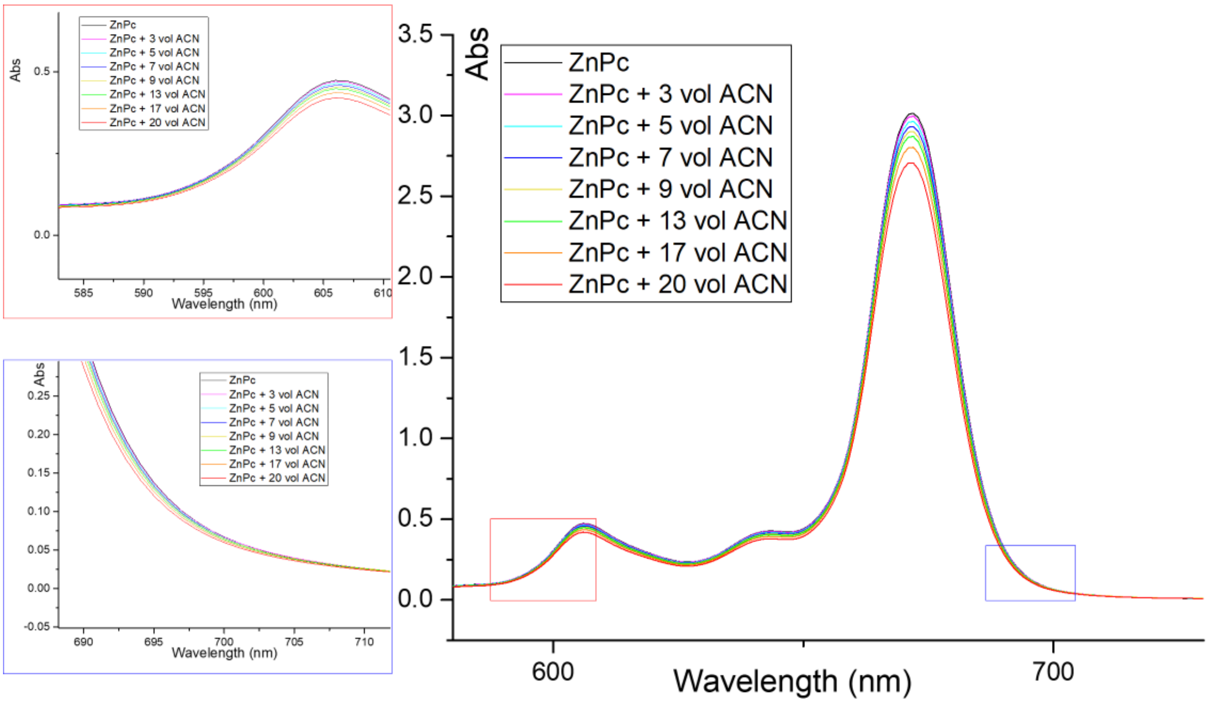

Figure 46 : UV-visible spectra of a solution of ZnPc in dichloromethane with the addition of volumes of acetonitrile equivalent to the volumes added in the experiment fig.46 containing the TBA[K^{Mo}(pyr)], with a zoom on the areas where isobestic points appeared previously (cf. Figure 46)

Interestingly, the blank UV-visible spectra Figure 46 show no isobestic points, confirming that their apparition (cf. Figure 45) is due to the formation of the complex TBA[K^{Mo}(pyr)]-ZnPc shown in Figure 47 (left) is demonstrated.

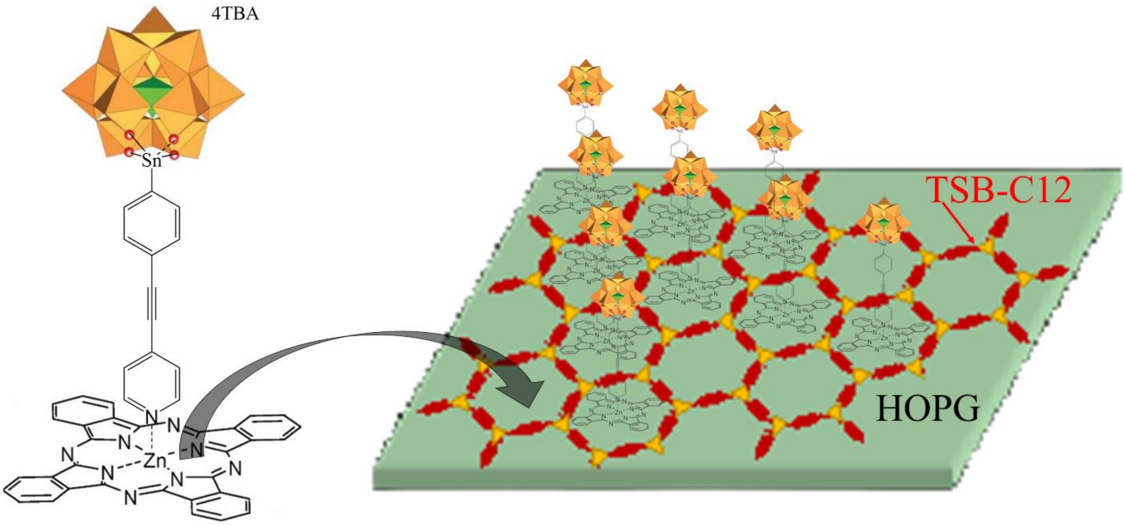

Figure 47 : Scheme of the TBA[K^{Mo}(pyr)] coordinated to the ZnPc named here after TBA[K^{Mo}(pyr)]-ZnPc

The data of UV-visible spectroscopy Figure 45 allowed the estimation of the equilibrium constant of the formation of the TBA[K^{Mo}(pyr)]-ZnPc complex by using the Hill equation at around $5*10^3$ as well as the stoichiometry of the complex that is composed of one ZnPc and one TBA[K^{Mo}(pyr)]. The details of the calculations can be found in the appendix.

In this chapter, the aim is to deposit the TBA[K^{Mo}(pyr)] linked to the ZnPc on TSB/HOPG substrate. It is expected that the ZnPc will drive the TBA[K^{Mo}(pyr)] into the pores, to have periodically organized distribution of POMs on the surface as shown in Figure 47 (right).

I.3 – Deposition of the complex TBA[K^{Mo}(pyr)]-ZnPc on TSB/HOPG substrate

Two solutions of ZnPc-TBA[K^{Mo}(pyr)] complex are prepared in the binary solvent $CH_3CN/CHCl_3$ (30/70) with 0.2/1 and 2/1 equivalents of TBA[K^{Mo}(pyr)]/ZnPc, respectively. The protocol of the preparation of these solutions can be found in the appendix. Adding 0.2 equivalents of the POM to the ZnPc solution would allow to see the difference between pores occupied by the ZnPc and pores occupied by the complex TBA[K^{Mo}(pyr)]-ZnPc. While adding two equivalents of the TBA[K^{Mo}(pyr)] would allow to push the equilibrium toward the formation of the complex and have the majority of the pores occupied by it. This solution of TBA[K^{Mo}(pyr)] and ZnPc is then diluted 20 times in the binary solvent to obtain the TBA[K^{Mo}(pyr)]-ZnPc.dil2, and 15 µL of this solution are drop casted on TSB/HOPG substrate, the sample is covered to allow the solvent to evaporate slowly.

I.3.1 – STM characterizations

The samples prepared are imaged by STM under ambient conditions.

I.3.1.1 – Sample with 0.2 equivalent of TBA[K^{Mo}(pyr)]

The first samples imaged are made with 0.2 equivalents of TBA[K^{Mo}(pyr)] vs. ZnPc. The sample is first imaged on several areas after the deposition of TSB to ensure the homogeneity of the 2D network formed on surface. Then, the complex is deposited and the sample is imaged. The images obtained are compared to the ZnPc-TSB/HOPG sample that is used as a reference (Figure 48).

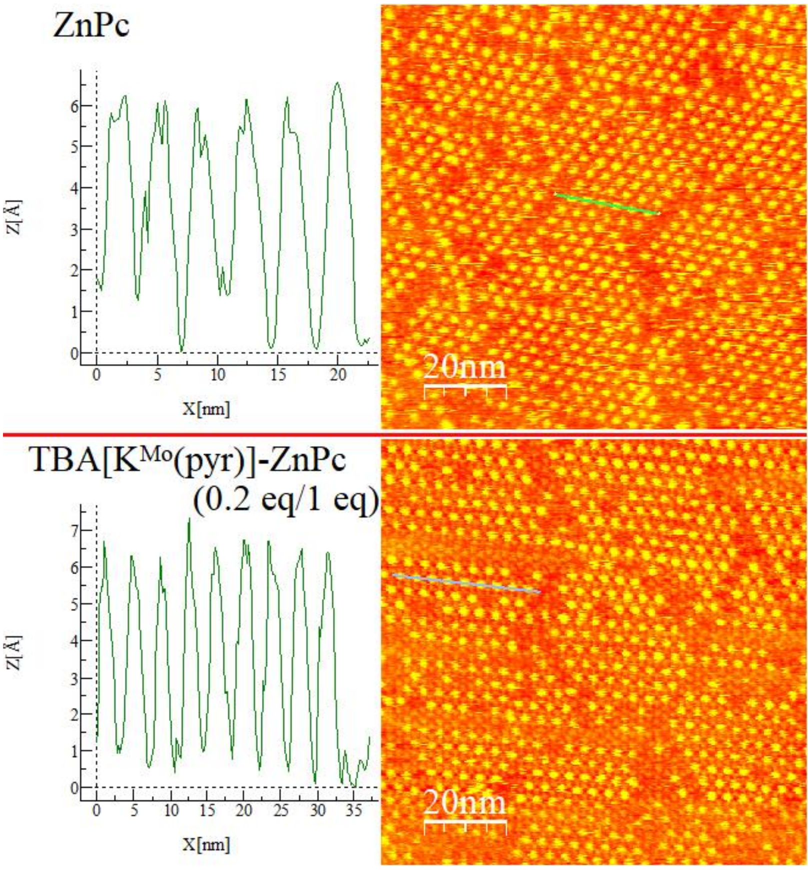

Figure 48 : STM images and apparent heights profile of ZnPc-TSB/HOPG sample (top) and ZnPc-TBA[K^{Mo}(pyr)] (solution 0.2 eq of TBA[K^{Mo}(pyr)]) on TSB-C12/HOPG sample (down) (100 x 100 nm^2) (Vbias = 1 V, Iset = 20 pA)

The STM images show no evidence of the organization of TBA[K^{Mo}(pyr)]-ZnPc in the pores, with no difference between the sample prepared with the complex (Figure 48 down) and the blank sample prepared with ZnPc (Figure 48 top), with the same apparent heights in both samples. The ratio 0.2 equivalent of TBA[K^{Mo}(pyr)] and 1 equivalent of ZnPc didn't allow to see any difference between the different molecules occupying the pores.

I.3.1.2 – STM Imaging of the sample with 2 equivalents of TBA[K^{Mo}(pyr)]

Given these results, the amount of the TBA[K^{Mo}(pyr)] was increased to two equivalents relatively to ZnPc in order to promote the formation of the complex TBA[K^{Mo}(pyr)]-ZnPc, and 15 µL of this solution are deposited on TSB/HOPG substrate and imaged by STM (Figure 49).

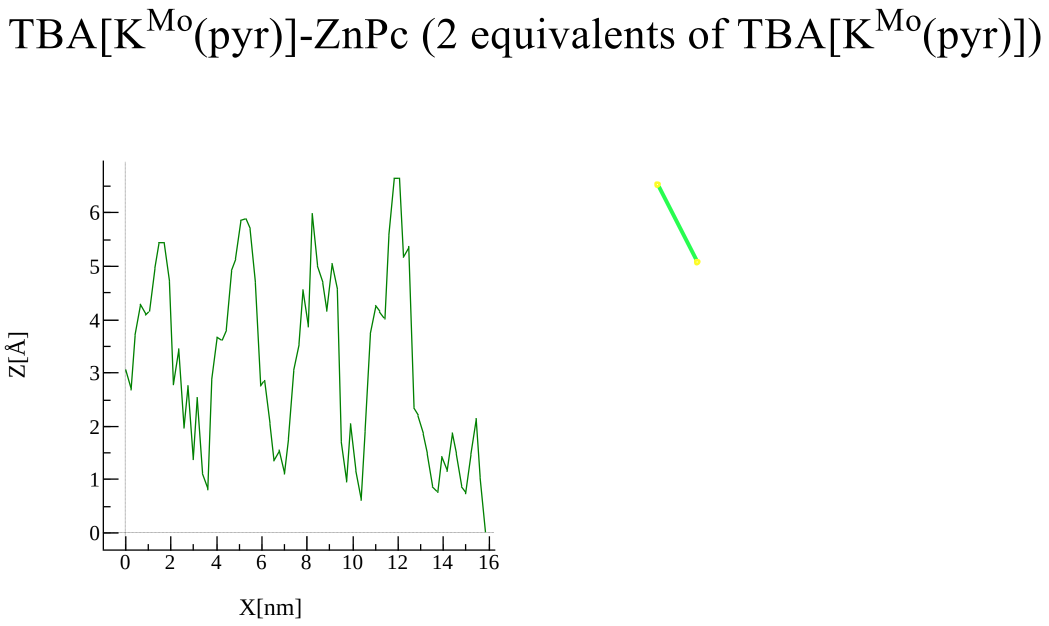

Figure 49 : STM image of sample made of ZnPc-TBA[K^{Mo}(pyr)] (solution of (with 2 eq of TBA[K^{Mo}(pyr)]) drop casted on TSB-C12/HOPG substrate (100 x 100 nm^2) (Vbias = 1.1 V, Iset = 20 pA)

Except for the filling rate on the surface, slightly lower in this case, the images obtained with the excess of TBA[K^{Mo}(pyr)] in solution are similar to the ones obtained previously using a solution with an excess of ZnPc. The sample shows also no difference with the blank sample in terms of the shape or heights of the molecules filling the pores on surface. No evidence of the organization of TBA[K^{Mo}(pyr)]-ZnPc complex according to the template used can be highlighted.

Despite the STM imaging using various parameters of the current and the tension on the samples with 0.2 and 2 equivalents of TBA[K^{Mo}(pyr)], no difference appeared compared to the reference sample with ZnPc only. In order to push the equilibrium further toward the formation of the ZnPc-TBA[K^{Mo}(pyr)] complex, the deposition method is changed. The method consists of preparing a sample of ZnPc-TS-C12/HOPG and to deposit a concentrated solution of TBA[K^{Mo}(pyr)] to form the coordination bond on surface rather than in solution.

I.3.1.3 – Step by step deposition of the ZnPc-TBA[K^{Mo}(pyr)] complex

As the deposition of the complex in solution seems to have failed, a new deposition method to organize the TBA[K^{Mo}(pyr)] on the surface of the functionalized HOPG is used. This method consists of preparing a substrate of ZnPc-TSB-C12/HOPG, then 15 µL of a solution of TBA[K^{Mo}(pyr)] with various concentrations (from 2.89*10^{-7} mol.L^{-1} to 3,36*10^{-4} mol.L^{-1}) are deposited on this substrate in a binary solvent of acetonitrile/chloroform (30/70 respectively). The aim is to form the coordination bond between the TBA[K^{Mo}(pyr)] and the ZnPc on surface rather than in solution. This method allows to reach a large excess of TBA[K^{Mo}(pyr)] relatively to the number of ZnPc occupying the pores, by depositing a concentrated solution of POM. The STM image made with a sample where 15 µL of TBA[K^{Mo}(pyr)] at 3,36*10^{-4} mol.L^{-1} in the binary solvent acetonitrile/chloroform (30/70 in volume) are deposited on the ZnPc-TSB/HOPG substrate is shown in Figure 50.

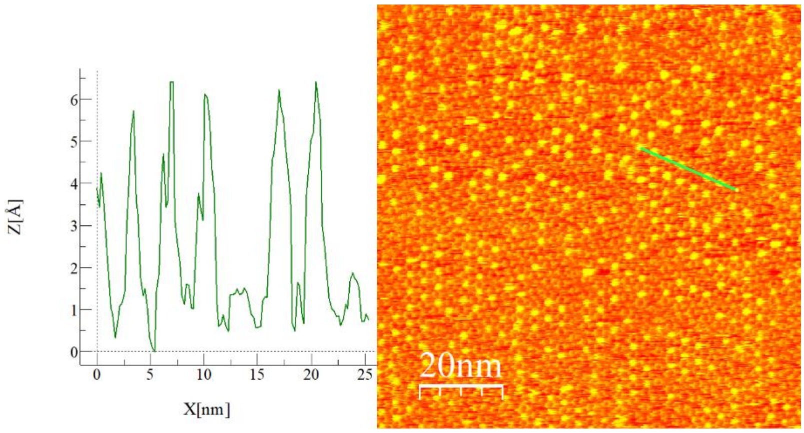

Figure 50 : STM image of sample made of TBA[K^{Mo}(pyr)] deposited on ZnPc-TSB-C12/HOPG substrate by drop casting in acetonitrile/chloroform (30/70 in volume) (100 x 100 nm^{2}) (Vbias = 1.3 V, Iset = 20 pA)

Indeed, the sample exhibit the same STM image and apparent heights as for the previous method, and still, no evidence of any organized deposition of TBA[K^{Mo}(pyr)] is shown.

I.3.1.4 – Discussion

The results of the different deposition methods tried in order to organize the hybrid POMs show no evidence of the expected organization on surface (cf. Figure 47). Indeed, the POMs remain "invisible" by STM, the signature of individual POMs couldn’t be observed at any area on the surface. Several hypotheses are suggested to explain these results.

The failure of the TBA[K^{Mo}(pyr)]-ZnPc to occupy the pores can be explained by the different affinities of the ZnPc linked to the TBA[K^{Mo}(pyr)] and the free ZnPc to fill these pores. Indeed, the formation of the complex TBA[K^{Mo}(pyr)]-ZnPc in solution happens through an equilibrium, and if the free ZnPc has a better affinity toward the host/guest interactions with the pores on surface. The equilibrium will be displaced toward the formation of the free ZnPc molecules as it occupies the pores on of the functionalized substrate (Figure 51), until these ones will be completely filled by the free ZnPc molecules. Moreover, and that is why the step by step method is not conclusive. The TBA[K^{Mo}(pyr)] as well as the remained TBA[K^{Mo}(pyr)]-ZnPc complex in solution will form aggregates due to cation driven electrostatic POM to POM interactions.[141]

Another hypothesis is that the ionic compound TBA[K^{Mo}(pyr)]-ZnPc complex occupy the pores of the functionalized TSB-C12/HOPG substrate as expected. However, due to the interactions of the STM tip generated by the huge electric field of several GV.m^{-1} during the scanning process[210], associated to the weakness of the POM-ZnPc bond, the TBA[K^{Mo}(pyr)] are torn off from the ZnPc pedestal, which for their part remain in the pores.

Additionally, the STM's scanning area is limited to 700 x 700 nm^2, with the largest scanned regions enabling to distinguish single molecules sufficiently on the surface being only around 400 x 400 nm^2. This small area might hinder a complete understanding of how the POMs are spread out on the surface. To get a clearer picture of their distribution, a wider scanning area is necessary.

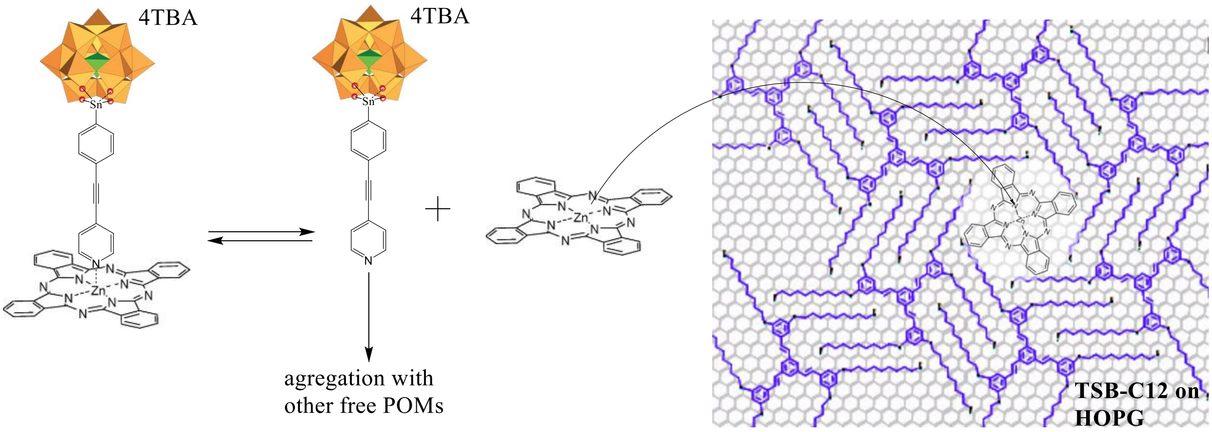

Figure 51 : Scheme of the competition between the free ZnPc and the ZnPc-TBA[K^{Mo}(pyr)] to occupy the pores

To conclude on these experiments and understand the system and its limitations, verifications of these hypotheses are needed. One obvious solution that can be provided consist of improving the strength of the bond between the TBA[K^{Mo}(pyr)] and the anchoring molecule, by using a direct covalent bond for example. But first, there is a fundamental question that needs addressing regarding this TBA[K^{Mo}(pyr)]-ZnPc system: how is the TBA[K^{Mo}(pyr)] distributed on the sample's surface? Thus, other characterization techniques will be needed. AFM, for example, would allow to have images of a larger scale of the surface, that could bring important information about this system. But this technique as well as STM has its own limitations like getting chemical information of the surface. Even if films could be observed at micrometer scale on the surface, it will not be possible to have a molecular resolution (with our setup) of their organization. In order to obtain as much usable information as possible, the experiment has to be methodic, proceeding by the deposition of the molecules step by step and comparing the images before and after the deposition of each layer of molecules.

I.3.2 – AFM characterizations

The first AFM images are made on HOPG substrate freshly cleaved, to see its aspect before depositing the layer of TSB-C12 (Figure 52).

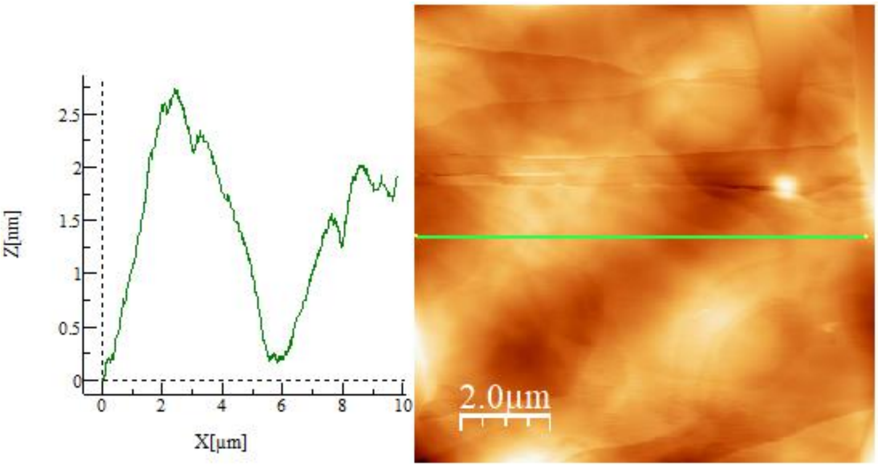

Figure 52 : AFM image of HOPG substrate (right) with height profile (left) (10 x 10 μm²)

The AFM images on HOPG show as expected, large flat terraces with some steps and defects created by the cleavage (Figure 52). The substrate exhibits minor variations of heights of 2-3 nm. This substrate will be used then to deposit the layers of TSB, ZnPc and the complex TBA[K^{Mo}(pyr)]-ZnPc.

I.3.2.1 – AFM images of deposited TSB-C12 on HOPG substrate

TSB-C12 solution was prepared (10^{-4} mol.L^{-1}) and deposited on HOPG substrate as described previously. The substrate was imaged by AFM on several areas (Figure 53).

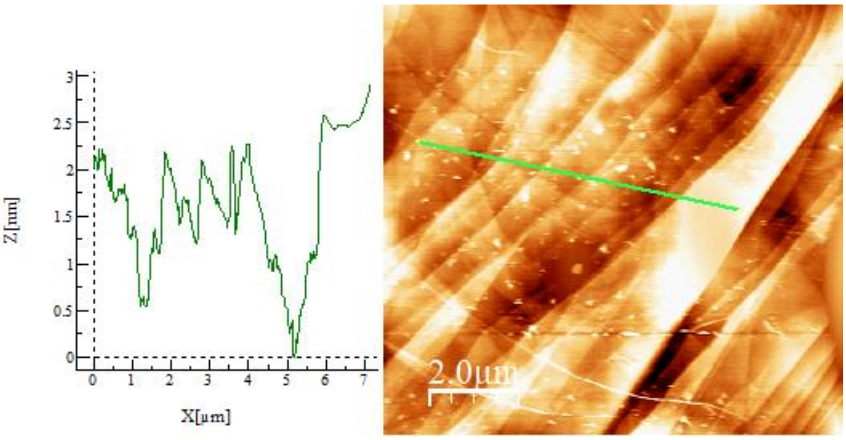

Figure 53 : AFM image of TSB-C12/HOPG substrate (right) and heights profile (left) (10 x 10 µm²)

The surface of the substrate after deposition of TSB-C12 presents some aggregates that can reach 10 nm height, that are assumed being formed by the excess of TSB-C12 molecules drop-casted on the surface (cf. part I.1 of this chapter). The molecule cannot be clearly distinguished on the flat zones on the image, but due to the STM images that have shown a complete coverage of the surface on many different areas of the substrate, it is assumed that the molecule follows the shapes of HOPG forming a layer on the surface.

These aggregates could have been insignificant given their number and their size, but as the aim is to deposit other layers and to be able to distinguish between the molecules on the surface, they could be problematic and confusing. Thus, the substrate was washed by several methods (drop casting 300 µL of toluene on the surface of tilted substrate or immersing it for 30 seconds to 1 hour into toluene) to get rid of these TSB aggregates. Figure 54 shows an AFM image of the substrate TSB-C12/HOPG after immersion in toluene for 10 min.

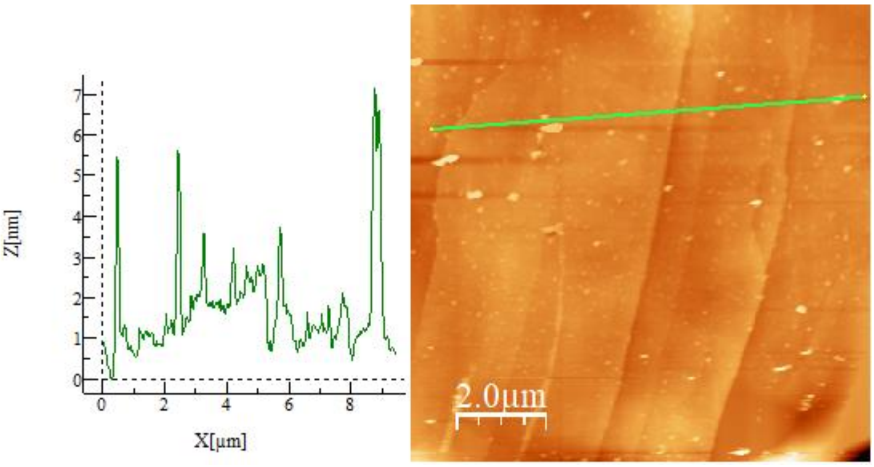

Figure 54 : AFM image of TCB-C12/HOPG substrate after 10 min immersion in toluene (right) and heights profile (left) (10 x 10 µm²)

The washing operations didn't give the expected result of removing the aggregates of TSB-C12 on the surface, as shown in Figure 54, the substrate still present aggregates of about 10 nm height.

I.3.2.2 – AFM imaging of ZnPc deposited on TSB-C12/HOPG substrate

Despite the presence of the TSB-C12 aggregates, ZnPc is drop casted on the surface of the substrate, in the same conditions as described previously, and the sample is imaged by AFM (Figure 55).

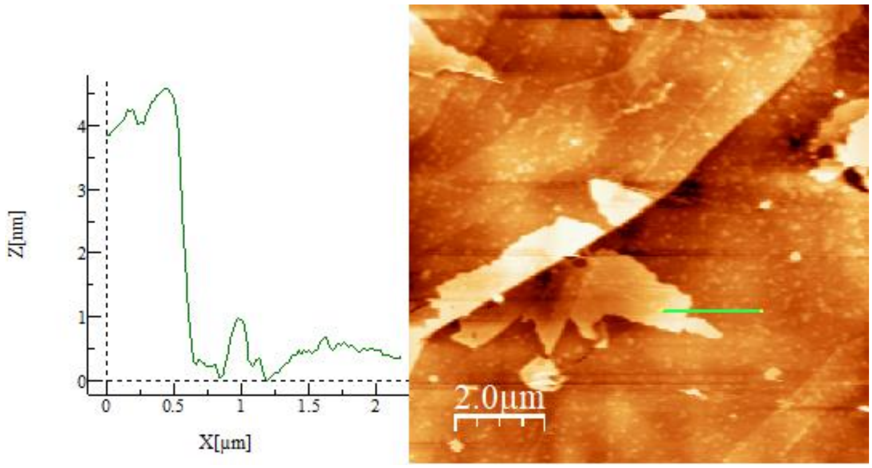

Figure 55 : AFM images of ZnPc-TSB-C12/HOPG (right) with height profile (left) (10 x 10 µm²)

The images obtained after the deposition of ZnPc (Figure 55 right) show the formation of a thin film on some areas on the surface, that has a height of around 5 nm (Figure 55 left). This film is present all over the sample surface with different coverage rates, with no big aggregates of ZnPc molecules found on the surface. One hypothesis is that ZnPc molecules pi-stack on each other on the surface forming these layers with a remarkable homogeneous thickness. The sample still presents the typical aggregates found after the deposition of the TSB, but due to the limitation of this technique (no chemical information), it is not possible to know if they are exclusively composed of TSB-C12 or if ZnPc form some aggregates as well.

I.3.2.3 – AFM images of the TBA[K^{Mo}(pyr)]-ZnPc complex deposited on TSB-C12/HOPG substrate

A substrate of TSB-C12/HOPG is prepared and imaged by AFM before and after deposition of TSB-C12 on HOPG. TBA[K^{Mo}(pyr)]-ZnPc complex is then drop casted on the surface of this substrate according to the conditions described previously for STM imaging, with 0.2 equivalents of TBA[K^{Mo}(pyr)] relatively to ZnPc. These conditions with an excess of ZnPc in solution should avoid the presence of a big quantity of free TBA[K^{Mo}(pyr)], that could form aggregates on the surface by pushing the equilibrium toward the formation of the TBA[K^{Mo}(pyr)]-ZnPc. The sample is then imaged by AFM and a typical image obtained is shown in Figure 56.

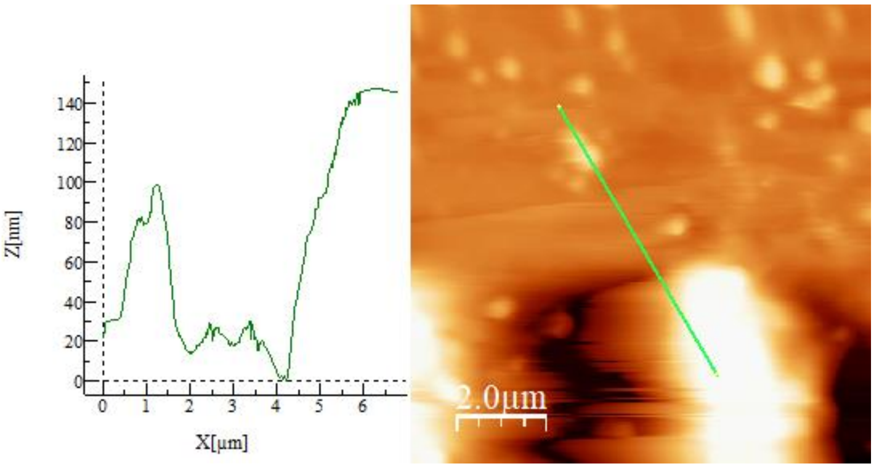

Figure 56 : AFM image of TBA[K^{Mo}(pyr)]-ZnPc complex drop casted on TSB-C12/HOPG substrate (right) and height profile (left) (10 x 10 µm^2)

The images obtained (Figure 56, right) show the formation of big aggregates on the surface of the sample, with heights over than 100 nm (Figure 56, left), making AFM imaging difficult as it is shown on the sides of the big aggregate at the bottom of the image in Figure 56 (right). The behavior of the complex is thus very different from ZnPc alone, which tend to show that the TBA[K^{Mo}(pyr)]-ZnPc form aggregates rather than to be guided into the pores on surface by the ZnPc.

I.3.2.4 – Images of TBA[K^{Mo}(pyr)] deposited on TSB-C12/HOPG substrate

In order to see if the deposition of the TBA[K^{Mo}(pyr)] is affected by its coordination in solution to the ZnPc, a solution of TBA[K^{Mo}(pyr)] in the binary solvent $CH_3CN/CHCl_3$ (30/70), with the same concentration as the solution deposited previously, is prepared. 15 µL of this solution is drop casted on the surface of a functionalized substrate TSB-C12/HOPG, imaged by AFM before and after the deposition of the POM. The aim is to see the distribution on surface of the free TBA[K^{Mo}(pyr)] and to compare it to what was obtained by depositing the complex (Figure 57).

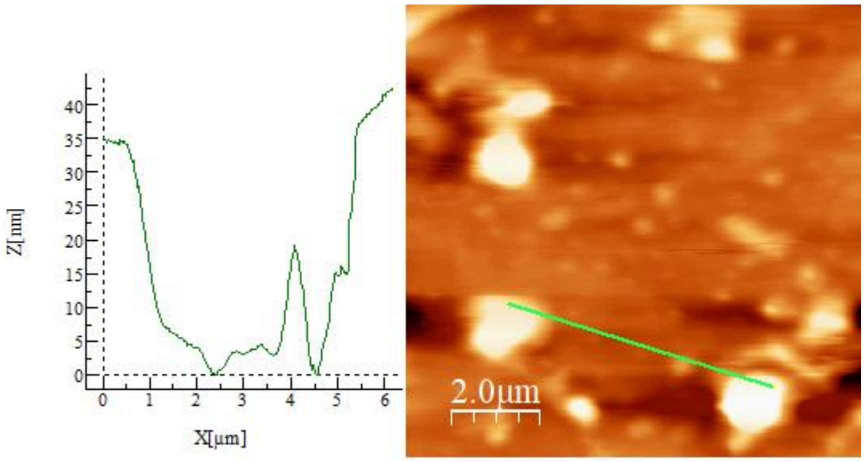

Figure 57 : AFM image of TBA[K^{Mo}(pyr)] deposited by drop casting on TSB-C12/HOPG substrate (right) with a heights profile (left) (10 x 10 µm^2)

As shown in Figure 57 (right), the sample gave similar images as the ones of the TBA[K^{Mo}(pyr)]-ZnPc complex, with many aggregates showing heights over 50 nm and up to 120 nm. The fact that no differences are observed in AFM between the sample with TBA[K^{Mo}(pyr)] alone, and the sample with the TBA[K^{Mo}(pyr)]-ZnPc complex tend to demonstrate that the organization of the functionalized POM on surface is not affected by its complexation to the ZnPc.

I.3.2.5 – Discussion

The results obtained by AFM give important information. Indeed, it is shown that the surface of the substrate remains globally flat with aggregates of maximum 15 nm heights when TSB-C12 and ZnPc are deposited and self-assembled on HOPG. But when the complex TBA[K^{Mo}(pyr)]-ZnPc is deposited, much bigger aggregates are formed, with heights over than 100 nm, as it is observed with the TBA[K^{Mo}(pyr)] alone. This result tends to confirm the hypothesis that POMs are not driven into the pores by the ZnPc and form aggregates on the surface of the functionalized substrate. This could be explained by the POM to POM interactions in solution, which maintains the POMs together even if they are complexed to ZnPc, forming aggregates of complexes and/or free POMs on the surface. This effect prevents POMs to be separated and go into the pores individually. Another parameter that certainly helps to form aggregates is the low affinity between the TBA[K^{Mo}(pyr)], an ionic inorganic molecule, and the HOPG surface composed of non-polar carbon layer. This low affinity makes the POMs form aggregates when they are drop casted on the surface, to minimize their contact surface with HOPG. Nevertheless, the limitations of our AFM don't allow obtaining a molecular resolution of the layers between the aggregates. As a result, the hypothesis of the deposition and organization of the TBA[K^{Mo}(pyr)]-ZnPc between the aggregates, in the flat areas of the sample, remains possible. In this case, the formation of aggregates could be due to the excess of the molecules deposited on the surface compared to the available pores. Another limitation of the AFM is the impossibility to get chemical information about the aggregates observed on the surface. Even though the characterization techniques tend all to converge to the aggregation of the POMs, a definite proof is still needed to be able to close this chapter. To be able to get such chemical information, spectroscopic techniques would be for a great help. But to probe a monolayer on surface and at the molecular scale, a particularly sensitive technique will be needed. During my thesis, I had the chance to have an access to a particularly interesting technique, that allows to have such precise and localized probe and to give the answer about the organization of this TBA[K^{Mo}(pyr)]-ZnPc on TSB-C12/HOPG system. This technique is the infrared nanospectroscopy, also known as AFM-IR. The characterizations with AFM IR were performed at the University of Paris Saclay, in the laboratory of Physical Chemistry, at the infrared laser center (CLIO) in collaboration with Dr. Alexandre Dazzi.

I.3.3 – AFM-IR characterizations

The AFM-IR is a sensitive technique that combines an atomic force microscope with an IR laser probe. This technique allows taking an IR spectrum on a very localized area on the sample selected on the AFM image. Moreover, it generates a surface map at a chosen IR wavelength, brightening all molecules exhibiting vibrational modes (IR bands) at that specific wavelength on the image.

I.3.3.1 – AFM-IR principle

AFM-IR, also called PTIR for Photo Thermal Induced Resonance, is a nanoscale infrared measurement technique developed during these two last decades. The first paper on AFM-based infrared spectroscopy was reported by Hammiche *et al*. in 1999[211] where they recorded infrared absorption spectra of polymeric samples by detecting photothermally induced temperature fluctuations at the sample surface, demonstrating that it is possible to reach high spatial infrared resolution. In 2001[212] they obtained the first probe-based infrared spectrum with a pulsed laser, but without reporting any image. AFM-IR nanoscale imaging using a pulsed laser was first reported by Dazzi *et al*. at the University of Paris-Sud in France. They first introduced the concept of AFM-IR in a publication in 2005.[213]

The technique works by using an infrared laser to locally heat up the sample surface underneath the AFM probe. As the sample heats up, it expands, causing the probe to deflect. By monitoring the deflection of the probe, the thermal expansion of the sample can be measured. The deflection of the probe is directly related to the absorption of the infrared radiation by the sample, providing information about its chemical composition. As the sample heats up, it also emits thermal radiation, including infrared radiation. By scanning the sample with the AFM probe while simultaneously measuring the infrared absorption, AFM-IR can generate nanoscale-resolution chemical maps of a sample's surface. It enables the identification and localization of different chemical species within a sample, even at the nanometer scale including monolayers and single molecules.[214–218]

AFM IR measurement consists of performing an AFM image with a gold coated silicon tip with an IR laser of about 1 mm diameter focused at the base of the AFM tip. Usual AFM images are obtained, including a topography image. In addition, by fixing the wavelength of the IR apparatus at a chosen value, generally at a known band of the probed molecule, an IR mapping of the surface is obtained where all the molecules possessing a band at this wavelength are brightened on the surface. The resolution on the x and y axis on the IR absorption map is limited by the AFM tip deconvolution. Typical AFM IR analysis and a scheme of the apparatus are shown in Figure 58.

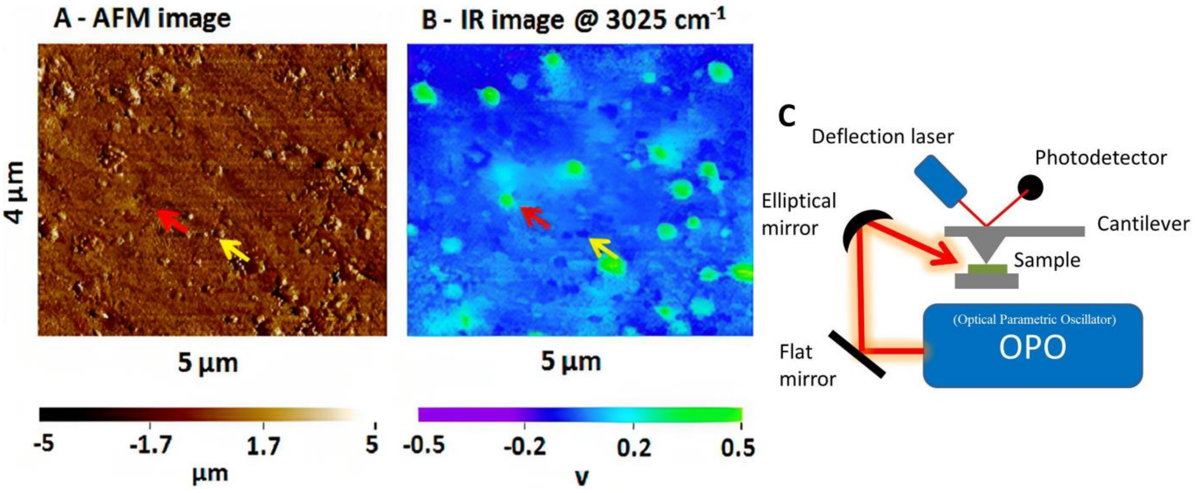

Figure 58: AFM-IR measurements of a 100% acrylonitrile butadiene styrene (ABS) polymer sample. (A) AFM topographic image. (B) AFM-IR absorption map with the IR source tuned to 3025 cm^{-1}, corresponding to a strong styrene absorption. Red arrows point to regions of high PS concentration. The yellow arrows indicate softer regions corresponding to higher PB content.[219] *C) schematic drawing of experimental AFM-IR setup*[219]

Several series of measurements were performed on the system TBA[K^{Mo}(pyr)]-ZnPc on TSB-C12/HOPG. The AFM-IR spectra obtained are systematically compared to IR spectra of the corresponding molecule (TSB, ZnPc, TBA[K^{Mo}(pyr)]) made by FTIR technique (using KBr crystal). The range of the wavelength measured by AFM-IR is from 900 cm^{-1} to 1900 cm^{-1}, thus, the FTIR spectra is reduced to this range as well.

I.3.3.2 – AFM-IR first series of measurements

The first series of AFM-IR measurements were carried out by taking IR spectra on various spots of AFM images (aggregates, flat areas, multilayer areas) of four samples: HOPG substrate, TSB-C12/HOPG functionalized substrate, ZnPc-TSB-C12/HOPG sample and the complex TBA[K^{Mo}(pyr)]-ZnPc on TSB-C12/HOPG sample. The spectra obtained are compared to the FTIR data of the molecules, as shown in Figure 59.

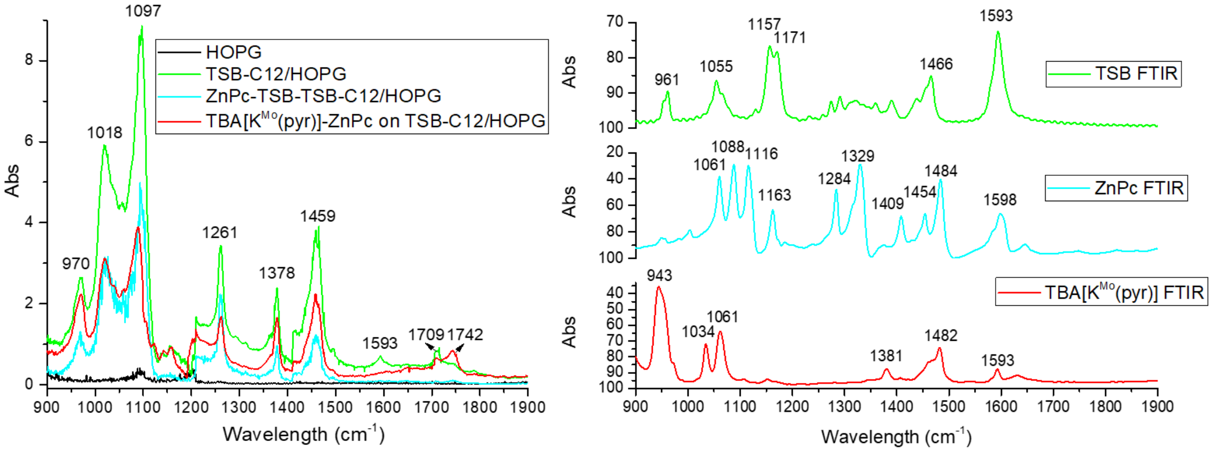

Figure 59 : (left) IR spectra of the superposed AFM-IR spectra made on HOPG (black) TSB-C12/HOPG substrate (green) ZnPc-TSB-C12/HOPG sample (blue) and TBA[K^{Mo}(pyr)]-ZnPc on TSB-C12/HOPG (red). (right) FTIR spectra of TSB (green), ZnPc (blue) and TBA[K^{Mo}(pyr)] (red)

The spectrum obtained on HOPG substrate by AFM-IR (Figure 59 left) shows the presence of two small peaks at about 1095 and 1200 cm^{-1}. It is worthy to mention that the absorbance of the HOPG spectrum is much weaker compare to the spectra obtained after the deposition of the different molecules on the surface. This means that the signal of HOPG will not mask the signal of the other molecules during the experiment.

The AFM-IR spectra of the samples after deposition of TSB-C12 and the addition of ZnPc alone or TBA[K^{Mo}(pyr)]-ZnPc complex (Figure 59 left, green, blue and red spectra, respectively) show globally the same features. One exception is the band at 1593 cm^{-1} obtained on the spectrum of TSB-C12/HOPG sample (Figure 59 left, green spectrum) and attributed to the band of TSB-C12 at the same wavelength obtained by FTIR (Figure 59 right, green spectrum) resulting probably from the C=C trans bond of the TSB-C12 molecule. This band it disappears after the deposition of ZnPc or TBA[K^{Mo}(pyr)]-ZnPc on the TSB-C12/HOPG substrate (Figure 59 left, spectra blue and red, respectively). Note that none of ZnPc or TBA[K^{Mo}(pyr)] have been detected on the AFM-IR spectra. The bands at 1378 and 1459 cm^{-1} are attributed to the methyl rock and to the C–H scissoring of a CH_3 group, respectively, and are generally present in almost all organic molecules.[220] Bands that are present on all spectra of AFM-IR except the HOPG and cannot be attributed are assumed to be contaminations. Particularly, the intense large bands at 1018 and 1097cm^{-1} (Figure 59 left, on the red, green and blue spectra) probably mask a part of the IR signal of the studied molecules. Also, a variation in the intensities and sometime the position of these contamination bands is noticed, making the subtraction of this signal impossible. The source of this contamination appeared to be, at least partly, related to the PDMS polymer which is found in the AFM tip storage boxes in which the latter are placed (Figure 60). The intensity of the bands also varies in function of the orientation of the beam (that is optimized before each measurement on a new substrate).

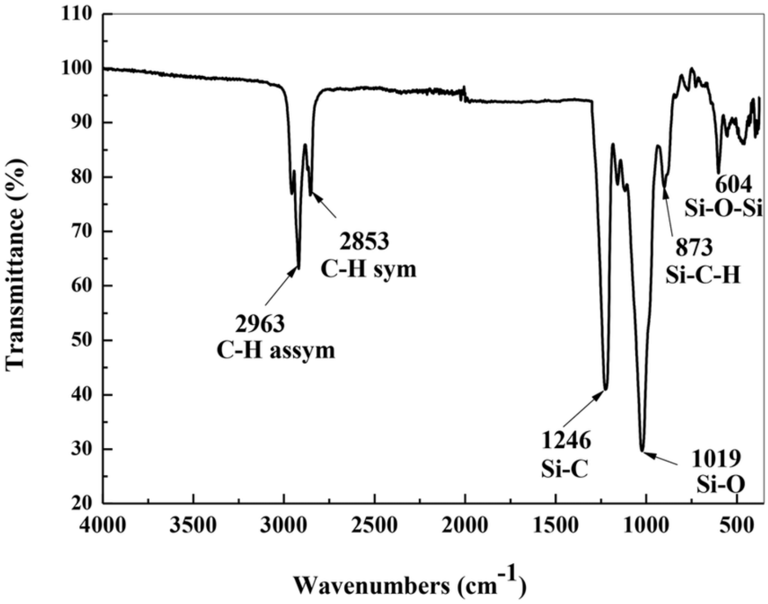

Figure 60 : FT-IR spectra of PDMS membranes.[221]

I.3.3.3 – AFM-IR second series of measurements

Another series of AFM-IR measurements were performed, and to get rid of the PDMS signal, new tips stored on metallic support are used. Additionally, reference samples are prepared, consisting of freshly cleaved HOPG on which important quantities of TSB, or ZnPc, or TBA[K^{Mo}(pyr)] are drop casted in order to increase the chances to get the signature of these molecules.

I.3.3.3.1 – Analysis of TSB-C12 on HOPG by AFM-IR

The first reference sample analyzed is that of TSB-C12, prepared by depositing on the HOPG substrate a solution approximately 10 times more concentrated than what is typically used to prepare a sample. The resulting spectrum was compared to the spectrum of TSB-C12 obtained by FTIR spectroscopy (Figure 61).

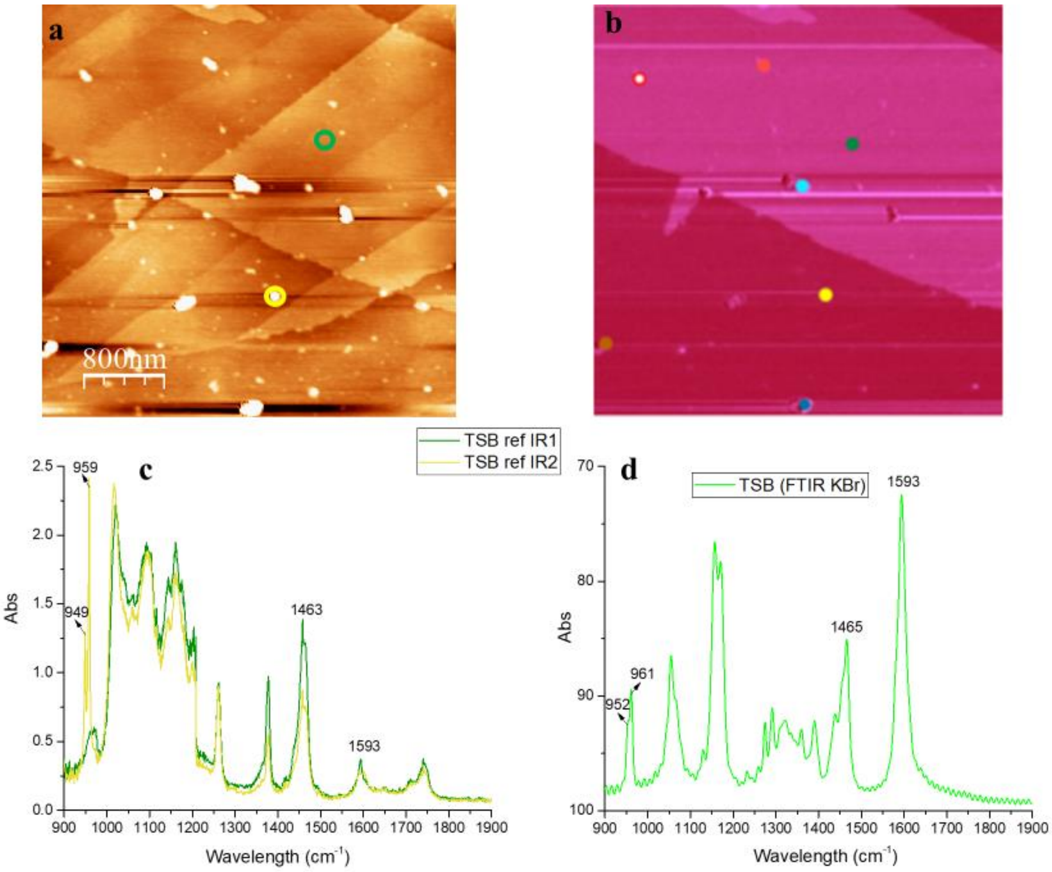

Figure 61 : Reference TSB-C12 on HOPG substrate sample measured by AFM-IR and compared to TSB-C12 FTIR spectrum (a) Topography AFM image of TSB-C12 on HOPG with the yellow and green spots of the IR measurements (b) AFM-IR image of TSB-C12 on HOPG with all spots of IR measurements(red, green, light and dark blue, yellow and white points) (c) AFM-IR spectra of TSB-C12 on HOPG on the corresponding yellow and green spots on the AFM-IR image (d) FTIR spectrum of TSB-C12 (IR source tuned to 1593 cm^{-1}*)*

The spectra of the TSB-12 reference sample still show the presence of several bands that cannot be attributed to this molecule, particularly the large intense bands between 1000 and 1200 cm^{-1} (Figure 61 c). These bands are not related to the PDMS polymer and come from another source of contamination. However, the band at 1593 cm^{-1} corresponding to the most intense band of the TSB-C12 in FTIR spectroscopy, and attributed to the stretching of the C=C trans bonds on the molecule as well as to the C=C aromatic bonds,[222,223] appear clearly. The bands at 1463 cm^{-1} and 959 cm^{-1} could also be attributed to the TSB-C12 on this sample. An interesting point about the band at 959 cm^{-1} is the variation of its shape. When the IR spectrum is taken on an aggregate of TSB-C12, a double band intense and thin (Figure 61 c, yellow spectrum) is detected. And when it is taken on a film of TSB-C12, a single large band with a weak intensity (Figure 61 (c), green spectrum) is detected. On the FTIR spectrum of the TSB-C12 in Figure 61 (d), the band at 961 cm^{-1}, reported in the literature for a similar molecule at 955 ± 5 cm^{-1} and attributed to the wagging vibration of the *trans* double C=C bond[224], has the shape of two overlapped thin bands. The difference of this band in AFM-IR between an aggregate and flat film could be due to the different orientations of the TSB-C12 molecule. Indeed, within aggregates, molecules are randomly oriented in space, but when they are pi-stacked on the surface, they all share the same orientation relative to the infrared beam, and this can have an effect on the intensity of the IR bands.[225–228]

After the measurements on this reference TSB-C12 substrate, a sample prepared by drop casting 10 µL of a solution of 10^{-4} mol.L^{-1} of TSB-C12 in toluene on HOPG freshly cleaved is prepared and measured by AFM-IR (Figure 62).

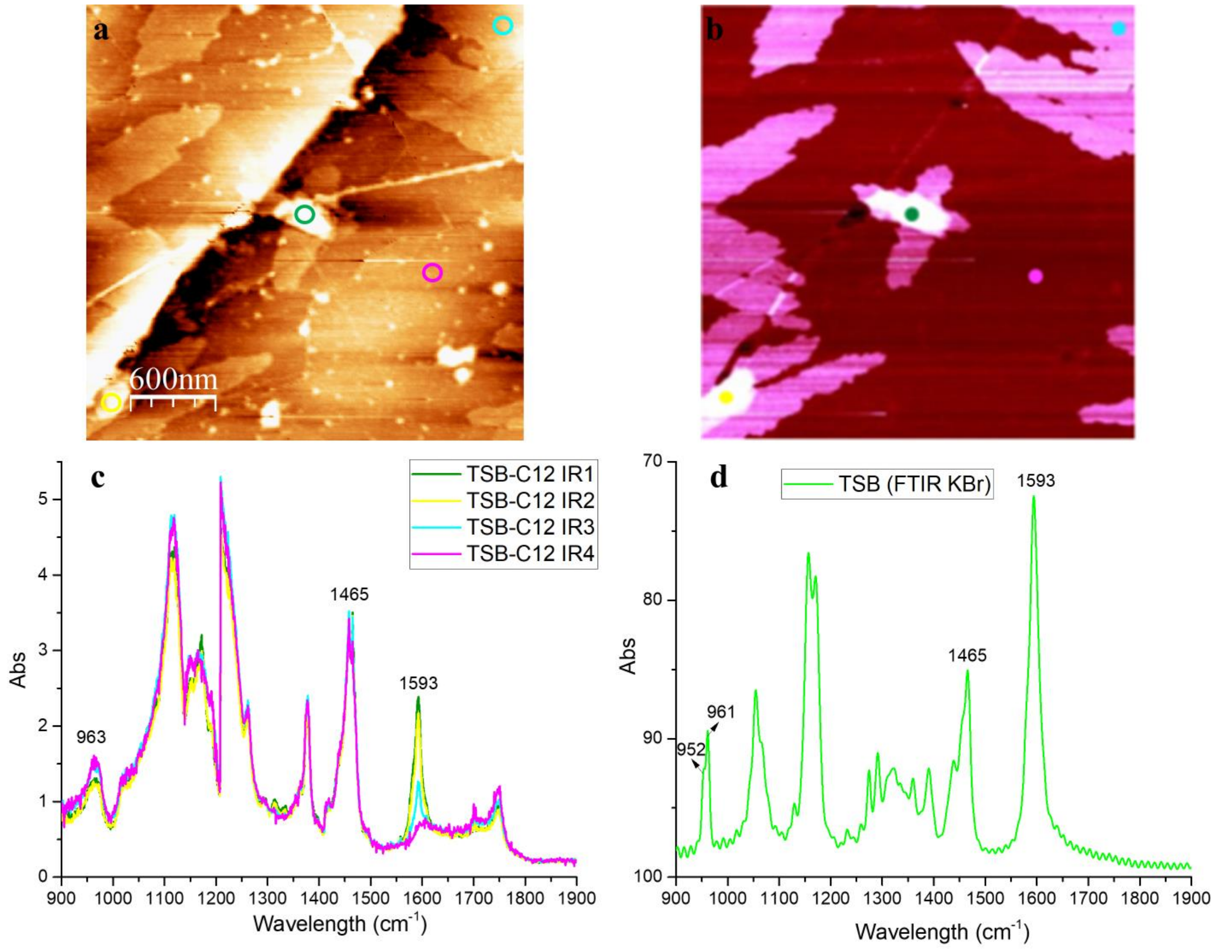

Figure 62 : TSB-C12 on HOPG substrate sample measured by AFM-IR and compared to TSB-C12 FTIR spectrum (a) Topography AFM image of TSB-C12 on HOPG with the yellow and green spots of the IR measurements (b) AFM-IR image of TSB-C12 on HOPG with all spots of IR measurements (c) AFM-IR spectra of TSB-C12 on HOPG on the corresponding yellow and green spots on the AFM-IR image (d) FTIR spectrum of TSB-C12 (IR source tuned to 1593 cm^{-1})

On the topography image (Figure 62 (a)) flat films with a thickness of about 2~3 nm are observed. More thick films are also noticed, with a thickness of around 5-6 nm on the yellow spot and around 8 nm on the green spot, that are assumed to be pi-stacked multilayers of TSB-C12. Some aggregates are also observed, with a size of no more than 15 nm. The AFM-IR image (Figure 62 (b)) shows these same films brightened, confirming their attribution to TSB-C12 molecule. Interestingly, the aggregates are not brightened on the AFM-IR image.

The evolution of the bands attributed to the TSB-C12 molecule depending on the spot measured (Figure 62 (c)) show that the band at 1593 cm^{-1} evolve logically in terms of intensity depending on the thickness of the layer measured. When the spectrum is taken on the purple spot Figure 62 (a) and (b), where there is no apparent TSB-C12 on the surface, the band appears very weak as it is shown on the purple spectra Figure 62 (c). Then, when a thin film of TSB-C12 is measured by AFM-IR (Figure 62 (a) and (b), blue spot) a clear band at 1593 cm^{-1} appears. The intensity of this band increase then logically when areas that seems to be multilayers of TSB-C12 are measured.

It is worth noting that the bands at 1465 cm^{-1} and 963 cm^{-1} did exhibit only a very small evolution depending on the thickness of the TSB-C12 film measured. The origin of this signal still requires further investigation, although it is certain that TSB-C12 plays a role in it.

I.3.3.3.2 – Analysis of ZnPC on HOPG and ZnPc on TSB-C12/HOPG by AFM-IR

After the results obtained for the TSB-C12/HOPG sample, a reference sample for the ZnPc molecule is prepared by drop casting a concentrated solution of ZnPc in toluene (about 10 times the concentration used usually to prepare the samples) on HOPG substrate without the presence of TSB-C12. AFM-IR measurements are performed on this reference sample and compared to the FTIR spectra of ZnPc (Figure 63).

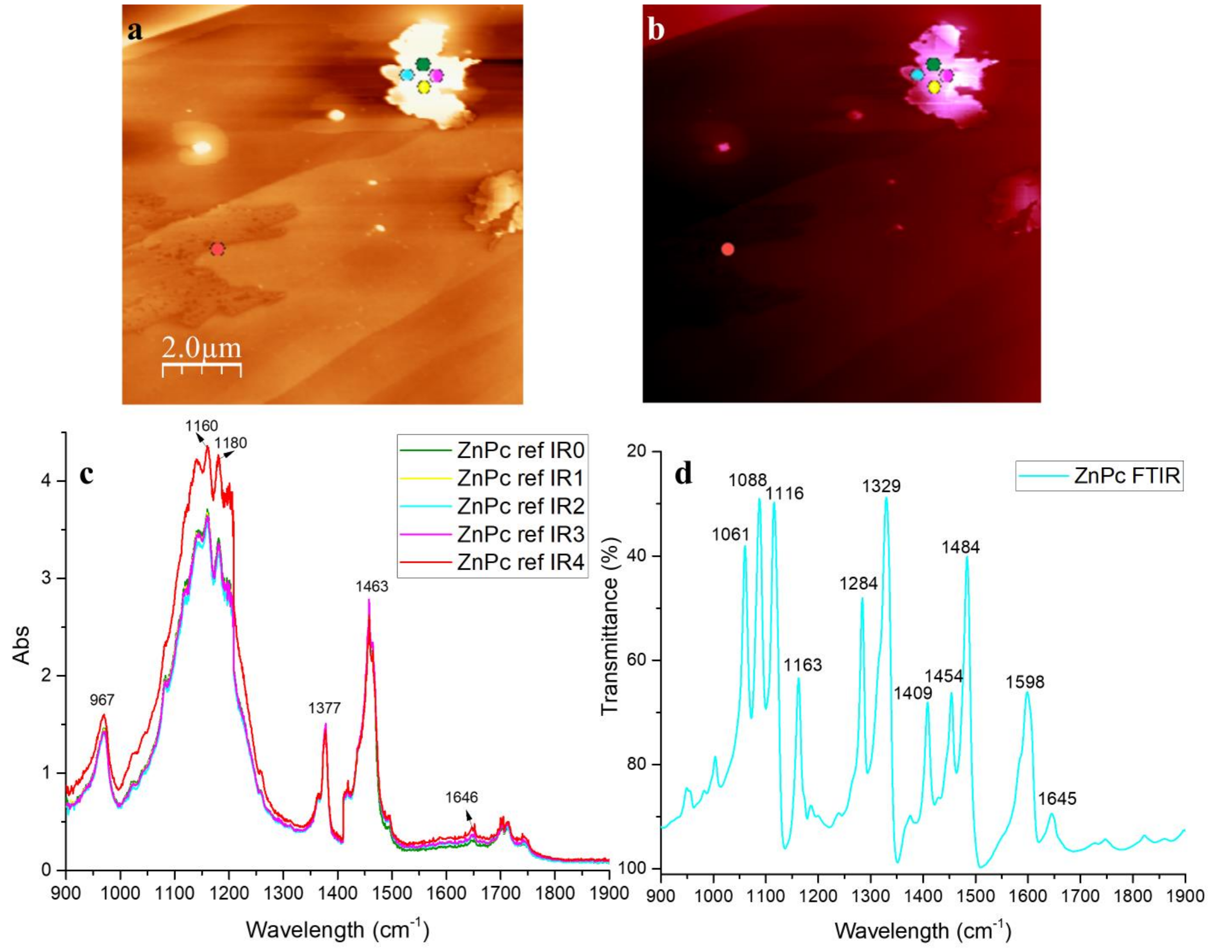

Figure 63 : ZnPc on HOPG substrate reference sample measured by AFM-IR and compared to ZnPc FTIR spectra (a) Topography AFM image of ZnPc on HOPG with the spots of IR measurements (blue, green, yellow and purple on the layer formed on the surface, and red on a flat area) (b) AFM-IR image of ZnPc on HOPG with spots of IR measurements (c) AFM-IR spectra of ZnPc on HOPG on the corresponding spots on the AFM-IR image (d) FTIR spectrum of ZnPc (IR source tuned to 1650 cm^{-1})

The topography image (Figure 63 a) show a flat surface with some aggregates and small films of around 4~5 nm height. The aggregates as well as the layers on the surface of the sample are brightened on the IR image of the surface.

Interestingly, the spectra show the presence of the band at 967 cm^{-1} despite no TSB-C12 was deposited on this sample. This shows that this weak band is not related to the TSB-C12. Still, the intense thin double band at 949-959 cm^{-1} detected on aggregates (cf. Figure 61 (c), yellow spectra) continues to clearly align with that of the TSB-C12 molecule, detected on the FTIR spectrum (cf. Figure 61 (d)), comforting the hypothesis that this band does not appear on the layers of pi-stacked TSB-C12 due to orientation effects.

Concerning the ZnPc, a weak band detected by AFM-IR (Figure 63 (c)) at 1646 cm^{-1} can be attributed to the molecule**.** This band is also reported in FTIR spectrum (Figure 63 (d)) and is characteristic of the C=N functions of the ZnPc and, more generally, in phtalocyanine molecules.[229,230] The intensity of this band remains fairly constant on all the spots measured on the enlightened surface, showing its presence with approximately the same amount on all these spots.

Notably, the band at 1598 cm^{-1} is not detected by AFM-IR despite the absence of contamination band at this wavelength, this can be explained by the orientation effect of the ZnPc that make this band not visible.

To summarize, this measurement on the ZnPc reference sample allowed detecting one distinctive band of the molecule at 1646 cm^{-1}. And also, it allowed showing that the weak large band at 967 cm^{-1} is not related to the TSB-C12 molecule.

The next AFM-IR measurement is done on ZnPc-TSB-C12/HOPG sample that is prepared as described in part II.1. The resulting spectra are compared to ZnPc FTIR spectrum (Figure 64).

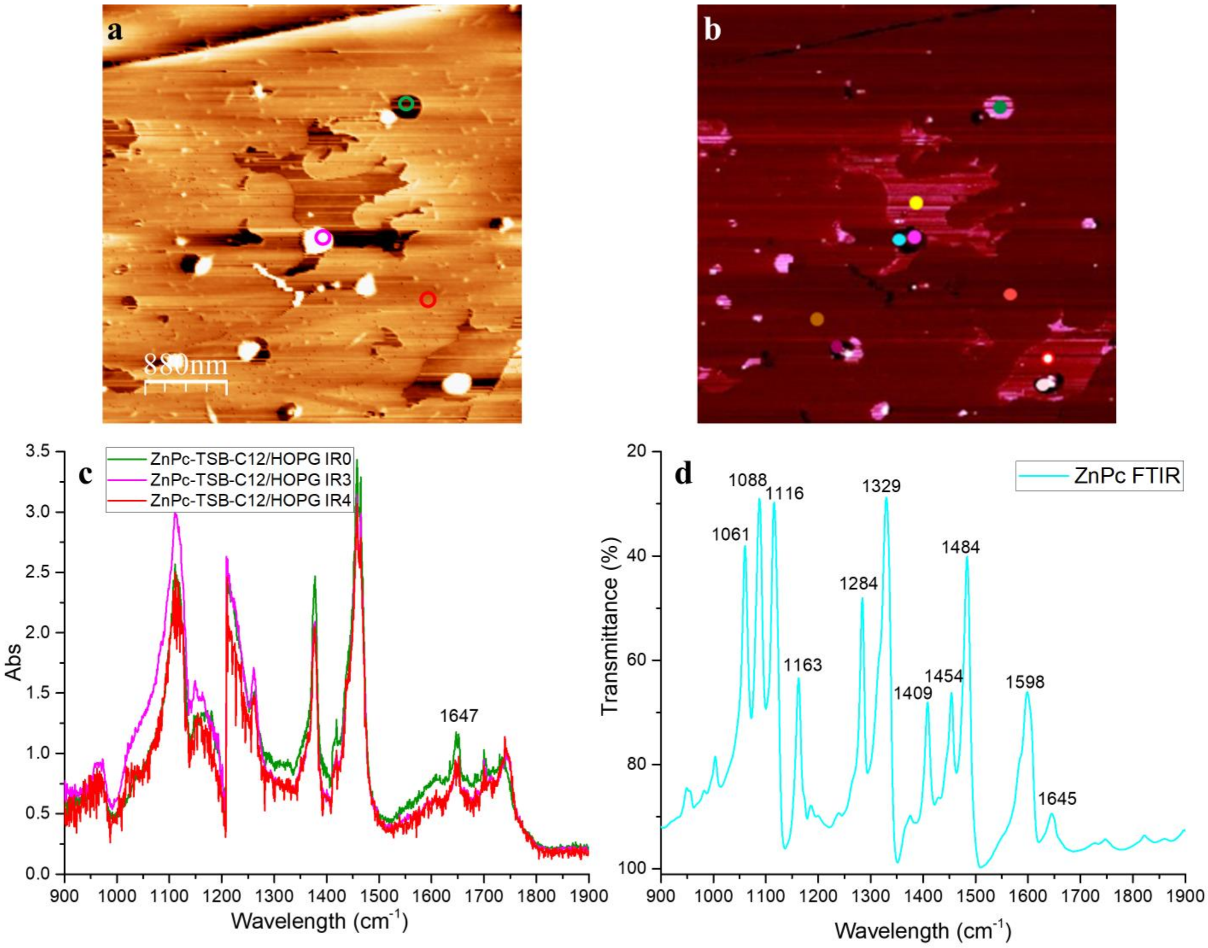

Figure 64 : ZnPc-TSB-C12/HOPG sample measured by AFM-IR and compared to ZnPc FTIR spectrum (a) Topography AFM image of ZnPc-TSB-C12/HOPG with the selected spots of IR measurements shown (b) AFM-IR image of ZnPc-TSB-C12/HOPG with all spots of IR measurements (c) AFM-IR spectra of ZnPc-TSB-C12/HOPG on the corresponding selected spots on the topography AFM-IR image (d) FTIR spectrum of ZnPc (IR source tuned to 1650 cm^{-1})

The topography image (Figure 64a) reveals the presence of flat films with a height ranging from 3 to 5 nm and some aggregates measuring around 15 to 20 nm. Note that due to imaging issues, the films and some aggregates appear darker than the flat areas. The AFM-IR image (Figure 64 b) enlightened both the aggregates and the films, with more intensity observed on the aggregates.

AFM-IR measurements of ZnPc-TCB-C12/HOPG sample Figure 64 (c) show the spectra measured on different spots (Figure 64 (a) and (b) green, red and purple spots). The band attributed to the C=N bond of the ZnPc molecule at 1647 cm^{-1}, appear ones more on this sample.

The position and the intensity of this band are also in line with the spectrum of the molecule made by FTIR. The remaining bands in the spectra cannot be attributed to either ZnPc or TSB-C12 molecules.

I.3.3.3.3 – Analysis of TBA[K^{Mo}(pyr)] on HOPG and TBA[K^{Mo}(pyr)]-ZnPc on TSB-C12/HOPG by AFM-IR

The last samples analyzed are the ones with the TBA[K^{Mo}(pyr)] POM. A reference sample where 10 µL of a solution of TBA[K^{Mo}(pyr)] at 3.36*10^{-4} mol.L^{-1} is drop casted on HOPG substrate and analyzed by AFM-IR. The spectra obtained are compared to the FTIR spectrum of the TBA[K^{Mo}(pyr)] (Figure 65).

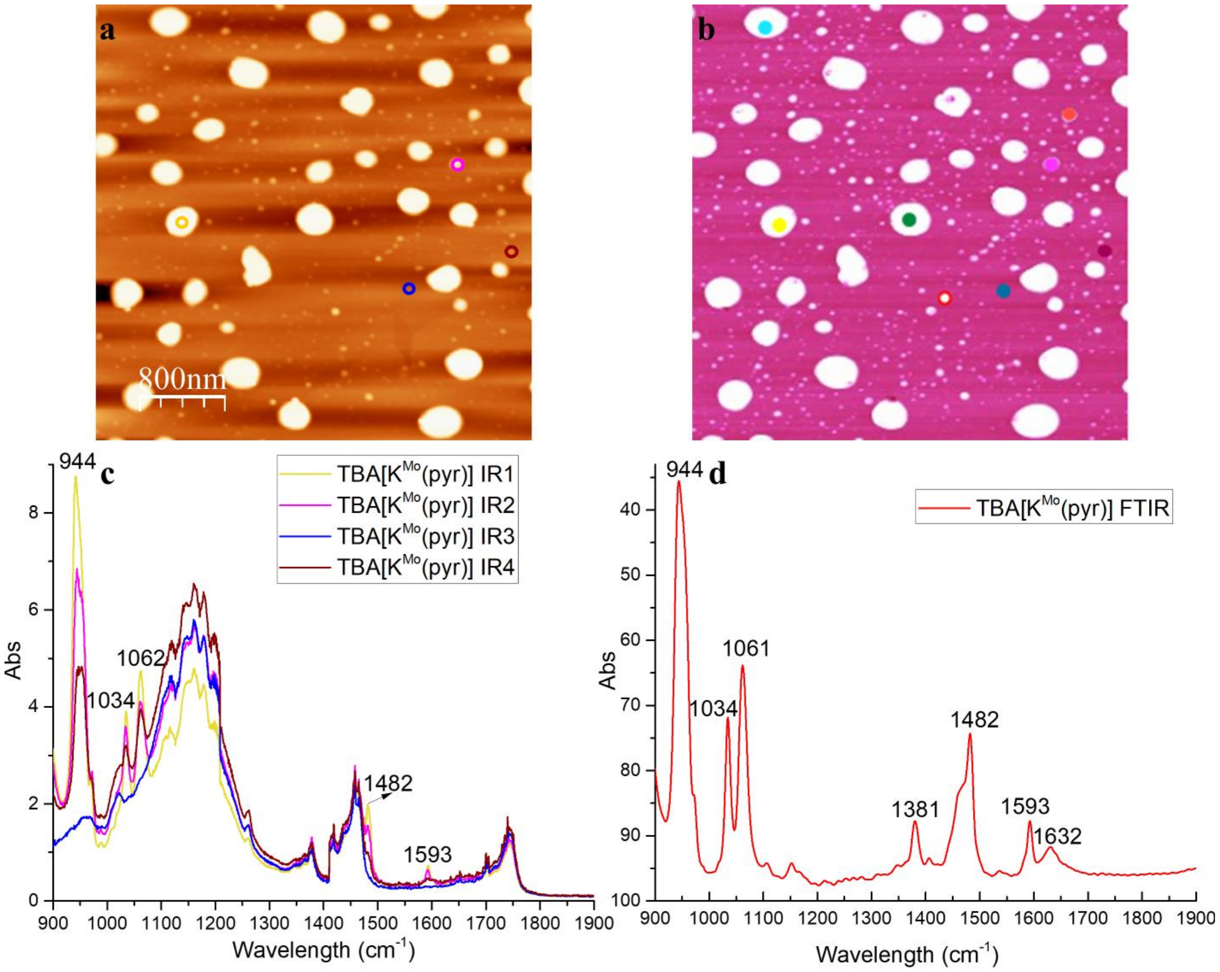

Figure 65 : TBA[K^{Mo}(pyr)] POM on HOPG substrate reference sample measured by AFM-IR and compared to TBA[K^{Mo}(pyr)] FTIR spectrum (a) Topography AFM image of TBA[K^{Mo}(pyr)] on HOPG with the spots of IR measurements (b) AFM-IR image of TBA[K^{Mo}(pyr)] on HOPG with spots of IR measurements (c) AFM-IR spectra of TBA[K^{Mo}(pyr)] on HOPG on the corresponding spots on the topography AFM-IR image (d) FTIR spectrum of TBA[K^{Mo}(pyr)] (IR source tuned to 944 cm^{-1})

As expected, the topography image (Figure 65 a) show that the TBA[K^{Mo}(pyr)] POM form aggregates that reach 100 nm in height and several hundred nm in width on the surface of the HOPG (Figure 65 (a)). The AFM-IR image enlightens all these aggregates.

The IR measurements reveal a clear signature of the TBA[K^{Mo}(pyr)]. Indeed, only two bands are missing in the spectra reported in Figure 65 (c) compare to the FTIR spectra of the molecule (Figure 65 (d)). The band at 1381 cm^{-1}, probably masked due to its weak intensity and its position near to the wavelength IR lamp switch of the apparatus, it is attributed to the TBA cations, and the band at 1632 cm^{-1} being one of the lowest intensity band of the molecule as shown by FTIR measurement (Figure 65 (d)), and attributed to residual H_2O molecule vibrations.[231]

All other bands of the TBA[K^{Mo}(pyr)] are detected on AFM-IR (Figure 65 (c), yellow, red and purple spectra). At 944 cm^{-1} and 1062 cm^{-1} these bands are typical Keggin POM bands related to (Mo-O) and (P-O) bonds, respectively.[231] The 1034 cm^{-1} is typical P-O bond of lacunar Keggin POMs,[232] and the band at 1482 cm^{-1} to the C-H bond of the TBA cations.[233] and even the band at 1593 cm^{-1} is detected, attributed to the aromatic C=C bond ring.[223]

The evolution of the intensity of these bands in function of the spot measured leaves no doubts about the nature of the aggregate observed. Indeed, the yellow spot situated on a big aggregate in Figure 65 (a) gives the yellow AFM-IR curve (Figure 65 (c)) with the most intense bands. And when a smaller aggregate is measured, such as the purple spot on a medium aggregate and the brown spot on a very small aggregate (Figure 65 (a)), the intensity of the peaks in the spectra obtained Figure 65 (c) decreases logically. Finally, when the measurement is made on a flat area on the surface, which is the case of the blue spot in Figure 65 (a), none of the bands attributed to the TBA[K^{Mo}(pyr)] are detected (blue curve Figure 65 (c)).

These results show that the technique is able to clearly detect the presence of the molecule even on very small aggregates such as the one on the brown spot Figure 65 (a) that has a height of 3 nm. It also shows that for the TBA[K^{Mo}(pyr)], the spectrum obtained by AFM-IR and FTIR spectroscopy are similar.

After the TBA[K^{Mo}(pyr)] on HOPG AFM-IR analysis, a sample of TBA[K^{Mo}(pyr)]-ZnPc drop casted on TSB-C12/HOPG is prepared. The solution of TBA[K^{Mo}(pyr)]-ZnPc used contains 0.2/1 equivalents of TBA[K^{Mo}(pyr)] and ZnPc respectively. The sample is prepared as described in the Chapter II.1 and measured by AFM-IR. The spectra obtained are compared to the FTIR spectra of TSB, ZnPc and TBA[K^{Mo}(pyr)] (Figure 66).

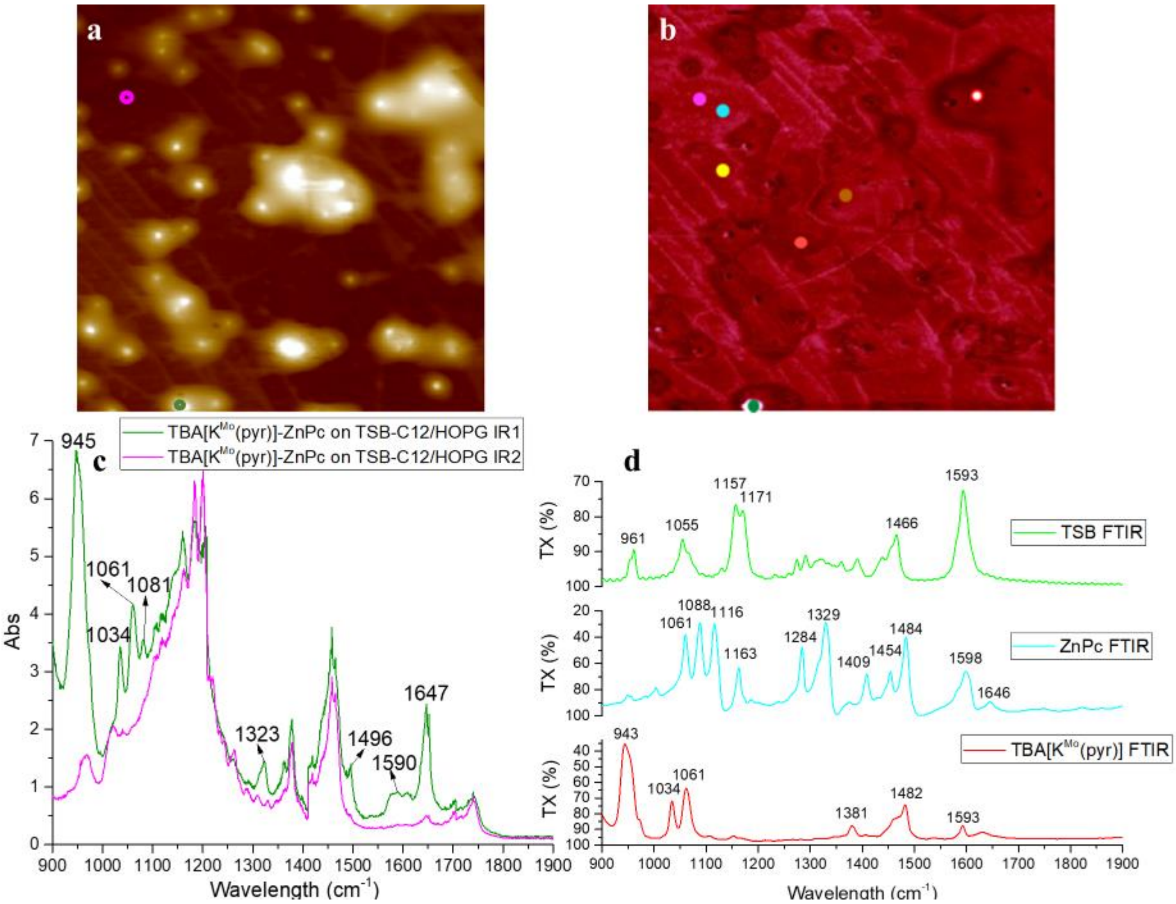

Figure 66 : TBA[K^{Mo}(pyr)]-ZnPc on TSB-C12/HOPG sample measured by AFM-IR and compared to TSB, ZnPc and TBA[K^{Mo}(pyr)] FTIR spectra (a) Topography AFM image of TBA[K^{Mo}(pyr)]-ZnPc on TSB-C12/HOPG with the green and purple spots of IR measurements (b) AFM-IR image of TBA[K^{Mo}(pyr)]-ZnPc on TSB-C12/HOPG with all spots of IR measurements (c) AFM-IR spectra of TBA[K^{Mo}(pyr)]-ZnPc on TSB-C12/HOPG on the corresponding spots on the topography AFM-IR image (d) FTIR spectrum of TSB-C12, ZnPc and TBA[K^{Mo}(pyr)] (IR source tuned to 944 cm^{-1})

The topography image (Figure 66 a) shows aggregates formed on the surface with heights up to 100 nm. Due to imaging problems, the IR image obtained (Figure 66 (b)) is not significant in terms of contrasts. However, the results of the AFM-IR measurements on the selected spots are significant and show the presence of the TBA[K^{Mo}(pyr)] in the aggregates formed on the surface. The IR peaks of TBA[K^{Mo}(pyr)] at 945 cm^{-1}, 1034 cm^{-1} and 1061 cm^{-1} Figure 66 (c) are detected on the green spot of Figure 66 (a) and (b) where the measurement is done on an aggregate. In contrary, when the IR measurement is made on the purple spot Figure 66 (a) and (b) that correspond to a flat area, the purple spectrum (Figure 66 (c)) where these peaks are not detected is obtained.

On the aggregate, ZnPc molecule is detected as well by the presence of its characteristic band at 1647 cm^{-1}. The presence of ZnPc and TBA[K^{Mo}(pyr)] in the same aggregate tend to demonstrate the aggregation of the entire TBA[K^{Mo}(pyr)]-ZnPc complex, but at this point, further investigations are needed to confirm it.

Low intensity bands are also detected around 1590 cm^{-1} that are difficult to attribute due to the presence of this signal in the three molecules, as shown in the FTIR spectra Figure 66 (d). The only apparent band on flat films of TSB-C12 in AFM-IR situated at 1593 cm^{-1} is probably included in this signal.

Even though these results show that at this ratio, the TBA[K^{Mo}(pyr)] is not driven to the pores of the TSB-C12/HOPG substrate but forms aggregates on the surface, the presence of the contaminations makes the IR imaging difficult and hide a part of the information given by the technique. Thus, two points still remains to be verified: the source of these contaminations, and the effect of the increase of the amount of TBA[K^{Mo}(pyr)] in solution to reach 1 equivalent versus ZnPc.

I.3.3.4 – Determination of the origin of the contamination signal

As the contamination signal appears from the deposition step of TSB-C12 molecule, one of their suspected source are the solvents. In order to verify it, freshly cleaved HOPG substrate is imaged and measured by AFM-IR to be used as a reference sample. A volume of 10 µL of pure toluene usually used as a solvent to deposit TSB-C12 is then drop casted on its surface and the sample is imaged and measured. The same operation is done with $CHCl_3$ solvent used to deposit ZnPc or the TBA[K^{Mo}(pyr)]-ZnPc complex on the functionalized substrate. The spectra obtained are then compared between them, and to the spectrum obtained during the previous series of measurements (Figure 67).

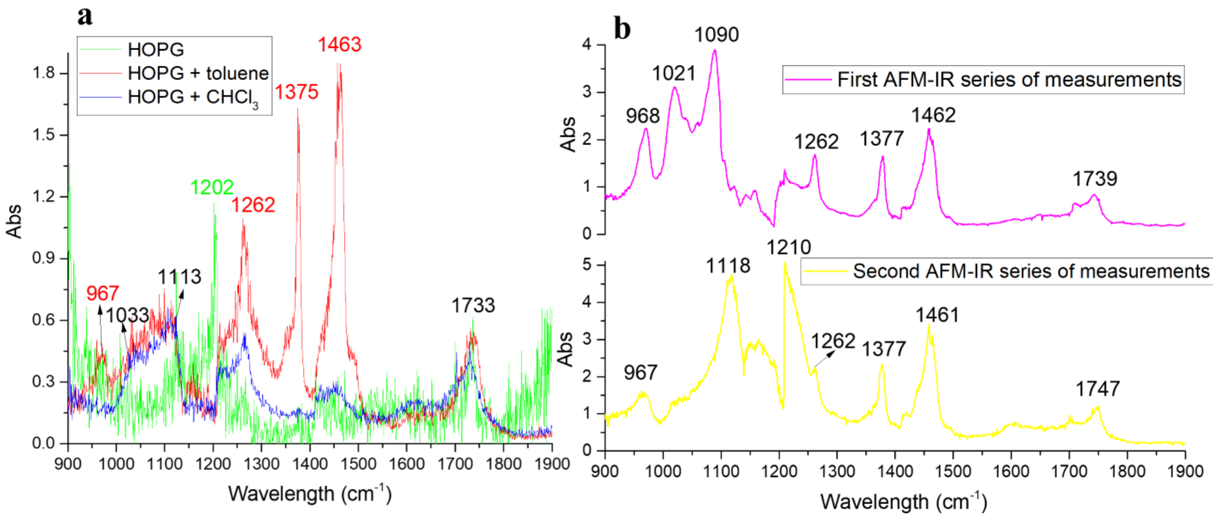

Figure 67 : (a) AFM-IR superposed spectra of HOPG (green), toluene on HOPG (red) and chloroform on HOPG (blue), (b) AFM-IR spectra of the contaminations noticed during the first (purple) and the second (yellow) series of AFM-IR measurements

The spectra show that the measurement on HOPG exhibit only two bands at 1202 cm^{-1} and 1733 cm^{-1} (Figure 67 (a), green curve). The band at 1202 cm^{-1} is reported in the literature as an OH bending of a protonated carbonyl oxygen,[234] while the one at 1733 cm^{-1} belong clearly to a carbonyl function. Thus, these two bands could be due to a slight oxidation of the surface of HOPG.

When toluene is deposited on the HOPG substrate, the spectrum reveals the presence of several bands with high intensity (Figure 67 (a), red curve). The two classic bands of CH_3 at 1375 cm^{-1} and 1463 cm^{-1}, generally present in almost all organic molecules are detected.[220] The use of toluene certainly contributed significantly to the presence of these bands on the two previous series of AFM-IR analysis, as shown in Figure 67 (b). The band at 1262 cm^{-1} is attributed to stretching vibrations of CH_3 and rocking, and to CH_2 wagging.[235–237] For the band at 967 cm^{-1} it is mainly attributed to an out-of-plane bending vibration of trans –HC=CH– group,[238] which confirm the orientation effects that explain why this band is not observed on the TSB-C12 films, but only on aggregates. The presence of this band in toluene reveals the possible contamination of this solvent.

The large overlapped bands from 1033 to 1113 cm^{-1}, common for both toluene and chloroform (Figure 67 (a), red and blue curves, respectively) could be attributed to C-C stretching for the first,[239] and C-H in plane bending for the second.[240]

The spectrum obtained after the deposition of $CHCl_3$ on HOPG substrate (Figure 67 (a), blue curve), shows the presence of less bands. The spectrum is close to the one obtained on HOPG alone (Figure

67 (a), green curve), the difference being the weak and large signal between 1033 cm^{-1} and 1113 cm^{-1} discussed previously.

Note that the band of HOPG (green curve Figure 67 (a)) is not detected on both other samples where chloroform and toluene are deposited.

These results demonstrate that unlike chloroform, the use of toluene as a deposition solvent leads to the appearance of several undesired bands. The replacement of toluene with chloroform for the depositions should result in IR spectra that are clearer and easier to interpret. However, there are still other contamination bands, located principally between 1000 and 1200 cm^{-1} (Figure 67 (b)), that cannot yet be attributed precisely, particularly due to the variation of the positions and intensities of the bands in this area from an experiment to another. One suspected origin of these contaminations is the AFM tip itself. Indeed, note that a change in the AFM tip typically results in a change in the IR contamination bands of this region, both in terms of intensity and position. To summarize, a table of all the bands observed during the two series of AFM-IR is presented below.

Table 3 : Summary of IR bands observed by AFM-IR for TSB-C12, ZnPc, TBA[K^{Mo}(pyr)] and different contaminations with their sources (tol = toluene)

Molecule	IR Bands (cm^{-1})
TSB-C12	949-959 (on aggregates only C=C trans), 1593 (C=C trans and aromatic rings)
ZnPc	1645 (typical C=N of some phtalocyanines)
TBA[K^{Mo}(pyr)]	944 (Mo-O), 1034 (P-O in lacunar POM), 1061 (P-O), 1482 (C-H of TBA), 1593 (C=C phenyl and pyridine groups)
Contaminations	968 (likely tol contaminations), 1000 ~ 1200 (likely the AFM tip), 1261 (likely tol), 1377 and 1462 (organic mol.) 1740 (likely substrate oxidation)

Despite the presence of these contaminations bands, the second series of AFM-IR characterizations shows clearly that for this sample where a solution with 0.2/1 equivalent of TBA[K^{Mo}(pyr)]/ZnPc, respectively, is deposited, the POM form aggregates on the functionalized substrate rather than to be driven into the pores by the ZnPc molecule. In particular, the use of reference samples, combined to the data of the FTIR spectra, permitted to leave no doubt for the identification and attribution of the bands on the AFM-IR belonging to each of TSB-C12, ZnPc and TBA[K^{Mo}(pyr)] molecules. This result is also consistent and helps explain the STM images obtained, where no TBA[K^{Mo}(pyr)] could be observed. Indeed, the STM tip passes through these big aggregates of POMs imaging only the ZnPc-TSB-C12 layer.

Nevertheless, one experiment is still required to fully characterize this TBA[K^{Mo}(pyr)]-ZnPc on TSB-C12/HOPG sample. An increase of the amount of TBA[K^{Mo}(pyr)] vs. ZnPc deposited on TSB-C12/HOPG to 1:1 equivalent could indeed give different results. In order to investigate this, another AFM-IR experiment is needed, and with the results obtained previously, the use of toluene will also be avoided and replaced by chloroform.

I.3.3.5 – Third series of AFM-IR measurements

For the last AFM-IR experiment performed at the end of my thesis, a sample is prepared consisting of HOPG functionalized with TSB-C12 on which a solution of TBA[K^{Mo}(pyr)]-ZnPc complex (1:1 equivalent of TBA[K^{Mo}(pyr)]/ZnPc) is drop casted. In this sample, the TSB-C12 is deposited in $CHCl_3$, then the TBA[K^{Mo}(pyr)]-ZnPc complex is deposited in the binary solvent acetonitrile/chloroform (30/70).

The sample is imaged using AFM-IR, and the same area is imaged first by setting the wavelength of the apparatus at 950 cm^{-1} to lighten the areas where the TBA[K^{Mo}(pyr)] is present (Figure 68 (a)), and secondly with the wavelength of the apparatus set at 1645 cm^{-1} to lighten the areas where the ZnPc is present (Figure 68 (b)). These values are chosen according to the peaks of these two molecules that was detected by AFM-IR during the previous AFM-IR measurement series. IR spectra are also made on a flat film attributed to the ZnPc molecule, on a big and on a small aggregate.

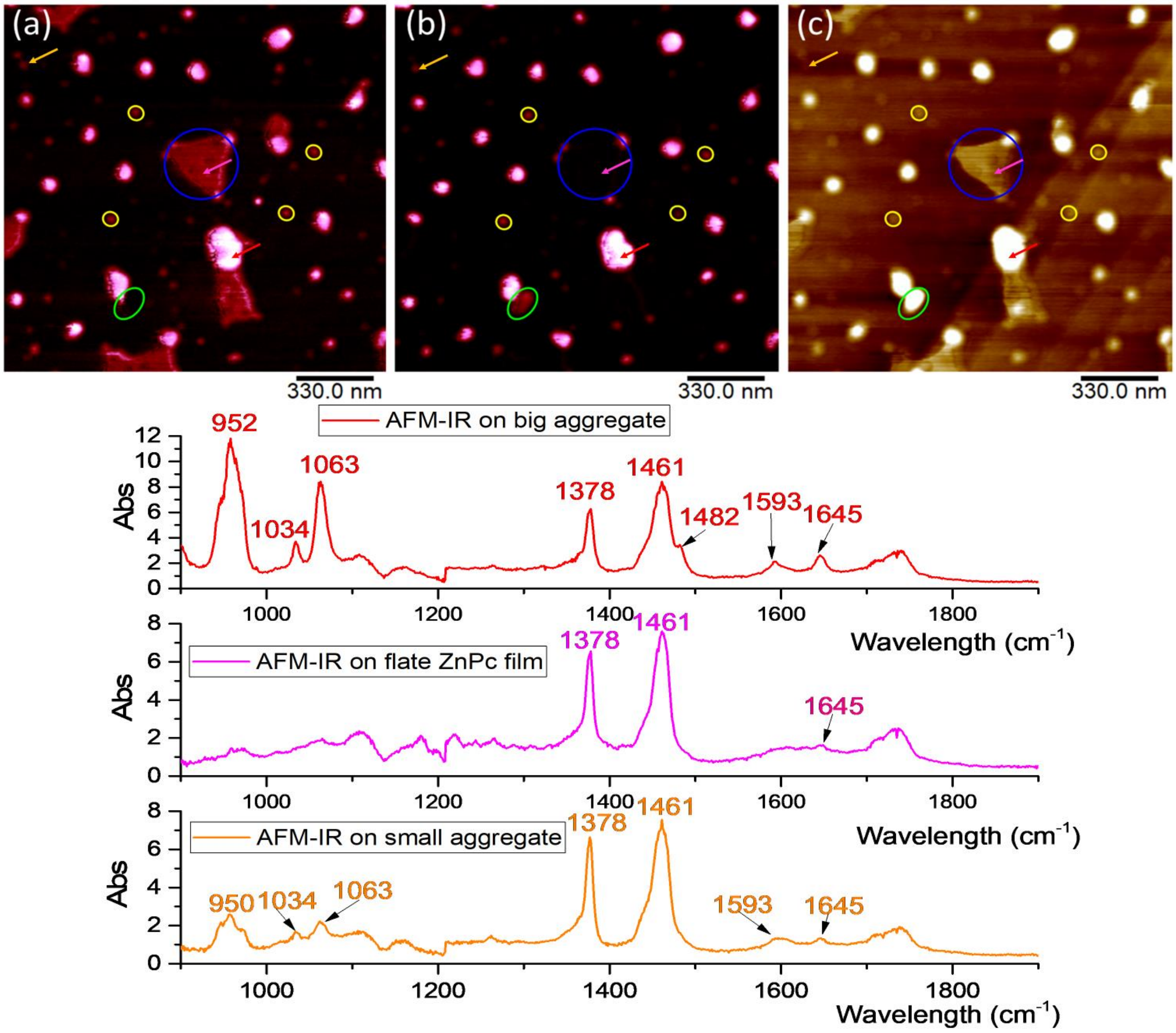

Figure 68 : AFM-IR and topography images of TBA[K^{Mo}(pyr)]-ZnPc (1/1 equivalent) drop casted on TSB-C12/HOPG sample with in blue a spot lightened only at 1645 cm^{-1}, in green a spot lightened only at 950 cm^{-1} and in yellow some spots lightened at both wavelength (a) IR image of the sample with the apparatus wavelength set at 950 cm^{-1} (b) IR image of the same area of the sample with the apparatus wavelength set at 1645 cm^{-1} (c) AFM topography image of the area imaged by AFM-IR, the orange, purple and red arrows on the images shows the spots where the corresponding IR spectra are taken

The AFM-IR images show a presence of several aggregates on the surface that are lightened at both 1645 cm^{-1} and 950 cm^{-1}, which correspond to the signal of the ZnPc observed by AFM-IR, and the most intense peaks of the TBA[K^{Mo}(pyr)], respectively. This shows that these aggregates are composed of the complex TBA[K^{Mo}(pyr)]-ZnPc.

The areas lightened at 1645 cm^{-1}, such as the one surrounded by a blue circle in the AFM-IR images in Figure 68 form mainly films with a height around to 2 nm and correspond to the free ZnPc molecules on the surface. Also, the areas lightened only at 950 cm^{-1}, with only one aggregate found and shown in the AFM-IR images (Figure 68) surrounded by green circles, are aggregates of free TBA[K^{Mo}(pyr)]. Lastly, the presence of several points that have the same size and lightened at both wavelengths is noticed, some are marked by the yellow circles in Figure 68. The height of these points is of about 1.5 nm to 2 nm corresponding to the height of a single TBA[K^{Mo}(pyr)]. Moreover, their width is around 20 nm which correspond to the lateral size of TBA[K^{Mo}(pyr)] POM taking into account the AFM contact point deconvolution. Therefore, these points could be attributed to a single TBA[K^{Mo}(pyr)]-ZnPc organized in a pore of the TSB-C12/HOPG functionalized substrate.

These results provide important information toward the comprehension of this system, showing that mostly, the TBA[K^{Mo}(pyr)]-ZnPc complex form aggregates on the surface when it is deposited by drop casting, aggregates of free TBA[K^{Mo}(pyr)] can also be found but with much less amount. This means that in solution, the TBA[K^{Mo}(pyr)] form the coordination bond with the ZnPc and drive it to the aggregates formed on surface, rather than to follow it into the pores. The presence of the points attributed to isolated single TBA[K^{Mo}(pyr)]-ZnPc in pores, shows that statistically, the organization expected occurs but gives randomly isolated molecules on surface rather than the periodic sub-monolayer desired.

The IR spectra made on the big aggregate, the small cluster that could be attributed to a single TBA[K^{Mo}(pyr)]-ZnPc complex and the film of ZnPc molecule (Figure 68, red, orange and purple curves, respectively) confirm this hypothesis. Notably, even in the absence of toluene, the IR spectra (Figure 68) show the presence of the two bands at 1378 and 1461 cm^{-1}. Indeed, these signals can also be detected on the TSB-C12, ZnPc and TBA[K^{Mo}(pyr)] molecules. Interestingly, the large and intense bands detected previously between 1000 and 1200 cm^{-1} are not present on this sample, giving much more clear IR spectra. The position and intensity of these bands vary from a series of measurement to another, and could be due to the AFM tip or the adjustement of the IR beam, or even other parameters. Further investigations could give clear answer about it.

The IR measurement made on the big aggregate enlightened at both wavelengths of the ZnPc and TBA[K^{Mo}(pyr)] (Figure 68, red arrow on the AFM-IR images giving the red IR spectrum) show clearly and without surprise the bands of both molecules, confirming that these big aggregates are composed mainly of the TBA[K^{Mo}(pyr)]-ZnPc complex. When the IR analysis is made on a very small point, assumed being a single TBA[K^{Mo}(pyr)]-ZnPc complex (Figure 68, orange arrow on the AFM-IR images giving orange IR spectrum), the characteristic bands of both molecules are still present, but with significantly lower intensity. Lastly, the IR analysis made on the flat film of ZnPc molecules (Figure 68, purple arrow on AFM-IR images giving the purple IR spectrum) shows the presence of the characteristic C=N band of ZnPc only, demonstrating that this film is composed of only ZnPc molecules.

I.3.4 – Conclusion

The use of this ultra-sensitive technique allowed providing relevant data to understand the organization at a molecular scale on surface. Remarkable results were obtained, with the characterization of thin films of ZnPc molecules and even what appeared as being eventually a single TBA[K^{Mo}(pyr)]-ZnPc complex, whereas STM images seem to show that no POMs are inserted into the pores. However, it appears that the TBA[K^{Mo}(pyr)] is not organized as wanted and tend to form aggregates. Likely, it seems that the main reason of this behavior is the POM to POM interactions through the electrosctatic interactions in solution, that tend to keep the POMs close to each other forming aggregates once deposited on the surface. To overcome this problem, an understanding of the aggregation mechanism and the different parameters that govern it is needed.

One of these parameters is the solvent. Indeed, the dispersion of molecules and nanoparticles in solution is based on the rule of “like dissolves like”, which means that the molecules are better dispersed in solvents that have close polarity to them.[241] Thus, the binary solvent used to dissolve both ZnPc and TBA[K^{Mo}(pyr)], composed of acetonitrile that solubilize the POM but not ZnPc, and chloroform that solubilize the ZnPc but not the POM, at a rate of 30/70 in volume respectively, can dramatically accentuate the aggregation phenomenon of the TBA[K^{Mo}(pyr)] leading to the results observed during the previous experiments. One potential solution to reduce the aggregation and allows the TBA[K^{Mo}(pyr)] to be driven in the pores is to have a solvent that can solubilize both the ZnPc and the functionalized POM. (cf. part I.3.4)

Another parameter that could help to organize the POMs into the pores is the strength of the POM-anchor bond. By putting a covalent bond rather than a coordination one, the competition between free anchor and anchored POM to occupy the pores will be eliminated. Thus, each one of the anchor molecules that will occupy a pore will drive a POM with it, and statistically, the amount of POMs in the pores will increase. (cf. part II)

Finally, the aggregation could decrease by modifying the charge number of the POM. Indeed, the TBA[K^{Mo}(pyr)] being charged -4, four counter ions are needed to balance this charge, increasing the ion exchange between the POMs statistically. By reducing the charge of the POM, the number of counter ions will be reduced, as well as the ion exchange interactions.

I.4 – First attempts with a hybrid POM soluble in toluene

To reduce the aggregation, we used a POM soluble in toluene, which is a good solvent for on surface depositions. Toluene has a higher boiling point than chloroform or acetonitrile, providing more time for the molecules to self-assemble before its evaporation. The system with the pyridine function coordinated to a ZnPc has to remain the same. In order to achieve this, a new POM is synthesized and it consists of a hybrid tungstate pyridine-terminated Keggin POM with tetraoctylammonium counter cations (TOA) (Figure 69) to allow the POM to be soluble in solvents with lower polarity such as toluene, chloroform…etc. The general formula of this POM is $[CH_3(CH_2)_7]_4N[PW_{11}O_{39}\{Sn(C_{13}H_8N)\}]$, and it will be called here after TOA[K^W(pyr)].

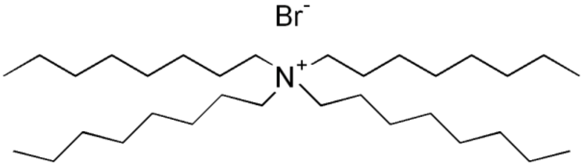

Figure 69 : Scheme of tetraoctylammonium bromide salt (TOABr)

I.4.1 – Synthesis of TOA[K^W(pyr)]

The TOA[K^W(pyr)] was synthesized by replacing the TBA cations of TBA[K^W(pyr)] by TOA cations. First, TBA[K^w(pyr)] is synthesized and deposited the same way as TBA[K^{Mo}(pyr)] on HOPG, to confirm that no difference is noticed by STM by replacing the nature of the metal in the POM. The synthesis of TBA[K^W(pyr)] starts from the potassium salt of the lacunar Keggin tungstate POM, that is made in our laboratory, and follow the same steps as for the TBA[K^{Mo}(pyr)] (Figure 70). The details of the synthesis can be found in the appendix.

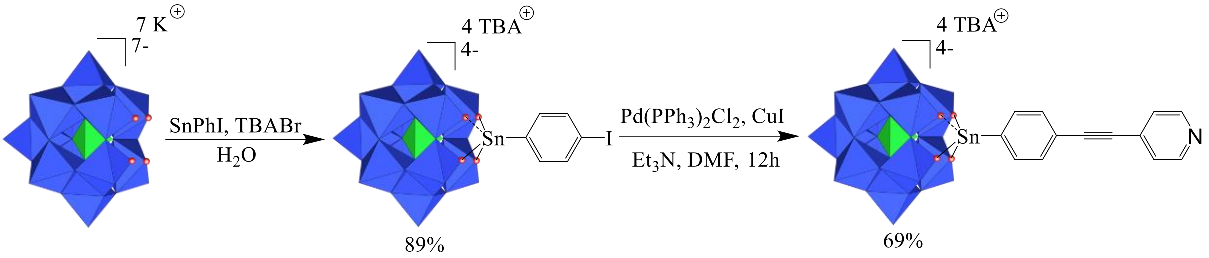

Figure 70 : Scheme of the synthesis of TBA[K^W(pyr)]

The cations exchange is made on the TBA[K^W(pyr)] because of its better stability in solution compared to its molybdate equivalent. It is performed by solubilizing the product in acetonitrile, and adding 4.02 equivalents of TOABr to the solution. The mixture is stirred for about 5 min, and basified water is added to precipitate the TOA[K^W(pyr)] avoiding protonation of the pyridine function. The product precipitates as a brownish gel. In order to eliminate any excess of TOABr, the gel is solubilized in toluene and 4 volumes of cyclohexane are added to precipitate the TOA[K^W(pyr)], while the TOABr remains soluble in this toluene/cyclohexane solvent (20/80 in volume respectively). The product is dried and analyzed by NMR ^{1}H and ^{31}P (Figure 71).

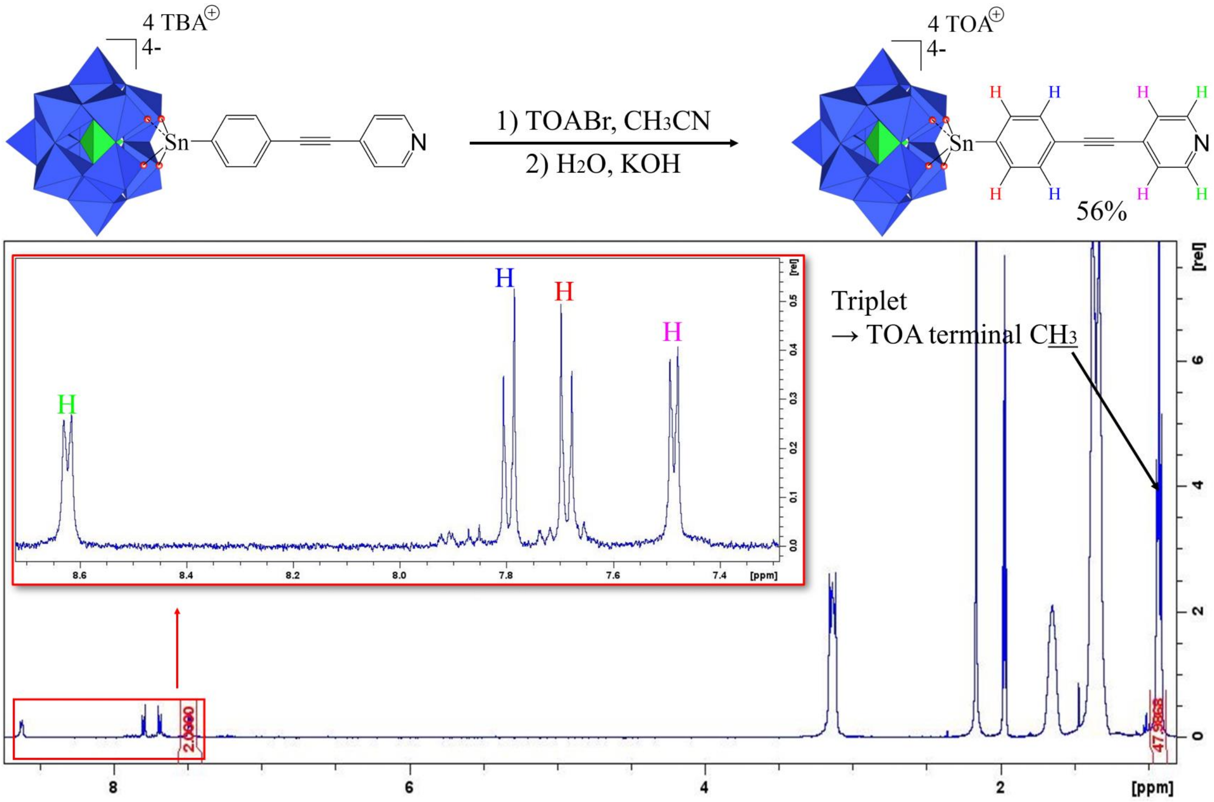

Figure 71 : Scheme of the exchange of TBA cations on the TBA[K^W(pyr)] by TOA cations and NMR ^{1}H of the TOA[K^W(pyr)] functionalized POM in CD$_3$CN, with the aromatic and TOA terminal CH$_3$ protons attribution

The NMR ^{1}H spectrum of the molecule shows the typical peaks of the TOA, with a small shift of the triplet around 1 ppm for the TBA[K^W(pyr)] to 0.93 ppm for the TOA[K^W(pyr)] (appendix). The presence of 4 TOA for one POM is confirmed by integration of the terminal CH$_3$ protons of TOA cations compared to the integration of two protons of the aromatic region. Thanks to the precipitation using basified water, the pyridine function is not protonated, as shown by the shape of the doublet at 8.65 ppm (Figure 71). The fact that this POM is now soluble in a large variety of solvents, including chloroform and toluene, confirms that the cation exchange was successfully performed. After drying, the TOA[K^W(pyr)] is obtained as a light brownish powder. The NMR ^{31}P of the TOA[K^W(pyr)] can be found in the appendix.

I.4.2 – Deposition of TOA[K^W(pyr)] on TSB-C12/HOPG substrate and STM imaging

The product was first characterized in solution using UV-vis spectroscopy and NMR in CDCl$_3$. As expected, the same results as the ones obtained with the TBA[K^{Mo}(pyr)] are observed showing the formation of the complex in solution.

For the deposition on TSB-C12/HOPG substrate, the solution is prepared by diluting 20 µL of a saturated ZnPc solution in toluene ($1.36*10^{-3}$ mol.L^{-1}) into 480 µL of toluene. Then a solution of 2 mg of TOA[K^{W}(pyr)] in 1 mL of toluene are prepared ($4{,}13*10^{-4}$ mol.L^{-1}) and 65 µL are added to the ZnPc diluted solution to have 1/1 equivalent for the POM/ZnPc, respectively. The solution obtained is diluted 20 times and 15 µL are deposited on a TSB-C12/HOPG substrate for STM imaging. The images obtained are compared to a reference image of ZnPc on TSB-C12/HOPG (Figure 72).

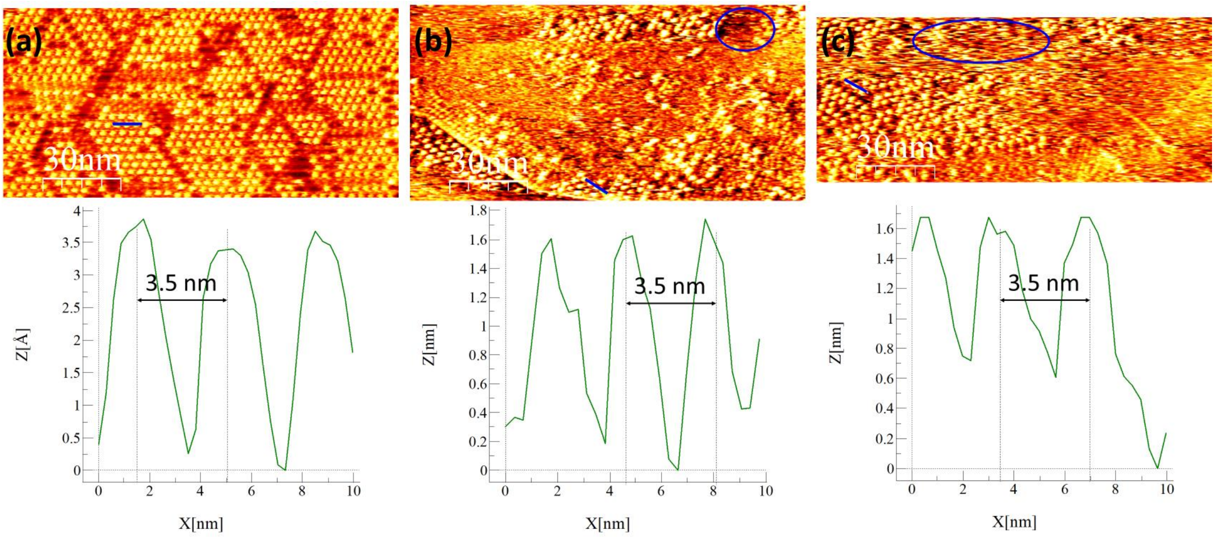

Figure 72 : STM images of (a) reference ZnPc on TSB-C12/HOPG, (b) and (c) TOA[K^{W}(pyr)]-ZnPc complex on TSB-C12/HOPG (blue circles show disturbed areas) with heights profile of the molecules of each image beneath it ((a) : 150 x 72 nm^{2} Vbias = 1 V, Iset = 20 pA, (b) : 150 x 74 nm^{2} Vbias = 1.5 V, Iset = 14 pA and (c) : 150 x 63 nm^{2} Vbias = 1.5 V, Iset = 14 pA)

Amongst the 6 samples of TOA[K^{W}(pyr)] on TSB-C12/HOPG imaged by STM, only one gave the images (b) and (c) in Figure 72 while others gave typical images of ZnPc on TSB-C12/HOPG, not different from the reference shown in Figure 72, (a). Indeed, these images (b) and (c) in Figure 72 show "molecules" that appears different from typical ZnPc molecules (Figure 72, (a)). Firstly, their apparent heights are approximately 1.6 nm, significantly greater than the apparent heights exhibited by ZnPc molecules. Secondly, their shape is slightly distinct, appearing "spherical" or in "3D" being outside of the pores formed by the TSB-C12 network on HOPG, while ZnPc molecules appear more "flat" and being inside of these pores. Lastly, the comparison between the distance between two of these molecules and between two ZnPc molecules on the height profiles (Figure 72) shows that their distribution on the surface closely follows that of the ZnPc molecules.

Moreover, the coverage rate of these molecules is lower than that of ZnPc molecules trapped by the TSB-C12 network. Additionally, in the case of these molecules, several disturbed areas are observed, as the ones surrounded by blue circle in the image (a) and (b) of Figure 72. These disturbed areas are typically the signature of a movement of molecules induced by the scanning of the STM tip.

These preliminary results on using the TOA[K^W(pyr)] POM soluble in toluene are very encouraging. The images of these molecules (Figure 72 (b) and (c)) and the differences they exhibit compared to the images of ZnPc molecules suggest the successful deposition of this hybrid POM into the pores of the functionalized TSB-C12/HOPG substrate.

I.4.3 – Conclusion

Changing the counter ions of the functionalized POM to make it soluble in the same solvent as the ZnPc gave encouraging results. First STM images of molecules that seems to be organized TOA[K^W(pyr)]-ZnPc complex in the pores of TSB-C12/HOPG substrate are obtained. However, caution is still needed, because firstly, the images of these molecules on the surface were observed only on one sample amongst several. Secondly, because of the STM that cannot provide chemical information to prove that these molecules are in fact the TOA[K^W(pyr)]. Thus, further characterization techniques are needed, and one of the most challenging aspects of this work, is indeed to be able to demonstrate that the POMs are organized at a molecular level, and at different scales in order to also have information about the coverage rate.

The next step to these preliminary results is to analyze a sample of TOA[K^W(pyr)]-ZnPc complex deposited on TSB-C12/HOPG using chloroform by AFM-IR.

II. – Hybrid POM with a pyrene anchoring group

Having a POM covalently bonded to the anchoring molecule presents some particularly interesting advantages when compared with the previously studied POM-anchor coordination bonded system. Having the anchoring molecule being a part of the POM will both eliminate equilibrium in solution and the competition between the free anchor and the POM-anchor in occupying the pores. Also, in such system the presence of molecules in the pores on surface will necessarily mean the presence of the POM as well. The challenge however is the synthesis of such molecule. Indeed, its geometry has to be precisely controlled to allow the anchoring molecule to occupy the pore while the POM is covalently bonded to it, and correctly oriented.

II.1 – Pyrene as covalent bonded anchoring molecule

Pyrene molecule (Figure 73 (a)) is one good candidate to be used as an anchoring molecule, it presents the advantage of a simple synthesis process to be bind to the POM, and it was reported in the literature for its pi-stacking on HOPG.[242] Nevertheless, this molecule has to fit the size of the pores formed by the functionalized HOPG with TSB molecule. Other aromatic compounds trapped in the pores of TSB formed on HOPG have been widely reported, such as coronene, pentacene...etc.[202,202,204] but never pyrene. Then, since pyrene with a diameter estimated at about 0.9~1.2 nm,[243] is a smaller molecule than ZnPc used previously, the TSB chosen to functionalize HOPG is TSB-C10, that forms smaller pores on HOPG surface (Figure 73 (b)),[204] able to trap pyrene molecules more efficiently. A solution of pyrene in toluene with a concentration of about 10^{-3} mo.L^{-1} is prepared and 10 µL are drop casted on TSB-C10/HOPG substrate, and the sample is imaged by STM (Figure 73 (c)). The following STM images are made by Jan Patrick Calupitan, a post doctoral researcher in our team involved in the project.

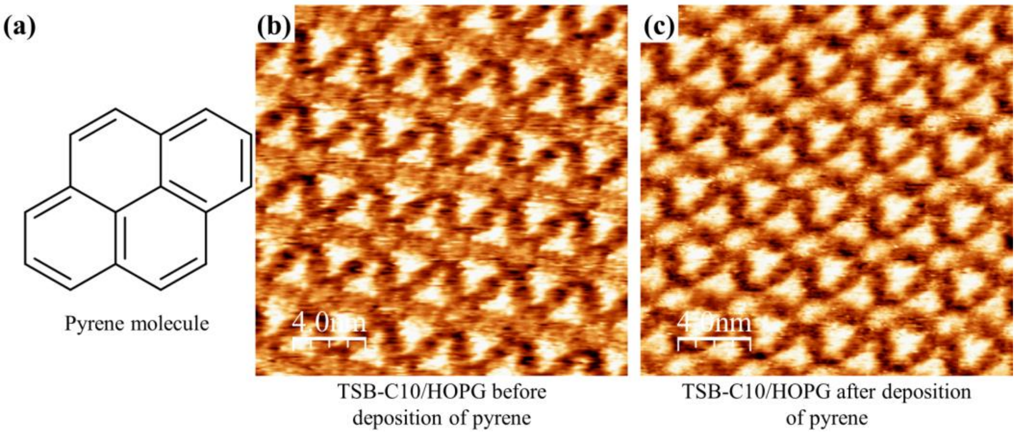

Figure 73 : (a) Scheme of the pyrene molecule, (b) and (c) STM images of TSB-C10/HOPG before and after depositon of pyene, respectively ((b) and (c) : 20 x 20 nm^2)

The results obtained (Figure 73) shows as expected, that pyrene molecules occupy the pores formed on the TSB-C10/HOPG substrate. This makes the pyrene a viable molecule to be used as an anchor by binding it to a functionalized POM.

II.2 – Synthesis of the functionalized tungstate POM with pyrene terminal function

The functionalized POM with a pyrene function needs to have some degrees of liberty that will allow the pyrene function to pi-stack inside of the pore with the POM bonded to it. To obtain such molecule, the synthesis started first by functionalizing a commercially available 1-pyrenecarboxaldehyde by addition of of propargyl bromide under argon atmosphere in presence of zinc activated with TMSCl to obtain the 1-(8,10-dihydropyren-1-yl)but-3-yn-1-ol (product (1) Figure 74). Product (1) is then reduced using triethylsilane in presence of BF_3Et_2O in chloroform to give the 3-butynylpyrene (product (2) Figure 74) that is purified by flash chromatography. This synthesis is reported in the literature.[244] Then the product is coupled to a functionalized POM through a Sonogashira reaction to obtain the final molecule called here after TBA[K^W(pyrene)]. The scheme of this synthesis with NMR ^1H and ^{31}P of the TBA[K^W(pyrene)] are shown in Figure 74. The details of the synthesis can be found in the appendix.

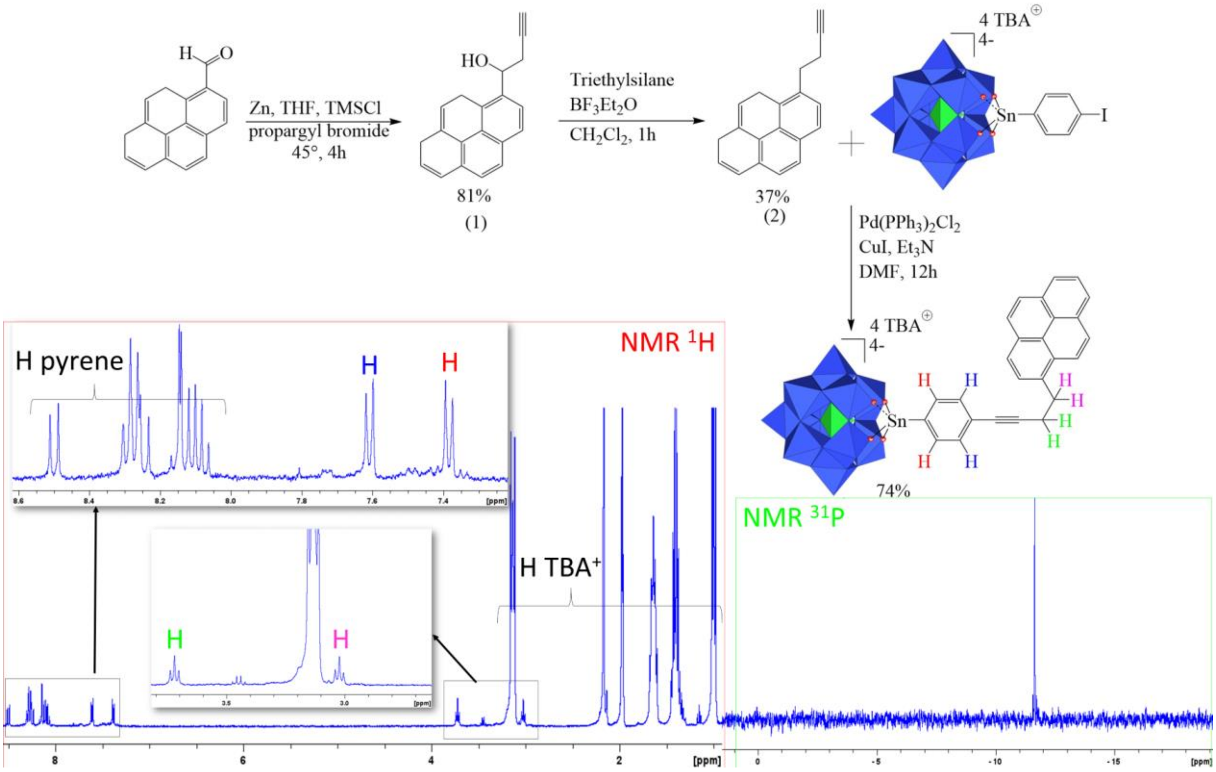

Figure 74 : Scheme of the synthesis of the pyrene with the terminal alkyn group and the TBA[K^W(pyrene)]

The arrangement of this POM is expected to be vertically attached on the top of the pyrene pi-stacked onto HOPG inside the pores. However, due to the angle formed by a $-C-CH_2-C$ bond of 109°, the part of the molecule composed of the POM, the phenyl group and the strait $-C\equiv C-CH_2-$ chain that will be vertically oriented toward the surface would not form a 90° angle with the substrate but an angle of about 109°. Figure 75 illustrates the expected organization of this functionalized POM.

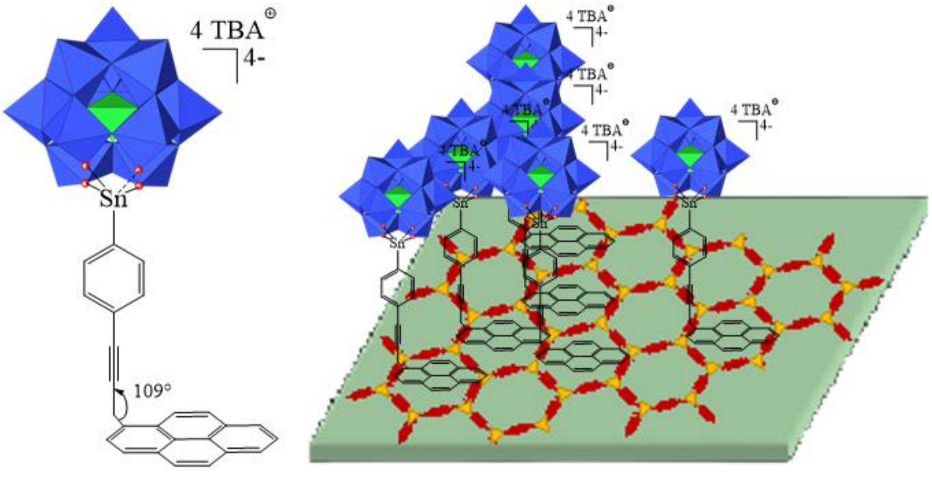

Figure 75 : Scheme of the expected organization of the TBA[K^W(pyrene)] on the functionalized substrate TSB-C10/HOPG

The deposition of the POM is made in a mixture of solvents composed of chloroform and acetonitrile at 50/50 in volume, because of the bad contact angle between HOPG and acetonitrile that forms droplets on the substrate. The POM is soluble in acetonitrile but not soluble in chloroform.

II.3 – Deposition and STM imaging of TBA[K^W(pyrene)]

Two samples are prepared by drop casting 15 µL solutions of TBA[K^W(pyrene)] with concentrations of $2.48*10^{-4}$ mol.L^{-1} and $4.97*10^{-7}$ mol.L^{-1} on two TSB-C10/HOPG substrates, respectively. The aim is to observe the effect of the concentration variation between these two samples that are compared to an STM image of TSB-C10/HOPG substrate used as a reference (Figure 76).

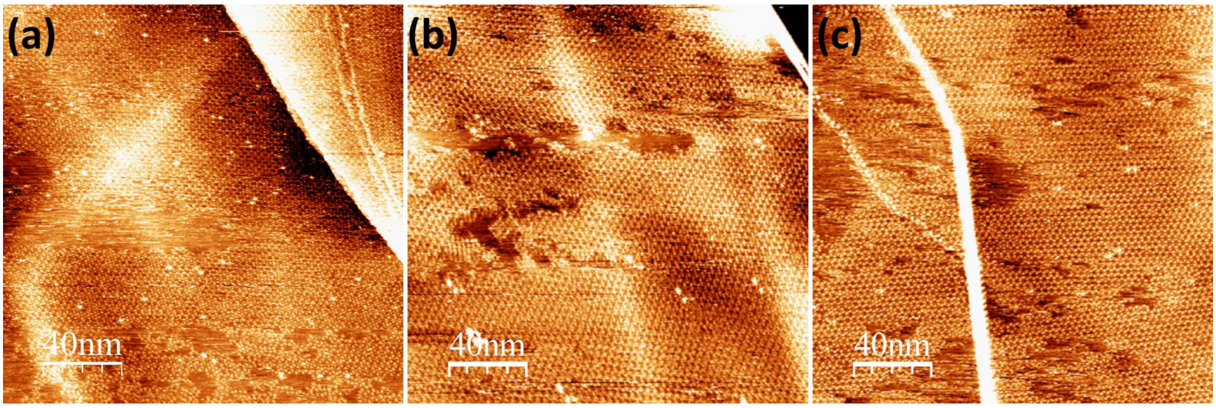

Figure 76 : STM images of (a) TSB-C10/HOPG reference sample (b) 15 µL of TBA[K^W(pyrene)] at $4.97*10^{-7}$ mol.L^{-1} drop casted on TSB-C10/HOPG and (c) 15 µL of TBA[K^W(pyrene)] at $2.48*10^{-4}$ mol.L^{-1} drop casted on TSB-C10/HOPG (images 200 x200 nm^2) (Vbias = 1 V, Iset = 20 pA)

No difference can be noticed between the reference sample of TSB-C10/HOPG (Figure 76, (a)) and the samples obtained after the deposition of the TBA[K^W(pyrene)] (Figure 76, (b) and (c)). The small bright spots on the images in Figure 76 are due to small contaminations by ZnPc. This result demonstrates that the TBA[K^W(pyrene)] is not driven to the pores by the pyrene anchor molecule as expected. The interesting remaining question concerns the influence of this covalently bonded pyrene on the behavior of the TBA[K^W(pyrene)] on the bare surface. Thus, a deposition of 15 µL of TBA[K^W(pyrene)] solution at $2.48*10^{-4}$ mol.L^{-1} is realized directly on a freshly cleaved HOPG without the self-assembled TSB-C10, and the sample is imaged by STM (Figure 77).

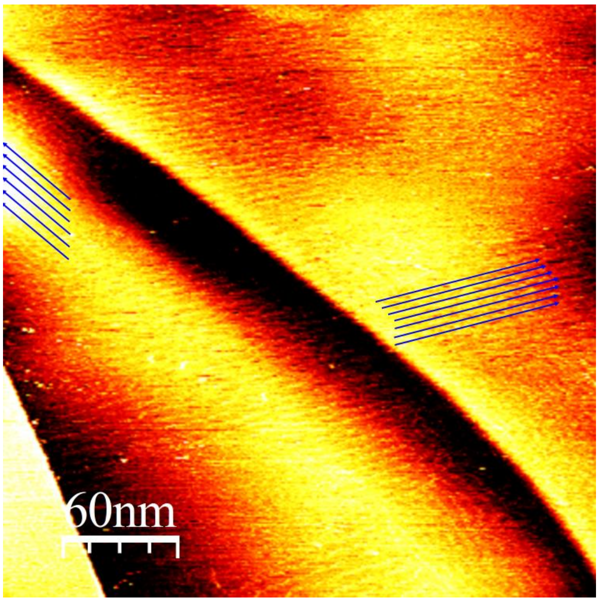

Figure 77 : STM image of the TBA[K^{W}(pyrene)] drop casted on the bare surface of HOPG substrate, the blue arrows show the orientation of the lines on the surface (300 x 300 nm^{2}) (Vbias = 1 V, Iset = 20 pA)

The STM image (Figure 77) shows a flat surface with apparent line that could correspond to organized molecules, however, these lines have apparent heights of no more than 2 Å, which does not correspond to the heights expected from the TBA[K^{W}(pyrene)]. The resolution obtained does not allow seeing the molecules individually which makes the attribution of these lines impossible. In order to have answers about the organization on surface, images at a higher scale that will allow to have a global vision about the distribution of the TBA[K^{W}(pyrene)] are needed. Thus, AFM is the appropriate technique that will allow to see the behavior of the TBA[K^{W}(pyrene)] molecules on the surface at a larger scale.

II.4 – AFM imaging of TBA[K^{W}(pyrene)] on TSB-C10/HOPG and on HOPG substrates

First, a sample of TBA[K^{W}(pyrene)] on TSB-C10/HOPG substrate is imaged. It is made with 15 µL solution of TBA[K^{W}(pyrene)] (C = 2.48*10^{-4}) deposited on TSB-C10/HOPG substrate. The AFM images obtained are compared with images of TSB-C10/HOPG used as a reference sample (Figure 78).

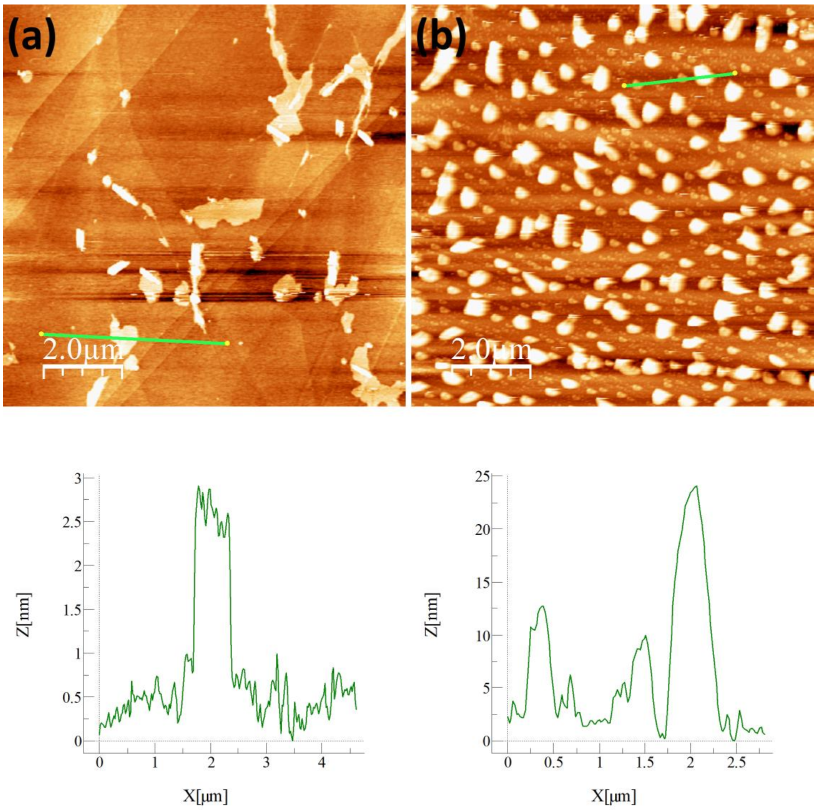

Figure 78 : AFM images of (a) TSB-C10 on HOPG substrate with below, a profile line of a layer on the surface and (b) TBA[K^W(pyrene)] deposited on TSB-C10/HOPG with below, a profile line of aggregates on the surface

The surface of the TSB-C10/HOPG substrate before the deposition of the POM is flat (Figure 78 (a)). The TSB-C10 covers the surface and can form multilayers on some areas, probably due to the excess of molecules deposited, with heights of about 2-3 nm as shown in Figure 78, (a). After the deposition of the TBA[K^W(pyrene)], the formation of aggregates is noticed over all the surface with heights around 25 nm for the biggest ones as shown in Figure 78 (b). This result combined with what was obtained by STM, shows that the TBA[K^W(pyrene)] form aggregates on the TSB-C10/HOPG substrate, and does not occupy the pores as expected.

The next experiment to better understand this system concerns the deposition of the TBA[K^W(pyrene)] on bare HOPG. Three concentrations of the TBA[K^W(pyrene)] solution are used, 10^{-6} mol.L^{-1}, 10^{-5} mol.L^{-1} and 10^{-4} mol.L^{-1}, and AFM images are made for each one (Figure 79).

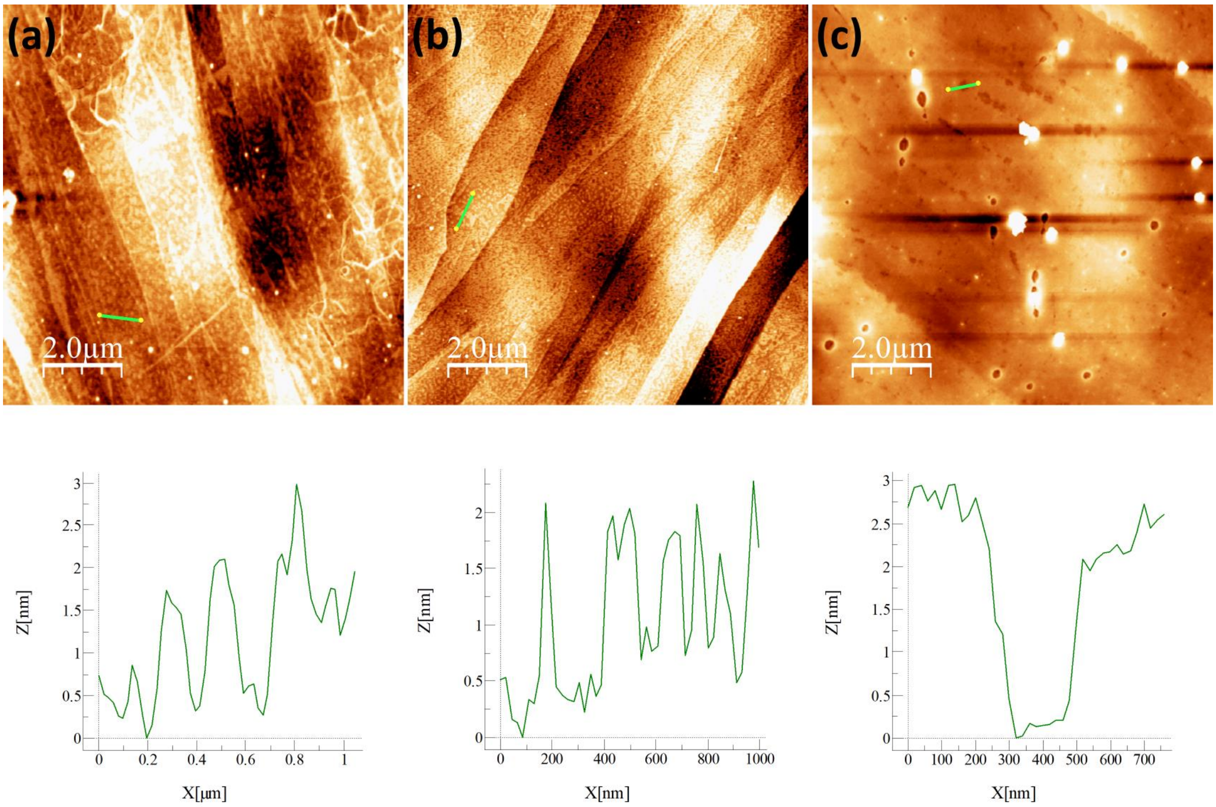

Figure 79 : AFM images of TBA[K^{W}(pyrene)] on HOPG substrate with (a) a concentration of 10^{-6} mol.L^{-1} and a profile line of the surface below, (b) a concentration of 10^{-5} mol.L^{-1} and a profile line of the surface below and (c) a concentration of 10^{-4} mol.L^{-1} with a profile line of the surface below

The results obtained for the deposition of a 10^{-6} mol.L^{-1} solution of TBA[K^{W}(pyrene)] on HOPG (Figure 79 (a)) show a sub-monolayer formed on the surface with a height of less than 2 nm. When the concentration of the deposited solution is increased to 10^{-5} mol.L^{-1}, the coverage of the sub-monolayer increases as well and the height of this layer remains around 2 nm as shown in Figure 79 (b). At a concentration of 10^{-4} mol.L^{-1} the image obtained Figure 79 (c) shows the formation of almost a complete layer on the surface, with the presence of some holes, whose depth is between 2 and 2.5 nm. This result shows that the TBA[K^{W}(pyrene)] does not form aggregates on HOPG, contrary to what was observed with the TBA[K^{Mo}(pyr)]. This is due to the effect of the pyrene function on the TBA[K^{W}(pyrene)] that pi-stack on the surface of HOPG substrate and prevents the POMs from aggregation. Interestingly, when the TBA[K^{W}(pyrene)] is deposited on the functionalized substrate made of TSB-C10/HOPG, the formation of aggregates is noticed. A possible explanation is the reduction of the pi-stacking surface available on surface, reduced to the surface inside the pores and induced by the 2D network formed by TSB-C12 on HOPG. This coud tend to promote the aggregation when the POM is deposited through cations exchange and even by pi-stacking between pyrene groups of the organic part of the TBA[K^{W}(pyrene)] unable to pi-stack on the surface. It also tends to show that the pi-stacking of the pyrene on HOPG is not enough strong to drive the POM into the pores. Thus, a change in the molecule used as an anchor (coronene, hexabenzocoronen…), with one that has a better affinity to go into the pores could give better results.

III – Conclusion

The organization of polyoxometalates on HOPG surface using templates needs to take several parameters into account. The main difficulties encountered to organize the POMs can be resumed to the POM/POM interactions in solution, by cations exchange that maintains them together leading the formation of aggregates on the surface. Also, the chemical nature of the POMs, that are polyanionic species, compared to the chemical nature of the TSB-C12/HOPG substrate composed of very low polar organic material, could make the POMs form aggregates to minimize their contact surface when deposited by drop-casting on this substrate.

To overcome these problems, the use of anchoring molecules to control the distribution of the POMs on surface seems to give encouraging results. Particularly, the TOA[K^W(pyr)] that use a coordination link to a zinc phtalocyanine used as the anchoring molecule, gave interesting STM images where molecules, that are assumed being the POMs, were organized according to the template induced by the substrate. However, additional characterization techniques like AFM-IR are required to provide conclusive evidence of the organization of the POMs.

In another hand, the TBA[K^W(pyrene)] covalently linked to a pyrene used as the anchor have shown that the pi-stacking of the pyrene is able to spread the POMs on the surface of HOPG, leading to the formation of thin films or a monolayer, given the height measured by AFM. One interesting thing is to determine how these TBA[K^W(pyrene)] are arranged at the molecular scale on HOPG. This result opens the way to the use of POMs covalently linked to various anchoring molecules that could help the POMs to organize on functionalized HOPG surface. Another possibility shown by this TBA[K^W(pyrene)], is the periodic self-assembling of hybrid POMs into 2D layer directly on the bare HOPG surface. Indeed, by functionalizing a POM with the right functions, a self-assembling hybrid POM through pi-stacking and van der Waals and/or hydrogen bonds on HOPG surface could be achieved.

Nevertheless, the aim of this thesis is not yet achieved, and to obtain a fully characterized surface with a sub-monolayer of periodically organized POMs, a new approach is needed. For this approach, a work will be carried out to modify the organic template on HOPG and make it able to attach POMs on specific spots on its surface. To do this, electrostatic interactions will be used, that are stronger than the pi-stacking interactions between the pedestal molecules used previously and HOPG surface. This could allow overcoming the POM/POM interactions to spread them on the substrate. The aim is to generate punctual positive charges, periodically distributed on the surface, which will serve as a cation to the POMs.

CHAPTER III: Periodic organization of polyoxometalates on functionalized HOPG surface by electrostatic interactions

A new strategy to organize polyoxometalates on surface is elaborated, and it relies on electrostatic interactions to deposit the POMs in a highly controlled way. To do so, the surface of HOPG needs to be modified to be able to provide periodically distributed positive charges, that will attract the polyanionic POMs serving as a part of their counter ions. The electrostatic interactions between these punctual periodic charges and the POMs would ensure a high binding energy to keep the POMs stuck on their positions. One of the challenges however is the STM imaging, particularly under ambient conditions. So, other techniques are required to demonstrate the organized deposition of POMs. As seen in Chapter II, one of the biggest challenges encountered is the ability to demonstrate the molecular organization of POMs at different scales on the surface. Cautious is required with surface characterization techniques such as X-ray Photoelectron Spectroscopy (XPS), contact angle measurements, Raman spectroscopy…etc. that allow to detect the presence of molecules or functional groups on surface but don't give enough precise information about the molecular arrangement, meaning that aggregates of several nanometers and a monolayer of molecules would give the same result with these techniques.

Here, the approach will require the use of the acid property of polyoxometalates. Indeed, several POMs can be obtained as acid salts, particularly, the kegging molybdate POM $H_3[PMo_{12}O_{40}]$ which is commercially available. POMs are known for their strong acidity[245]. Thus, if periodically organized protonable functions are exhibited on the substrate, the heteropolyacid POMs will protonate the functions generating a positive charge that they will compensate, inducing their deposition on these functions (Figure 80).

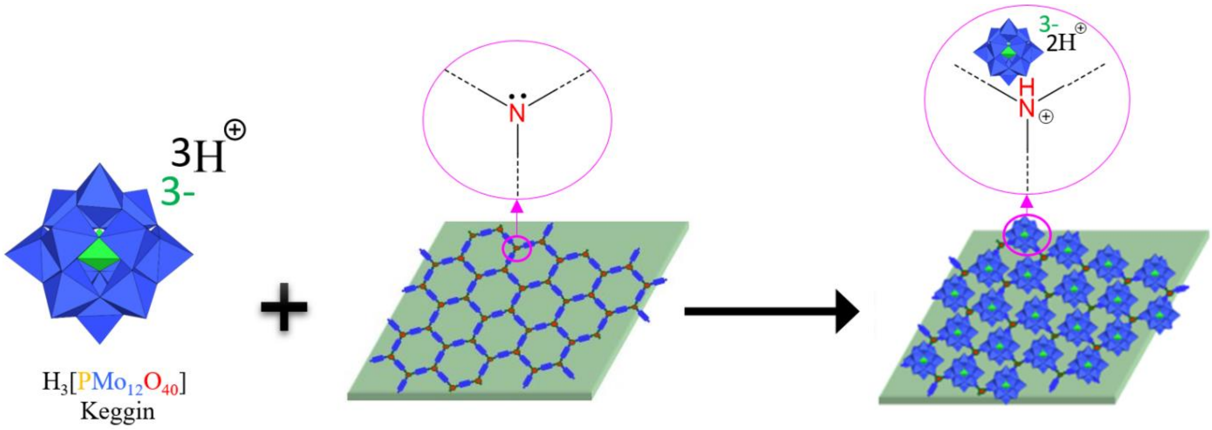

Figure 80 : Scheme of the strategy to organize POMs by electrostatic interactions on surface

Probing the protonation rate on the surface provide information about the POMs coverage rate, as each protonated nitrogen will be accompanied by the deposition of a polyoxometalate as a counter anion.

I – New molecule for the functionalization of HOPG

The first step toward this new system consists of elaborating a new functionalized substrate with periodic protonable functions on its surface. In order to accomplish this, specific molecules that self-assemble on HOPG should be considered. The model chosen for this molecule is based on that of TSB, which forms large homogeneous self-assembled layer on HOPG. A modification of the 1,3,5-tris((E)-3,5-bis(alkoxy)styryl)benzene molecule, named here after TSB-3,5 have been carried out by Dr. Claire Arrigoni during her PhD thesis at Sorbonne Université defended in 2010.[246] The aim of these modifications were to modify the chemical affinity of the pores formed on surface.[247] Indeed, the pores formed on the TSB-Cn/HOPG substrates allow to host only very specific molecules that present the characteristics of being planar, non-polar and aromatic. By modifying the chemical affinity of the pores and making them more hydrophilic or polar, the selectivity of the molecules hosted could be controlled. This modification consisted of incorporating hydroxyl functions at the end of the alkyl chains of the molecule as shown in Figure 81 (left).

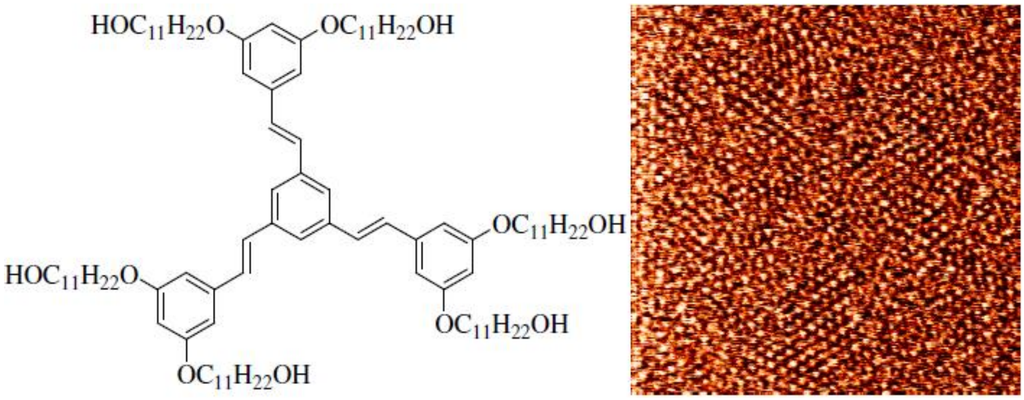

Figure 81 : TSB-C11OH containing hydroxyl groups at the end of each alkyl chain (left) and STM image (183 x 183 nm^2) of a monolayer of TSB-C11OH at the interface HOPG-1-Bromonaphthalene showing a disorganized layer (right)[246]

As shown in the STM image of Figure 81 (right), the incorporation of new functions on the TSB-3,5 molecule led to a disorganization of the monolayer formed on HOPG compared to the one formed with TSB-C12 molecules (cf. Figure 35). This disorganization is probably due to a modification in the intermolecular interactions, through the hydrogen bonds induced by the hydroxyl groups of the molecule. By reducing the number of hydroxyl groups, the network formed on the surface regains its stability, and the honeycomb/herringbone arrangements are restored, as depicted in Figure 82.

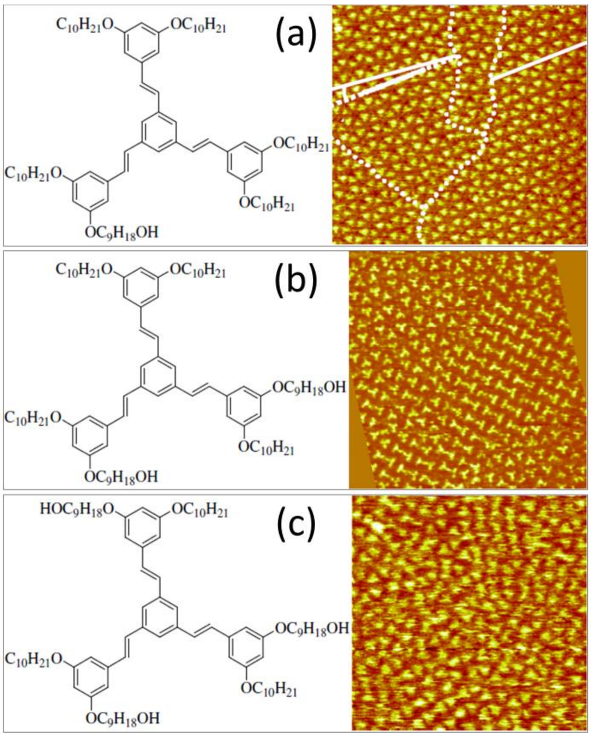

Figure 82 : (a) Scheme of the TSB-C10 with one hydroxyl group (left) and STM image (61 x 57 nm^2) of layer of this molecule deposited on HOPG substrate, (b) scheme of the TSB-C10 with two hydroxyl group (left) and STM image (42 x 42 nm^2) and (c) scheme of the TSB-C10 with three hydroxyl group (left) and STM image (39 x 39 nm^2)[246]

This work showed that a modification on the TSB-3,5 induced an important disorganization of its arrangement on the surface. Therefore, the protonable function wanted to be incorporated on this molecule has to be chosen carefully to ensure the stability and the periodicity of the network.

Another modification made on TSB-3,5 molecule has been reported by Schull *et al*. where the central phenyl ring of the TSB-3,5 molecule was replaced by a pyridine ring, in order to track the motion of the molecule by STM. This molecule named TSP self-assemble on HOPG in a way identical to the TSB molecule forming a long-range regular honeycomb lattice.[248] This work have shown that a substitution of the central ring of the TSB-3,5 molecule leads to much less self-assembling issues compared to the introduction of a function on the alkyl chains (Figure 83).

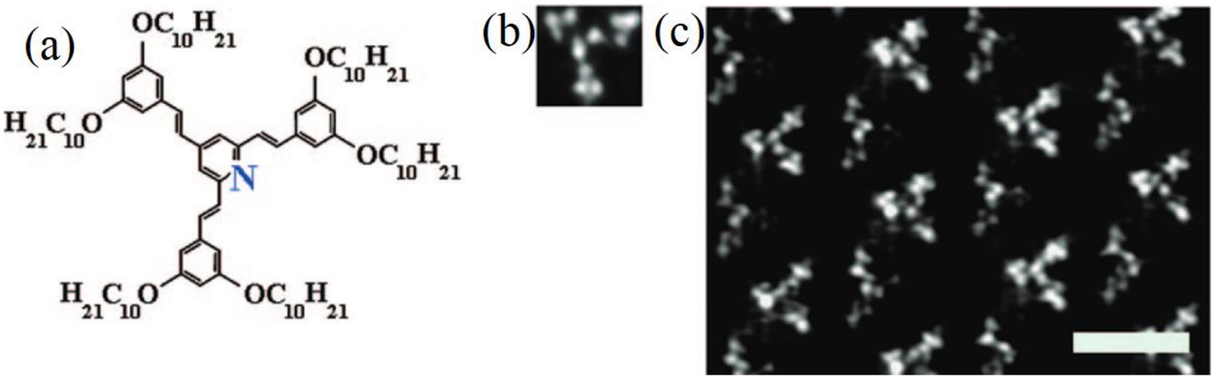

Figure 83 : (a) Model structure of the N-substituted TSPmolecule. (b) High-resolution STM image of one single substitutedTSP molecule. (c) Honeycomb supramolecular network obtained byself-assembling of the TSP molecules on HOPG surface.[248]

II – Triazine derivative as a modified-TSB-3,5 molecule with protonable group

Triazine molecule is an aromatic heterocyclic compound with three carbon atoms and three nitrogen atoms. Particularly, the 1,3,5-triazine that present a symmetry center (Figure 84) is a good candidate to be incorporated as a protonable group into the TSB molecule. Indeed, it offers the possibility to potentially be protonated two times (the pKa of the third nitrogen atom being too low and necessiting super acids) generating tow positive charges equally distributed on the molecule due to its symmetry (proton exchange between nitrogen atoms).

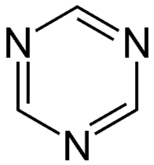

Figure 84 : Scheme of the 1,3,5-triazine

Indeed, many triazine based molecules have been reported for their self-assembling on HOPG substrate, with some of them having a close structure to the TSB molecule.[249–253] This shows that the presence of this group allows to obtain stable highly ordered 2D networks on surface.

Another important point concerning this approach is the ability of the chosen group to be protonated. The p*K*a of 1,3,5-triazine is lower than zero,[254] meaning that its protonation will be difficult. However, when the triazine is conjugated with other groups such as aromatic rings, there is an increase in electron density within the triazine ring, induced by mesomeric effects that shift the π electrons of the molecule toward the electronegative triazine ring, resulting in an increase of its pKa value. It is reported that a molecule with triazine central ring linked to three other aromatic rings, a close configuration to the central phenyl ring of TSB-3,5 molecule, can be protonated by trifluoroacetic acid (TFA) (Figure 85).[255]

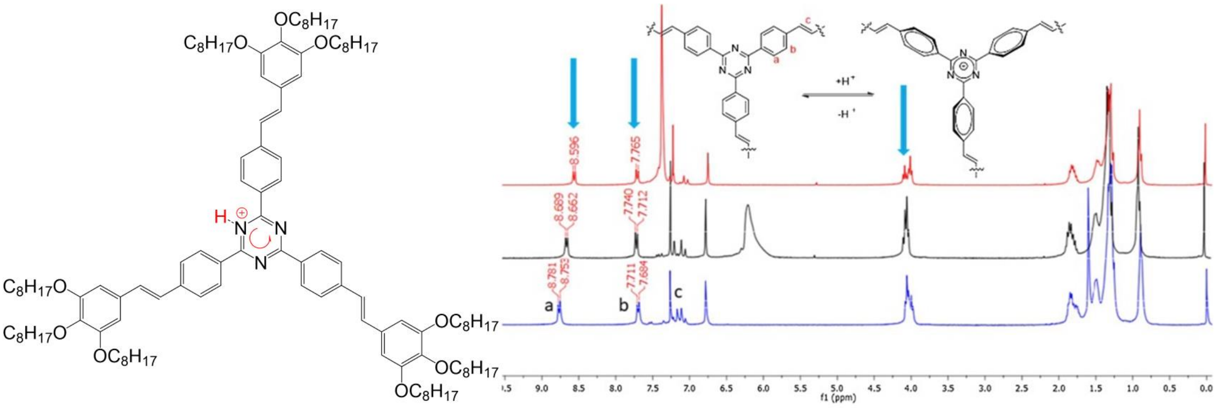

Figure 85 : (left) Scheme of the protonated triazine ring of C8TR molecule with TFA (right) ^{1}H NMR spectra of C8TR in CDCl3 (blue) and 20 µL (black) and 40 µL (red) addition of TFA (10^{-1} M).[255]

By adding an excess of TFA to the molecule presented in Figure 85 (left) in chloroform, a shift in characteristic peaks of the molecule is noticed in the NMR ^{1}H spectra (Figure 85, right) indicating the protonation of the triazine. However, the authors did not investigate the number of nitrogen atoms that have been protonated, and did not give an exact ratio of TFA added to the molecule.

TFA has a P*K*a of 0.52[256], and the p*K*a of heteropolyacids (HPAs) are reported as being much higher than usual inorganic acids like HCl, HNO_3, H_3PO_4 and even $HClO_4$.[257] For example the acidity of Keggin POMs such as $H_3[PW_{12}O_{40}]$, due to the simultaneous dissociation of its three protons, is suggested in some studies as being even stronger than sulfuric acid.[239–241] Thus the protonation of triazine modified-TSB-3,5 molecule, enriched with the electrons of aromatic groups using an heteropolyacid POM is definitely feasible.

II.1 – Synthesis of triazine modified-TSB-3,5 molecule

The chosen triazine modified-TSB-3,5 molecule consists of replacing the central phenyl ring of TSB-C12 by a central triazine ring (Figure 86). This molecule will be named Tz-C12.

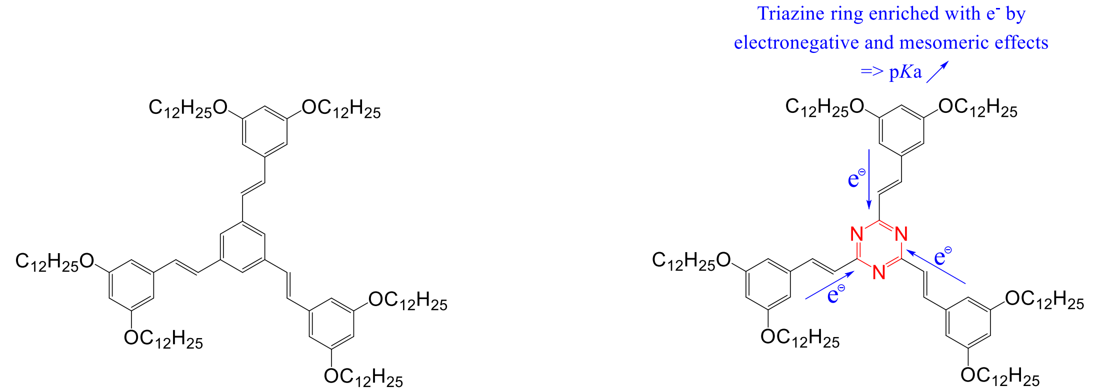

1,3,5-tris((*E*)-3,5-bis(dodecyloxy)styryl)benzene (TSB-C12)

2,4,6-tris((*E*)-3,5-bis(dodecyloxy)styryl)-1,3,5-triazine (Tz-C12)

Figure 86 : Scheme of TSB-C12 (left) and Tz-C12 with the direction of the mesomeric effects induced by the electronegativity of the triazine ring (right)

The presence of C12 alkoxy chains on the molecule is important. Indeed, once pi-stacked on HOPG, the distance between two triazine rings will be determined by the length of these chains.[248] This distance is needed to be sufficient to be able to put one POM on each triazine ring on the surface (see Figure 80). With a too short distance, the POMs will be too much packed and not isolated enough from each other, and/or due to steric hindrance, only a part of the triazine functions will be able to bind a POM, leading to a disordered arrangement with a reduced coverage rate. With a too large distance, there will large spaces between the POMs that will just be a “lost” space on the surface. If the Tz-C12 molecule exhibits the same arrangement as TSB-C12, this configuration with 12 carbons on the alkoxy chains will allow to have around 2 nm between the charge carriers in both hexagonal and herringbone arrangements as shown in Figure 87.[210] It seems to be the best choice given size of the anionic form of Keggin type polyoxometalates reported is 1.06 nm for the molybdate ones.[97]

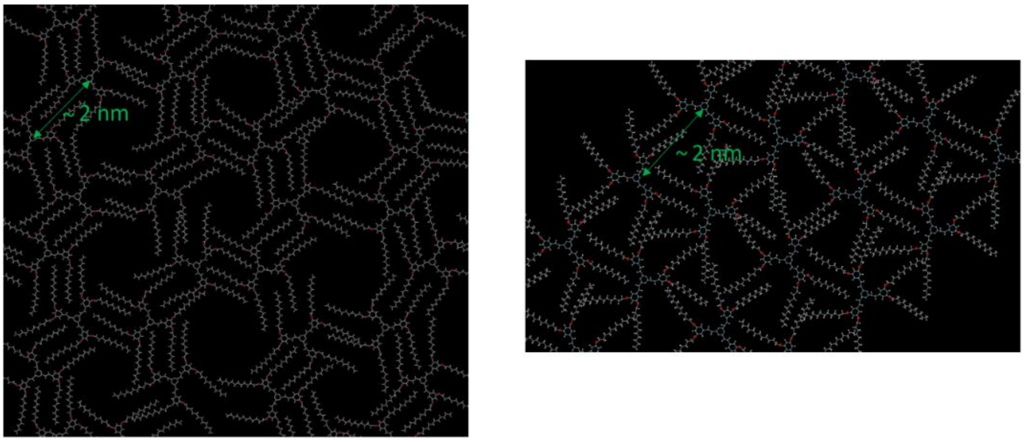

Figure 87 : Scheme of the supramolecular assembly from the Tz-C12 with the distance between two triazine rings in honeycomb (left) or herringbones (right) arrangements (supporting information of reference 210)[210]

The synthesis of the molecule starts by synthesizing the 2,4,6-trimethyl-1,3,5-triazine (1) according to a reported method.[258] Then the 3,5-(tridecyloxy)benzaldehyde (2) is synthesized by a Williamson reaction on the 3,5-dihydroxybenzaldehyde using 1-bromododecane and potassium carbonate. Finally, the molecule is obtained by condensation under basic conditions of molecule (1) and (2), inspired from a method reported in the literature (Figure 88).[259]

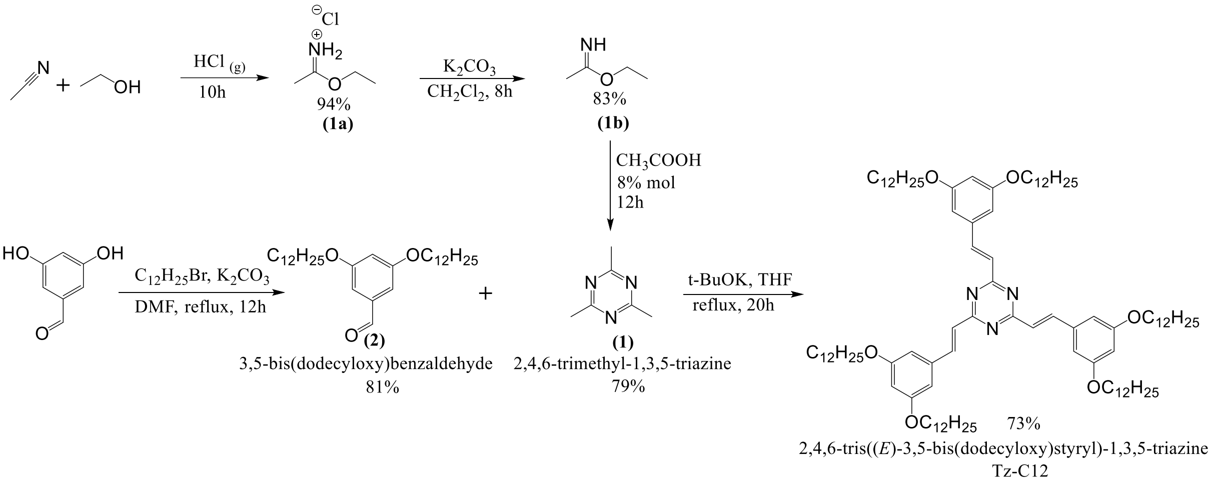

Figure 88 : Scheme of the synthesis of Tz-C12 molecule

After purification by flash chromatography, the product is obtained as a white powder, the NMR ^{1}H of the molecule in $CDCl_3$ with the attribution of the protons is shown in Figure 89. The details of the synthesis with NMR ^{13}C and mass spectroscopy can be found in the appendix.

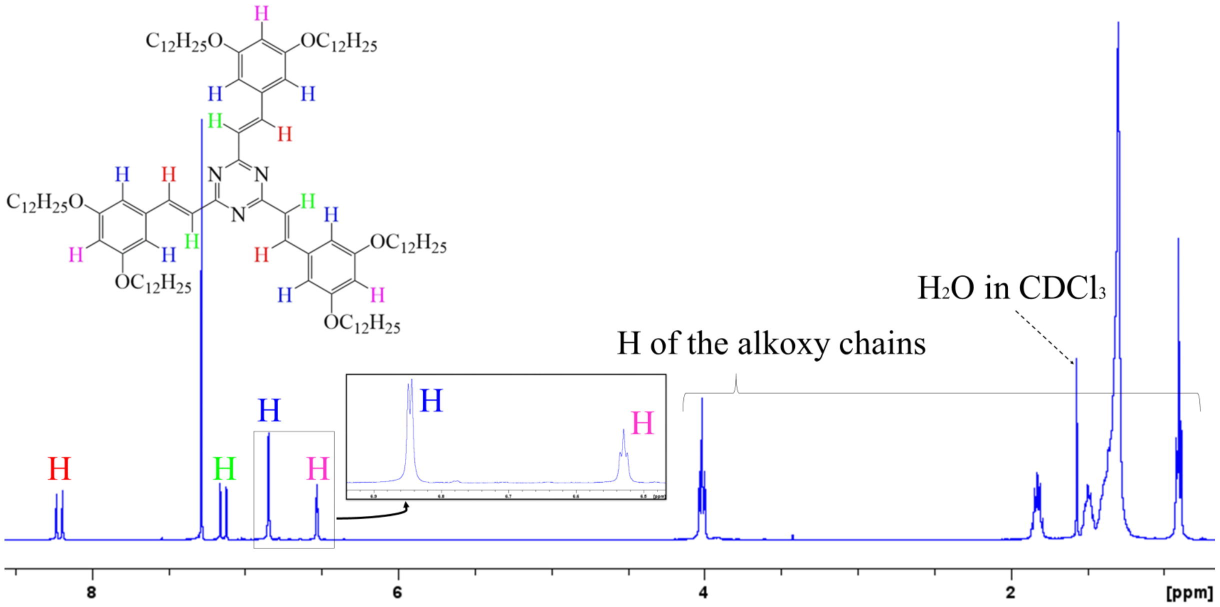

Figure 89 : NMR ^{1}H of Tz-C12 in $CDCl_3$ with the attribution of the protons

The NMR ^{1}H of the Tz-C12 molecule is shown in Figure 89. The triplets around 0.9 and 4 ppm are attributed to the terminal -CH_3 and first –CH_2–O– of the alkoxy chains, respectively. In the aromatic area, the doublet and triplet at 6.85 and 6.53 ppm, respectively, are those of the protons on the phenyl rings. The two large doublets at 8.21 and 7.14 ppm are the protons of the –HC=CH– double bond. Note that the value of the coupling constant on these doublets is J = 15.58 Hz, confirming that the molecule has a trans configuration. DFT calculation made by Jan Patrick Calupitan, a post doctoral researcher in our team, allowed to attribute the most deshielded doublet to the proton on beta to the triazine ring, and the less deshielded doublet to the proton on alpha position to the same ring.

II.2 – Protonation of Tz-C12 in solution

The first characterization performed concerns the ability of this molecule to be protonated. With chloroform as solvent, protonation is first verified in solution, employing trifluoroacetic acid. For this purpose, NMR ^{1}H and UV-visible spectroscopy are used.

II.2.1 – NMR ^{1}H characterization of the protonation of Tz-C12

To probe the protonation of the molecule by NMR ^{1}H, 5 mg of Tz-C12 ($3*10^{-3}$ mmol) are solubilized in 0.5 mL of $CDCl_3$ and NMR ^{1}H of this tubeis recorded and used as a reference. Three NMR tubes with 5 mg of Tz-C12 solubilized in 474, 448 and 422 µL of $CDCl_3$, respectively are prepared, and 26, 52 and 78 µL of $CDCl_3$ containing $3*10^{-3}$, $6*10^{-3}$ and $9*10^{-3}$ mmol of TFA respectively are added into these tubes to obtain 1/1, 1/2 and 1/3 equivalents of Tz-C12/TFA solutions respectively. Three other tubes with the same amounts of Tz-C12 and $CDCl_3$ are prepared, and 26, 52 and 78 µL of $CDCl_3$ containing $3*10^{-2}$, $6*10^{-2}$ and $9*10^{-2}$ mmol of TFA are added into these tubes to obtain 1/10, 1/20 and 1/30 equivalents of Tz-C12/TFA respectively. All the tubes are recorded using NMR ^{1}H and compared to each other. Figure 90 shows NMR ^{1}H of the aromatic region of each tube.

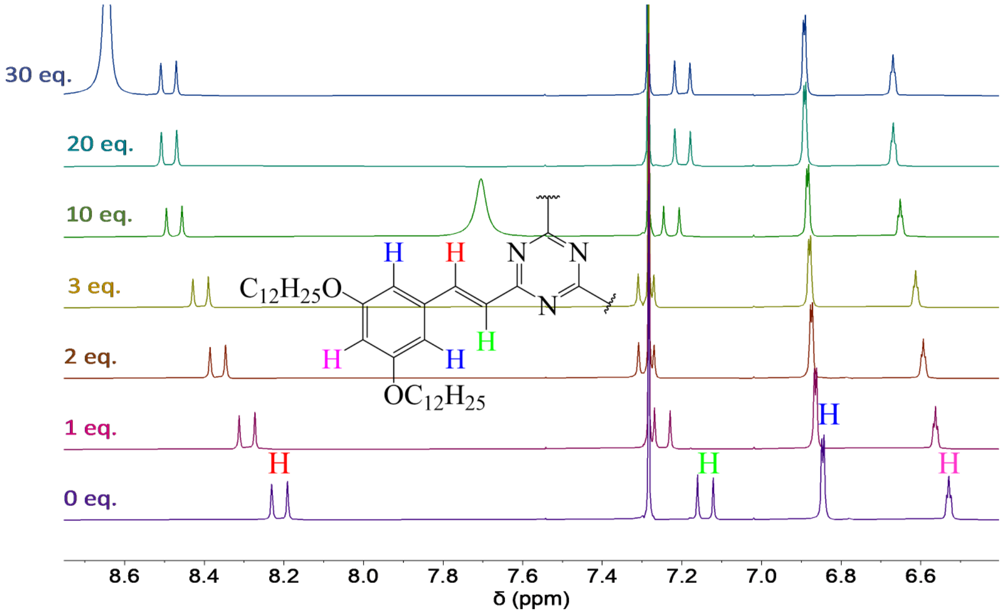

Figure 90 : NMR ^{1}H of the aromatic protons of Tz-C12 with 0 (purple), 1 (magenta), 2 (red), 3 (yellow), 10 (green), 20 (light blue) and 30 (blue) equivalents of TFA

The NMR spectra show shifts of all the aromatic protons of the molecule after adding TFA to highest δ (ppm) showing that the protons become more deshielded. This evolution is attributed to protonation of the triazine ring, which generates positive charges and makes it even more electrons attractive. The protons of the double bound (red and green protons in Figure 90) are the most affected ones due to their proximity to the triazine ring. Interestingly, after the addition of 10 equivalents of TFA, a change in the direction of the shift of the closest proton to the triazine ring (green proton in Figure 90) is noticed. This behavior could indicate the protonation of second nitrogen of the triazine ring, but a UV-visible spectroscopy would give more information.

II.2.2 – UV-visible characterization of the protonation of Tz-C12

Another technique that gives valuable information in solution is UV-visible spectroscopy. The acidification of 1 mL of Tz-C12 solution in $CHCl_3$ with a concentration of $4*10^{-4}$ $mol.L^{-1}$ using TFA is followed by UV-visible spectroscopy. Three solutions of TFA with different concentrations are used to add 7.6 µL of TFA with 1, 10 or 100 equivalents of TFA, respectively, into the Tz-C12 solution. The results are shown in Figure 91.

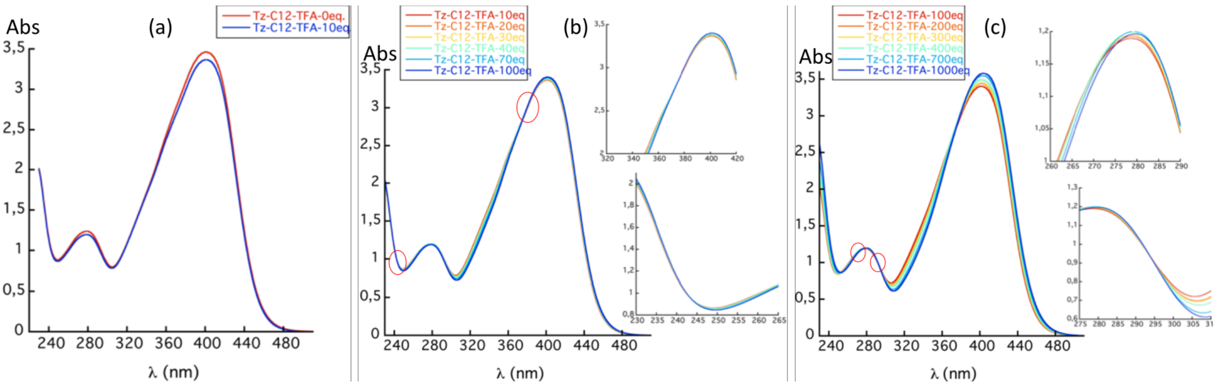

Figure 91 : UV-visible spectra of (a) Tz-C12 in chloroform with 10 equivalents of TFA showing no isobestic point, (b) Tz-C12 in chloroform with up to 100 equivalents of TFA showing two isobestic points surrounded in red, and Tz-C12 in chloroform with up to 1000 equivalents of TFA showing two new isobestic points surrounded in red.

The first 10 equivalents of TFA added to the Tz-C12 solution shows no effect on the spectra, as it appears in Figure 91 (a). From 10 equivalents to 100 equivalents of TFA, two isobestic points appears on the spectra (Figure 91 (b)) showing an equilibrium in solution attributed to the protonation of one nitrogen of the triazine ring. After 100 equivalents of TFA and up to 1000 equivalents, two other isobestic points appeared (Figure 91 (c)) showing the presence of another equilibrium attributed to a protonation of a second nitrogen atom of the triazine ring.

These characterizations in solution demonstrated that the Tz-C12 can be protonated in solution using TFA. It also tends to show that a protonation of a second nitrogen atom of the triazine ring is reached. The heteropolyacid $H_3[PMo_{12}O_{40}]$ having a pKa below TFA, will definitely be able to protonate the Tz-C12 molecule.

II.3 – On surface characterizations of $H_3[PMo_{12}O_{40}]$-Tz-C12/HOPG sample

The Tz-C12/HOPG sample is prepared by drop casting 10 µL of the molecule in toluene on HOPG substrate ($C = 10^{-4}$ mol.L^{-1}). The next step is to prepare the sample with the POMs, by protonating the self-assembled Tz-C12 using a POM solution. The Keggin $H_3[PMo_{12}O_{40}]$, that will be named H_3K^{Mo} is used for its easier ability to be reduced compare to the tungstate equivalent, as explained before (cf. chapter II).

The protonation procedure is also important, and in order to have a large aexcess of heteropolyacid POMs vs. the self-assembled Tz-C12 on the HOPG surface and avoid the formation of aggregates on the surface of the sample, drop-casting method will be avoided. It has to take advantage of the different solubility of the molecules. Indeed, the H_3K^{Mo} is soluble in polar solvents such as water and acetonitrile, and Tz-C12 is soluble in non-polar or low-polar solvents such as toluene and chloroform. Then, I choose to prepare a solution of H_3K^{Mo} in acetonitrile at a concentration of 1 mM, and to immerse the Tz-C12/HOPG sample vertically in this solution for about 1 min in order to protonate the self-assembled Tz-C12 to deposit the POMs through electrostatic interactions. As Tz-C12 is not soluble in acetonitrile and HOPG have a low affinity with this solvent (poor wettability), the 2D network formed on surface should not be disturbed by the immersion. In another hand, due to their ionic polar character, the H_3K^{Mo} have a low affinity with bare HOPG and Tz-C12 molecule. Thus, they should remain in the acetonitrile solution when the substrate will be slowly removed from it. As a result, only the H_3K^{Mo} that would protonate the Tz-C12 on surface will stay on the surface after the removal of the sample, thanks to the electrostatic interactions. This substrate obtained after the immersion will be named H_3K^{Mo}-Tz-C12/HOPG. A scheme of the deposition method is shown in Figure 92.

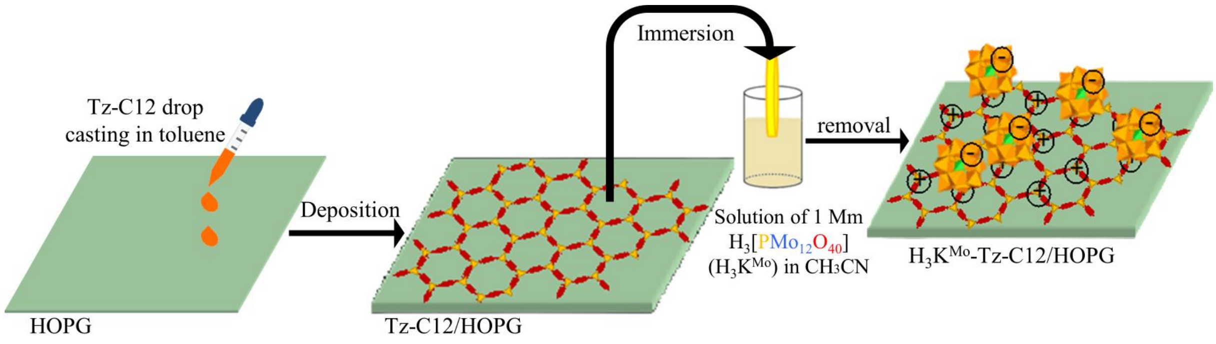

Figure 92 : Scheme of the deposition method of the H_3K^{Mo} by on-surface protonation of the Tz-C12

For the next steps, the question to answer is, what about Tz-C12 self-assembly on HOPG? And STM is the appropriate technique to probe it.

II.3.1 – STM characterizations of Tz-C12/HOPG sample and the effect of protonation on the arrangement of the molecules on surface

For STM imaging, a Tz-C12/HOPG sample is first prepared. 10 µL of the Tz-C12 molecules in toluene with a concentration of 10^{-4} mol.L^{-1} are deposited on freshly cleaved HOPG substrate and after the evaporation of the solvent the sample is imaged by STM (Figure 93).

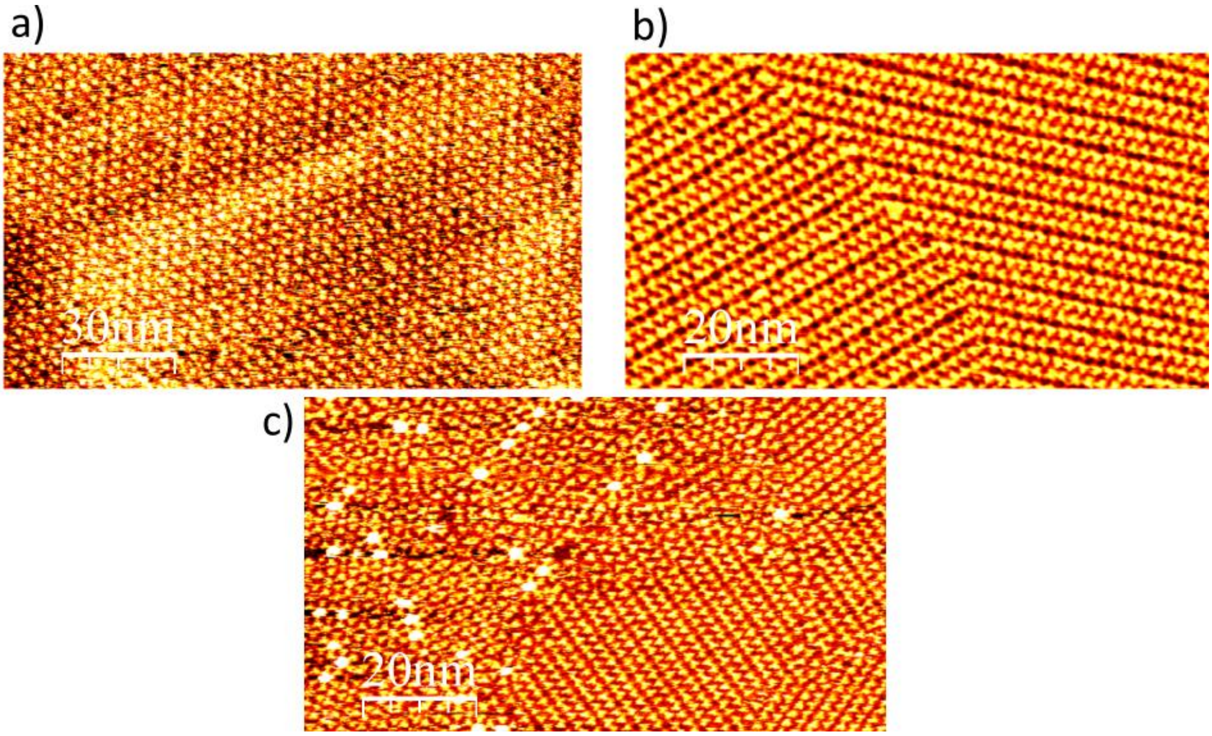

Figure 93 : STM images of Tz-C12/HOPG samples with (a) honeycomb arrangement (150 x 88 nm^2), (b) herringbone arrangement (100 x 58 nm^2) and (c) mix of honeycomb and herringbone arrangement (100 x 58 nm^2) (blight dots are ZnPc contamination) (Vbias = 1.1 V, Iset = 18 pA)

Tz-C12 self-assembly observed by STM is similar to the arrangement of TSB-C12, with two different organizations, honeycomb and herringbone networks, as shown in Figure 93. The tendency of this molecule to form herringbone arrays is however much higher than for TSB-C12. Nevertheless, this herringbone arrangement is not problematic for this system to reach our goal to organize and individualize POMs onto surface.

Another important point is the effect of the protonation on the Tz-C12 self-assembling. In order to probe this, the sample is immersed in a solution of 1M of HCl in acetonitrile during about 1 min, slowly removed and imaged by STM (Figure 94).

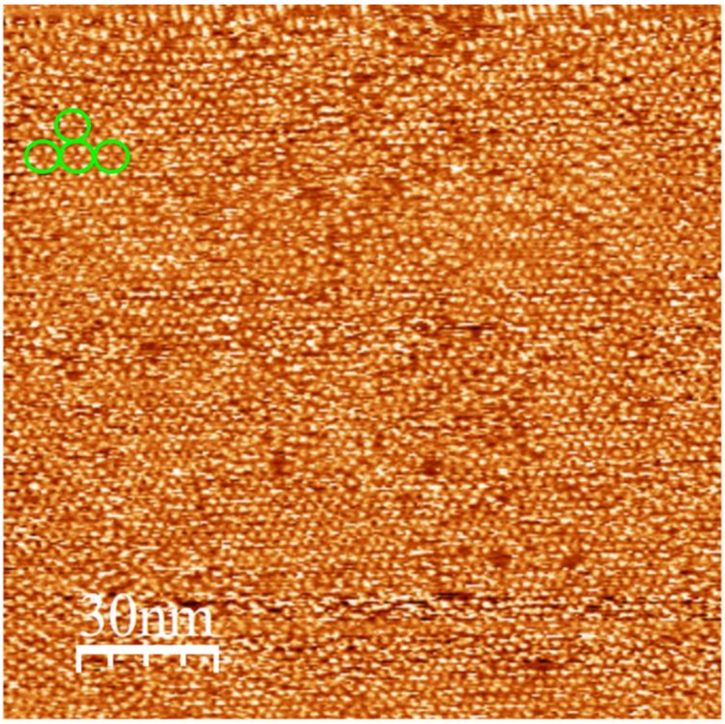

Figure 94 : STM image of Tz-C12/HOPG sample after immersion into 1M solution of HCl in acetonitrile for 1 min with green circles showing some hexagons formed by the Tz-C12 (150 x 150 nm^2) (Vbias = 1.3 V, Iset = 17 pA)

The STM image (Figure 94) shows a honeycomb arrangement of the Tz-C12 molecule on HOPG substrate after the immersion into 1M of HCl solution in acetonitrile. This result demonstrates that the network of Tz-C12 is not disturbed by the protonation onto the surface of HOPG.

Thus, after the immersion of a Tz-C12/HOPG substrate into a 1 mM solution of heteropolyacid H_3K^{Mo} in acetonitrile, the determination of the protonation is the first information needed. Indeed, for each nitrogen atom protonated, an H_3K^{Mo} will be deposited. As a result, the protonation rate on surface would allow knowing the coverage rate of the POM over the surface. To obtain this crucial information, X-ray photoelectron spectroscopy (XPS) will be used.

II.3.2 – XPS spectroscopy on Tz-C12/HOPG and H$_3$K^{Mo}-Tz-C12/HOPG samples

XPS is a surface sensitive technique that allows probing the chemical composition of materials. The measurements rely on the photoelectric effect, where high-energy X-rays are directed at a sample, causing the ejection of photoelectrons from the surface of the material. The energy of these emitted electrons is measured and provides information about the binding energies of electrons in the outermost layers of a material. By analyzing these binding energies, it is possible to identify the elements present, their chemical states (oxidation states), and their relative concentrations by measuring the area of photoelectron peaks. This will allow differentiating between the non-protonated and protonated nitrogen atoms of the Tz-C12 on surface, and having quantitative information about their rate. It will also be possible to probe the presence of H$_3$K^{Mo} through Mo core level signal.

Two samples are studied. First, the Tz-C12/HOPG sample as a reference with no protonated nitrogen atoms (Tz-C12-H$^+$). Second, an H$_3$K^{Mo}-Tz-C12/HOPG sample to determine the Tz-C12-H$^+$/Tz-C12 ratio on surface, and prove the deposition of the H$_3$K^{Mo} by the presence of molybdenum.

Thus, the XPS results related to H$_3$K^{Mo}-Tz-C12/HOPG and Tz-C12/HOPG samples prepared according to the procedure previously described are shown in Figure 95.

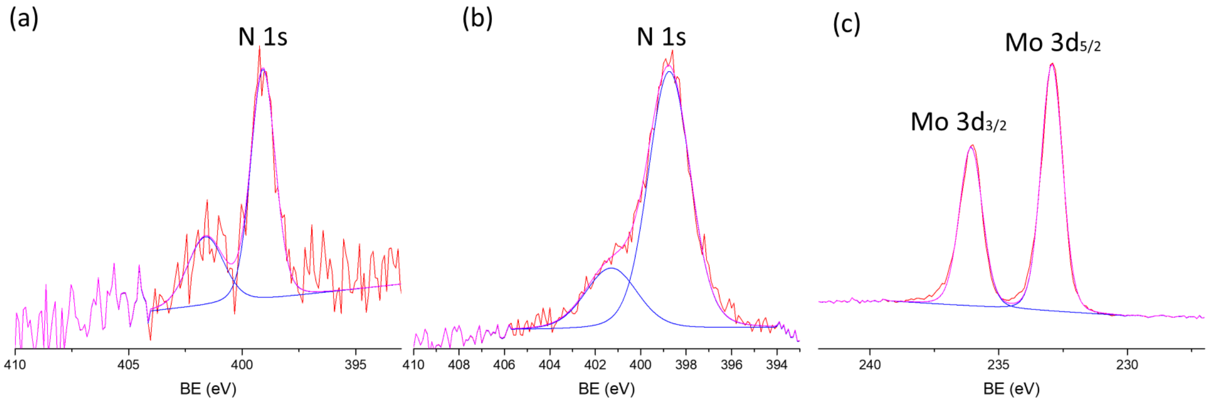

Figure 95 : High resolution XPS spectra of (a) Tz-C12/HOPG reference sample at the N 1s core level, (b) and (c) the H$_3$K^{Mo}-Tz-C12/HOPG sample at the N 1s core level and Mo 3d core level respectively

The survey XPS spectrum of the H$_3$K^{Mo}-Tz-C12/HOPG sample shows the presence of oxygen, carbon, phosphorus, molybdenum and nitrogen. More specifically, high resolution XPS spectrum at the Mo core level shows the doublet at 233 and 236 eV corresponding to the 3d 3/2 and the 3d 5/2 levels, respectively, and typical of the Mo^{6+} oxide (Figure 95 (c)).[260] In the nitrogen high resolution XPS spectrum, non protonated Tz-C12 is detected at 398.6 eV and, as expected, the presence of ammonium on the surface with the peak at ~401.8 eV[261] (Figure 95 (b)) is detected as well. Nevertheless, the peak at about 401.8 eV is also detected in the reference sample (Figure 95 (a)). The presence of this peak before the immersion in the H_3K^{Mo} was not expected. A possible interpretation of this peak is the presence of hydrogen bonds due to water molecules, as proposed by Song et al.[262] To check this hypothesis and show the effective protonation of the Tz-C12 on surface, we performed an experiment under dry conditions.

The preparation of the sample in dry conditions is carried out inside a glovebox under dry nitrogen atmosphere. The H_3K^{Mo} is dried at 180 C° during 180 min under vacuum and solvents (toluene and acetonitrile) dried from water are used to prepare the solutions. Reference Tz-C12/HOPG and the H_3K^{Mo}-Tz-C12/HOPG samples are made in the glove box and transferred under nitrogen into the XPS chamber (Figure 96).

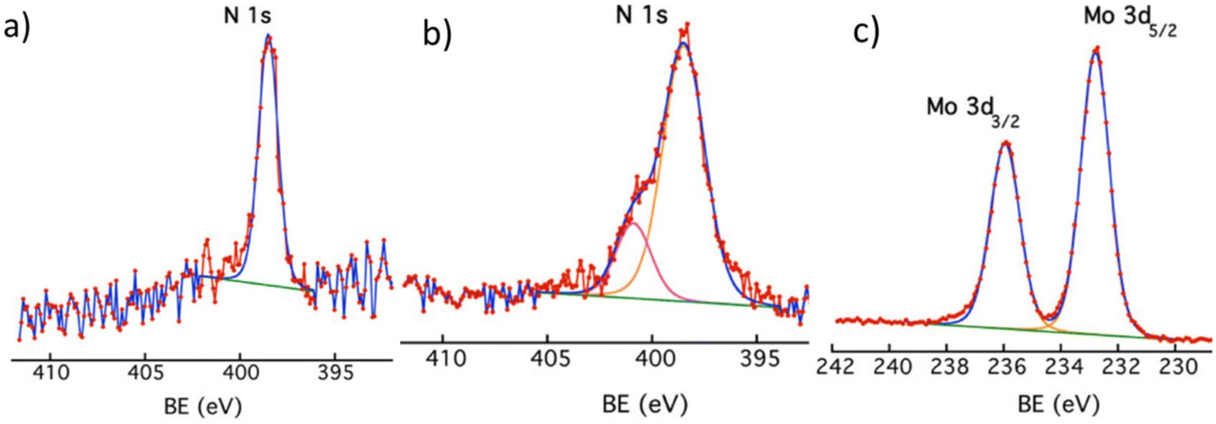

Figure 96 : High resolution XPS spectra made under dry conditions of (a) Tz-C12/HOPG reference sample at the N 1s core level, (b) and (c) the H_3K^{Mo}-Tz-C12/HOPG sample at the N 1s core level and Mo 3d core level respectively[210]

The spectra obtained on the samples prepared under dry conditions show that a single peak is present on the Tz-C12/HOPG reference as expected (Figure 96 a). This result confirms that the signal observed previously (Figure 95 (a)) is due to hydrogen bonds formed between the Tz-C12 and molecules of water. The apparition of the peak at 401.5 eV alongside the peaks of molybdenum (Figure 96 (b) and (c) respectively) after the immersion into the dry solution of POM in acetonitrile proves the formation of the ammonium functions on the surface. The area ratio of the ammonium relatively to amine measured by XPS is 20%, which means that around 60% of the Tz-C12 molecules on surface are protonated. Indeed, as each Tz-C12 molecule has 3 nitrogen atoms, if 100% of the molecules are protonated once, a ratio of 33.33% would have been detected. The fact that all Tz-C12 molecules are not protonated on surface despite the supposed protonation of a second nitrogen atom reached in solution can be explained by a change of the pKa of the molecule when it is pi-staked on HOPG substrate. Indeed, several studies have reported a pKa variations for molecules when passing from solution to on surface or at air/liquid interface.[263–265]

These XPS results give valuable information. Firstly, protonation of the Tz-C12 molecule on the surface is proved as well as the deposition of the H_3K^{Mo} POMs. Secondly, a protonation rate on surface is determined and shows that 60% of the surface can be covered by H_3K^{Mo} POMs.

The XPS technique has however its own limitations related to the fact that no information about the morphology of the surface probed is given. In order to observe the surface where the molybdenum (i.e. presumably the H_3K^{Mo} POMs) is detected, Field Emission Scanning Electron Microscopy (FESEM) with energy dispersive spectroscopy (EDS) is used in order to get cross-linked information about morphology and chemical composition of the surface at micrometric scale.

II.3.3 – Field emission scanning electron microscopy (FESEM) and energy dispersive X-ray spectroscopy (EDS) characterizations

Field Emission Scanning Electron Microscopy (FESEM) associated to Energy-dispersive X-ray spectroscopy (EDS) is a powerful analytical technique used for material characterization. FESEM provides high-resolution imaging of a sample's surface, while EDS simultaneously collects and analyzes X-rays emitted from the sample when it is bombarded with electrons. This combination allows for the determination of the sample's elemental composition and distribution up to the micrometric scale.

A blank sample consisting of TSB-C12/HOPG substrate immersed in a solution of H_3K^{Mo} in acetonitrile is first analyzed. In this case, because there are no nitrogen atoms on the surface, there should not be any homogeneous layer of POMs. FESEM images are made at a normal incidence (0°) at different scales and areas of the surface. And due to the deep bulk analysis capabilities of EDS, the samples are analyzed at grazing incidence (85°) to enhance sensitivity to the outer surface. The images and analysis of the blank sample are shown in Figure 97.

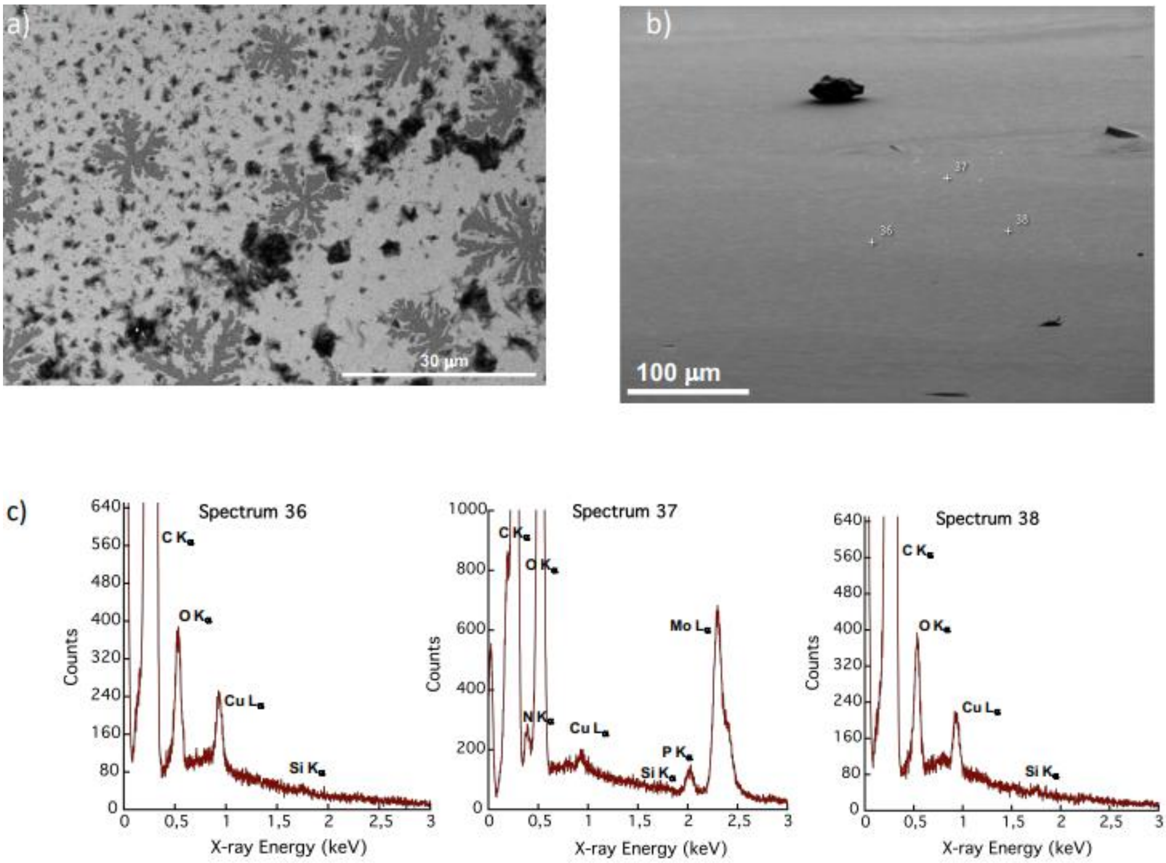

Figure 97 : FESEM images of the TSB-C12/HOPG sample immersed in an H_3K^{Mo} solution at a) 0° and b) 85° and c) EDS spectra corresponding to image b) with the spectrum 37 recorded on a POMs aggregate[210]

The FESEM images a) and b) Figure 97 at 0° and 85° respectively shows the presence of a film of TSB-C12 on the surface appearing on the white contrast in image (Figure 97 a)). When the sample is tilted for EDS measurements, some white spots appear on the surface corresponding apparently to aggregates (Figure 97 b)). Analyses are made on three spots of the tilted substrate, with the spots 36 and 38 on flat areas and the spot 37 on the apparent aggregate. As expected, there is no molybdenum detected on both sopts 36 and 38 (Figure 97 c)). Interestingly, for the measurements made on the aggregate of spot 37, an important signal of molybdenum is detected allowing the quantification of the % atomic ratios, i.e Mo/P = 12.4, Mo/O = 0.33 corresponding to the stoichiometry of $H_3[PMo_{12}O_{40}]$. Considering its high intensity, it allows to confidently conclude that it corresponds to an aggregate. These results show that except for some aggregates, no H_3K^{Mo} were deposited on this TSB-C12/HOPG sample.

After the analysis of this reference, a H_3K^{Mo}-Tz-C12/HOPG sample is prepared and analyzed using the same conditions. The results are shown in Figure 98.

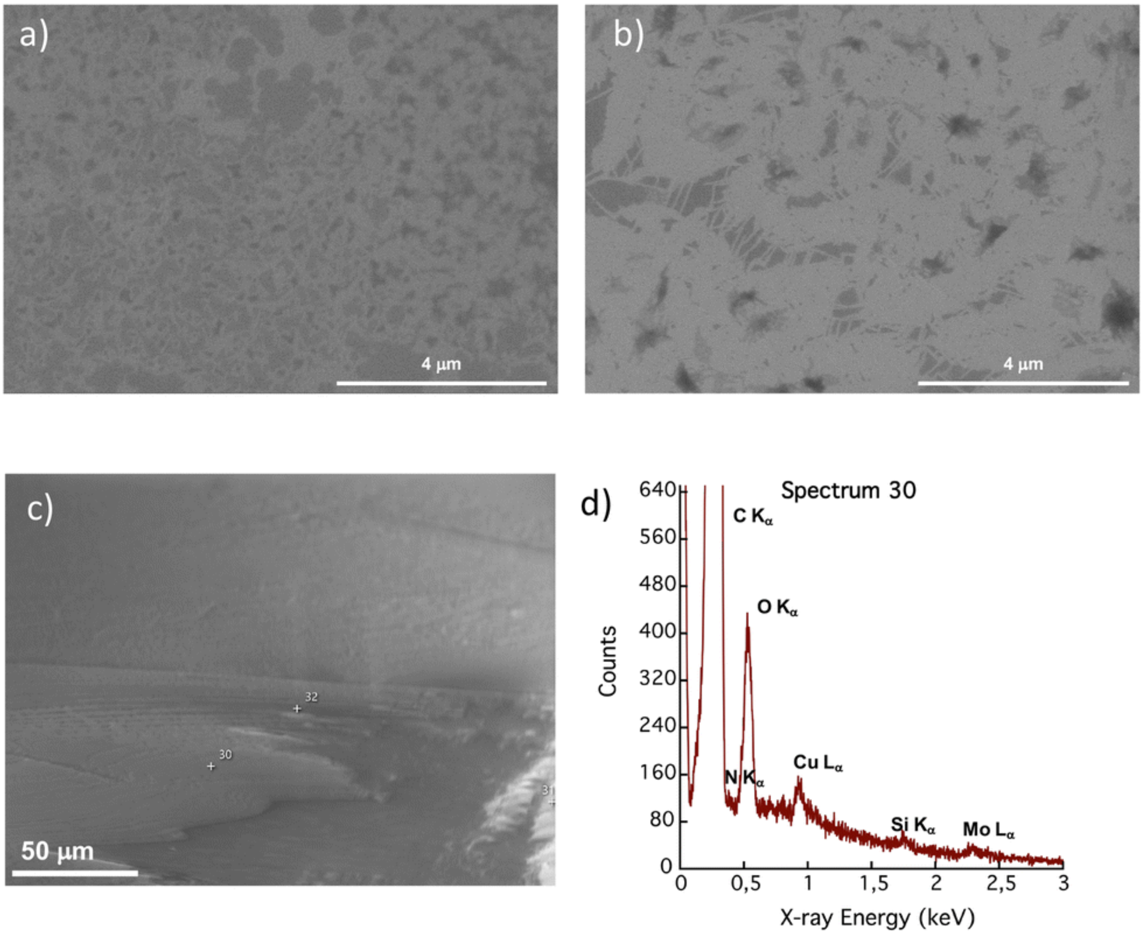

Figure 98 : FESEM images at 0° tilt (normal incidence) of (a) the Tz-C12/HOPG sample (white contrast corresponds to Tz-C12 film) and (b) the H_3K^{Mo}-Tz-C12/HOPG sample (white contrast corresponds to the POMs layer); (c) FESEM image at 85° tilt of the H_3K^{Mo}-Tz-C12/HOPG sample; (d) EDS spectrum at 85° tilt of the H_3K^{Mo}-Tz-C12/HOPG sample showing the presence of molybdenum[210]

The FESEM images obtained with an incidence of 0° before and after deposition of the POMs (Figure 98 a) and b) respectively) show the formation of a thin homogenous film (in white) on the surface as attested by the white contrast on the images. No aggregates are detected on the entire sample's surface. The images show an evolution of the film on the surface before the immersion and deposition of the POMs (Figure 98 a)) and after the deposition of the POMs on the sample (Figure 98 b)). The aspect of the film after the deposition of the H_3K^{Mo} changes, exhibiting larger areas covered on the surface (white regions) connected with linear bridges and an apparent increase in thickness. This evolution is probably related to the POM layer formed on the surface of the Tz-C12/HOPG substrate. This is confirmed by the analysis made on flat areas of this thin layer with a grazing angle of 85° (Figure 98 c)). Indeed, molybdenum is detected with a quantity of about 1%. Note that the presence of molybdenum is detected all over the sample, in a homogeneous way. These results are in accordance with what was obtained by XPS, and give one supplementary information about the distribution of the 60% estimated coverage of H_3K^{Mo} over the surface by detecting its presence on these films.

The presence of this layer attributed to the POMs over the entire surface of the H_3K^{Mo}-Tz-C12/HOPG substrate, and the absence of this layer in the case of TSB-C12/HOPG sample, show the necessity of the presence of this triazine protonable function on surface in order to trap H_3K^{Mo} POMs by electrostatic interactions. Furthermore, the absence of aggregates along with the thin films observed and the differences noticed before and after the deposition (Figure 98 image a) and b) respectively), combined to the results obtained by XPS, confirm undoubtedly the electrostatic deposition of H_3K^{Mo}.

To further investigate the distribution of this H_3K^{Mo} layer on the surface, AFM is used. AFM allows imaging under ambient conditions, and it is a powerful technique for 3D shape characterizations at the nanometric scale.

II.3.4 – AFM characterizations of H_3K^{Mo}-Tz-C12/HOPG sample

A Tz-C12/HOPG sample is prepared and imaged by AFM before the deposition of H_3K^{Mo}. The H_3K^{Mo} are then deposited as described previously and the sample imaged again by AFM (Figure 99).

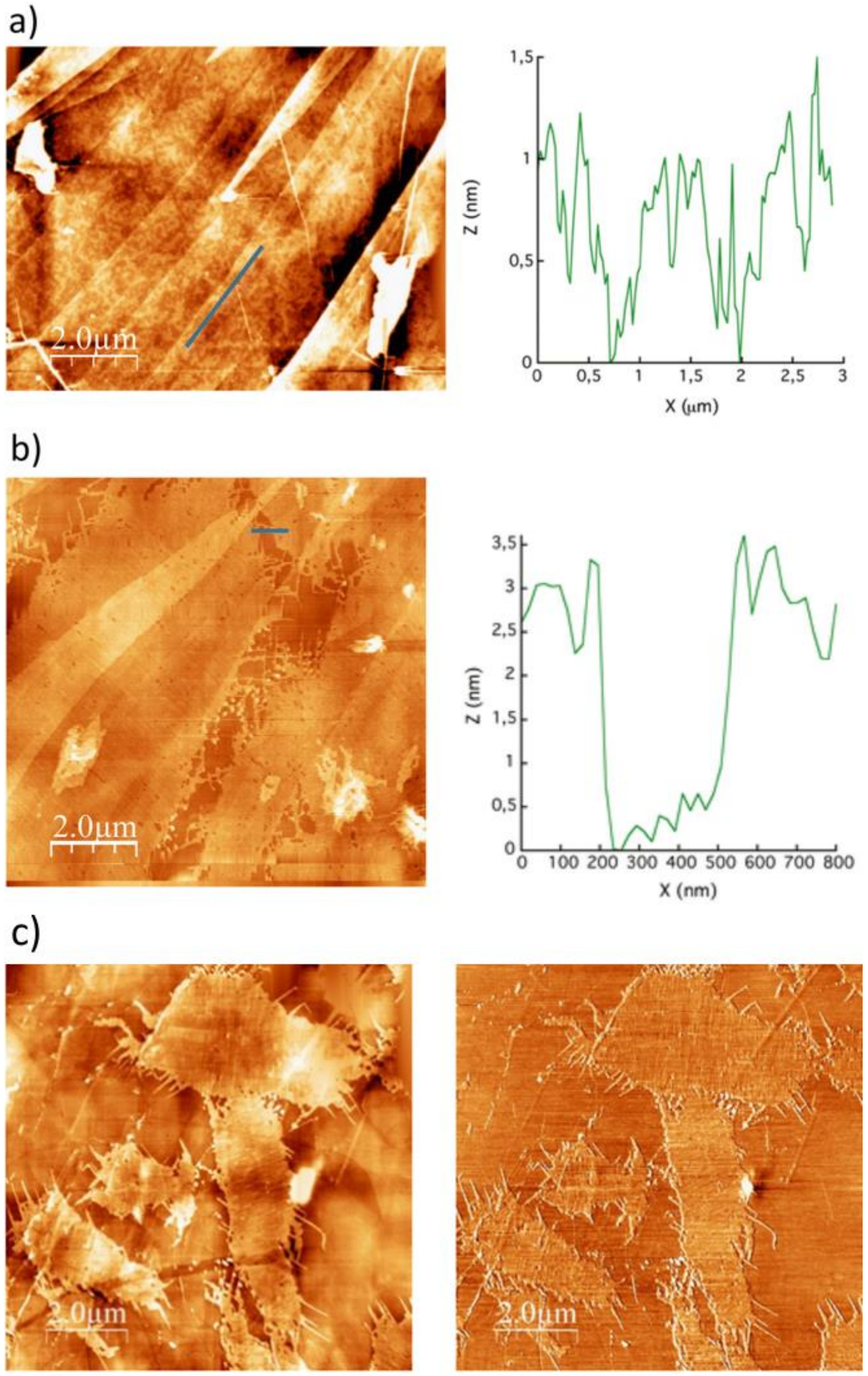

Figure 99 : AFM images of (a) the Tz-C12/HOPG sample and height profile showing the presence of a flat film of ~1 nm thickness, (b) the H_3K^{Mo}-Tz-C12/HOPG sample and height profile showing a film of ~3 nm and (c) H_3K^{Mo}-Tz-C12/HOPG sample with topography (left) and corresponding phase image (right) (images 10 x 10 µm^2)

The AFM images of the Tz-C12/HOPG sample show a formation of the film with height of around 1 nm (Figure 99 (a)). These images are in accordance with what were observed by FESEM, showing a homogenous flat surface. Following the H_3K^{Mo} POM deposition, thin films are formed on the substrate, with an average coverage of around 60% determined from the image 97 b), which is consistent with the protonation rate estimated by XPS. The films cover large areas on the surface connected between them by linear bridges, exactly as observed previously by FESEM. The heights of the film are around 2.5 ~ 3 nm as shown in Figure 99 (b), which could be associated to a monolayer of H_3K^{Mo} on the top of a Tz-C12 monolayer. Furthermore, these films exhibit a finely structured network, suggesting the presence of well-organized POM arrays as it can be clearly observed in Figure 99 (c).

The images and information obtained by AFM confirm and complete the characterization made by XPS and FESEM/EDS, showing a deposition of the H_3K^{Mo} all over the surface into a thin film. One question however concerns the molecular arrangement of the H_3K^{Mo} inside these films, and the STM should provide some answers.

II.3.5 – STM characterization of the H_3K^{Mo}-Tz-C12/HOPG sample

The purpose of STM imaging is to probe at a nanometric scale the arrangement of the molecules on the surface. Indeed, the previous characterization techniques allowed to demonstrate the deposition of the H_3K^{Mo} POMs on the functionalized Tz-C12/HOPG substrate into thin films, and even to quantify their coverage rate at around 60%. Nevertheless, the arrangement of the H_3K^{Mo} is still unknown (are they individualized? Periodically organized?), and STM is the appropriate technique to achieve this goal. However, as mentioned before, STM imaging on such system under ambient conditions is challenging, due for example to the huge electric field generated between the tip and the molecules that can reach several $GV.m^{-1}$ and could disturb the Tz-C12/POM ionic layer.[150]

After checking the self-assembly on a prepared Tz-C12/HOPG substrate, it is immersed into the 1 mM of H_3K^{Mo} acetonitrile solution for about 1 min and imaged again by STM (Figure 100).

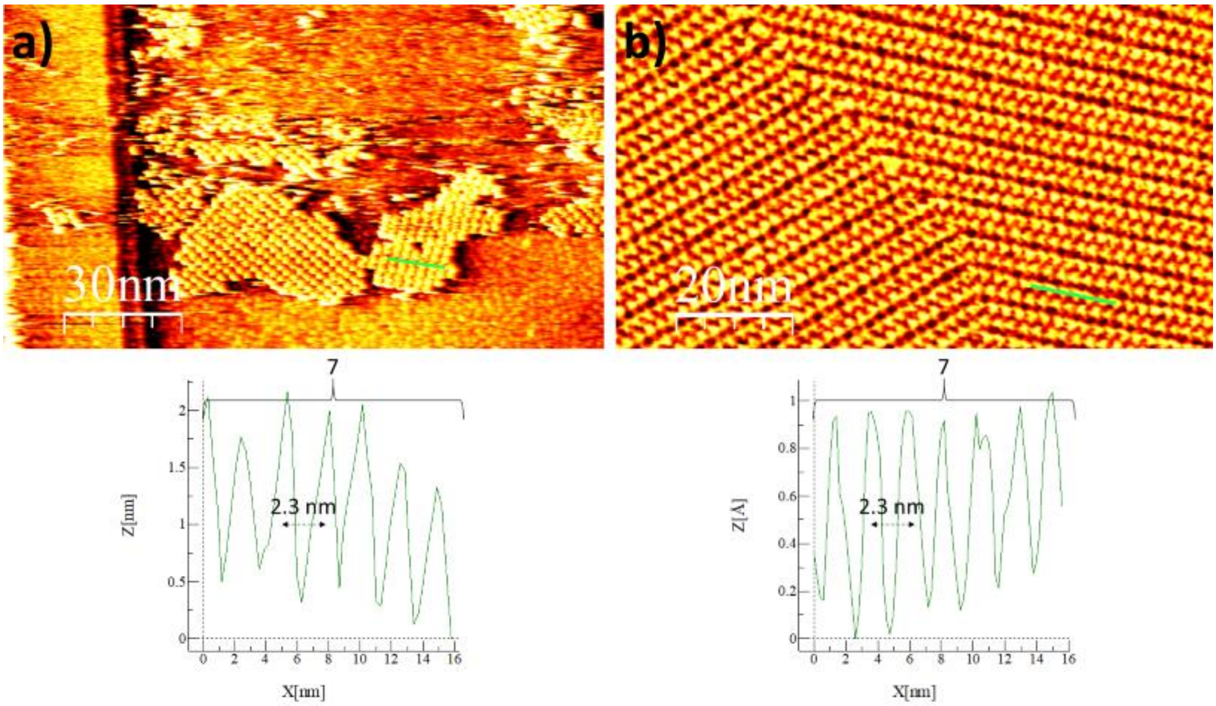

Figure 100 : STM images with heights profile of (a) the H_3K^{Mo}-Tz-C12/HOPG samples (150 x 71 nm^2) and (b) the Tz-C12/HOPG sample (100 x 47 nm^2) ((a) : Vbias = 1.5 V, Iset = 16 pA, (b) : Vbias = 1 V, Iset = 20 pA)

The STM images before (Figure 100 b)) and after (Figure 100 a)) the deposition of the H_3K^{Mo} are very different. The arrangement of Tz-C12 molecule on HOPG before the deposition of the POMs exhibits herringbone arrangements. Their height profile reveals apparent heights of approximately 1 Å, and there are seven Tz-C12 molecules counted over a line of 16 nm in length, with a separation of 2.3 nm between each molecule. On the STM image of the H_3K^{Mo}-Tz-C12/HOPG sample obtained after the deposition of the POMs (Figure 100 a)), molecules different from the Tz-C12 are observed forming islands on the surface. The shape of these molecules is spherical, in contrast to the triangular shape of Tz-C12. They exhibit apparent heights between 1.5 and 2 nm (Figure 100 below image a)), much higher than the apparent heights of Tz-C12 molecule. These observations allow attributing these molecules to the H_3K^{Mo} POMs as they are in accordance with the expected STM images of this POM. Moreover, the assumed H_3K^{Mo} form arrays on the surface, following precisely the same pattern as the Tz-C12 molecule, being separated from each other by 2.3 nm and counting 7 POMs over 16 nm line.

These results, along with the combination of the different characterization techniques showing the deposition of the H_3K^{Mo}, leaves no doubt about the nature of the molecules observed in Figure 100 a), and demonstrate that the Tz-C12 pattern induces the periodic organization of the POMs.

Remarkably, the image of the POMs within the bulk of the islands remains stable, displaying individualized H_3K^{Mo} structures. Indeed, at the edges and within small clusters (comprising approximately 6-7 molecules or fewer), disturbances that are typically indicative of the movement of the molecules induced by the scanning STM tip appear on the image. This suggests that within the bulk, the packed POMs are more stable and less susceptible to the interactions caused by the scanning STM tip. But on the edges, where they have more degree of freedom to move, they exhibit lower stability and are affected by the scanning STM tip, moving and being torn off from the surface.

An image of the POMs that seem to be organized on the honeycomb arrangement is presented in Figure 101 b). This image presents more disturbances on the molecules compared to the one where the H_3K^{Mo} follows the herringbone pattern of the Tz-C12.

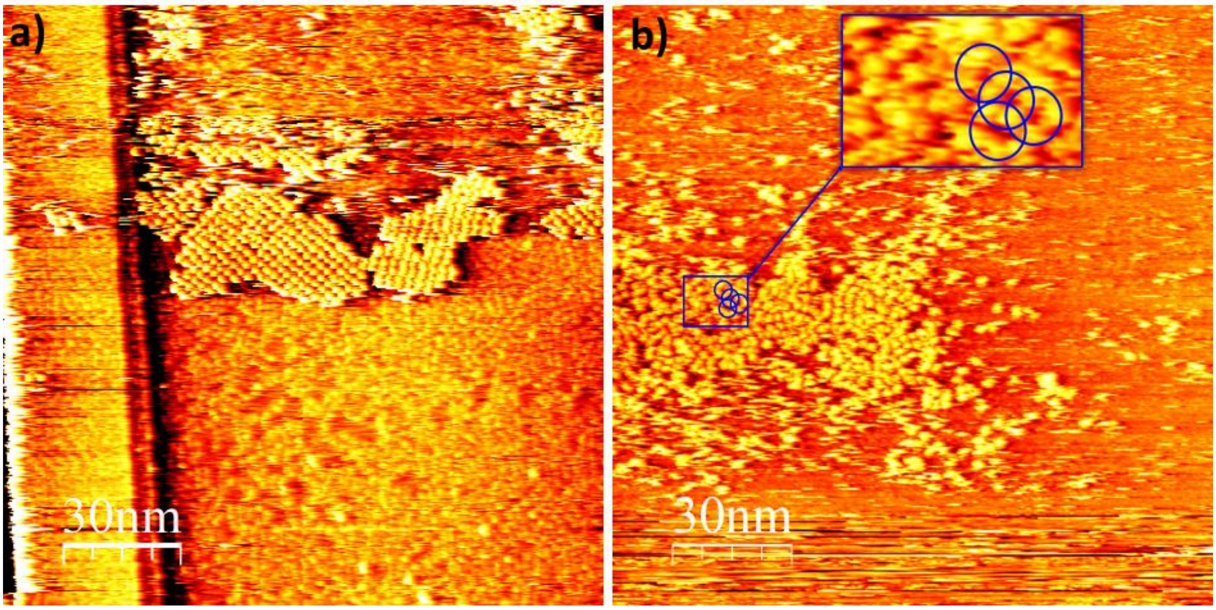

Figure 101 : STM images (150 x 150 nm^2) of H_3K^{Mo}-Tz-C12/HOPG samples with H_3K^{Mo} organized on (a) herringbones arrangement of Tz-C12 and (b) honeycomb arrangement of Tz-C12

Obtaining a less stable layer when the H_3K^{Mo} follow the honeycomb pattern comfort the hypothesis that POMs are more affected by the interactions induced by the STM tip when they exhibit more degrees of libety to move. Indeed, the layer formed over the honeycomb pattern presents pores within it (Figure 101 b), blue rectangle), granting the POMs with greater freedom of movement compared to when they follow the herringbone pattern. This could reasonably explain the disturbances observed in the image of the H_3K^{Mo} over the honeycomb pattern of Tz-C12 molecules (Figure 101 b)). The herringbone pattern appears to provide greater stability, forming a denser layer of POMs that restricts their movement within the bulk. In contrast, the POM layer formed on the honeycomb pattern contains pores, enabling the POMs to move and making STM imaging more difficult, as illustrated in Figure 101.

Regardless, STM imaging of the POMs on this system under ambient conditions remains complicated to interpret, as illustrated by Figure 102.

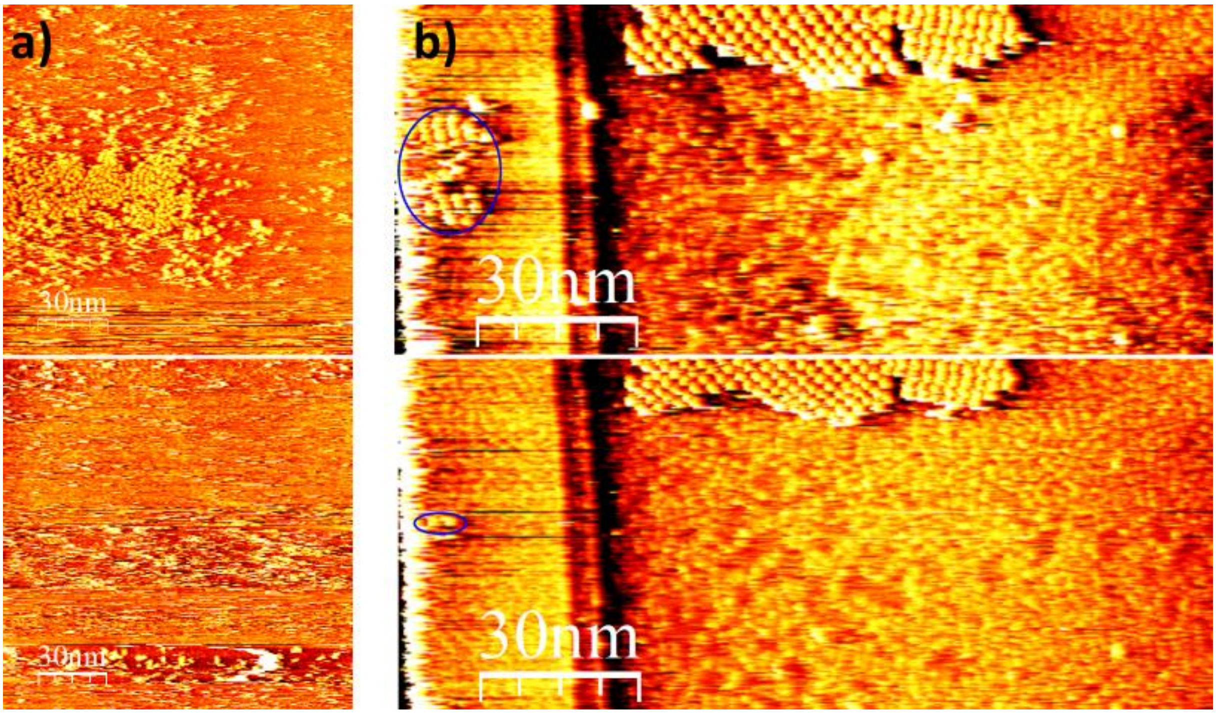

Figure 102 : (a) STM images of H_3K^{Mo} on hexagonal arrangement with (top) the first scan and (bottom) second scan of the same area (b) STM images of H_3K^{Mo} on herringbones arrangement (top) first scan and (bottom) second scan of the same area

Indeed, two scans of the same area by STM results in different images, with a depletion in POM coverage as noticed for the case where POMs follow the herringbones arrangement (Figure 102 (b)), and a loss of the entire POMs layer when they follow the hexagonal arrangement (Figure 102 (a)). This shows once more the different stability of the two arrangements.

II.3.6 – Conclusion

With these results, this electrostatic deposition method has proven its viability to deposit and organize POMs periodically on surface, and very convincing STM images have been obtained. Moreover, several cross-linked characterization techniques helped to define the chemical nature of the organized molecules observed by STM on the patterned substrate, and to prove the organization at a larger scale. Also, the similarity between the H_3K^{Mo} POMs images obtained in terms of shape, heights and behavior on the surface (movement) with the STM images obtained by depositing the functionalized TOA[K^W(pyr)] POM with terminal pyridine function anchored to ZnPc molecule (see Figure 72), lean toward demonstrating that it was indeed the POMs that are observed.

However, one aspect that can still be enhanced is the protonation rate on the surface. Indeed, the Tz-C12 molecule with a triazine core is not easy to protonate and the use of strong acids such as TFA is needed. Even though in solution, the H_3K^{Mo} would likely be able to protonate one or two nitrogen atoms of the Tz-C12 molecule, when it is pi-stacked on the surface, the pKa of the Tz-C12 molecule is affected, making it more difficult to protonate. This could explain the protonation rate estimated at only 60% on surface. Thus, a new molecule, able to self-assemble on HOPG, with higher pKa could reach near to 100% protonation rate giving higher coverage rate.

This deposition method based on protonable self-assembling molecule also opens the way to various patterns to organize the POMs, by controlling the distance, the geometry or the distribution of the protonable functions on surface through the synthesis of new self-assembling molecules.

In order to investigate these possibilities, another TSB based molecule has been synthesized, incorporating pyridine rings around a phenyl core that are easier to protonate and should give a different distribution of the protonable functions on surface.

III. – New molecule as a modified-TSB-3,5 molecule with protonable group incorporating pyridine rings

The shape of this new molecule that will be called hereafter TPY-C12 displays three pyridines (Figure 103).

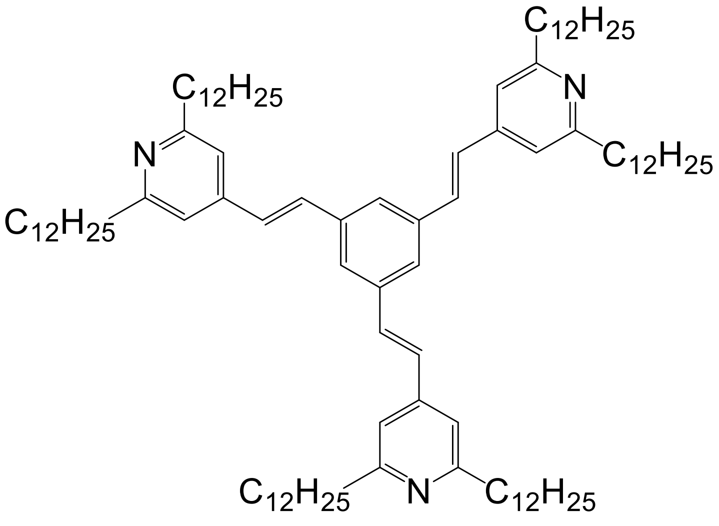

1,3,5-tris((*E*)-2-(2,6-didodecylpyridin-4-yl)vinyl)benzene

Figure 103 : Scheme of TPY-C12 molecule

As mentioned before, this molecule should induce an increase of the pKa of the protonable functions. Moreover, the distribution of these functions will be different in the final self-assembly. Indeed, this kind of molecule generally leads to hexagonal network on HOPG surface, with the “head” of each aromatic ring around the phenyl core oriented toward the pore. Thus, the pyridine function, and consequently the charges generated by their protonation, will be oriented toward the pores (Figure 104).

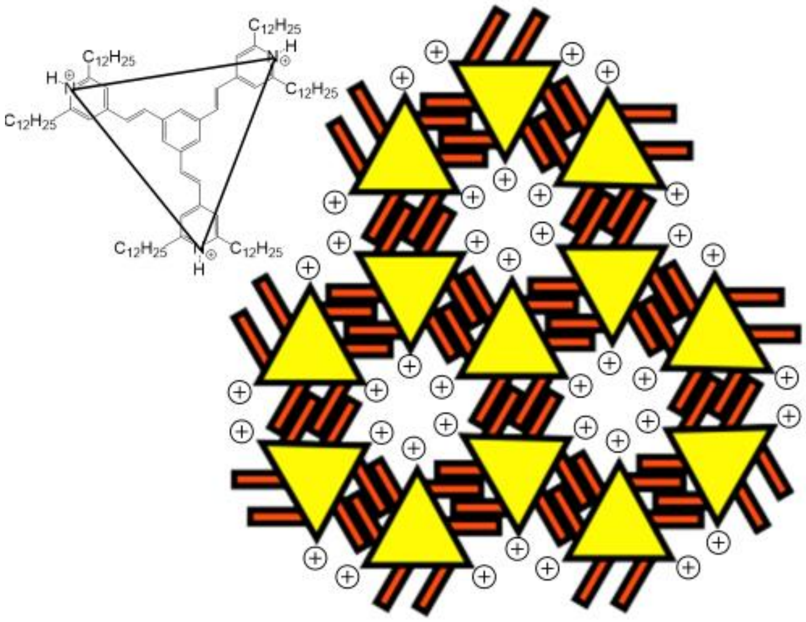

Figure 104 : Scheme of the self-assembled protonated TPY-C12 with the charges oriented inside the pores

III.1 – Synthesis of the TPY-C12 molecule

The synthesis of an aldehyde intermediate, the 2,6-didodecynepyridine-4-methanal (5), is first done starting from the bromination of the citrazinic acid using $POBr_3$. The 2,6-Dibromoisonicotinic acid (1) obtained is then reduced by borane-THF complex to give the 2,6-Dibromopyridine-4-methanol (2). Dodecyne chains are added to this product through a Sonogashira coupling reaction to form the compound (3), and then the triple carbon-carbon bonds are reduced on Pd/C to give compound (4) (Figure 105). Finally, an aldehyde is formed by a Swern oxidation to lead to compound (5) (Figure 105). The scheme of this synthesis is shown in Figure 105.

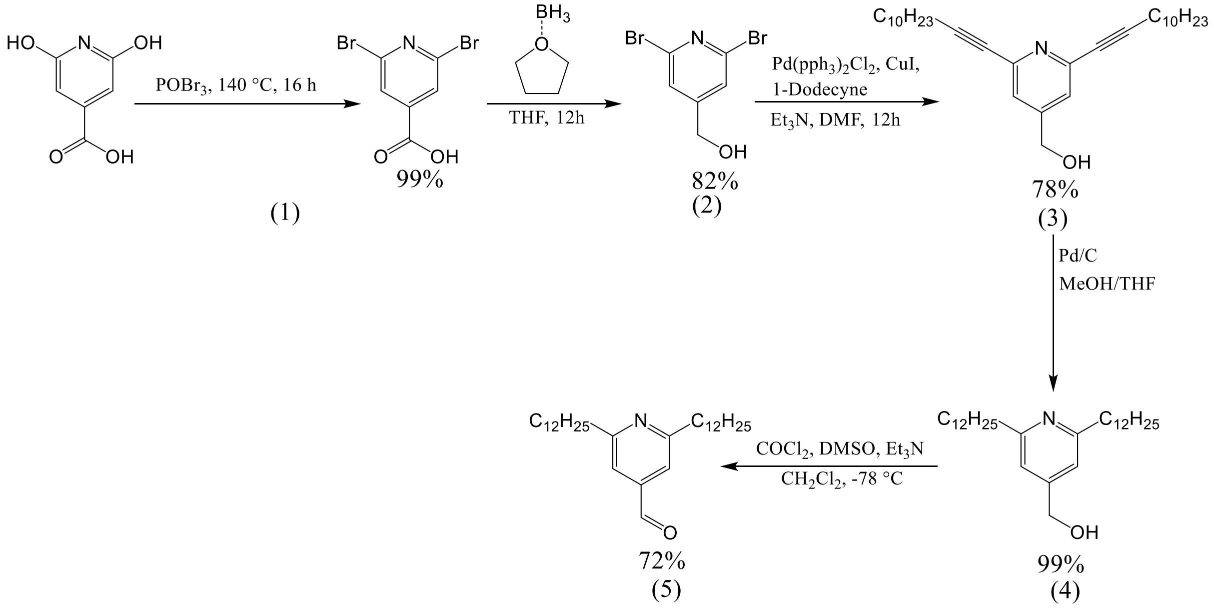

Figure 105 : Steps of the synthesis of the 2,6-didodecynepyridine-4-methanal for the synthesis of the TPY-C12 molecule

To obtain the final molecule, a coupling reaction with 1,3,5-tribromobenzene through an in-situ decarboxylation followed by a Heck coupling is attempted (Figure 106 a)). This reaction is inspired from a similar coupling reaction reported in the literature (Figure 106 b)).[266]

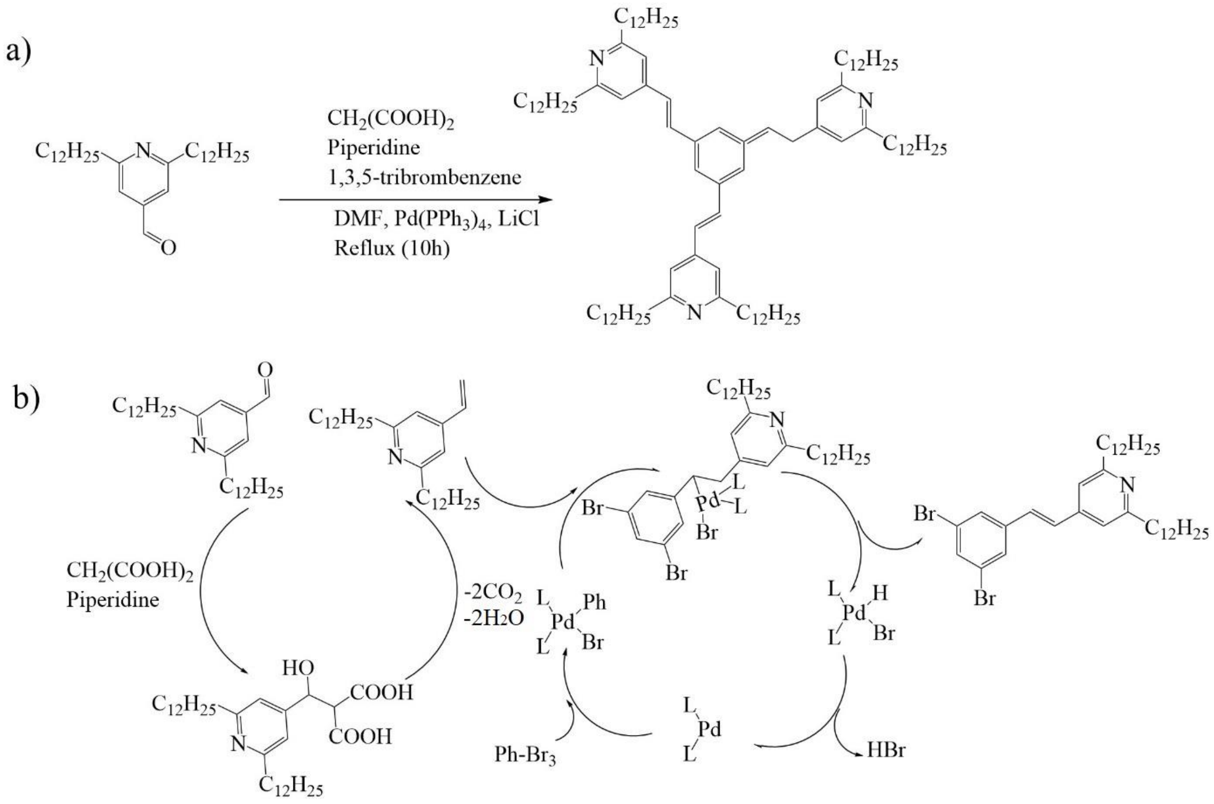

Figure 106 : scheme of (a) reagents involved in the reaction (b) the expected reaction mechanism found in the litterature[266]

The product obtained is analyzed by NMR ^{1}H, and it shows that it does not correspond to the TPY-C12 molecule. Indeed, a singlet related to the central phenyl ring of the TPY-C12 is missing (Figure 107).

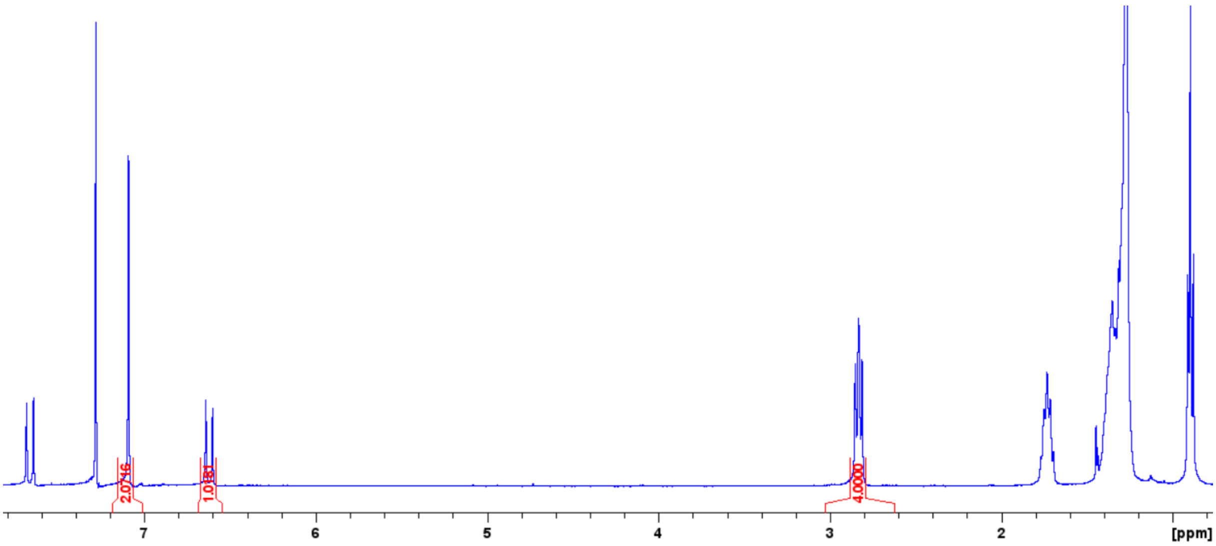

Figure 107 : NMR ^{1}H of the molecule obtained after the reaction Figure 106

After NMR ^{13}C shows a typical carboxylic acid peak, and mass spectroscopy analysis showing that the main product has a molecular mass of 486 g.mol^{-1}, the molecule obtained is resolved. It appears that the second decarboxylation expected did not occur and a carboxylic acid was formed with the mechanism proposed in in Figure 108.

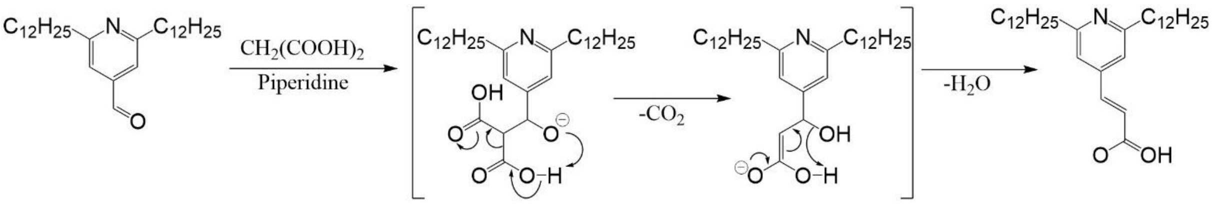

Figure 108 : Schema of the reaction and product obtained

As the reaction was carried out under basic conditions, the carboxylic acid group of the molecule is obtained deprotonated. Adding TFA to the molecule and analyzing it by NMR ^{1}H shows the apparition of the characteristic peak of the –COOH group, definitely confirming its structure (Figure 109).

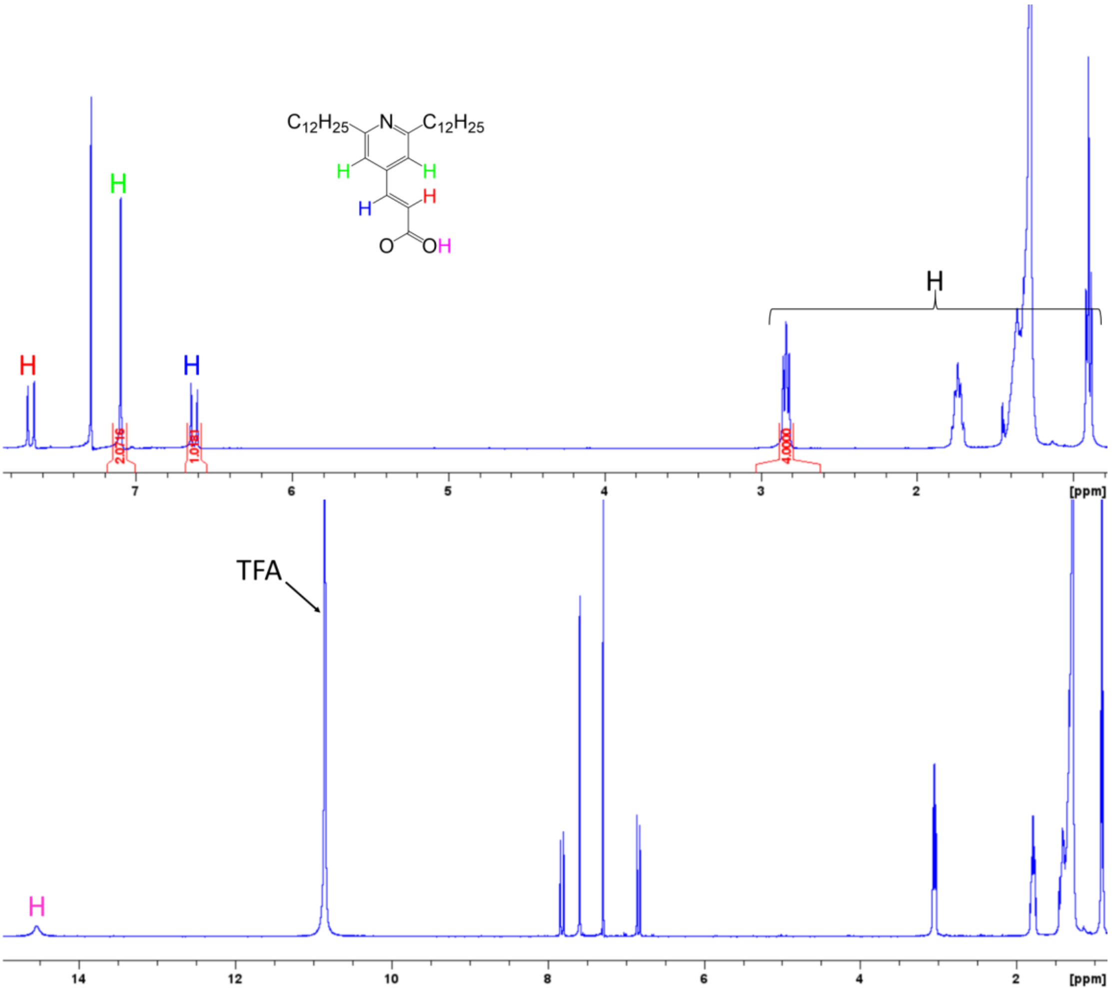

Figure 109 : : NMR 1H of the molecule obtained before (top) and after (down) protonation with TFA noticing the apparition of the carboxylic acid peak

Another attempt consisting of a Wittig-Horner reaction is then used to perform the coupling reaction (Figure 110). It required to preliminary synthesize a phosphonate intermediate (product (6), Arbuzov reaction).

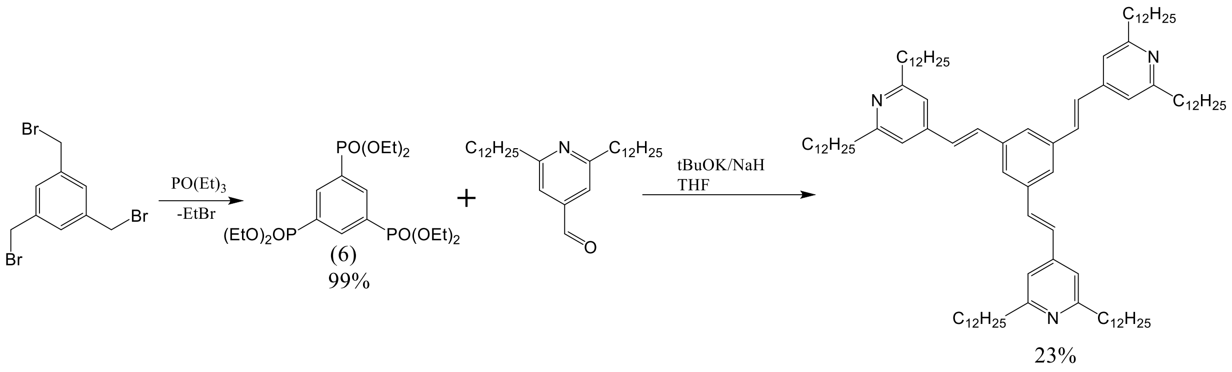

Figure 110 : Scheme of the final steps of the synthesis of TPY-C12

A purification of the raw product is attempted by flash chromatography but has failed to separate the components. Then, a recrystallization in absolute ethanol was carried out and a small quantity of the pure product was obtained. The NMR ^{1}H of the molecule before and after the purification is shown in Figure 111.

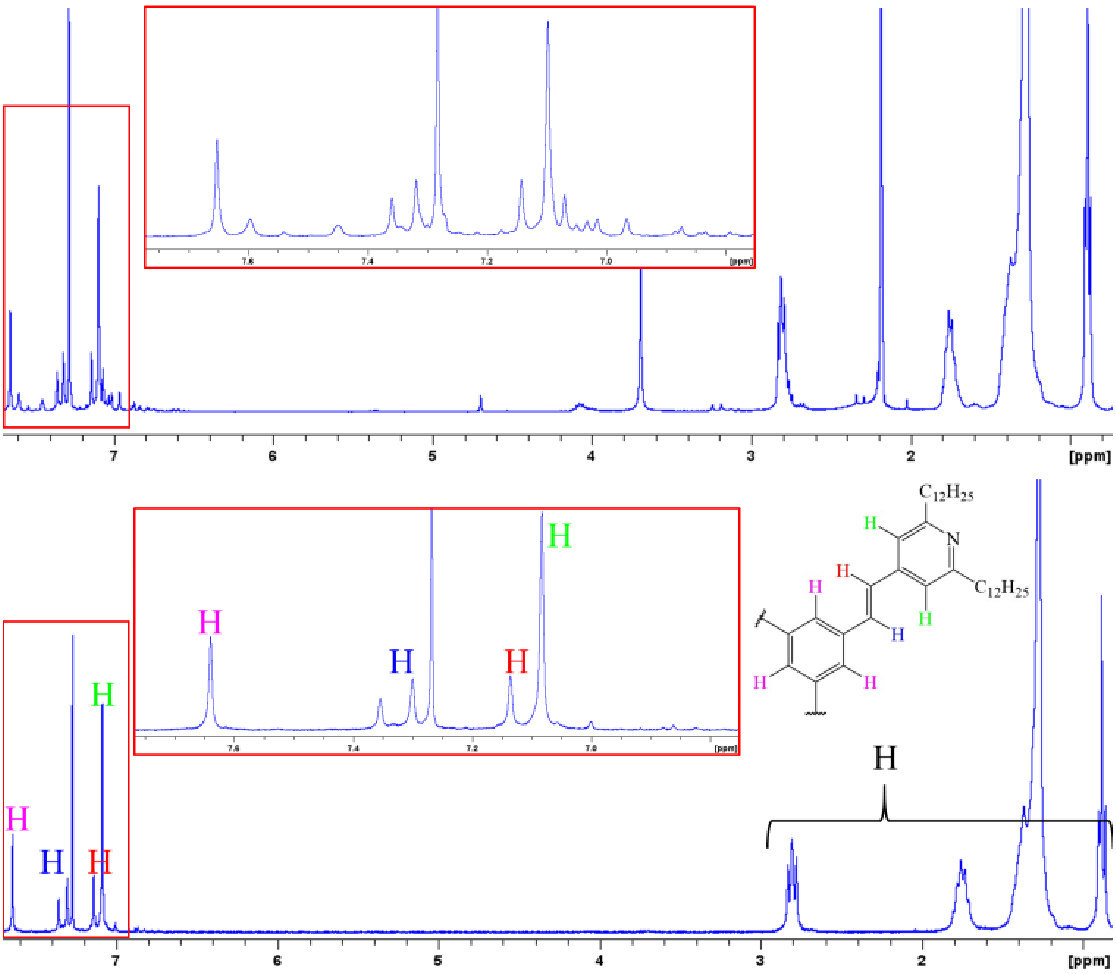

Figure 111 : NMR ^{1}H of the TPY-C12 raw product (top) and pure product (down) with the protons signals attributed

The NMR ^{1}H of the TPY-C12 shows all the expected peaks of the molecule. In the aromatic region, the singlet of the central phenyl ring at 7.65 ppm is the most deshielded signal (Figure 111, purple proton), this is due to the effect of the three electroatractive pyridine rings withdrawing electrons from it. The protons of the pyridine rings show a singlet at 7.1 ppm (Figure 111, red proton) with intensity twice the one exhibited by the protons of the phenyl ring, as expected. The large doublets of the HC=CH double bond appears at 7.33 and 7.11 ppm (Figure 111, blue and green protons respectively). The most deshielded one is attributed to the proton on alpha position to the central phenyl ring due to the mesomer effects that makes a positive charge appear on its carbon. The protons of the alkyl chains (Figure 111, black proton) exhibit the triplet of the terminal CH_3 at 0.88 ppm and the triplet on alpha position to the pyridine rings slightly deshielded at 2.81 ppm because of its proximity to the nitrogen atom of the pyridine.

The molecule is finally obtained; the next step is the characterizations in solution in order to follow its protonation.

III.2 – Characterization of the protonation of TPY-C12 in solution

The protonation of the molecule will be followed by NMR ^{1}H and UV-vis using TFA as acid and chloroform as a solvent.

III.2.1 – Characterization of the protonation of TPY-C12 by NMR ^{1}H

5 mg ($3.58*10^{-6}$ mol) of TPY-C12 are solubilized in 500 µL of deuterated chloroform. 1 to 6 equivalents of TFA are then added into small volumes of deuterated chloroform and NMR ^{1}H is performed after each addition. The results are shown in Figure 112.

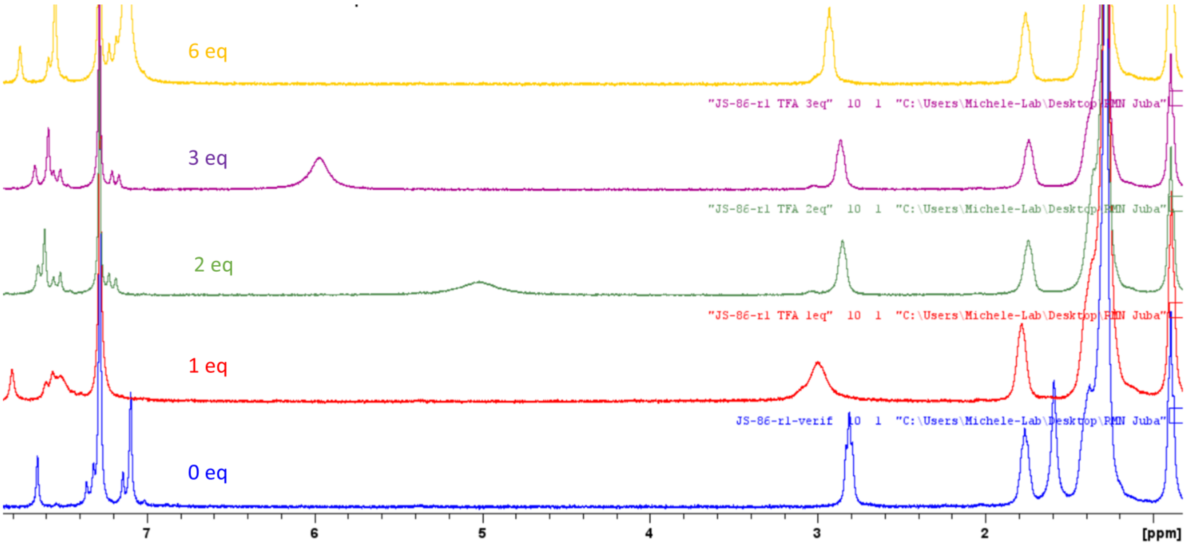

Figure 112 : NMR ^{1}H of TPY-C12 with 0 (blue) 1 (red) 2 (green) 3 (purple) and 6 (yellow) equivalents of TFA in $CDCl_3$

The effect of the addition of TFA on the NMR ^{1}H spectrum of the TPY-C12 appears clearly even after the addition of one equivalent. The most affected signals are the one of pyridine protons and the signal of the protons of the double bond (cf. Figure 111). Interestingly, the effect of the protonation is noticed also on the signal of the first and second CH_2 of the alkyl chains, showing that it occurs on the nitrogen atom of the pyridine function (cf. Figure 111). This NMR ^{1}H characterization demonstrate qualitatively the protonation of the molecule in solution.

In order to obtain more information, UV-visible spectroscopy is performed on the same system.

III.2.2 – UV-visible characterization of the protonation of TPY-C12

0.5 ml solution of TPY in chloroform at $7.16*10^{-5}$ $mol.L^{-1}$ is introduced into a UV-vis cuvette. 0 to 30 quivalents of TFA are added into small volumes of chloroform and UV spectra of the solution are recorded at each step. The results are shown in Figure 113.

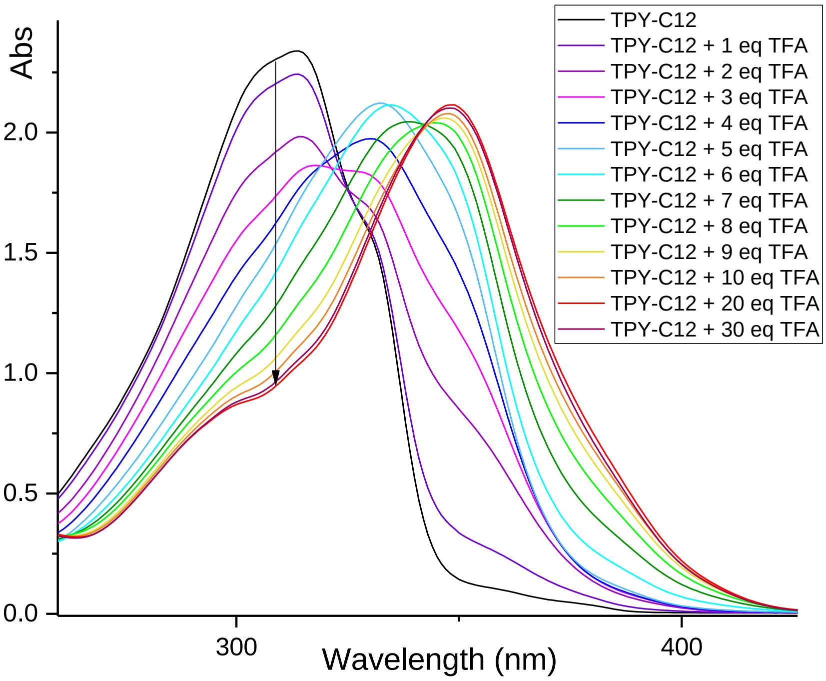

Figure 113 : UV-visible spectra of TPY-C12 with 0 to 30 equivalents of TFA in chloroform

The UV-vis spectra show an evolution right after the addition of 1 equivalent of TFA, showing that the molecule is much easier to protonate than the Tz-C12. By adding more equivalents of the acid, a decrease of the non-protonated species is observed, as shown by the reduction of the intensity of the peak at 309 nm (the arrow in Figure 113). The evolution of the spectra seems to stop after 20 equivalents of TFA with a protonated species band at 348 nm. The spectrum appears to be tricky to analyze due to intermediate species that appears between the not protonated one at 309 nm and the final molecule at 348 nm. Theoretical calculations would allow to determine the wavelength of each one of the mono, di, and tri protonated TPY-C12, and to attribute the nature of the species that absorbe at 348 nm.

This UV-visible characterization confirms that the TPY-C12 molecules can be protonated easily in solution with only 20 equivalents of TFA and can probably reach a higher protonation rate on the surface compared to the Tz-C12.

After the characterizations in solution, the molecule is characterized by STM to probe its organization.

III.3 – STM imaging of TPY-C12 on HOPG

These STM images have been made by Jan Patrick Calupitan during my thesis writing, a post-doctoral reasercher of our team involved in the project. The sample is made by depositing 10 µL solution of TPY-C12 at 10^{-4} mol.L^{-1} in toluene on HOPG. After the evaporation of the solvent 5 µL of phenyloctane are added on the surface to make STM images at the solid/liquid interface (Figure 114).

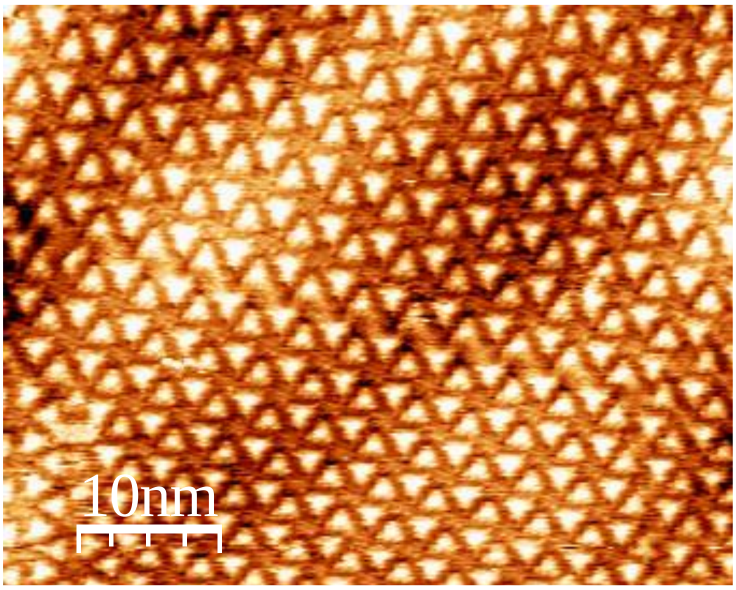

Figure 114 : STM image of TPY-C12 on HOPG at the solid/liquid interface (50 x 50 nm^2)

The self-assembling of the TPY-C12 forms honeycomb network on the surface of HOPG, the same way as TSB-C12 and Tz-C12. The principal difference noticed is the absence of herringbone assemblies. Indeed, on all the samples imaged, only hexagonal arrangements are observed. Theoretical calculation would allow understanding better this behavior.

The characterizations on this molecule did not go further as the timing of my thesis arrived to the end. However, it exhibited very interesting and promising properties and is worth to investigate for the deposition of POMs.

IV – General conclusion and perspectives

During this thesis, we investigated several approaches to organize Keggin polyoxometalates at a molecular scale on functionalized HOPG substrate. The general strategy relies on the use of intermolecular and molecule/substrate interactions. Several challenges had to be overcome, and the organization of the molecules on the surface was achieved. As a result, we have published the first paper reporting the highly organized self-assembly of POMs on a solid substrate.[210] This last part of this manuscript will conclude about this work and present some perspectives opened by the results obtained.

The first approach attempted consisted of using a functionalized POM linked to an anchor molecule through a coordination bond. The anchor was expected to drive the functionalized POM onto periodic network of pores exhibited on the surface of a functionalized HOPG substrate, through host/guest interactions led by pi-stacking. This approach has shown several challenges, starting from the formation of the coordination bond between the functionalized POM and the anchor molecule in solution due to solubility differences. Also, the equilibrium of formation of the POM-anchor species in solution contributed to making this system furthermore complex, by adding several parameters to take in account. For instance, the competition between the free anchors and the POM-anchor to occupy the pores, the optimal number of POM/anchoring molecule equivalents to use and the amount of anchored POM available at the equilibrium state. Once the POM-anchor were deposited on the functionalized HOPG surface using a binary solvent composed of chloroform/acetonitrile (70/30) to solubilize both molecules, it turned out that one of the biggest challenges of this system was the sample characterization. Indeed, there are only few techniques that can provide information about the organization rate of the molecules at different scales. Nevertheless, the use of AFM-IR, a particularly interesting technique, allowed this type of characterizations. This technique permitted a very fine analysis of the samples, leading to the observation of very thin molecular layers of around 2 nm in height and 1.5 nm-sized nanoobjets height. The latter were assumed to be the signature of the presence of isolated POM-anchor molecules on the surface. Naturally, the next challenge consisted of avoiding the aggregation phenomenon of the POM-anchor on the surface. By changing the counter ions of the POMs, it was possible to make them soluble in the same solvent as ZnPc molecule, which is the anchoring molecule, interesting results were obtained by STM. Indeed, STM image seems to show that some POM-ZnPc complexes are traped into the pores of the functionalized HOPG substrate. Thus, in order to avoid the aggregation of the POMs, the control over the POM to POM interactions by using the appropriate solvent, proved to be crucial. Moreover, this strategy seems promising toward a controlled deposition of POMs on surface, and it is worth to investigate it further.

Another approach, similar to the one described above where the POM is covalently linked to the anchor molecule was studied. This method allowed to get rid of the different solubilities of the POM and the anchoring molecule, and to facilitate the interpretation of STM images, as filled pores on the surface will necessarily mean the deposition of the POMs. Unfortunately, only a few experiments were performed on this system at the beginning of my thesis, and the deposition was tested using a binary solvent made of chloroform/acetonitrile (70/30) where the solubility of the POM is not optimum. As a result, no POMs were found to be trapped by the functionalized HOPG surface. Several things could be tested concerning this approach, such as changing the nature of the counter ion both to increase the solubility in solvents like toluene or chloroform (T_{eb}, wetting on HOPG…etc.) and to decrease the aggregation phenomenon. Then, along with the use of a more appropriate anchor molecule with more affinity with the pores (better pi-stacking) such as coronene or hexabenzocoronene could give better results. Interestingly, the deposition of this POM covalently linked to the anchor molecule on a freshly cleaved HOPG substrate led to the formation of a thin film on the surface, preventing the aggregation phenomenon. This open a way for the synthesis of self-assembling functionalized POMs able to form a layer of periodically organized molecules.

The last approach consisted of modifying the chemical nature of the assembling molecule to capture the POMs on specific areas of the self-assembled network. It is based on the synthesis of a TSB-like molecule carrying a protonable function periodically distributed on HOPG substrate after the self-assembling. Keggin heteropolyacids were used to protonate these functions, and they remained stuck to it as a counter ion thanks to electrostatic interactions. This system, unlike the previous ones, was analyzed by different techniques. For instance, with XPS due to the formation of a new chemical species on the surface after the POMs deposition, that could be probed and quantified to know the deposition rate. This method allowed demonstrating undoubtedly the deposition and periodic organization of POMs on the functionalized HOPG substrate, with 60% coverage rate. In order to improve the coverage rate, another TSB-like molecule able to self-assemble on HOPG was synthesized carrying more basic functions that would allow reaching a higher on surface protonation rate, and thus, a higher deposition rate. This molecule was characterized in solution and exhibited suitable protonation properties. Besides, from the STM images, the network formed by these molecules on HOPG was shown to be similar to that formed by unmodified TSB molecules. Next characterizations on this molecule could be the protonation on surface, first using an acid, following the same method of immersion in an HCl solution in acetonitrile for example. Then, it would be interesting to deposit the molecule already protonated and probe its arrangement by STM. One equivalent of a strong acid could be used to protonate one pyridine group only. Then, precipitate the protonated molecule and deposit it in toluene or chloroform on HOPG substrate. The same experiment could be done with a molecule protonated twice and three times. A deposition of Keggin heteropolyacids should be investigated as well.

Finally, one particular point noticed during this work is the difficulty for STM imaging of POMs under ambient conditions. As stated previously, STM imaging under ambient conditions on such system presents challenges. One of the difficulties arises from the significant electric field generated between the STM tip and the molecules, which can reach several GV.m^{-1} and may disrupt the Tz-C12/POM ionic layer. Thus, the use of low temperature UHV STM would allow to fixe the molecules and reduce their movements on the surface, as well as to work under milder conditions (without the disturbances of the molecules present in air such as H_2O) to obtain higher quality images. UHV LT STM also allows to perform STS measurements and to study the electronic properties of the POMs, then to try to switch the redox state of the POMs organized on the surface with the STM tip, and measure IV curves of an isolated POM, the final aim being to perform a reading/writing operations on the POMs using the STM tip to show the potential of these assemblies in the field molecular of data storage materials.

V – References

(1) Anžel, A.; Heider, D.; Hattab, G. The Visual Story of Data Storage: From Storage Properties to User Interfaces. *Comput. Struct. Biotechnol. J.* **2021**, *19*, 4904–4918. https://doi.org/10.1016/j.csbj.2021.08.031.

(2) *Handbook of Microlithography, Micromachining, and Microfabrication*; Rai-Choudhury, P., Ed.; IEE materials and devices series; SPIE Optical Engineering Press ; Institution of Electrical Engineers: Bellingham, Wash., USA : London, UK, 1997.

(3) Li, S.; Chu, D. A Review of Thin-Film Transistors/Circuits Fabrication with 3D Self-Aligned Imprint Lithography. *Flex. Print. Electron.* **2017**, *2* (1), 013002. https://doi.org/10.1088/2058-8585/aa5c6d.

(4) Koo, N.; Schmidt, M.; Mollenhauer, T.; Moormann, C.; Schlachter, F.; Kurz, H. Fabrication of MOSFETs by 3D Soft UV-Nanoimprint. *Microelectron. Eng.* **2012**, *97*, 85–88. https://doi.org/10.1016/j.mee.2012.05.015.

(5) *Samsung Electronics Starts Producing Industry's First 16-Gigabit GDDR6 for Advanced Graphics Systems*. https://news.samsung.com/global/samsung-electronics-starts-producing-industrys-first-16-gigabit-gddr6-for-advanced-graphics-systems (accessed 2023-05-01).

(6) Sze, S. M.; Lee, M. K. *Semiconductor Devices, Physics and Technology*, 3rd ed.; Wiley: Hoboken, N.J, 2012.

(7) Siu, C. Introduction to MOSFETs. In *Electronic Devices, Circuits, and Applications*; Springer International Publishing: Cham, 2022; pp 65–84. https://doi.org/10.1007/978-3-030-80538-8_5.

(8) Adams, J. *Mastering Electronics Workbench*, Version 5 and Multisim version 6.; McGraw-Hill: New York, 2001.

(9) Neamen, D. A. *Semiconductor Physics and Devices: Basic Principles*, 4th ed.; McGraw-Hill: New York, NY, 2012.

(10) *What are Enhancement-mode MOSFETs? - Technical Articles*. https://eepower.com/technical-articles/what-are-enhancement-mode-mosfets/ (accessed 2023-08-22).

(11) Cavin, R. K.; Lugli, P.; Zhirnov, V. V. Science and Engineering Beyond Moore's Law. *Proc. IEEE* **2012**, *100* (Special Centennial Issue), 1720–1749. https://doi.org/10.1109/JPROC.2012.2190155.

(12) *3nm Technology - Taiwan Semiconductor Manufacturing Company Limited*. http://www.tsmc.com/english/dedicatedFoundry/technology/logic/l_3nm (accessed 2023-05-24).

(13) Moore, G. E. Cramming More Components Onto Integrated Circuits. *Proc. IEEE* **1998**, *86* (1), 82–85. https://doi.org/10.1109/JPROC.1998.658762.

(14) *What is Moore's Law? – Is Moore's Law Finally Ending? | Synopsys*. https://www.synopsys.com/glossary/what-is-moores-law.html (accessed 2023-08-22).

(15) Salahuddin, S.; Ni, K.; Datta, S. The Era of Hyper-Scaling in Electronics. *Nat. Electron.* **2018**, *1* (8), 442–450. https://doi.org/10.1038/s41928-018-0117-x.

(16) *The future of data storage must handle heavy volume | TechTarget*. Storage. https://www.techtarget.com/searchstorage/feature/The-future-of-data-storage-must-handle-heavy-volume (accessed 2023-05-01).

(17) Kargar, S.; Nawab, F. Challenges and Future Directions for Energy, Latency, and Lifetime Improvements in NVMs. *Distrib. Parallel Databases* **2022**. https://doi.org/10.1007/s10619-022-07421-x.

(18) *Data Centres and Data Transmission Networks – Analysis*. IEA. https://www.iea.org/reports/data-centres-and-data-transmission-networks (accessed 2023-05-28).

(19) *3D NAND fash and FeFET in the data storage roadmap | imec*. https://www.imec-int.com/en/articles/role-3d-nand-flash-and-fefet-data-storage-roadmap (accessed 2023-05-27).

(20) Liao, F.; Guo, Z.; Wang, Y.; Xie, Y.; Zhang, S.; Sheng, Y.; Tang, H.; Xu, Z.; Riaud, A.; Zhou, P.; Wan, J.; Fuhrer, M. S.; Jiang, X.; Zhang, D. W.; Chai, Y.; Bao, W. High-Performance Logic and Memory Devices Based on a Dual-Gated MoS2 Architecture. *ACS Appl. Electron. Mater.* **2020**, *2* (1), 111–119. https://doi.org/10.1021/acsaelm.9b00628.

(21) Huang, X.; Liu, C.; Zhou, P. 2D Semiconductors for Specific Electronic Applications: From Device to System. *Npj 2D Mater. Appl.* **2022**, *6* (1), 1–19. https://doi.org/10.1038/s41699-022-00327-3.

(22) Naqi, M.; Kwon, N.; Jung, S. H.; Pujar, P.; Cho, H. W.; Cho, Y. I.; Cho, H. K.; Lim, B.; Kim, S. High-Performance Non-Volatile InGaZnO Based Flash Memory Device Embedded with a Monolayer Au Nanoparticles. *Nanomaterials* **2021**, *11* (5), 1101. https://doi.org/10.3390/nano11051101.

(23) Doricchi, A.; Platnich, C. M.; Gimpel, A.; Horn, F.; Earle, M.; Lanzavecchia, G.; Cortajarena, A. L.; Liz-Marzán, L. M.; Liu, N.; Heckel, R.; Grass, R. N.; Krahne, R.; Keyser, U. F.; Garoli, D. Emerging Approaches to DNA Data Storage: Challenges and Prospects. *ACS Nano* **2022**, *16* (11), 17552–17571. https://doi.org/10.1021/acsnano.2c06748.

(24) Cafferty, B. J.; Ten, A. S.; Fink, M. J.; Morey, S.; Preston, D. J.; Mrksich, M.; Whitesides, G. M. Storage of Information Using Small Organic Molecules. *ACS Cent. Sci.* **2019**, *5* (5), 911–916. https://doi.org/10.1021/acscentsci.9b00210.

(25) *Single-molecule magnet breaks performance records*. Chemical & Engineering News. https://cen.acs.org/articles/95/i35/Single-molecule-magnet-breaks-performance.html (accessed 2023-05-30).

(26) Li, C.; Fan, W.; Lei, B.; Zhang, D.; Han, S.; Tang, T.; Liu, X.; Liu, Z.; Asano, S.; Meyyappan, M.; Han, J.; Zhou, C. Multilevel Memory Based on Molecular Devices. *Appl. Phys. Lett.* **2004**, *84* (11), 1949–1951. https://doi.org/10.1063/1.1667615.

(27) Gaita-Ariño, A.; Luis, F.; Hill, S.; Coronado, E. Molecular Spins for Quantum Computation. *Nat. Chem.* **2019**, *11* (4), 301–309. https://doi.org/10.1038/s41557-019-0232-y.

(28) *Molecular Memory: Small Molecules Could Be the Future of Data Storage*. Informatics from Technology Networks. http://www.technologynetworks.com/informatics/news/molecular-memory-small-molecules-could-be-the-future-of-data-storage-318986 (accessed 2023-05-28).

(29) Lörtscher, E. Wiring Molecules into Circuits. *Nat. Nanotechnol.* **2013**, *8* (6), 381–384. https://doi.org/10.1038/nnano.2013.105.

(30) Peurifoy, S. R. Organic Electronics Enhanced via Molecular Contortion, Columbia University, 2020. https://doi.org/10.7916/d8-v1cz-6v61.

(31) Fairlamb, I. J. S.; Dickinson, J. M. 1.22 - Ions, Radicals, Carbenes, and Other Monocoordinated Systems. In *Comprehensive Organic Functional Group Transformations II*; Katritzky, A. R., Taylor, R. J. K., Eds.; Elsevier: Oxford, 2005; pp 1177–1259. https://doi.org/10.1016/B0-08-044655-8/00022-2.

(32) Katsonis, N.; Lubomska, M.; Pollard, M. M.; Feringa, B. L.; Rudolf, P. Synthetic Light-Activated Molecular Switches and Motors on Surfaces. *Prog. Surf. Sci.* **2007**, *82* (7), 407–434. https://doi.org/10.1016/j.progsurf.2007.03.011.

(33) Fu, H.; Zhu, X.; Li, P.; Li, M.; Yang, L.; Jia, C.; Guo, X. Recent Progress in Single-Molecule Transistors: Their Designs, Mechanisms and Applications. *J. Mater. Chem. C* **2022**, *10* (7), 2375–2389. https://doi.org/10.1039/D1TC04079K.

(34) Quan, L. N.; Kang, J.; Ning, C.-Z.; Yang, P. Nanowires for Photonics. *Chem. Rev.* **2019**, *119* (15), 9153–9169. https://doi.org/10.1021/acs.chemrev.9b00240.

(35) Sukegawa, J.; Schubert, C.; Zhu, X.; Tsuji, H.; Guldi, D. M.; Nakamura, E. Electron Transfer through Rigid Organic Molecular Wires Enhanced by Electronic and Electron–Vibration Coupling. *Nat. Chem.* **2014**, *6* (10), 899–905. https://doi.org/10.1038/nchem.2026.

(36) Irie, M. Photochromism: Memories and SwitchesIntroduction. *Chem. Rev.* **2000**, *100* (5), 1683–1684. https://doi.org/10.1021/cr980068l.

(37) Sekkat, Z.; Knoll, W. *Photoreactive Organic Thin Films*; Elsevier, 2002.

(38) Wu, P.; Dharmadhikari, B.; Patra, P.; Xiong, X. Rotaxane Nanomachines in Future Molecular Electronics. *Nanoscale Adv.* **2022**, *4* (17), 3418–3461. https://doi.org/10.1039/D2NA00057A.

(39) Bailey, B. *Product Lifecycle Management For Semiconductors*. Semiconductor Engineering. https://semiengineering.com/product-lifecycle-management-for-semiconductors/ (accessed 2023-05-25).

(40) Ohtake, T. Bottom-up Approaches for Material and Device Designing Using Practical Aspects of Self-Assembled Molecular Architectures. *Mol. Syst. Des. Eng.* **2018**, *3* (5), 804–818. https://doi.org/10.1039/C8ME00020D.

(41) Jung, W.-B.; Jang, S.; Cho, S.-Y.; Jeon, H.-J.; Jung, H.-T. Recent Progress in Simple and Cost-Effective Top-Down Lithography for ≈10 Nm Scale Nanopatterns: From Edge Lithography to Secondary Sputtering Lithography. *Adv. Mater.* **2020**, *32* (35), 1907101. https://doi.org/10.1002/adma.201907101.

(42) Mayer, J. W.; Lau, S. S. *Electronic Materials Science: For Integrated Circuits in Si and GaAs*; Macmillan, 1990.

(43) Madou, M. J. *Fundamentals of Microfabrication: The Science of Miniaturization, Second Edition*, 2nd ed.; CRC Press: Boca Raton, 2017. https://doi.org/10.1201/9781482274004.

(44) Arora, V. K. *Nanoelectronics: Quantum Engineering of Low-Dimensional Nanoensembles*; 2015; p 401. https://doi.org/10.1201/b18131.

(45) *ASML EUV lithography systems*. https://www.asml.com/en/products/euv-lithography-systems (accessed 2023-04-13).

(46) Stan, M. R.; Franzon, P. D.; Goldstein, S. C.; Lach, J. C.; Ziegler, M. M. Molecular Electronics: From Devices and Interconnect to Circuits and Architecture. *Proc. IEEE* **2003**, *91* (11), 1940–1957. https://doi.org/10.1109/JPROC.2003.818327.

(47) Nánai, L.; Benk?, Z. I.; Letfullin, R. R.; George, T. F. Laser-Matter Interactions: Nanostructures, Fabrication and Characterization. In *Computational Studies of New Materials II*; WORLD SCIENTIFIC, 2011; pp 1–36. https://doi.org/10.1142/9789814287197_0001.

(48) Teo, B. K.; Sun, X. H. From Top-Down to Bottom-Up to Hybrid Nanotechnologies: Road to Nanodevices. *J. Clust. Sci.* **2006**, *17* (4), 529–540. https://doi.org/10.1007/s10876-006-0086-5.

(49) Characterization Techniques for Molecular Electronics. In *Molecular-Scale Electronics*; Guo, X., Xiang, D., Li, Y., Eds.; Wiley, 2020; pp 157–207. https://doi.org/10.1002/9783527818914.ch7.

(50) SCHEER, E.; CUEVAS, J. C. *Molecular Electronics: An Introduction to Theory and Experiment*, 2nd edition.; WSPC: New Jersey, 2017.

(51) Petty, M. C.; Nagase, T.; Suzuki, H.; Naito, H. Molecular Electronics. In *Springer Handbook of Electronic and Photonic Materials*; Kasap, S., Capper, P., Eds.; Springer Handbooks; Springer International Publishing: Cham, 2017; pp 1–1. https://doi.org/10.1007/978-3-319-48933-9_51.

(52) Griffiths, R.-R.; L. Greenfield, J.; R. Thawani, A.; R. Jamasb, A.; B. Moss, H.; Bourached, A.; Jones, P.; McCorkindale, W.; A. Aldrick, A.; J. Fuchter, M.; A. Lee, A. Data-Driven Discovery of Molecular Photoswitches with Multioutput Gaussian Processes. *Chem. Sci.* **2022**, *13* (45), 13541–13551. https://doi.org/10.1039/D2SC04306H.

(53) Amar, A.; Savel, P.; Akdas-Kilig, H.; Katan, C.; Meghezzi, H.; Boucekkine, A.; Malval, J.-P.; Fillaut, J.-L. Photoisomerisation in Aminoazobenzene-Substituted Ruthenium(II) Tris(Bipyridine) Complexes: Influence of the Conjugation Pathway. *Chem. – Eur. J.* **2015**, *21* (22), 8262–8270. https://doi.org/10.1002/chem.201406002.

(54) Jensen, P. W. K.; Kristensen, L. B.; Lavigne, C.; Aspuru-Guzik, A. Toward Quantum Computing with Molecular Electronics. *J. Chem. Theory Comput.* **2022**, *18* (6), 3318–3326. https://doi.org/10.1021/acs.jctc.2c00162.

(55) Sessoli, R. Toward the Quantum Computer: Magnetic Molecules Back in the Race. *ACS Cent. Sci.* **2015**, *1* (9), 473–474. https://doi.org/10.1021/acscentsci.5b00384.

(56) Moreno-Pineda, E.; Godfrin, C.; Balestro, F.; Wernsdorfer, W.; Ruben, M. Molecular Spin Qudits for Quantum Algorithms. *Chem. Soc. Rev.* **2018**, *47* (2), 501–513. https://doi.org/10.1039/C5CS00933B.

(57) Moseley, D. H.; Stavretis, S. E.; Thirunavukkuarasu, K.; Ozerov, M.; Cheng, Y.; Daemen, L. L.; Ludwig, J.; Lu, Z.; Smirnov, D.; Brown, C. M.; Pandey, A.; Ramirez-Cuesta, A. J.; Lamb, A. C.; Atanasov, M.; Bill, E.; Neese, F.; Xue, Z.-L. Spin–Phonon Couplings in Transition Metal Complexes with Slow Magnetic Relaxation. *Nat. Commun.* **2018**, *9* (1), 2572. https://doi.org/10.1038/s41467-018-04896-0.

(58) Dorn, M.; Hunger, D.; Förster, C.; Naumann, R.; van Slageren, J.; Heinze, K. Towards Luminescent Vanadium(II) Complexes with Slow Magnetic Relaxation and Quantum Coherence. *Chem. – Eur. J.* **2023**, *29* (9), e202202898. https://doi.org/10.1002/chem.202202898.

(59) Govia, L. C. G.; Lingenfelter, A.; Clerk, A. A. Stabilizing Two-Qubit Entanglement by Mimicking a Squeezed Environment. *Phys. Rev. Res.* **2022**, *4* (2), 023010. https://doi.org/10.1103/PhysRevResearch.4.023010.

(60) Loft, N. J. S.; Kjaergaard, M.; Kristensen, L. B.; Andersen, C. K.; Larsen, T. W.; Gustavsson, S.; Oliver, W. D.; Zinner, N. T. Quantum Interference Device for Controlled Two-Qubit Operations. *Npj Quantum Inf.* **2020**, *6* (1), 1–9. https://doi.org/10.1038/s41534-020-0275-3.

(61) RAJARAMAN, V.; ADABALA, N. *FUNDAMENTALS OF COMPUTERS*; PHI Learning Pvt. Ltd., 2014.

(62) Mandviwalla, A.; Ohshiro, K.; Ji, B. Implementing Grover's Algorithm on the IBM Quantum Computers. In *2018 IEEE International Conference on Big Data (Big Data)*; 2018; pp 2531–2537. https://doi.org/10.1109/BigData.2018.8622457.

(63) Tanttu, T.; Lim, W. H.; Huang, J. Y.; Stuyck, N. D.; Gilbert, W.; Su, R. Y.; Feng, M.; Cifuentes, J. D.; Seedhouse, A. E.; Seritan, S. K.; Ostrove, C. I.; Rudinger, K. M.; Leon, R. C. C.; Huang, W.; Escott, C. C.; Itoh, K. M.; Abrosimov, N. V.; Pohl, H.-J.; Thewalt, M. L. W.; Hudson, F. E.; Blume-Kohout, R.; Bartlett, S. D.; Morello, A.; Laucht, A.; Yang, C. H.; Saraiva, A.; Dzurak, A. S. Stability of High-Fidelity Two-Qubit Operations in Silicon. arXiv March 7, 2023. https://doi.org/10.48550/arXiv.2303.04090.

(64) Soe, W.-H.; Manzano, C.; Renaud, N.; de Mendoza, P.; De Sarkar, A.; Ample, F.; Hliwa, M.; Echavarren, A. M.; Chandrasekhar, N.; Joachim, C. Manipulating Molecular Quantum States with Classical Metal Atom Inputs: Demonstration of a Single Molecule NOR Logic Gate. *ACS Nano* **2011**, *5* (2), 1436–1440. https://doi.org/10.1021/nn1033899.

(65) Lavroff, R. H.; Pennington, D. L.; Hua, A. S.; Li, B. Y.; Williams, J. A.; Alexandrova, A. N. Recent Innovations in Solid-State and Molecular Qubits for Quantum Information Applications. *J. Phys. Chem. Lett.* **2021**, *12* (44), 10742–10745. https://doi.org/10.1021/acs.jpclett.1c03269.

(66) Zadrozny, J. M.; Niklas, J.; Poluektov, O. G.; Freedman, D. E. Millisecond Coherence Time in a Tunable Molecular Electronic Spin Qubit. *ACS Cent. Sci.* **2015**, *1* (9), 488–492. https://doi.org/10.1021/acscentsci.5b00338.

(67) Baldoví, J. J.; Cardona-Serra, S.; Clemente-Juan, J. M.; Coronado, E.; Gaita-Ariño, A.; Prima-García, H. Coherent Manipulation of Spin Qubits Based on Polyoxometalates: The Case of the Single Ion Magnet [GdW30P5O110]14−. *Chem. Commun.* **2013**, *49* (79), 8922. https://doi.org/10.1039/c3cc44838j.

(68) Liu, Z.; Wang, Y.-X.; Fang, Y.-H.; Qin, S.-X.; Wang, Z.-M.; Jiang, S.-D.; Gao, S. Electric Field Manipulation Enhanced by Strong Spin-Orbit Coupling: Promoting Rare-Earth Ions as Qubits. *Natl. Sci. Rev.* **2020**, *7* (10), 1557–1563. https://doi.org/10.1093/nsr/nwaa148.

(69) Reddy, I. R.; Oppeneer, P. M.; Tarafder, K. Interfacial Spin Manipulation of Nickel-Quinonoid Complex Adsorbed on Co(001) Substrate. *Magnetochemistry* **2019**, *5* (1), 2. https://doi.org/10.3390/magnetochemistry5010002.

(70) Ariciu, A.-M.; Woen, D. H.; Huh, D. N.; Nodaraki, L. E.; Kostopoulos, A. K.; Goodwin, C. A. P.; Chilton, N. F.; McInnes, E. J. L.; Winpenny, R. E. P.; Evans, W. J.; Tuna, F. Engineering Electronic Structure to Prolong Relaxation Times in Molecular Qubits by Minimising Orbital Angular Momentum. *Nat. Commun.* **2019**, *10* (1), 3330. https://doi.org/10.1038/s41467-019-11309-3.

(71) Bertaina, S.; Gambarelli, S.; Mitra, T.; Tsukerblat, B.; Müller, A.; Barbara, B. Quantum Oscillations in a Molecular Magnet. *Nature* **2008**, *453* (7192), 203–206. https://doi.org/10.1038/nature06962.

(72) Amoza, M.; Gómez-Coca, S.; Ruiz, E. Magnetic Anisotropy in Yb ^{III} Complex Candidates for Molecular Qubits: A Theoretical Analysis. *Phys. Chem. Chem. Phys.* **2021**, *23* (3), 1976–1983. https://doi.org/10.1039/D0CP05422D.

(73) Zhu, H.; Li, Q. Novel Molecular Non-Volatile Memory: Application of Redox-Active Molecules. *Appl. Sci.* **2016**, *6* (1), 7. https://doi.org/10.3390/app6010007.

(74) Dixon, I. M.; Rat, S.; Sournia-Saquet, A.; Molnár, G.; Salmon, L.; Bousseksou, A. On the Spin-State Dependence of Redox Potentials of Spin Crossover Complexes. *Inorg. Chem.* **2020**, *59* (24), 18402–18406. https://doi.org/10.1021/acs.inorgchem.0c03043.

(75) Watanabe, E.; Zhao, W.; Sugahara, A.; Mortemard de Boisse, B.; Lander, L.; Asakura, D.; Okamoto, Y.; Mizokawa, T.; Okubo, M.; Yamada, A. Redox-Driven Spin Transition in a Layered Battery Cathode Material. *Chem. Mater.* **2019**, *31* (7), 2358–2365. https://doi.org/10.1021/acs.chemmater.8b04775.

(76) Busche, C.; Vilà-Nadal, L.; Yan, J.; Miras, H. N.; Long, D.-L.; Georgiev, V. P.; Asenov, A.; Pedersen, R. H.; Gadegaard, N.; Mirza, M. M.; Paul, D. J.; Poblet, J. M.; Cronin, L. Design and Fabrication of Memory Devices Based on Nanoscale Polyoxometalate Clusters. *Nature* **2014**, *515* (7528), 545–549. https://doi.org/10.1038/nature13951.

(77) Zhu, C.; Ji, X.; You, D.; Chen, T. L.; Mu, A. U.; Barker, K. P.; Klivansky, L. M.; Liu, Y.; Fang, L. Extraordinary Redox Activities in Ladder-Type Conjugated Molecules Enabled by B ← N Coordination-Promoted Delocalization and Hyperconjugation. *J. Am. Chem. Soc.* **2018**, *140* (51), 18173–18182. https://doi.org/10.1021/jacs.8b11337.

(78) Lindsey, J. S.; Bocian, D. F. Molecules for Charge-Based Information Storage. *Acc. Chem. Res.* **2011**, *44* (8), 638–650. https://doi.org/10.1021/ar200107x.

(79) Espinoza, E. M.; Clark, J. A.; Soliman, J.; Derr, J. B.; Morales, M.; Vullev, V. I. Practical Aspects of Cyclic Voltammetry: How to Estimate Reduction Potentials When Irreversibility Prevails. *J. Electrochem. Soc.* **2019**, *166* (5), H3175–H3187. https://doi.org/10.1149/2.0241905jes.

(80) Dai, Y.; Xie, Z.; Bao, M.; Liu, C.; Su, Y. Multiple Stable Redox States and Tunable Ground States *via* the Marriage of Viologens and Chichibabin's Hydrocarbon. *Chem. Sci.* **2023**, *14* (13), 3548–3553. https://doi.org/10.1039/D3SC00102D.

(81) Zhu, H.; Li, Q.; Zhu, H.; Li, Q. *Redox-Active Molecules for Novel Nonvolatile Memory Applications*; IntechOpen, 2017. https://doi.org/10.5772/intechopen.68726.

(82) Yan, Y.; Robinson, S. G.; Vaid, T. P.; Sigman, M. S.; Sanford, M. S. Simultaneously Enhancing the Redox Potential and Stability of Multi-Redox Organic Catholytes by Incorporating Cyclopropenium Substituents. *J. Am. Chem. Soc.* **2021**, *143* (33), 13450–13459. https://doi.org/10.1021/jacs.1c07237.

(83) Casañ-Pastor, N.; Gómez-Romero, P. Polyoxometalates: From Inorganic Chemistry to Materials Science. *Front. Biosci.-Landmark* **2004**, *9* (2), 1759–1770. https://doi.org/10.2741/1365.

(84) Yang, L.; Lei, J.; Fan, J.; Yuan, R.; Zheng, M.; Chen, J.; Dong, Q. The Intrinsic Charge Carrier Behaviors and Applications of Polyoxometalate Clusters Based Materials. *Adv. Mater.* **2021**, *33* (50), 2005019. https://doi.org/10.1002/adma.202005019.

(85) Baldoví, J. J.; Cardona-Serra, S.; Gaita-Ariño, A.; Coronado, E. Design of Magnetic Polyoxometalates for Molecular Spintronics and as Spin Qubits. In *Advances in Inorganic Chemistry*; Elsevier, 2017; Vol. 69, pp 213–249. https://doi.org/10.1016/bs.adioch.2016.12.003.

(86) Huez, C.; Guérin, D.; Lenfant, S.; Volatron, F.; Calame, M.; Perrin, M. L.; Proust, A.; Vuillaume, D. Correction: Redox-Controlled Conductance of Polyoxometalate Molecular Junctions. *Nanoscale* **2023**, *15* (1), 387–387. https://doi.org/10.1039/D2NR90231A.

(87) Gumerova, N. I.; Rompel, A. Synthesis, Structures and Applications of Electron-Rich Polyoxometalates. *Nat. Rev. Chem.* **2018**, *2* (2), 1–20. https://doi.org/10.1038/s41570-018-0112.

(88) Rathee, B.; Wati, M.; Sindhu, R.; Sindhu, S. Review of Some Applications of Polyoxometalates. *Orient. J. Chem.* **2022**, *38* (2), 327–335.

(89) d, R. S. B. de los A. *Extractos De Las Juntas Generales Celebradas Por La Real Sociedad Bascongada De Los Amigos Del País En La Villa De Vergara Por Septiembre De 1773*; Nabu Press, 2011.

(90) Berzelius, J. J. Beitrag Zur Näheren Kenntniss Des Molybdäns. *Ann. Phys.* **1826**, *82* (4), 369–392. https://doi.org/10.1002/andp.18260820402.

(91) Keggin, J. F. Structure of the Molecule of 12-Phosphotungstic Acid. *Nature* **1933**, *131* (3321), 908–909. https://doi.org/10.1038/131908b0.

(92) Keggin, J. F.; Bragg, W. L. The Structure and Formula of 12-Phosphotungstic Acid. *Proc. R. Soc. Lond. Ser. Contain. Pap. Math. Phys. Character* **1934**, *144* (851), 75–100. https://doi.org/10.1098/rspa.1934.0035.

(93) Misra, A.; Kozma, K.; Streb, C.; Nyman, M. Beyond Charge Balance: Counter-Cations in Polyoxometalate Chemistry. *Angew. Chem. Int. Ed.* **2020**, *59* (2), 596–612. https://doi.org/10.1002/anie.201905600.

(94) Anderson, J. S. Constitution of the Poly-Acids. *Nature* **1937**, *140* (3550), 850–850. https://doi.org/10.1038/140850a0.

(95) Evans, H. T. Jr. THE CRYSTAL STRUCTURES OF AMMONIUM AND POTASSIUM MOLYBDOTELLURATES. *J. Am. Chem. Soc.* **1948**, *70* (3), 1291–1292. https://doi.org/10.1021/ja01183a521.

(96) Wang, X.-S.; Huang, Y.-B.; Lin, Z.-J.; Cao, R. Phosphotungstic Acid Encapsulated in the Mesocages of Amine-Functionalized Metal–Organic Frameworks for Catalytic Oxidative Desulfurization. *Dalton Trans.* **2014**, *43* (31), 11950–11958. https://doi.org/10.1039/C4DT01043D.

(97) Sun, J.; Abednatanzi, S.; Van Der Voort, P.; Liu, Y.-Y.; Leus, K. POM@MOF Hybrids: Synthesis and Applications. *Catalysts* **2020**, *10* (5), 578. https://doi.org/10.3390/catal10050578.

(98) Hervé, G.; Tézé, A.; Contant, R. General Principles of The Synthesis of Polyoxometalates in Aqueous Solution. In *Polyoxometalate Molecular Science*; Borrás-Almenar, J. J., Coronado, E., Müller, A., Pope, M., Eds.; NATO Science Series; Springer Netherlands: Dordrecht, 2003; pp 33–54. https://doi.org/10.1007/978-94-010-0091-8_2.

(99) *De la solution à l'oxyde - 2e ED: Chimie aqueuse des cations métalliques - synthèse de nanostructures chimie aqueuse des cations métalliques synthèse de nanostructures (Savoirs actuels) eBook : Jolivet Jean-Pierre: Amazon.fr: Boutique Kindle*. https://www.amazon.fr/solution-%C3%A0-loxyde-2e-ED-ebook/dp/B01HOLSG2Q (accessed 2023-04-17).

(100) Rubio, L. R.; Vilela, J. L. V.; Artetxe, B.; Gutiérrez-Zorrilla, J. M. *Polyoxometalates: Advances, Properties, and Applications*; Jenny Stanford Publishing, 2022.

(101) Ni, Z.; Lv, H.; Yang, G. Recent Advances of Ti/Zr-Substituted Polyoxometalates: From Structural Diversity to Functional Applications. *Molecules* **2022**, *27* (24), 8799. https://doi.org/10.3390/molecules27248799.

(102) Dolbecq, A.; Dumas, E.; Mayer, C. R.; Mialane, P. Hybrid Organic−Inorganic Polyoxometalate Compounds: From Structural Diversity to Applications. *Chem. Rev.* **2010**, *110* (10), 6009–6048. https://doi.org/10.1021/cr1000578.

(103) Ding, Y.-X.; Zheng, Q.-H.; Peng, M.-T.; Liu, W.-L.; Teng, Y.-L. A New Ɛ-Keggin Polyoxometalate-Based Metal-Organic Framework: From Design and Synthesis to Electrochemical Hydrogen Evolution. *Catal. Commun.* **2021**, *161*, 106367. https://doi.org/10.1016/j.catcom.2021.106367.

(104) Chen, X.; Huang, P.; Zhu, X.; Zhuang, S.; Zhu, H.; Fu, J.; Nissimagoudar, A. S.; Li, W.; Zhang, X.; Zhou, L.; Wang, Y.; Lv, Z.; Zhou, Y.; Han, S.-T. Keggin-Type Polyoxometalate Cluster as an Active Component for Redox-Based Nonvolatile Memory. *Nanoscale Horiz.* **2019**, *4* (3), 697–704. https://doi.org/10.1039/C8NH00366A.

(105) Laurans, M.; Mattera, M.; Salles, R.; K'Bidi, L.; Gouzerh, P.; Renaudineau, S.; Volatron, F.; Guillemot, G.; Blanchard, S.; Izzet, G.; Solé-Daura, A.; Poblet, J. M.; Proust, A. When Identification of the Reduction Sites in Mixed Molybdenum/Tungsten Keggin-Type

Polyoxometalate Hybrids Turns Out Tricky. *Inorg. Chem.* **2022**, *61* (20), 7700–7709. https://doi.org/10.1021/acs.inorgchem.2c00866.

(106) Wang, S.-M.; Liu, L.; Huang, Z.-Y.; Han, Z.-B. Vanadium Substituted Keggin-Type POM-Based Electrochromic Films Showing High Performance in a Li+-Based Neutral Non-Aqueous Electrolyte. *RSC Adv.* **2016**, *6* (45), 38782–38789. https://doi.org/10.1039/C6RA03037H.

(107) Li, Q.; Zhang, L.; Dai, J.; Tang, H.; Li, Q.; Xue, H.; Pang, H. Polyoxometalate-Based Materials for Advanced Electrochemical Energy Conversion and Storage. *Chem. Eng. J.* **2018**, *351*, 441–461. https://doi.org/10.1016/j.cej.2018.06.074.

(108) Macht, J.; Janik, M. J.; Neurock, M.; Iglesia, E. Mechanistic Consequences of Composition in Acid Catalysis by Polyoxometalate Keggin Clusters. *J. Am. Chem. Soc.* **2008**, *130* (31), 10369–10379. https://doi.org/10.1021/ja803114r.

(109) Zhang, D.; Zhang, W.; Lin, Z.; Dong, J.; Zhen, N.; Chi, Y.; Hu, C. Mono- and Di-Sc-Substituted Keggin Polyoxometalates: Effective Lewis Acid Catalysts for Nerve Agent Simulant Hydrolysis and Mechanistic Insights. *Inorg. Chem.* **2020**, *59* (14), 9756–9764. https://doi.org/10.1021/acs.inorgchem.0c00976.

(110) Bardin, B. B.; Bordawekar, S. V.; Neurock, M.; Davis, R. J. Acidity of Keggin-Type Heteropolycompounds Evaluated by Catalytic Probe Reactions, Sorption Microcalorimetry, and Density Functional Quantum Chemical Calculations. *J. Phys. Chem. B* **1998**, *102* (52), 10817–10825. https://doi.org/10.1021/jp982345y.

(111) Malmir, M.; Heravi, M. M.; Yekke-Ghasemi, Z.; Mirzaei, M. Incorporating Heterogeneous Lacunary Keggin Anions as Efficient Catalysts for Solvent-Free Cyanosilylation of Aldehydes and Ketones. *Sci. Rep.* **2022**, *12* (1), 11573. https://doi.org/10.1038/s41598-022-15831-1.

(112) Kortz, U.; Müller, A.; van Slageren, J.; Schnack, J.; Dalal, N. S.; Dressel, M. Polyoxometalates: Fascinating Structures, Unique Magnetic Properties. *Coord. Chem. Rev.* **2009**, *253* (19–20), 2315–2327. https://doi.org/10.1016/j.ccr.2009.01.014.

(113) Rong, C. C.; So, H.; Pope, M. T. Electron Paramagnetic Resonance Investigation of Some 11-Tungstoruthenate(III) Polyoxoanions. *Eur. J. Inorg. Chem.* **2009**, *2009* (34), 5211–5214. https://doi.org/10.1002/ejic.200900578.

(114) Gumerova, N. I.; Roller, A.; Giester, G.; Krzystek, J.; Cano, J.; Rompel, A. Incorporation of Cr ^{III} into a Keggin Polyoxometalate as a Chemical Strategy to Stabilize a Labile {Cr ^{III} O $_4$ } Tetrahedral Conformation and Promote Unattended Single-Ion Magnet Properties. *J. Am. Chem. Soc.* **2020**, *142* (7), 3336–3339. https://doi.org/10.1021/jacs.9b12797.

(115) Shi, Z.; Peng, J.; Gómez-García, C. J.; Benmansour, S.; Gu, X. Influence of Metal Ions on the Structures of Keggin Polyoxometalate-Based Solids: Hydrothermal Syntheses, Crystal Structures and Magnetic Properties. *J. Solid State Chem.* **2006**, *179* (1), 253–265. https://doi.org/10.1016/j.jssc.2005.09.051.

(116) Kuramochi, S.; Shiga, T.; Cameron, J.; Newton, G.; Oshio, H. Synthesis, Crystal Structures and Magnetic Properties of Composites Incorporating an Fe(II) Spin Crossover Complex and Polyoxometalates. *Inorganics* **2017**, *5* (3), 48. https://doi.org/10.3390/inorganics5030048.

(117) Laurans, M.; Trinh, K.; Dalla Francesca, K.; Izzet, G.; Alves, S.; Derat, E.; Humblot, V.; Pluchery, O.; Vuillaume, D.; Lenfant, S.; Volatron, F.; Proust, A. Covalent Grafting of Polyoxometalate Hybrids onto Flat Silicon/Silicon Oxide: Insights from POMs Layers on Oxides. *ACS Appl. Mater. Interfaces* **2020**, *12* (42), 48109–48123. https://doi.org/10.1021/acsami.0c12300.

(118) Yi, X.; Izarova, N. V.; Stuckart, M.; Guérin, D.; Thomas, L.; Lenfant, S.; Vuillaume, D.; van Leusen, J.; Duchoň, T.; Nemšák, S.; Bourone, S. D. M.; Schmitz, S.; Kögerler, P. Probing Frontier Orbital Energies of {Co $_9$ (P $_2$ W $_{15}$) $_3$ } Polyoxometalate Clusters at Molecule–Metal and Molecule–Water Interfaces. *J. Am. Chem. Soc.* **2017**, *139* (41), 14501–14510. https://doi.org/10.1021/jacs.7b07034.

(119) Amin, S. S.; Cameron, J. M.; Cousins, R. B.; Wrigley, J.; Liirò-Peluso, L.; Sans, V.; Walsh, D. A.; Newton, G. N. Redox-Active Hierarchical Assemblies of Hybrid Polyoxometalate Nanostructures at Carbon Surfaces. *Inorg. Chem. Front.* **2022**, *9* (8), 1777–1784. https://doi.org/10.1039/D2QI00174H.

(120) Clemente-León, M.; Agricole, B.; Mingotaud, C.; Gómez-García, C. J.; Coronado, E.; Delhaes, P. Toward New Organic/Inorganic Superlattices: Keggin Polyoxometalates in Langmuir and Langmuir−Blodgett Films. *Langmuir* **1997**, *13* (8), 2340–2347. https://doi.org/10.1021/la960576v.

(121) Clemente-León, M.; Coronado, E.; Gómez-García, C. J.; Mingotaud, C.; Ravaine, S.; Romualdo-Torres, G.; Delhaès, P. Polyoxometalate Monolayers in Langmuir–Blodgett Films. *Chem. – Eur. J.* **2005**, *11* (13), 3979–3987. https://doi.org/10.1002/chem.200401063.

(122) Clemente-Leon, M.; Mingotaud, C.; Gomez-Garcia, C. J.; Coronado, E.; Delhaes, P. Polyoxometalates in Langmuir–Blodgett Films: Toward New Magnetic Materials. *Thin Solid Films* **1998**, *327–329*, 439–442. https://doi.org/10.1016/S0040-6090(98)00681-6.

(123) Li, H.; Pang, S.; Wu, S.; Feng, X.; Müllen, K.; Bubeck, C. Layer-by-Layer Assembly and UV Photoreduction of Graphene–Polyoxometalate Composite Films for Electronics. *J. Am. Chem. Soc.* **2011**, *133* (24), 9423–9429. https://doi.org/10.1021/ja201594k.

(124) Gam Derouich, S.; Rinfray, C.; Izzet, G.; Pinson, J.; Gallet, J.-J.; Kanoufi, F.; Proust, A.; Combellas, C. Control of the Grafting of Hybrid Polyoxometalates on Metal and Carbon Surfaces: Toward Submonolayers. *Langmuir* **2014**, *30* (8), 2287–2296. https://doi.org/10.1021/la500067e.

(125) Volatron, F.; Noël, J.-M.; Rinfray, C.; Decorse, P.; Combellas, C.; Kanoufi, F.; Proust, A. Electron Transfer Properties of a Monolayer of Hybrid Polyoxometalates on Silicon. *J. Mater. Chem. C* **2015**, *3* (24), 6266–6275. https://doi.org/10.1039/C5TC00074B.

(126) Rinfray, C.; Brasiliense, V.; Izzet, G.; Volatron, F.; Alves, S.; Combellas, C.; Kanoufi, F.; Proust, A. Electron Transfer to a Phosphomolybdate Monolayer on Glassy Carbon: Ambivalent Effect of Protonation. *Inorg. Chem.* **2016**, *55* (14), 6929–6937. https://doi.org/10.1021/acs.inorgchem.6b00485.

(127) Tang, Z.; Liu, S.; Wang, E.; Dong, S. Self-Assembled Monolayer of Polyoxometalate on Gold Surfaces: Quartz Crystal Microbalance, Electrochemistry, and in-Situ Scanning Tunneling Microscopy Study. *Langmuir* **2000**, *16* (11), 4946–4952. https://doi.org/10.1021/la9907127.

(128) Velessiotis, D.; Douvas, A. M.; Athanasiou, S.; Nilsson, B.; Petersson, G.; Södervall, U.; Alestig, G.; Argitis, P.; Glezos, N. Molecular Junctions Made of Tungsten-Polyoxometalate Self-Assembled Monolayers: Towards Polyoxometalate-Based Molecular Electronics Devices. *Microelectron. Eng.* **2011**, *88* (8), 2775–2777. https://doi.org/10.1016/j.mee.2011.01.039.

(129) Huez, C.; Guérin, D.; Lenfant, S.; Volatron, F.; Calame, M.; Perrin, M. L.; Proust, A.; Vuillaume, D. Redox-Controlled Conductance of Polyoxometalate Molecular Junctions. *Nanoscale* **2022**, *14* (37), 13790–13800. https://doi.org/10.1039/D2NR03457C.

(130) De Luca, G.; Bisignano, F.; Figoli, A.; Galiano, F.; Furia, E.; Mancuso, R.; Saoncella, O.; Carraro, M.; Bonchio, M.; Gabriele, B. Bromide Ion Exchange with a Keggin Polyoxometalate on Functionalized Polymeric Membranes: A Theoretical and Experimental Study. *J. Phys. Chem. B* **2014**, *118* (9), 2396–2404. https://doi.org/10.1021/jp411401v.

(131) Kasem, K. K.; Schultz, F. A. Electrochemistry of Polyoxometalates Immobilized in Ion Exchange Polymer Films. *Can. J. Chem.* **1995**, *73* (6), 858–864. https://doi.org/10.1139/v95-107.

(132) Francesca, K. D.; Lenfant, S.; Laurans, M.; Volatron, F.; Izzet, G.; Humblot, V.; Methivier, C.; Guerin, D.; Proust, A.; Vuillaume, D. Charge Transport through Redox Active [H7P8W48O184]33− Polyoxometalates Self-Assembled onto Gold Surfaces and Gold Nanodots. *Nanoscale* **2019**, *11* (4), 1863–1878. https://doi.org/10.1039/C8NR09377F.

(133) Vergnani, L.; Barra, A.-L.; Neugebauer, P.; Rodriguez-Douton, M. J.; Sessoli, R.; Sorace, L.; Wernsdorfer, W.; Cornia, A. Magnetic Bistability of Isolated Giant-Spin Centers in a Diamagnetic Crystalline Matrix. *Chem. - Eur. J.* **2012**, *18* (11), 3390–3398. https://doi.org/10.1002/chem.201103251.

(134) Llanos, L.; Aravena, D. Relaxation Time Enhancement by Magnetic Dilution in Single-Molecule Magnets: An Ab Initio Study. *J. Magn. Magn. Mater.* **2019**, *489*, 165456. https://doi.org/10.1016/j.jmmm.2019.165456.

(135) McElhinny, K. M.; Park, J.; Ahn, Y.; Huang, P.; Joo, Y.; Lakkham, A.; Pateras, A.; Wen, H.; Gopalan, P.; Evans, P. G. Photoisomerization Dynamics in a Densely Packed Optically

Transformable Azobenzene Monolayer. *Langmuir* **2018**, *34* (37), 10828–10836. https://doi.org/10.1021/acs.langmuir.8b01524.

(136) Linnenberg, O.; Moors, M.; Solé-Daura, A.; López, X.; Bäumer, C.; Kentzinger, E.; Pyckhout-Hintzen, W.; Monakhov, K. Yu. Molecular Characteristics of a Mixed-Valence Polyoxovanadate {VIV/V18O42} in Solution and at the Liquid–Surface Interface. *J. Phys. Chem. C* **2017**, *121* (19), 10419–10429. https://doi.org/10.1021/acs.jpcc.7b02138.

(137) de Bruijckere, J.; Gehring, P.; Palacios-Corella, M.; Clemente-León, M.; Coronado, E.; Paaske, J.; Hedegård, P.; van der Zant, H. S. J. Ground-State Spin Blockade in a Single-Molecule Junction. *Phys. Rev. Lett.* **2019**, *122* (19), 197701. https://doi.org/10.1103/PhysRevLett.122.197701.

(138) Tessonnier, J.-P.; Goubert-Renaudin, S.; Alia, S.; Yan, Y.; Barteau, M. A. Structure, Stability, and Electronic Interactions of Polyoxometalates on Functionalized Graphene Sheets. *Langmuir* **2013**, *29* (1), 393–402. https://doi.org/10.1021/la303408j.

(139) Linnenberg, O.; Moors, M.; Notario-Estévez, A.; López, X.; de Graaf, C.; Peter, S.; Baeumer, C.; Waser, R.; Monakhov, K. Yu. Addressing Multiple Resistive States of Polyoxovanadates: Conductivity as a Function of Individual Molecular Redox States. *J. Am. Chem. Soc.* **2018**, *140* (48), 16635–16640. https://doi.org/10.1021/jacs.8b08780.

(140) Lombana, A.; Rinfray, C.; Volatron, F.; Izzet, G.; Battaglini, N.; Alves, S.; Decorse, P.; Lang, P.; Proust, A. Surface Organization of Polyoxometalate Hybrids Steered by a 2D Supramolecular PTCDI/Melamine Network. *J. Phys. Chem. C* **2016**, *120* (5), 2837–2845. https://doi.org/10.1021/acs.jpcc.5b11945.

(141) Di, A.; Xu, J.; Zinn, T.; Sztucki, M.; Deng, W.; Ashok, A.; Lian, C.; Bergström, L. Tunable Ordered Nanostructured Phases by Co-Assembly of Amphiphilic Polyoxometalates and Pluronic Block Copolymers. *Nano Lett.* **2023**, *23* (5), 1645–1651. https://doi.org/10.1021/acs.nanolett.2c03068.

(142) Zhang, J.; Chang, S.; Suryanto, B. H. R.; Gong, C.; Zeng, X.; Zhao, C.; Zeng, Q.; Xie, J. Efficient Synthesis of Ir-Polyoxometalate Cluster Using a Continuous Flow Apparatus and STM Investigation of Its Coassembly Behavior on HOPG Surface. *Inorg. Chem.* **2016**, *55* (11), 5585–5591. https://doi.org/10.1021/acs.inorgchem.6b00670.

(143) Prashar, D. Self Assembled Monolayers -A Review. *Int. J. ChemTech Res.* **2012**, *4*.

(144) Casalini, S.; Bortolotti, C. A.; Leonardi, F.; Biscarini, F. Self-Assembled Monolayers in Organic Electronics. *Chem. Soc. Rev.* **2017**, *46* (1), 40–71. https://doi.org/10.1039/C6CS00509H.

(145) Mirkin, C. A.; Letsinger, R. L.; Mucic, R. C.; Storhoff, J. J. A DNA-Based Method for Rationally Assembling Nanoparticles into Macroscopic Materials. *Nature* **1996**, *382* (6592), 607–609. https://doi.org/10.1038/382607a0.

(146) Decher, G. Fuzzy Nanoassemblies: Toward Layered Polymeric Multicomposites. *Science* **1997**, *277* (5330), 1232–1237. https://doi.org/10.1126/science.277.5330.1232.

(147) Wang, L.; Gong, C.; Yuan, X.; Wei, G. Controlling the Self-Assembly of Biomolecules into Functional Nanomaterials through Internal Interactions and External Stimulations: A Review. *Nanomaterials* **2019**, *9* (2), 285. https://doi.org/10.3390/nano9020285.

(148) Cengiz, B.; Gevrek, T. N.; Chambre, L.; Sanyal, A. Self-Assembly of Cyclodextrin-Coated Nanoparticles:Fabrication of Functional Nanostructures for Sensing and Delivery. *Molecules* **2023**, *28* (3), 1076. https://doi.org/10.3390/molecules28031076.

(149) Brisse, R.; Guianvarc'h, D.; Mansuy, C.; Sagan, S.; Kreher, D.; Sosa-Vargas, L.; Hamitouche, L.; Humblot, V.; Arfaoui, I.; Labet, V.; Paris, C.; Petit, C.; Attias, A.-J. Probing the In-Air Growth of Large Area of 3D Functional Structures into a 2D Supramolecular Nanoporous Network. *Chem. Commun.* **2018**, *54* (72), 10068–10071. https://doi.org/10.1039/C8CC06125D.

(150) Fernez, Q.; Moradmand, S.; Mattera, M.; Djampa-Tapi, W.; Fiorini, C.; Charra, F.; Mathevet, F.; David, K.; Arfaoui, I.; Sosa Vargas, L. From Molecules in Solution to Molecules on Surfaces – Using Supramolecular Dyads to Form Functional Self-Assembled Networks on Graphene. *J. Mater. Chem. C* **2022**, *10*. https://doi.org/10.1039/D2TC01331B.

(151) Famili, M.; Jia, C.; Liu, X.; Wang, P.; Grace, I. M.; Guo, J.; Liu, Y.; Feng, Z.; Wang, Y.; Zhao, Z.; Decurtins, S.; Häner, R.; Huang, Y.; Liu, S.-X.; Lambert, C. J.; Duan, X. Self-Assembled Molecular-

Electronic Films Controlled by Room Temperature Quantum Interference. *Chem* **2019**, *5* (2), 474–484. https://doi.org/10.1016/j.chempr.2018.12.008.

(152) Wang, P.; Jia, C.; Huang, Y.; Duan, X. Van Der Waals Heterostructures by Design: From 1D and 2D to 3D. *Matter* **2021**, *4* (2), 552–581. https://doi.org/10.1016/j.matt.2020.12.015.

(153) Lemme, M. C.; Akinwande, D.; Huyghebaert, C.; Stampfer, C. 2D Materials for Future Heterogeneous Electronics. *Nat. Commun.* **2022**, *13* (1), 1392. https://doi.org/10.1038/s41467-022-29001-4.

(154) Naydenov, B.; Torsney, S.; Bonilla, A. S.; El Garah, M.; Ciesielski, A.; Gualandi, A.; Mengozzi, L.; Cozzi, P. G.; Gutierrez, R.; Samorì, P.; Cuniberti, G.; Boland, J. J. Self-Assembled Two-Dimensional Supramolecular Networks Characterized by Scanning Tunneling Microscopy and Spectroscopy in Air and under Vacuum. *Langmuir* **2018**, *34* (26), 7698–7707. https://doi.org/10.1021/acs.langmuir.8b01374.

(155) Uemura, S.; Tanoue, R.; Yilmaz, N.; Ohira, A.; Kunitake, M. Molecular Dynamics in Two-Dimensional Supramolecular Systems Observed by STM. *Materials* **2010**, *3* (8), 4252–4276. https://doi.org/10.3390/ma3084252.

(156) Zhang, Z.; Li, Y.; Song, B.; Zhang, Y.; Jiang, X.; Wang, M.; Tumbleson, R.; Liu, C.; Wang, P.; Hao, X.-Q.; Rojas, T.; Ngo, A. T.; Sessler, J. L.; Newkome, G. R.; Hla, S. W.; Li, X. Intra- and Intermolecular Self-Assembly of a 20-Nm-Wide Supramolecular Hexagonal Grid. *Nat. Chem.* **2020**, *12* (5), 468–474. https://doi.org/10.1038/s41557-020-0454-z.

(157) Fung, S. Y.; Hong, Y.; Keyes-baig, C.; Chen, P. 12 - Self-Assembly of Peptides and Its Potential Applications. In *Molecular Interfacial Phenomena of Polymers and Biopolymers*; Chen, P., Ed.; Woodhead Publishing Series in Biomaterials; Woodhead Publishing, 2005; pp 421–474. https://doi.org/10.1533/9781845690830.3.421.

(158) Li, W.; Leng, X.; Xu, C.; Liu, N. Formation of Hydrogen Bond-Based 2D Two-Component Supramolecular Networks at Liquid-Solid Surface. *Phys. E Low-Dimens. Syst. Nanostructures* **2018**, *101*, 197–200. https://doi.org/10.1016/j.physe.2018.04.013.

(159) Xu, L.; Miao, X.; Ying, X.; Deng, W. Two-Dimensional Self-Assembled Molecular Structures Formed by the Competition of van Der Waals Forces and Dipole–Dipole Interactions. *J. Phys. Chem. C* **2012**, *116* (1), 1061–1069. https://doi.org/10.1021/jp210000e.

(160) Gerbelli, B. B.; Vassiliades, S. V.; Rojas, J. E. U.; Pelin, J. N. B. D.; Mancini, R. S. N.; Pereira, W. S. G.; Aguilar, A. M.; Venanzi, M.; Cavalieri, F.; Giuntini, F.; Alves, W. A. Hierarchical Self-Assembly of Peptides and Its Applications in Bionanotechnology. *Macromol. Chem. Phys.* **2019**, *220* (14), 1970027. https://doi.org/10.1002/macp.201970027.

(161) Wang, Y.; Miao, X.; Deng, W.; Brisse, R.; Jousselme, B.; Silly, F. Coronene and Phthalocyanine Trapping Efficiency of a Two-Dimensional Kagomé Host-Nanoarchitecture. *Nanomaterials* **2022**, *12* (5), 775. https://doi.org/10.3390/nano12050775.

(162) Velpula, G.; Takeda, T.; Adisoejoso, J.; Inukai, K.; Tahara, K.; Mali, K. S.; Tobe, Y.; Feyter, S. D. On the Formation of Concentric 2D Multicomponent Assemblies at the Solution–Solid Interface. *Chem. Commun.* **2017**, *53* (6), 1108–1111. https://doi.org/10.1039/C6CC09188A.

(163) Lee, S.-L.; Fang, Y.; Velpula, G.; Cometto, F. P.; Lingenfelder, M.; Müllen, K.; Mali, K. S.; De Feyter, S. Reversible Local and Global Switching in Multicomponent Supramolecular Networks: Controlled Guest Release and Capture at the Solution/Solid Interface. *ACS Nano* **2015**, *9* (12), 11608–11617. https://doi.org/10.1021/acsnano.5b06081.

(164) Schull, G.; Douillard, L.; Fiorini-Debuisschert, C.; Charra, F.; Mathevet, F.; Kreher, D.; Attias, A.-J. Selectivity of Single-Molecule Dynamics in 2D Molecular Sieves. *Adv. Mater.* **2006**, *18* (22), 2954–2957. https://doi.org/10.1002/adma.200600683.

(165) Schull, G.; Douillard, L.; Fiorini-Debuisschert, C.; Charra, F.; Mathevet, F.; Kreher, D.; Attias, A.-J. Single-Molecule Dynamics in a Self-Assembled 2D Molecular Sieve. *Nano Lett.* **2006**, *6* (7), 1360–1363. https://doi.org/10.1021/nl060292n.

(166) Li, Y.; Cheng, L.; Liu, C.; Liu, W.; Fan, Y.; Fan, X.; Zeng, Q. On-Surface Observation of the Formation of Organometallic Complex in a Supramolecular Network. *Sci. Rep.* **2015**, *5* (1), 10972. https://doi.org/10.1038/srep10972.

(167) Brom, C. R. van den; Rudolf, P.; Palstra, T. T. M.; Hessen, B. Selective Co-Aggregation of Gold Nanoparticles Functionalised with Complementary Hydrogen-Bonding Groups. *Chem. Commun.* **2007**, No. 46, 4922–4924. https://doi.org/10.1039/B711435D.

(168) van den Brom, C. R.; Arfaoui, I.; Cren, T.; Hessen, B.; Palstra, T. T. M.; De Hosson, J. T. M.; Rudolf, P. Selective Immobilization of Nanoparticles on Surfaces by Molecular Recognition Using Simple Multiple H-Bonding Functionalities. *Adv. Funct. Mater.* **2007**, *17* (13), 2045–2052. https://doi.org/10.1002/adfm.200600497.

(169) *Hydrogen bonding in life - Labster Theory*. https://theory.labster.com/h-bonding-life-vdw/ (accessed 2023-08-22).

(170) Hunter, C. A.; Sanders, J. K. M. The Nature of .Pi.-.Pi. Interactions. *J. Am. Chem. Soc.* **1990**, *112* (14), 5525–5534. https://doi.org/10.1021/ja00170a016.

(171) *6.5.1: Química Host-Invitado e Interacciones de apilamiento π-π*. LibreTexts Español. https://espanol.libretexts.org/Quimica/Qu%C3%ADmica_Inorg%C3%A1nica/Mapa%3A_Qu%C3%ADmica_Inorg%C3%A1nica_(LibreTextos)/06%3A_Qu%C3%ADmica_%C3%A1cido-base_y_donador-aceptor/6.05%3A_Fuerzas_intermoleculares/6.5.01%3A_Qu%C3%ADmica_Host-Invitado_e_Interacciones_de_apilamiento_%CF%80-%CF%80 (accessed 2023-08-22).

(172) Georgakilas, V.; Tiwari, J. N.; Kemp, K. C.; Perman, J. A.; Bourlinos, A. B.; Kim, K. S.; Zboril, R. Noncovalent Functionalization of Graphene and Graphene Oxide for Energy Materials, Biosensing, Catalytic, and Biomedical Applications. *Chem. Rev.* **2016**, *116* (9), 5464–5519. https://doi.org/10.1021/acs.chemrev.5b00620.

(173) Dhotel, A.; Chen, Z.; Delbreilh, L.; Youssef, B.; Saiter, J.-M.; Tan, L. Molecular Motions in Functional Self-Assembled Nanostructures. *Int. J. Mol. Sci.* **2013**, *14* (2), 2303–2333. https://doi.org/10.3390/ijms14022303.

(174) Gao, H.-Y.; Wagner, H.; Held, P. A.; Du, S.; Gao, H.-J.; Studer, A.; Fuchs, H. In-Plane Van Der Waals Interactions of Molecular Self-Assembly Monolayer. *Appl. Phys. Lett.* **2015**, *106* (8), 081606. https://doi.org/10.1063/1.4907777.

(175) Altman, M.; Lee, P.; Rich, A.; Zhang, S. Conformational Behavior of Ionic Self-Complementary Peptides. *Protein Sci.* **2000**, *9* (6), 1095–1105. https://doi.org/10.1110/ps.9.6.1095.

(176) Zhao, X. Design of Self-Assembling Surfactant-like Peptides and Their Applications. *Curr. Opin. Colloid Interface Sci.* **2009**, *14* (5), 340–348. https://doi.org/10.1016/j.cocis.2009.07.002.

(177) Decher, G.; Hong, J. D.; Schmitt, J. Buildup of Ultrathin Multilayer Films by a Self-Assembly Process: III. Consecutively Alternating Adsorption of Anionic and Cationic Polyelectrolytes on Charged Surfaces. *Thin Solid Films* **1992**, *210–211*, 831–835. https://doi.org/10.1016/0040-6090(92)90417-A.

(178) Cherevan, A. S.; Nandan, S. P.; Roger, I.; Liu, R.; Streb, C.; Eder, D. Polyoxometalates on Functional Substrates: Concepts, Synergies, and Future Perspectives. *Adv. Sci.* **2020**, *7* (8), 1903511. https://doi.org/10.1002/advs.201903511.

(179) Cook, T. R.; Zheng, Y.-R.; Stang, P. J. Metal–Organic Frameworks and Self-Assembled Supramolecular Coordination Complexes: Comparing and Contrasting the Design, Synthesis, and Functionality of Metal–Organic Materials. *Chem. Rev.* **2013**, *113* (1), 734–777. https://doi.org/10.1021/cr3002824.

(180) Burnett, B. J.; Choe, W. Sequential Self-Assembly in Metal–Organic Frameworks. *Dalton Trans.* **2012**, *41* (14), 3889–3894. https://doi.org/10.1039/C2DT12103D.

(181) Kim, B.; Cho, C.; Arfaoui, I.; Paris, C.; Petit, C.; Bahers, T. L.; Kim, E.; Attias, A.-J. 2D Host–Guest Supramolecular Chemistry for an on-Monolayer Graphene Emitting Platform. *Mater. Horiz.* **2020**, *7* (10), 2741–2748. https://doi.org/10.1039/D0MH00950D.

(182) Teyssandier, J.; De Feyter, S.; S. Mali, K. Host–Guest Chemistry in Two-Dimensional Supramolecular Networks. *Chem. Commun.* **2016**, *52* (77), 11465–11487. https://doi.org/10.1039/C6CC05256H.

(183) Tahara, K.; Lei, S.; Adisoejoso, J.; Feyter, S. D.; Tobe, Y. Supramolecular Surface-Confined Architectures Created by Self-Assembly of Triangular Phenylene–Ethynylene Macrocycles via

van Der Waals Interaction. *Chem. Commun.* **2010**, *46* (45), 8507–8525. https://doi.org/10.1039/C0CC02780D.

(184) Griessl, S.; Lackinger, M.; Edelwirth, M.; Hietschold, M.; Heckl, W. M. Self-Assembled Two-Dimensional Molecular Host-Guest Architectures From Trimesic Acid. *Single Mol.* **2002**, *3* (1), 25–31. https://doi.org/10.1002/1438-5171(200204)3:1<25::AID-SIMO25>3.0.CO;2-K.

(185) Bléger, D.; Kreher, D.; Mathevet, F.; Attias, A.-J.; Schull, G.; Huard, A.; Douillard, L.; Fiorini-Debuischert, C.; Charra, F. Surface Noncovalent Bonding for Rational Design of Hierarchical Molecular Self-Assemblies. *Angew. Chem.* **2007**, *119* (39), 7548–7551. https://doi.org/10.1002/ange.200702376.

(186) Plas, J.; Ivasenko, O.; Martsinovich, N.; Lackinger, M.; Feyter, S. D. Nanopatterning of a Covalent Organic Framework Host–Guest System. *Chem. Commun.* **2015**, *52* (1), 68–71. https://doi.org/10.1039/C5CC07557B.

(187) Bellamy-Carter, A.; Roche, C.; Anderson, H. L.; Saywell, A. Self-Assembly of a Strapped Linear Porphyrin Oligomer on HOPG. *Sci. Rep.* **2021**, *11* (1), 20388. https://doi.org/10.1038/s41598-021-99881-x.

(188) Qin, Y.; Yang, Y.; Yao, M.; Xue, X.; Wang, X.; Huang, H.; Chen, T.; Wang, D.; Wan, L. Self-Assembly of an Oligo(p -Phenylenevinylene)-Based Molecule on an HOPG Surface: Insights from Multi-Scale Simulation and STM Observation. *RSC Adv.* **2018**, *8* (56), 31868–31873. https://doi.org/10.1039/C8RA05477K.

(189) Jaroch, T.; Maranda-Niedbala, A.; Kotwica, K.; Wamil, D.; Bujak, P.; Pron, A.; Nowakowski, R. Self-Assembly of Tetraalkoxydinaphthophenazines in Monolayers on HOPG by Scanning Tunneling Microscopy. *Surf. Sci.* **2015**, *641*, 252–259. https://doi.org/10.1016/j.susc.2015.04.016.

(190) Gurdumov, K.; Mazur, U.; Hipps, K. W. Self-Assembly Dynamics and Stability through Concentration Control at the Solution/HOPG Interface. *J. Phys. Chem. C* **2022**, *126* (30), 12916–12927. https://doi.org/10.1021/acs.jpcc.2c03766.

(191) Moore, A. W. Pyrolytic Carbon and Graphite. In *Encyclopedia of Materials: Science and Technology*; Buschow, K. H. J., Cahn, R. W., Flemings, M. C., Ilschner, B., Kramer, E. J., Mahajan, S., Veyssière, P., Eds.; Elsevier: Oxford, 2001; pp 7933–7937. https://doi.org/10.1016/B0-08-043152-6/01428-5.

(192) Bashir, A. Growth and Structural Characterization of Self-Assembled Monolayers (SAMs) on Gold Made from Functionalized Thiols and Selenols. *Httpwww-Brsubruhr-Uni-BochumdenetahtmlHSSDissBashirAsifdisspdf* **2023**.

(193) Wang, Z.; Xu, F.; Lu, C.; Zhang, H.; Xu, Q.; Zhu, J. Electronic Conductivity Upturn of HOPG Contrast to Transport Properties of Polycrystal Graphite. arXiv January 21, 2008. https://doi.org/10.48550/arXiv.0801.3298.

(194) Yan, H.-J.; Liu, J.; Wang, D.; Wan, L.-J. Two-Dimensional Self-Assemblies of Telechelic Organic Compounds: Structure and Surface Host–Guest Chemistry. *Philos. Trans. R. Soc. Math. Phys. Eng. Sci.* **2013**, *371* (2000), 20120302. https://doi.org/10.1098/rsta.2012.0302.

(195) Otero, R.; Gallego, J. M.; de Parga, A. L. V.; Martín, N.; Miranda, R. Molecular Self-Assembly at Solid Surfaces. *Adv. Mater. Deerfield Beach Fla* **2011**, *23* (44), 5148–5176. https://doi.org/10.1002/adma.201102022.

(196) Rosei, F. Nanostructured Surfaces: Challenges and Frontiers in Nanotechnology. *J. Phys. Condens. Matter* **2004**, *16* (17), S1373. https://doi.org/10.1088/0953-8984/16/17/001.

(197) Feyter, S. D.; Schryver, F. C. D. Two-Dimensional Supramolecular Self-Assembly Probed by Scanning Tunneling Microscopy. *Chem. Soc. Rev.* **2003**, *32* (3), 139–150. https://doi.org/10.1039/B206566P.

(198) De Feyter, S.; De Schryver, F. C. Self-Assembly at the Liquid/Solid Interface: STM Reveals. *J. Phys. Chem. B* **2005**, *109* (10), 4290–4302. https://doi.org/10.1021/jp045298k.

(199) Xiao, Y.; Tao, J.; Peng, X.; Song, Y.; Lei, P.; Xu, H.; Xiao, X.; Tu, B.; Zeng, Q. Two-Dimensional Molecular Network Built from Hierarchy Self-Assembly of Perylene Bisimide Derivatives. *ACS Appl. Mater. Interfaces* **2021**, *13* (14), 17129–17138. https://doi.org/10.1021/acsami.1c03201.

(200) Bellec, A.; Arrigoni, C.; Schull, G.; Douillard, L.; Fiorini-Debuisschert, C.; Mathevet, F.; Kreher, D.; Attias, A.-J.; Charra, F. Solution-Growth Kinetics and Thermodynamics of Nanoporous Self-Assembled Molecular Monolayers. *J. Chem. Phys.* **2011**, *134* (12), 124702. https://doi.org/10.1063/1.3569132.

(201) Gutzler, R.; Cardenas, L.; Rosei, F. Kinetics and Thermodynamics in Surface-Confined Molecular Self-Assembly. *Chem. Sci.* **2011**, *2* (12), 2290–2300. https://doi.org/10.1039/C1SC00531F.

(202) Kalashnyk, N.; Gouesmel, A.; Kim, E.; Attias, A.-J.; Charra, F. Functional Hybrid Multilayered van Der Waals Heterostructures from Graphene and Self-Assembled Supramolecular 2D Crystals. *2D Mater.* **2019**, *6* (4), 045016. https://doi.org/10.1088/2053-1583/ab2ba7.

(203) Kalashnyk, N.; Jaouen, M.; Fiorini-Debuisschert, C.; Douillard, L.; Attias, A.-J.; Charra, F. Electronic Effects of the Bernal Stacking of Graphite on Self-Assembled Aromatic Adsorbates. *Chem. Commun.* **2018**, *54* (69), 9607–9610. https://doi.org/10.1039/C8CC05806G.

(204) Schull, G. Dynamique d'auto-assemblages moléculaires bidimensionnels. phdthesis, École normale supérieure de Cachan - ENS Cachan, 2006. https://theses.hal.science/tel-00143236 (accessed 2023-04-28).

(205) Xu, S.; Zeng, Q.; Lu, J.; Wang, C.; Wan, L.; Bai, C.-L. The Two-Dimensional Self-Assembled n-Alkoxy-Substituted Stilbenoid Compounds and Triphenylenes Studied by Scanning Tunneling Microscopy. *Surf. Sci.* **2003**, *538* (1), L451–L459. https://doi.org/10.1016/S0039-6028(03)00698-8.

(206) Laurans, M.; Mattera, M.; Salles, R.; K'Bidi, L.; Gouzerh, P.; Renaudineau, S.; Volatron, F.; Guillemot, G.; Blanchard, S.; Izzet, G.; Solé-Daura, A.; Poblet, J. M.; Proust, A. When Identification of the Reduction Sites in Mixed Molybdenum/Tungsten Keggin-Type Polyoxometalate Hybrids Turns Out Tricky. *Inorg. Chem.* **2022**, *61* (20), 7700–7709. https://doi.org/10.1021/acs.inorgchem.2c00866.

(207) K/Bidi, L.; Desjonquères, A.; Izzet, G.; Guillemot, G. H2 Evolution at a Reduced Hybrid Polyoxometalate and Its Vanadium-Oxo Derivative Used as Molecular Models for Reducible Metal Oxides. *Inorg. Chem.* **2023**, *62* (5), 1935–1941. https://doi.org/10.1021/acs.inorgchem.2c01741.

(208) Himeno, S.; Takamoto, M. Difference in Voltammetric Properties between the Keggin-Type [XW12O40]N− and [XMo12O40]N− Complexes. *J. Electroanal. Chem.* **2002**, *528* (1–2), 170–174. https://doi.org/10.1016/S0022-0728(02)00901-4.

(209) *Zinc phthalocyanine, [ZnPc]*. https://omlc.org/spectra/PhotochemCAD/html/026.html (accessed 2023-09-14).

(210) Salhi, J.; Calupitan, J. P.; Mattera, M.; Montero, D.; Miche, A.; Maruchenko, R.; Proust, A.; Izzet, G.; Kreher, D.; Arfaoui, I.; Volatron, F. Ready-to-Be-Addressed Oxo-Clusters: Individualized, Periodically Organized and Separated from the Substrate. *Nanoscale* **2023**, *15* (32), 13233–13238. https://doi.org/10.1039/D3NR02649C.

(211) Hammiche, A.; Pollock, H. M.; Reading, M.; Claybourn, M.; Turner, P. H.; Jewkes, K. Photothermal FT-IR Spectroscopy: A Step towards FT-IR Microscopy at a Resolution Better Than the Diffraction Limit. *Appl. Spectrosc.* **1999**, *53* (7), 810–815. https://doi.org/10.1366/0003702991947379.

(212) Bozec, L.; Hammiche, A.; Pollock, H. M.; Conroy, M.; Chalmers, J. M.; Everall, N. J.; Turin, L. Localized Photothermal Infrared Spectroscopy Using a Proximal Probe. *J. Appl. Phys.* **2001**, *90* (10), 5159–5165. https://doi.org/10.1063/1.1403671.

(213) Dazzi, A.; Prazeres, R.; Glotin, F.; Ortega, J. M. Local Infrared Microspectroscopy with Subwavelength Spatial Resolution with an Atomic Force Microscope Tip Used as a Photothermal Sensor. *Opt. Lett.* **2005**, *30* (18), 2388–2390. https://doi.org/10.1364/OL.30.002388.

(214) Dazzi, A.; Glotin, F.; Carminati, R. Theory of Infrared Nanospectroscopy by Photothermal Induced Resonance. *J. Appl. Phys.* **2010**, *107* (12), 124519. https://doi.org/10.1063/1.3429214.

(215) Katzenmeyer, A. M.; Aksyuk, V.; Centrone, A. Nanoscale Infrared Spectroscopy: Improving the Spectral Range of the Photothermal Induced Resonance Technique. *Anal. Chem.* **2013**, *85* (4), 1972–1979. https://doi.org/10.1021/ac303620y.

(216) Lahiri, B.; Holland, G.; Centrone, A. Chemical Imaging Beyond the Diffraction Limit: Experimental Validation of the PTIR Technique. *Small* **2013**, *9* (3), 439–445. https://doi.org/10.1002/smll.201200788.

(217) Pollock, H. M.; Kazarian, S. G. Microspectroscopy in the Mid-Infrared. In *Encyclopedia of Analytical Chemistry*; John Wiley & Sons, Ltd, 2014; pp 1–26. https://doi.org/10.1002/9780470027318.a5609.pub2.

(218) Lu, F.; Jin, M.; Belkin, M. A. Tip-Enhanced Infrared Nanospectroscopy via Molecular Expansion Force Detection. *Nat. Photonics* **2014**, *8* (4), 307–312. https://doi.org/10.1038/nphoton.2013.373.

(219) Dazzi, A.; Prater, C. B. AFM-IR: Technology and Applications in Nanoscale Infrared Spectroscopy and Chemical Imaging. *Chem. Rev.* **2017**, *117* (7), 5146–5173. https://doi.org/10.1021/acs.chemrev.6b00448.

(220) *IR: alkenes*. https://orgchemboulder.com/Spectroscopy/irtutor/alkenesir.shtml (accessed 2023-09-21).

(221) Hamouni, S.; Arous, O.; Abdessemed, D.; Nezzal, G.; Van der Bruggen, B. Alcohol and Alkane Organic Extraction Using Pervaporation Process. *Macromol. Symp.* **2019**, *386* (1), 1800247. https://doi.org/10.1002/masy.201800247.

(222) Preketes, N. K.; Biggs, J. D.; Ren, H.; Andricioaei, I.; Mukamel, S. Simulations of Two-Dimensional Infrared and Stimulated Resonance Raman Spectra of Photoactive Yellow Protein. *Chem. Phys.* **2013**, *422*, 10.1016/j.chemphys.2012.09.002. https://doi.org/10.1016/j.chemphys.2012.09.002.

(223) Kalisz, G.; Gieroba, B.; Chrobak, O.; Suchora, M.; Starosta, A. L.; Sroka-Bartnicka, A. Vibrational Spectroscopic Analyses and Imaging of the Early Middle Ages Hemp Bast Fibres Recovered from Lake Sediments. *Molecules* **2021**, *26* (5), 1314. https://doi.org/10.3390/molecules26051314.

(224) Meier, H.; Lehmann, M.; Kolb, U. Stilbenoid Dendrimers. *Chem. – Eur. J.* **2000**, *6* (13), 2462–2469. https://doi.org/10.1002/1521-3765(20000703)6:13<2462::AID-CHEM2462>3.0.CO;2-A.

(225) Skoog, D. A.; Crouch, S. R.; Holler, F. J. *Principles of Instrumental Analysis*, 6th ed.; Thomson Brooks/Cole: Belmont, CA, 2007.

(226) G.D. christan. *Analytical Chemistry By Gary D. Christian*; 2018.

(227) Drago, R. S. *Physical Methods for Chemists*; Saunders College Pub., 1992.

(228) Blinder, S. M. *Introduction to Quantum Mechanics*, 2nd edition.; Academic Press: London ; San Diego, CA, 2020.

(229) Lv, F.; Cao, B.; Cui, Y.; Liu, T. Zinc Phthalocyanine Labelled Polyethylene Glycol: Preparation, Characterization, Interaction with Bovine Serum Albumin and Near Infrared Fluorescence Imaging in Vivo. *Molecules* **2012**, *17* (6), 6348–6361. https://doi.org/10.3390/molecules17066348.

(230) Keshipour, S.; Mohammad-Alizadeh, S. Nickel Phthalocyanine@graphene Oxide/TiO2 as an Efficient Degradation Catalyst of Formic Acid toward Hydrogen Production. *Sci. Rep.* **2021**, *11* (1), 16148. https://doi.org/10.1038/s41598-021-95382-z.

(231) Díaz, J.; Pizzio, L. R.; Pecchi, G.; Campos, C. H.; Azócar, L.; Briones, R.; Romero, R.; Henríquez, A.; Gaigneaux, E. M.; Contreras, D. Tetrabutyl Ammonium Salts of Keggin-Type Vanadium-Substituted Phosphomolybdates and Phosphotungstates for Selective Aerobic Catalytic Oxidation of Benzyl Alcohol. *Catalysts* **2022**, *12* (5), 507. https://doi.org/10.3390/catal12050507.

(232) Coronel, N. C.; da Silva, M. J. Lacunar Keggin Heteropolyacid Salts: Soluble, Solid and Solid-Supported Catalysts. *J. Clust. Sci.* **2018**, *29* (2), 195–205. https://doi.org/10.1007/s10876-018-1343-0.

(233) Yang, L.; May, P. W.; Yin, L.; Smith, J. A.; Rosser, K. N. Ultra Fine Carbon Nitride Nanocrystals Synthesized by Laser Ablation in Liquid Solution. *J. Nanoparticle Res.* **2007**, *9* (6), 1181–1185. https://doi.org/10.1007/s11051-006-9192-4.

(234) Yoon, S. H.; Chamot-Rooke, J.; Perkins, B. R.; Hilderbrand, A. E.; Poutsma, J. C.; Wysocki, V. H. IRMPD Spectroscopy Shows That AGG Forms an Oxazolone B2+ Ion. *J. Am. Chem. Soc.* **2008**, *130* (52), 17644–17645. https://doi.org/10.1021/ja8067929.

(235) Dvoryaninova, O. P.; Sokolov, A. V.; Peregonchaya, O. V.; Solovyeva, E. A.; Syanov, D. A. Identification of Composition and Structure of Functional Groups of Ferment Lysates Based on IR Spectroscopy. *IOP Conf. Ser. Earth Environ. Sci.* **2021**, *640* (3), 032062. https://doi.org/10.1088/1755-1315/640/3/032062.

(236) Rathjens, G. W. Jr.; Freeman, N. K.; Gwinn, W. D.; Pitzer, K. S. Infrared Absorption Spectra, Structure and Thermodynamic Properties of Cyclobutane1. *J. Am. Chem. Soc.* **1953**, *75* (22), 5634–5642. https://doi.org/10.1021/ja01118a048.

(237) Rohman, A.; Musfiroh, A.; Wijaya, E. G.; Mada, G. Quantitative Determination of Simethicone in Antacid Suspension and Chewable Tablet Using FTIR Spectroscopy; 2013.

(238) Poiana, M.-A.; Alexa, E.; Munteanu, M.-F.; Gligor, R.; Moigradean, D.; Mateescu, C. Use of ATR-FTIR Spectroscopy to Detect the Changes in Extra Virgin Olive Oil by Adulteration with Soybean Oil and High Temperature Heat Treatment. *Open Chem.* **2015**, *13* (1). https://doi.org/10.1515/chem-2015-0110.

(239) Guo, Y.-C.; Cai, C.; Zhang, Y.-H. Observation of Conformational Changes in Ethylene Glycol–Water Complexes by FTIR–ATR Spectroscopy and Computational Studies. *AIP Adv.* **2018**, *8* (5), 055308. https://doi.org/10.1063/1.4995975.

(240) Kumar, T.; Umamaheswari, S. FTIR, FTR and UV-Vis Analysis of Carbamazepine. *Res. J. Pharm. Biol. Chem. Sci.* **2011**, *2*, 685–693.

(241) Zhu, J.; Cao, X.; Li, J. Ethanol-Induced Aggregation of Nonpolar Nanoparticles in Water/Ethanol Mixed Solvents. *Langmuir* **2022**, *38* (45), 13910–13915. https://doi.org/10.1021/acs.langmuir.2c02126.

(242) Zhao, H.; Zhang, S.; Li, S.; Song, X.; Liu, W.; Liu, B.; Dong, M. Investigation of the Non-Covalent Interactions of Molecular Self-Assembly by Scanning Tunneling Microscopy Using the Association of Aromatic Structures in Pyrene-4,5,9,10-Tetraone and Phenanthrene-9,10-Dione Molecules. *RSC Adv.* **2015**, *5* (125), 103316–103320. https://doi.org/10.1039/C5RA20316C.

(243) Camerman, A.; Trotter, J. The Crystal and Molecular Structure of Pyrene. *Acta Crystallogr.* **1965**, *18* (4), 636–643. https://doi.org/10.1107/S0365110X65001494.

(244) Sau, S. P.; Hrdlicka, P. J. C2′-Pyrene-Functionalized Triazole-Linked DNA: Universal DNA/RNA Hybridization Probes. *J. Org. Chem.* **2012**, *77* (1), 5–16. https://doi.org/10.1021/jo201845z.

(245) Kozhevnikov, I. V. Catalysis by Heteropoly Acids and Multicomponent Polyoxometalates in Liquid-Phase Reactions. *Chem. Rev.* **1998**, *98* (1), 171–198. https://doi.org/10.1021/cr960400y.

(246) Arrigoni, C. Monocouches Nanoporeuses Auto-Assemblées Sur Graphite : Contrôle et Modulation Des Propriétés de Tamis Moléculaire. These de doctorat, Paris 6, 2010. https://www.theses.fr/2010PA066681 (accessed 2023-08-28).

(247) Bellec, A.; Arrigoni, C.; Douillard, L.; Fiorini-Debuisschert, C.; Mathevet, F.; Kreher, D.; Attias, A.-J.; Charra, F. Formation of Hydroxyl-Functionalized Stilbenoid Molecular Sieves at the Liquid/Solid Interface on Top of a 1-Decanol Monolayer. *Nanotechnology* **2014**, *25* (43), 435604. https://doi.org/10.1088/0957-4484/25/43/435604.

(248) Schull, G.; Ness, H.; Douillard, L.; Fiorini-Debuisschert, C.; Charra, F.; Mathevet, F.; Kreher, D.; Attias, A.-J. Single Atom Substitution for Marking and Motion Tracking of Individual Molecules by Scanning Tunneling Microscopy. *J. Phys. Chem. C* **2008**, *112* (36), 14058–14063. https://doi.org/10.1021/jp8030013.

(249) Li, S.; Gong, C.; Zhang, Y.; Fu, S.; Wang, Z.; Lu, Y.; Gu, S.; Liu, X.; Wang, L. Transformation of the Coordination Nanostructures of 4,4′,4′′-(1,3,5-Triazine-2,4,6-Triyl) Tribenzoic Acid Molecules on HOPG Triggered by the Change in the Concentration of Metal Ions. *RSC Adv.* **2022**, *12* (7), 3892–3896. https://doi.org/10.1039/D1RA09073A.

(250) Liu, C.; Yang, L.; Wang, Y.; Lei, S.; Hu, W. Substrate Effects in the Supramolecular Self-Assembly of 2,4,6-Tris(4-Bromophenyl)-1,3,5-Triazine on Graphite and Graphene. *J. Phys. Chem. C* **2018**, *122* (23), 12307–12314. https://doi.org/10.1021/acs.jpcc.8b02979.

(251) Qiao, Y.; Zeng, Q.; Tan, Z.; Xu, S.; Wang, C.; Bai, C. STM Observation of 1,3,5-Triazines Bearing Rod-like Benzeneazonaphthalene Moieties Monolayers Self-Assembled on Graphite Surface. *J. Mater. Chem.* **2002**, *12* (5), 1239–1241. https://doi.org/10.1039/B200043C.

(252) Gatti, R.; MacLeod, J. M.; Lipton-Duffin, J. A.; Moiseev, A. G.; Perepichka, D. F.; Rosei, F. Substrate, Molecular Structure, and Solvent Effects in 2D Self-Assembly via Hydrogen and Halogen Bonding. *J. Phys. Chem. C* **2014**, *118* (44), 25505–25516. https://doi.org/10.1021/jp507729w.

(253) Silly, F. Elucidating the Intramolecular Contrast in the STM Images of 2,4,6-Tris(4′,4′′,4′′′-Trimethylphenyl)-1,3,5-Triazine Molecules Recorded at Room-Temperature and at the Liquid-Solid Interface. *RSC Adv.* **2020**, *10* (10), 5742–5746. https://doi.org/10.1039/C9RA09681G.

(254) *Baran, Richter Essentials of Heterocyclic Chemistry-I ... / baran-richter-essentials-of-heterocyclic-chemistry-i.pdf / PDF4PRO*. PDF4PRO. https://pdf4pro.com/amp/view/baran-richter-essentials-of-heterocyclic-chemistry-i-1b5f0.html (accessed 2023-09-25).

(255) Duraimurugan, K.; Dhanamoorthy, V.; Madhavan, J.; Siva, A. Synthesis and Photophysical Investigations of C3-Triazine Based Star-like Conjugated Molecules. *J. Photochem. Photobiol. Chem.* **2018**, *359*, 164–171. https://doi.org/10.1016/j.jphotochem.2018.04.016.

(256) *eBook: CRC Handbook of Chemistry and Physics von William M. Haynes | ISBN 978-1-4987-5429-3 | Sofort-Download kaufen - Lehmanns.de*. https://www.lehmanns.de/shop/technik/39568473-9781498754293-crc-handbook-of-chemistry-and-physics (accessed 2023-08-29).

(257) Heravi, M. M.; Vazin Fard, M.; Faghihi, Z. Heteropoly Acids-Catalyzed Organic Reactions in Water: Doubly Green Reactions. *Green Chem. Lett. Rev.* **2013**, *6* (4), 282–300. https://doi.org/10.1080/17518253.2013.846415.

(258) SCHAEFER, F. C.; PETERS, G. A. Synthesis of the S-Triazine System. III.1 Trimerization of Imidates. *J. Org. Chem.* **1961**, *26* (8), 2778–2784. https://doi.org/10.1021/jo01066a036.

(259) Meier, H.; Holst, H. C.; Oehlhof, A. Star-Shaped Compounds Having 1,3,5-Triazine Cores. *Eur. J. Org. Chem.* **2003**, *2003* (21), 4173–4180. https://doi.org/10.1002/ejoc.200300132.

(260) Wu, H.; Lian, K. The Development of Pseudocapacitive Molybdenum Oxynitride Electrodes for Supercapacitors. *ECS Trans.* **2014**, *58* (25), 67. https://doi.org/10.1149/05825.0067ecst.

(261) Chen, R.; Li, T.; Zhang, Q.; Ding, Z.; Ma, P.; Zhang, S.; Chen, M.; Dong, W.; Ming, W. Design of Polyurethane Acrylic Antimicrobial Films via One-Step UV Curing. *New J. Chem.* **2017**, *41* (18), 9762–9768. https://doi.org/10.1039/C7NJ02023F.

(262) Song, X.; Ma, Y.; Wang, C.; Dietrich, P. M.; Unger, W. E. S.; Luo, Y. Effects of Protonation, Hydrogen Bonding, and Photodamaging on X-Ray Spectroscopy of the Amine Terminal Group in Aminothiolate Monolayers. *J. Phys. Chem. C* **2012**, *116* (23), 12649–12654. https://doi.org/10.1021/jp302716w.

(263) Bryant, M. A.; Crooks, R. M. Determination of Surface pKa Values of Surface-Confined Molecules Derivatized with pH-Sensitive Pendant Groups. *Langmuir* **1993**, *9* (2), 385–387. https://doi.org/10.1021/la00026a005.

(264) Vysotsky, Y. B.; Kartashynska, E. S.; Vollhardt, D.; Fainerman, V. B. Surface pKa of Saturated Carboxylic Acids at the Air/Water Interface: A Quantum Chemical Approach. *J. Phys. Chem. C* **2020**, *124* (25), 13809–13818. https://doi.org/10.1021/acs.jpcc.0c03785.

(265) Wellen, B. A.; Lach, E. A.; Allen, H. C. Surface pKa of Octanoic, Nonanoic, and Decanoic Fatty Acids at the Air–Water Interface: Applications to Atmospheric Aerosol Chemistry. *Phys. Chem. Chem. Phys.* **2017**, *19* (39), 26551–26558. https://doi.org/10.1039/C7CP04527A.

(266) Sharma, A.; Sharma, N.; Kumar, R.; Shard, A.; Sinha, A. K. Direct Olefination of Benzaldehydes into Hydroxy Functionalized Oligo (p-Phenylenevinylene)s via Pd-Catalyzed Heterodomino Knoevenagel-Decarboxylation-Heck Sequence and Its Application for Fluoride Sensing π-

Conjugated Units. *Chem. Commun.* **2010**, *46* (19), 3283–3285. https://doi.org/10.1039/C001980A.

(267) Matt, B.; Moussa, J.; Chamoreau, L.-M.; Afonso, C.; Proust, A.; Amouri, H.; Izzet, G. Elegant Approach to the Synthesis of a Unique Heteroleptic Cyclometalated Iridium(III)-Polyoxometalate Conjugate. *Organometallics* **2012**, *31* (1), 35–38. https://doi.org/10.1021/om200910p.

(268) Laurans, M. Synthèse d'hybrides de Polyoxométallates: Greffage Contrôlé Sur Électrodes Pour l'étude de Jonctions Moléculaires. 320.

(269) Combs-Walker, L. A.; Hill, C. L. Stabilization of the Defect ("lacunary") Complex Polymolybdophosphate, PMo11O397-. Isolation, Purification, Stability Characteristics, and Metalation Chemistry. *Inorg. Chem.* **1991**, *30* (21), 4016–4026. https://doi.org/10.1021/ic00021a010.

(270) Rinfray, C. Greffage de polyoxométallates hybrides sur surfaces planes. 199.

(271) Piot, M. Auto-assemblages d'hybrides de polyoxométallates par coordination dirigée. phdthesis, Sorbonne Université, 2018. https://theses.hal.science/tel-02865498 (accessed 2023-10-01).

(272) Mathurin, J.; Deniset-Besseau, A.; Bazin, D.; Dartois, E.; Wagner, M.; Dazzi, A. Photothermal AFM-IR Spectroscopy and Imaging: Status, Challenges, and Trends. *J. Appl. Phys.* **2022**, *131* (1), 010901. https://doi.org/10.1063/5.0063902.

(273) Horcas, I.; Fernández, R.; Gómez-Rodríguez, J. M.; Colchero, J.; Gómez-Herrero, J.; Baro, A. M. WSXM: A Software for Scanning Probe Microscopy and a Tool for Nanotechnology. *Rev. Sci. Instrum.* **2007**, *78* (1), 013705. https://doi.org/10.1063/1.2432410.

Appendix

Content table

I – Synthesis

I.1 – Synthesis of $TBA_4[PW_{11}O_{39}\{Sn(C_6H_4)I]$[267,268]

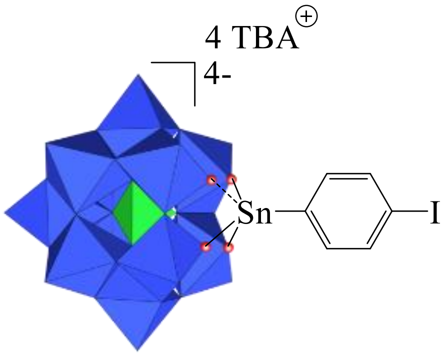

W = 3969.31 g/mol

1 g (0.31 mmol, 1 eq) de $K_7[PW_{11}O_{39}].14H_2O$ are dissolved in 10 ml of distilled water. 0.228 g (0.53 mmol, 1.7 eq) of $Cl_3Sn(C_6H_4)I$ are added to this solution and the mixture form a slurry which is left under agitation for 15 min at room temperature. The pH is maintained at 3.1 with a KOH solution (1 M). The mixture is centrifuged (10 min, 4000 rpm), filtered on membrane and 1.5 ml of distilled water containing 507 mg of TBABr are added to the filtrate. The solution is centrifuged (10 min, 4000 rpm) and the solid is washed 3 times with 15 ml of ethanol and twice with 15 ml of diethyl ether then, dried under vacuum. 958 mg (yield = 78%) of white powder are obtained.

Analysis

^{1}H NMR (400 MHz, CD3CN, ppm): δ 7.88 (d+dd, $J_{H\text{-}H}$ = 8.2 Hz, $J_{Sn\text{-}H}$ = 31 Hz, 2H, Ar-H), δ 7.49 (d+dd, $J_{H\text{-}H}$ = 8.2 Hz, $J_{Sn\text{-}H}$ = 93.5 Hz, 2H, Ar-H), δ 3.15 (m, 32H, N-CH2-CH2-CH2-CH3), δ 1.65 (m, 32H, N-CH2- CH2-CH2-CH3), δ 1.41 (sex, J = 7.4 Hz, 32H, N-CH2-CH2-CH2-CH3), δ 1.01 (t, J = 7.4 Hz, 48H, N-CH2-CH2-CH2-CH3).

^{31}P NMR (162 MHz, CD3CN, ppm): δ = -11.64 (s, $J_{Sn,P}$ = 23.5 Hz)

NMR ^{31}P

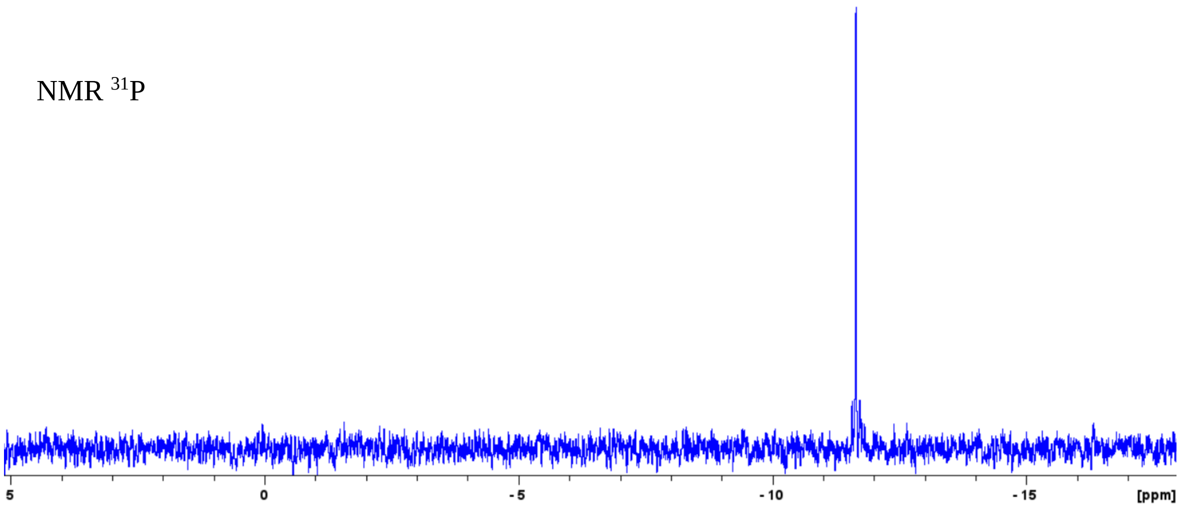

NMR ^{1}H

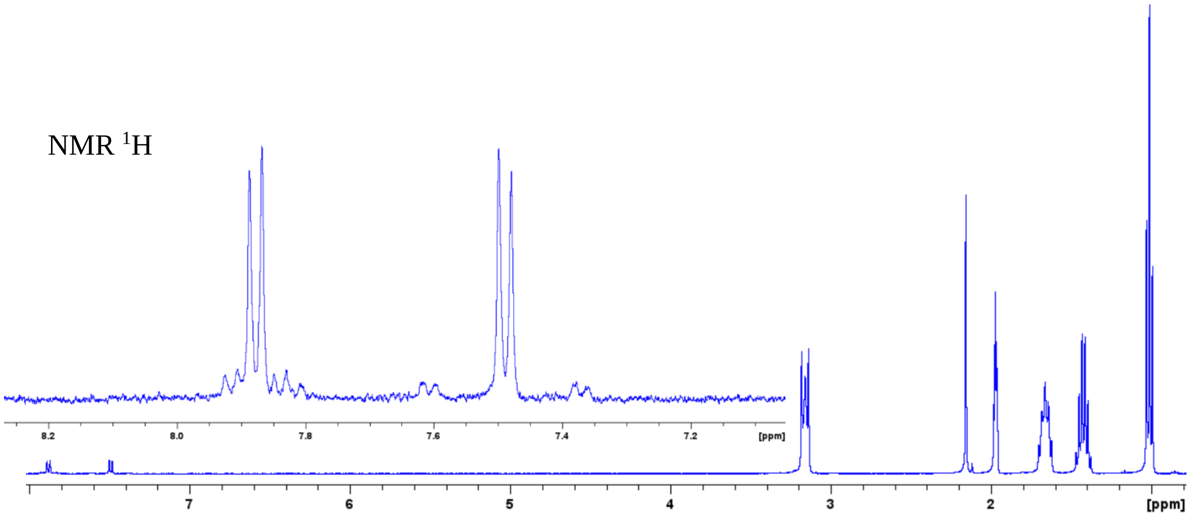

I.2 – Synthesis of 1-(pyren-1-yl)but-3-yn-1-ol[244]

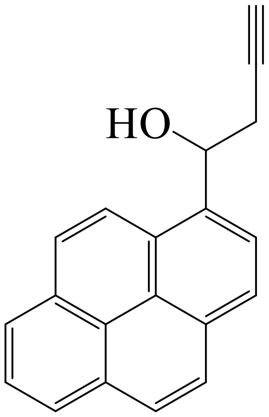

W = 270 g/mol

In a dry Schlenk under argon 300 mg (1.3 mmol, 1eq) of pyrene-1-carboxaldehyde are dissolved in 5 ml of anhydrous THF, 130 mg (1.98 mmol, 1.53 eq) of Zn powder and 12.5 µl (0.1 mmol, 0.077 eq) of TMSCl are added to the solution. The mixture is stirred for 15 min before the addition of 0.21 ml (1.94 mmol, 1.5 eq) of propargyl bromide. The temperature of the solution is raised to 45 °C and stirred for 4 h. 1 ml of saturated NH_4Cl in water are added to the solution and the product precipitate. the product is extracted with 2 x 20 ml of ethyl acetate. The organic phase is washed with 20 ml of saturated NaCl solution, dried on Na_2SO_4, filtered and the solvent evaporated. The product is purified by column chromatography with ethyl acetate/petroleum ether (10/90, 15/85, 20/80). 219 mg (yield = 81%) of product is obtained as a brown/orange solid.

Analysis

^{1}H NMR (400 MHz, $CDCl_3$, ppm): δ 8.46-8.02 (m, 9H, Py), δ 6.02 (m, 1H, **H**C(OH)CH$_2$C≡CH), δ 3.05-2.87 (m, 2H, CHC$\mathbf{H_2}$C≡CH), δ 8.20–8.16 (m, 2H, Py), δ 2.72 (d, 1H, J = 3.3 Hz, O**H**CH), δ 2.18 (t, 1H, J = 2.61 Hz, C**H**≡CCH$_2$)

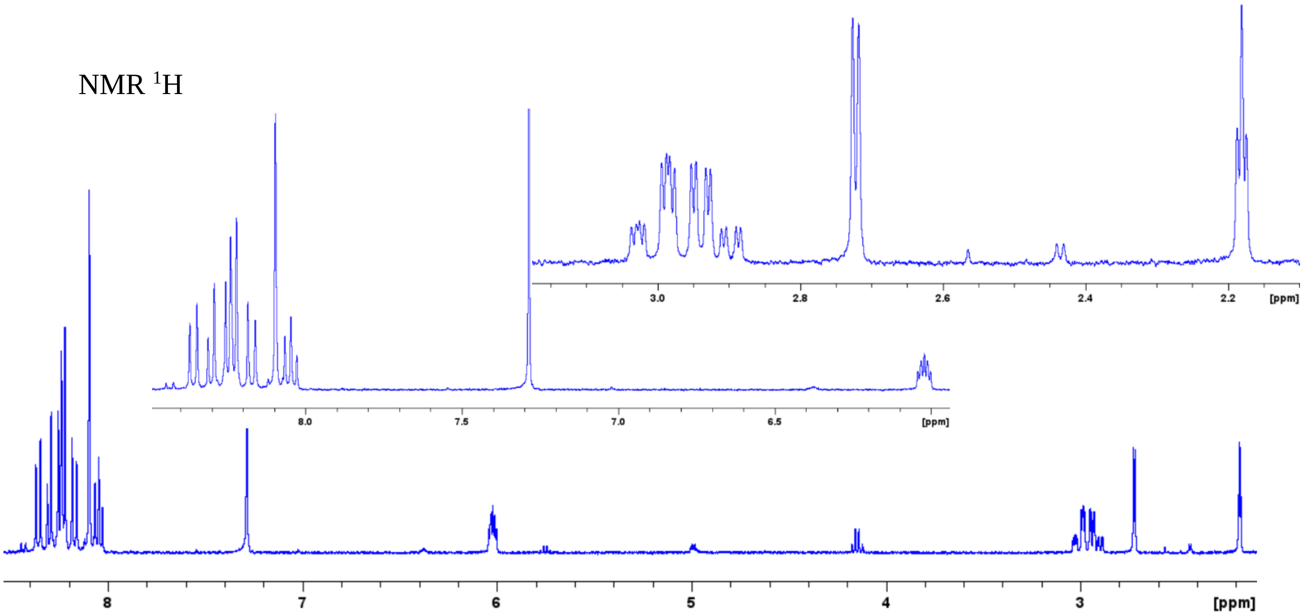

I.3 – Synthesis of 1-(but-3-yn-1-yl)pyrene[244]

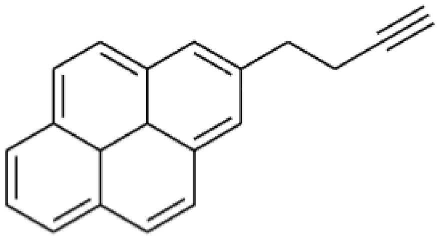

W = 253 g/mol

300 mg (1.1 mmol, 1eq) of 1-(pyren-1-yl)but-3-yn-1-ol are placed in a round bottom flask and dissolved in 5 ml of dichloromethane. 1 ml (6.1 mmol, 5.52 eq) of triethylsilane and 1 ml (8 mmol, 7.3 eq) of BF_3Et_2O are added to the solution and the mixture is stirred during 1h at room temperature. 20 ml of dichloromethane and 3 ml of saturated potassium bicarbonate solution are added. The organic phase is washed 2 times with 20 ml of NaCl saturated solution and 1 time with 20 ml of distillated water, dried on Na_2SO_4 then the solvent is evaporated. The solid product obtained was purified by column chromatography with ethyl acetate/petroleum ether (0/100 – 3/97). 105 mg (yield = 37.2 %) of white powder was obtained.

Analysis

^{1}H NMR (400 MHz, $CDCl_3$, ppm): δ 8.31 (d, J = 9.25 Hz, 1H, Py), δ 8.23-8.13 (m, 4H, Py), δ 8.06 (s, 2H, Py), δ 8.05-7.99 (m, 3H, Py), 7.95 (d, J = 8 Hz, 1H, Py), δ 3.64 (t, 2H, J = 7.76, C**H₂**CH2), δ 2.76 (dt, 2H, J = 2.61 Hz, 7.76 Hz, $CH_2C\mathbf{H_2}C\equiv CH$), δ 2.07 (t, 1H, J = 2.61 Hz, $C\mathbf{H}\equiv CCH_2$)

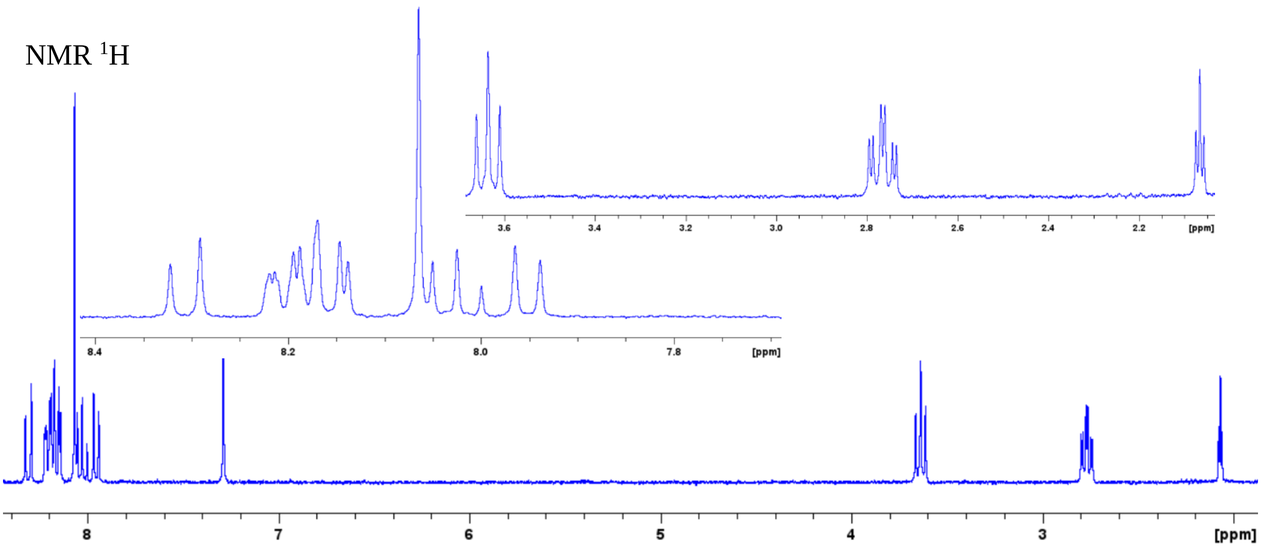

I.4 – Synthesis of $TBA_{3.5}Et_3NH_{0.5}[PW_{11}O_{39}\{Sn(C_{26}H_{16})\}]$ (TBA[KW(pyrene)])

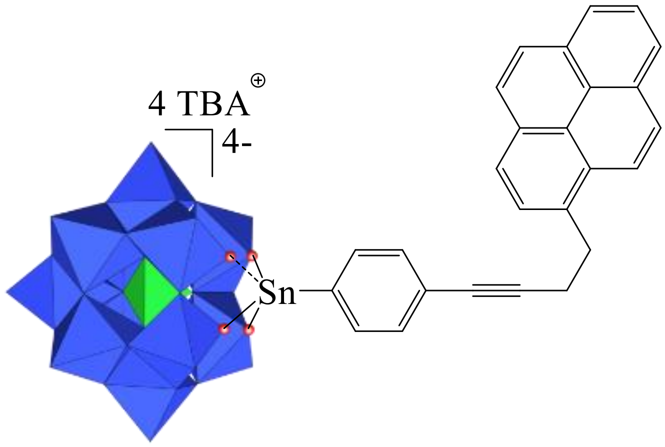

W = 3983.9 g/mol

TBA[K^W(pyrene)]

In a dry Schlenk filled with argon, 200 mg (0.05 mmol, 1 eq) of PW$_{11}$^{K}SnPhI.TBA, 2.3 mg (0.012 mmol, 0.24 eq) of CuI, 30.5 mg (0.12 mmol, 2.4 eq) of 1-(but-3-yn-1-yl)pyrene and 7.3 mg (0.01 mmol, 0.2 eq) of bis(triphenylphosphine)palladium(II) are dissolved in 4 ml of dry and degassed DMF, 50 µl of triethylamine are added and the mixture is stirred during one night at room temperature. A large excess of diethyl ether is added to the mixture to precipitate the product, the solution is centrifuged and the supernatant eliminated. The solid is dissolved in a minimum volume of acetonitrile, 25 ml of dichloromethane containing 250 mg (0.78 mmol, 15.5 eq) of TBABr are added and the mixture is stirred for 5 min. The solution is centrifuged and the solid phase is eliminated. The supernatant is concentrated under vacuum, and the pure product is precipitated with an excess of ethanol, washed twice with an excess of EtOH and once with Et$_2$O before drying under vacuum. 173 mg (yield = 86.8 %) of a dry white powder is obtained.

Analysis

^{1}H NMR (400 MHz, CD3CN, ppm): δ 8.5 (d, J = 9.36 Hz, 1H, Py), δ 8.31 - 8.22 (m, 4H, Py), δ 8.17 – 8.05 (m, 4H, Py), δ 7.61 (d, 2H, J = 7.63 Hz, Ar), δ 7.38 (d, J = 7.38, 2H, Ar), δ 3.72 (t, J = 7.15 Hz, 2H, CH2-CH2), δ 3.13 (t, J = 8.40 Hz, 32H, O-C**H2**-CH2), δ 3.02 (t, J = 7.15 Hz, 2H, CH2-CH2), δ 1.64 (m, 32H, N-CH2- CH2-CH2-CH3), δ 1.40 (sex, J = 7.43 Hz, 32H, N-CH2-CH2-CH2-CH3), δ 1 (t, J = 7.43 Hz, 48H, N-CH2-CH2-CH2-CH3).

^{31}P NMR (162 MHz, CD3CN, ppm): δ = -11.56 (s, J$_{Sn,P}$ = 23 Hz)

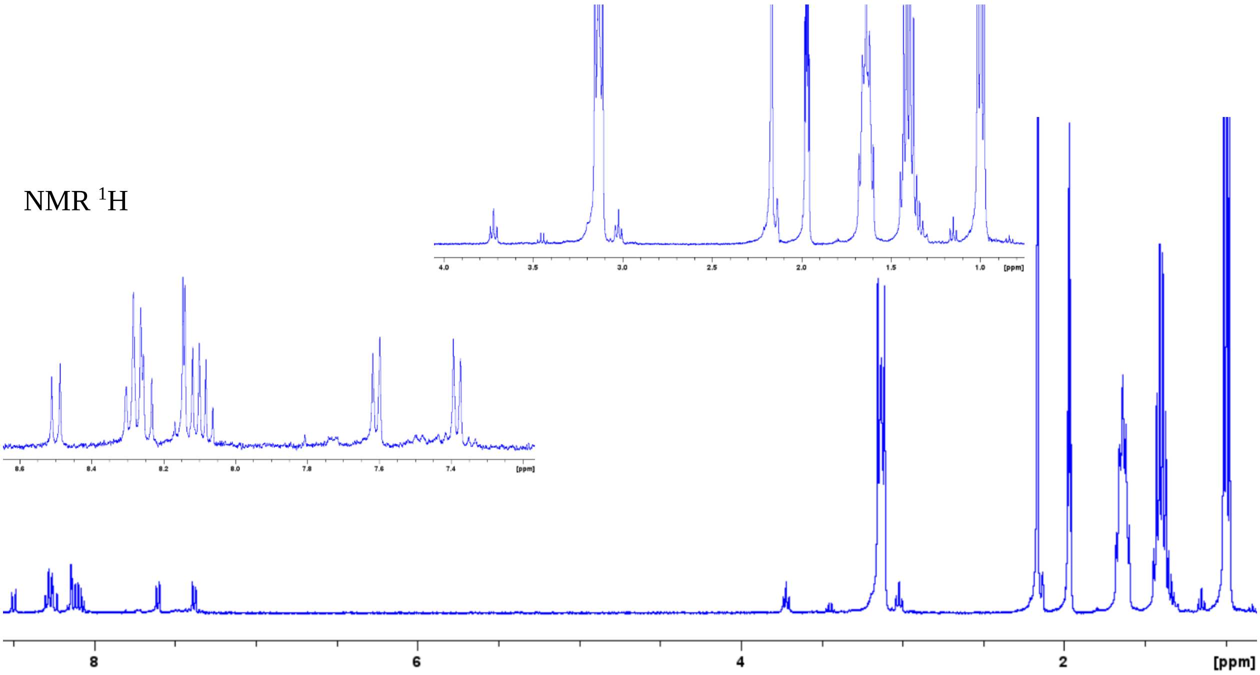

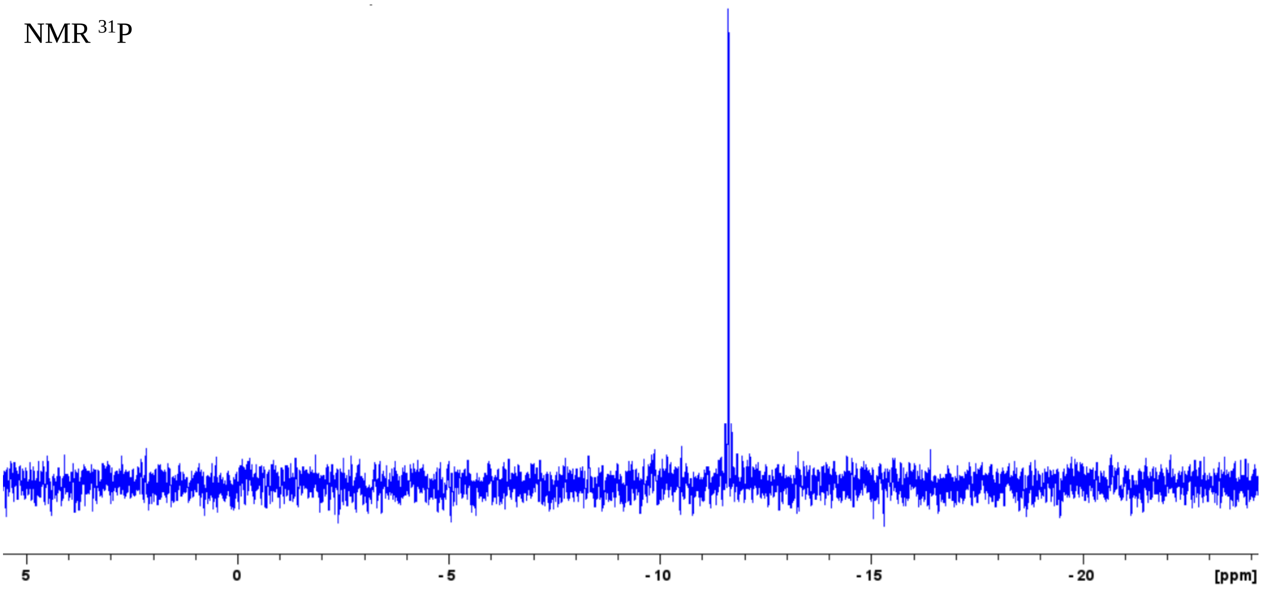

I.5 – Synthesis of TBA$_4$H$_3$[PMo$_{11}$O$_{39}$][269]

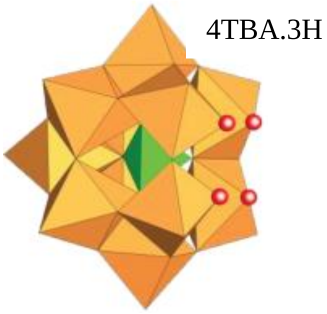

W = 2683.42 g/mol

7.30 g (2.72 mmol) of $H_3[PMo_{12}O_{40}]$ are dissolved in 40 ml of distillated water. The solution becomes yellow and acid (pH = 0). Lithium carbonate is added by steps to reach pH = 4.29, the solution becomes light green. 18 g (0.056 mol, 20 eq) of TBABr are added to the solution and the precipitated solid is filtrated and dried. The light green powder obtained is dissolved in a minimum of acetonitrile and left for 24 hours to obtain the first fraction of pure product after a slow recrystallization. Other fractions are obtained after more time.

Analysis

^{31}P NMR (162 MHz, CD3CN, ppm): δ = -1.69 (s)

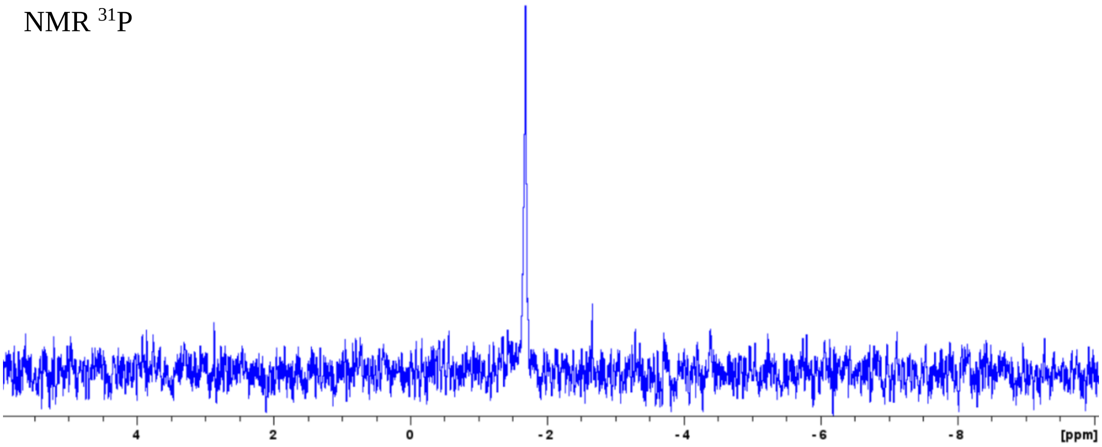

I.6 – Synthesis of $TBA_4[PMo_{11}O_{39}\{Sn(C_6H_4)I\}]$[270]

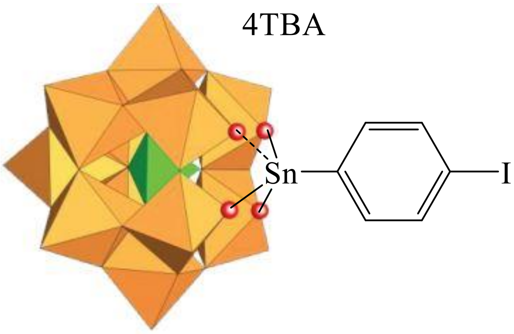

W = 3002.3 g/mol

1 g (0.37 mmol, 1eq) of $TBA_4H3[PMo_{11}O_{39}]$ are placed in a dry Schlenk under argon atmosphere and dissolved in 25 ml of dry acetonitrile and 0.1 ml (0.717, 20 eq) of freshly distilled triethylamine are added to the solution. 245 mg (0.573 mmol, 2.1 eq) of $Cl_3Sn(C_6H_4)I$ are dissolved in 5 ml of dry acetonitrile in another dry Schlenk under argon atmosphere. This second solution is transferred into the first one containing the POM and the mixture is stirred for 15 min. 361 mg (1.1 mmol, 3 eq) of TBABr are added and the product precipitates by addition of a large volume of THF/Et_2O (50/50 in volume). After centrifugation, the solid is dissolved in a minimal amount of acetonitrile, and the product precipitates by adding an excess of ethanol. The product is washed with ethanol and then dissolved in acetonitrile (5 ml) and dichloromethane (25 ml) containing 414 mg (0.28 mmol) of TBABr. The organic phase is washed three times with 40 ml of water, collected, and concentrated using a rotary evaporator. The product precipitates by adding an excess of diethyl ether. The solid is washed with ethanol 3 times and then with diethyl ether and dried under vacuum. A light green powder is obtained (687 mg, 62%).

Analysis

1H NMR (400 MHz, CD3CN, ppm): δ 7.82 (d+dd, $J_{H\text{-}H}$ =7.65 Hz, $J_{Sn\text{-}H}$ =30.75 Hz, 2H, Ar-H), δ 7.44 (d+dd, $J_{H\text{-}H}$ = 7.65 Hz, $J_{Sn\text{-}H}$ =95.1 Hz, 2H, Ar-H), δ 3.17 (m, 32H, N-CH2-CH2-CH2-CH3), δ 1.66 (m, 32H, N-CH2-CH2- CH2-CH3), δ 1.43 (sex, J = 7.26 Hz, 32H, N-CH2-CH2-CH2-CH3), δ 1.02 (t, J = 7.26 Hz, 48H, N-CH2-CH2-CH2- CH3)

^{31}P NMR (162 MHz, CD3CN, ppm): δ = -3.09 (s, $J_{Sn,P}$ = 35 Hz)

NMR ^1H

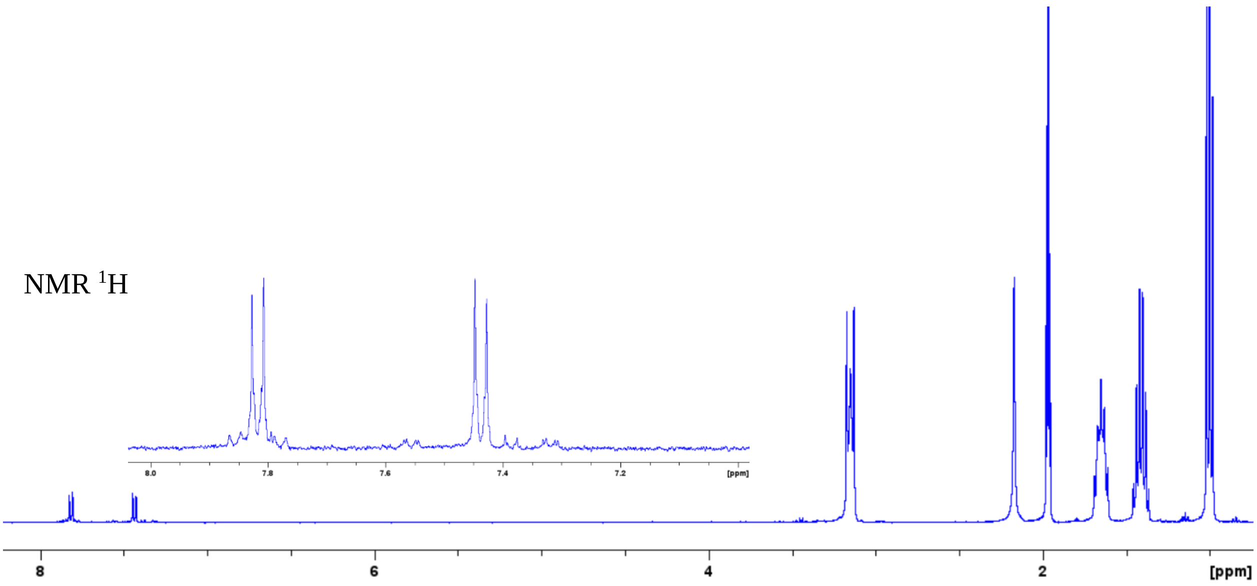

NMR ^{31}P

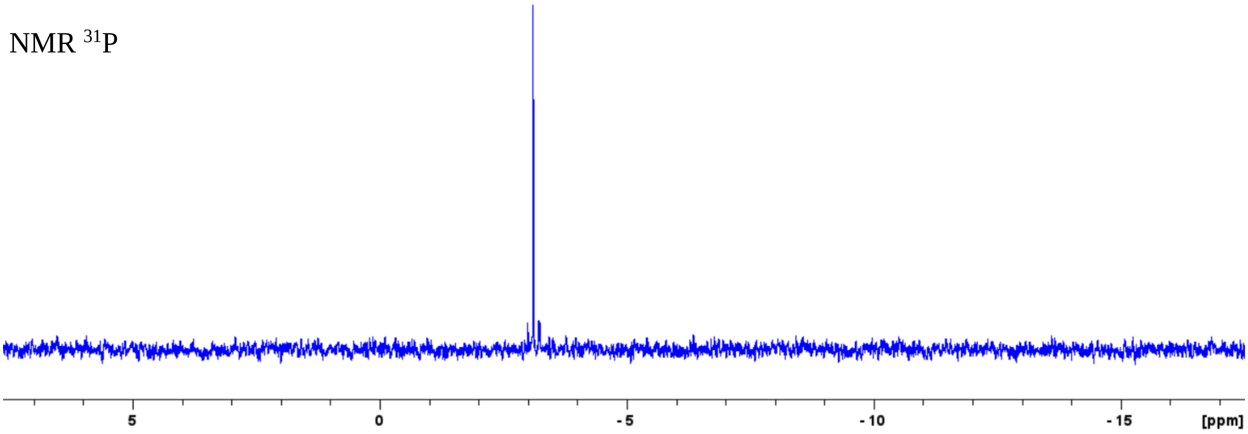

I.7 – Synthesis of TBA$_4$[PMo$_{11}$O$_{39}${Sn(C$_{13}$H$_8$N)}][271]

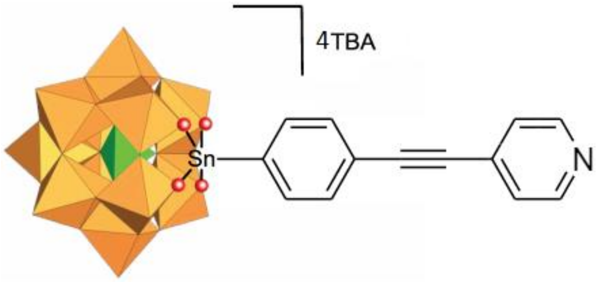

W = 2977.4 g/mol

TBA[K^{Mo}(pyr)]

200 mg (0.067 mmol, 1 eq) of TBA$_4$[PMo$_{11}$O$_{39}${Sn(C$_6$H$_4$)I}], 3.2 mg of CuI (0.017 mmol, 0.25 eq), 7.3 mg of Pd(PPh$_3$)$_2$Cl$_2$ (0.01 mmol, 0.15 eq), 20 mg of 4-ethynylpyridine hydrochloride (0.143 mmol, 2.13 eq) are dissolved with 4 ml of dry degassed DMF in a dry schlenk and stirred under argon, 50 µl of Et$_3$N are added and the mixture is stirred overnight. 20 ml of diethyl ether are added to the solution and a dark solid powder precipitate. After centrifugation, the solid is dissolved in a minimum volume of acetonitrile, then 20 ml of dichloromethane containing 300 mg (0.936 mmol, 14 eq) of TBABr are added to the solution and the mixture is stirred during 5 min, centrifuged for 10 min at 4000 rpm and the solid phase is eliminated. The supernatant is concentrated at the rotary evaporator, the product is precipitated by addition of ethanol, centrifuged, washed twice with 25 ml of ethanol and solubilized in 5 ml of acetonitrile. 1.2 eq of tetrabutylammonium hydroxide (0.081 mmol) are taken from a 1M solution of TBAOH in methanol and diluted 40 times in acetonitrile, then added slowly to the solution containing the POM. The mixture is stirred during 5 min and 20 ml of dichloromethane containing 300 mg of TBABr (0.94 mmol, 14 eq) are added. The organic phase is washed 3 times with 40 ml of distillated water, the product is precipitated by addition of diethyl ether in the organic phase and dried during 2 hours under vacuum. 123 mg (61% yield) of the product are obtained.

Analysis

1H NMR (400 MHz, CD3CN, ppm): δ 8.62 (d+dd, J = 5.08 Hz, 2H, Ar-H), δ 7.74 (d+dd, $J_{H\text{-}H}$ = 7.79 Hz, $J_{Sn\text{-}H}$ = 96 Hz, 2H, Ar-H), δ 7.65 (d, $J_{H\text{-}H}$ = 7.79 Hz, $J_{Sn\text{-}H}$ = 34 Hz, 2H, Ar-H), δ 7.49 (d, J = 5.08 Hz, 2H, Ar-H), δ 3.16 (m, 32H, N-CH2-CH2-CH2-CH3, CH2), δ 1.66 (m, 32H, N-CH2-CH2-CH2-CH3), δ 1.42 (sex, J = 7.02 Hz, 32H, N-CH2-CH2-CH2-CH3), δ 1.00 (t, J = 7.02 Hz, 48H, N-CH2-CH2-CH2-CH3)

31P NMR (162 MHz, CD3CN, ppm): δ = -3.08 (s, $J_{Sn,P}$ = 35 Hz)

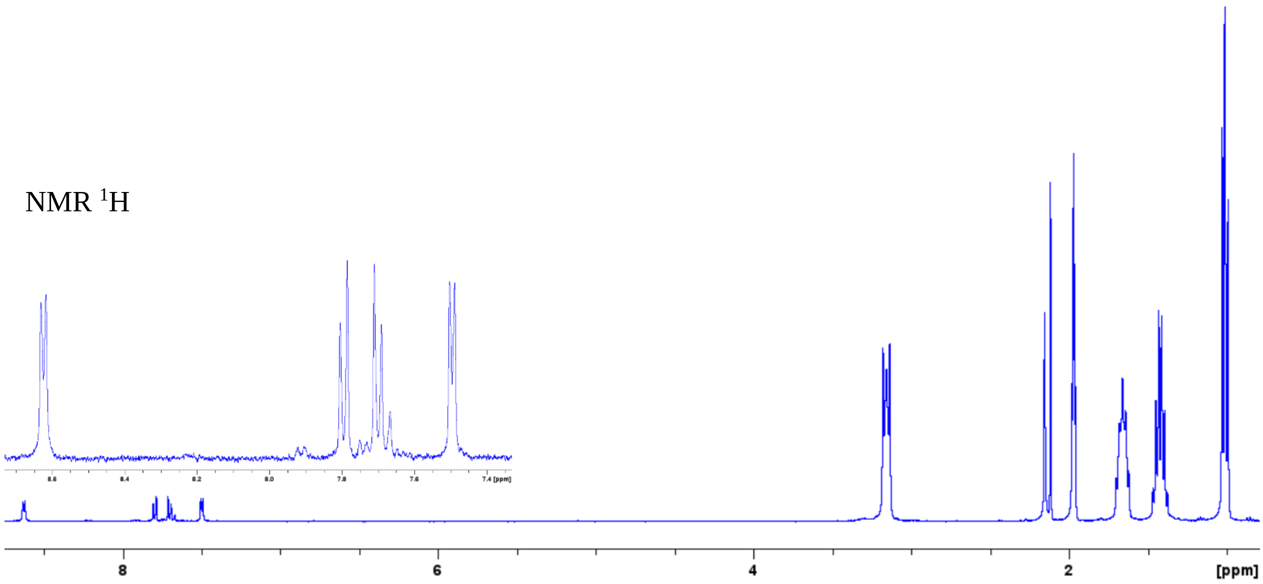

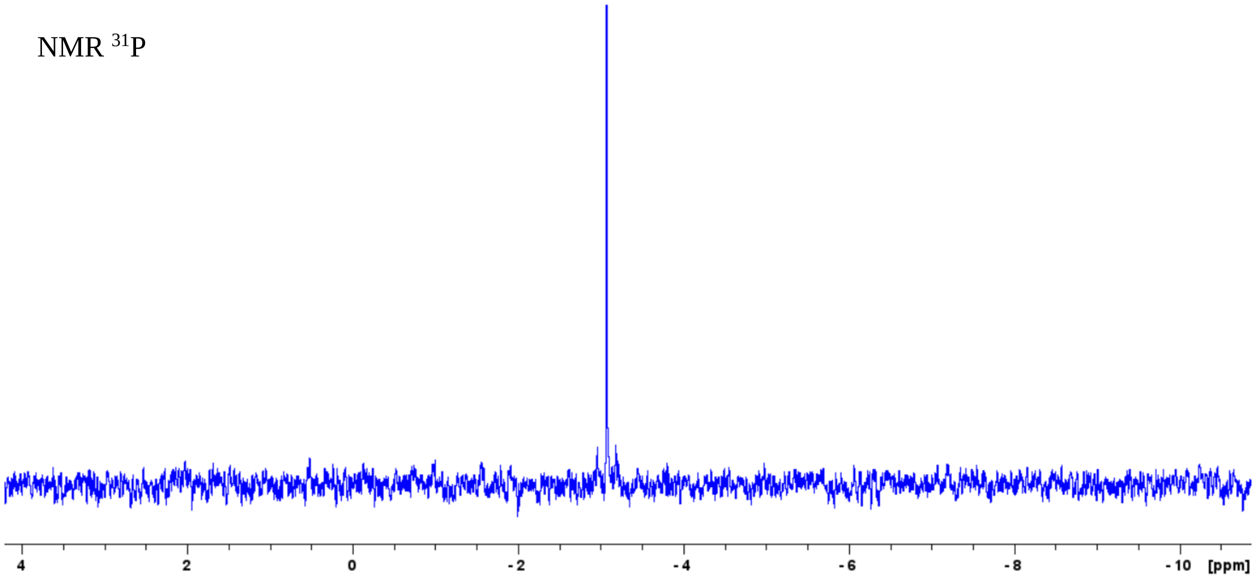

I.8 – Synthesis of $TBA_4[PW_{11}O_{39}\{Sn(C_{13}H_8N)\}]$[271]

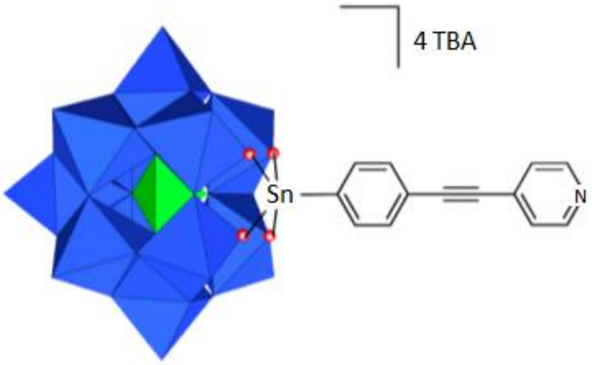

W = 3944.41 g/mol

TBA[K^W(pyr)]

200 mg of $TBA_4[PW_{11}O_{39}\{Sn(C_6H_4)I]$ (0.05 mmol, 1 eq), 3 mg of CuI (0.015 mmol, 0.3 eq), 7.5 mg of $Pd(PPh_3)_2Cl_2$ (0.011 mmol, 0.22 eq) and 21 mg of 4-ethynylpyridine hydrochloride (0.15 mmol, 3 eq) are placed in a dry schlenk under argon and solubilized in 4 ml of dry degassed DMF, 50 µl of ET_3N are added and the mixture is stirred overnight. The product is precipitated by addition of diethyl ether, centrifuged, and solubilized in a minimum of acetonitrile, then 25 ml of dichloromethane containing 300 mg of TBABr (0.936 mmol, 18.7 eq) are added to the solution. The mixture is stirred during 5 min, centrifuged, and the solid eliminated. The supernatant is concentrated with a rotary evaporator and the product is precipitated by addition of ethanol and solubilized in a 5 ml of acetonitrile. 0.5 eq of TBAOH 1M diluted 40 times in acetonitrile are added by a slow dripping, the mixture is stirred during 5 min and the product is precipitated by addition of diethyl ether. After centrifugation, the powder is dried under vacuum for 1 hour. 139 mg (yield = 70.2%) of powder are obtained.

Analysis

1H NMR (400 MHz, CD3CN, ppm): δ 8.63 (d+dd, $J_{H\text{-}H}$ = 5.15 Hz, 2H, Ar-H), δ 7.8 (d+dd, $J_{H\text{-}H}$ = 7.6 Hz, $J_{Sn\text{-}H}$ = 35 Hz, 2H, Ar-H), δ 7.7 (d, $J_{H\text{-}H}$ = 7.6 Hz, $J_{Sn\text{-}H}$ = 92 Hz, 2H, Ar-H), δ 7.5 (d, J = 5.41 Hz, 2H, Ar-H), δ 3.16 (m, 32H, N-CH2-CH2-CH2-CH3, CH2), δ 1.66 (m, 32H, N-CH2-CH2-CH2-CH3), δ 1.42 (sex, J = 7.05 Hz, 32H, N-CH2-CH2-CH2-CH3), δ 1.00 (t, J = 7.05 Hz, 48H, N-CH2-CH2-CH2-CH3)

31P NMR (162 MHz, CD3CN, ppm): δ = -11.61 (s, $J_{Sn,P}$ = 23 Hz)

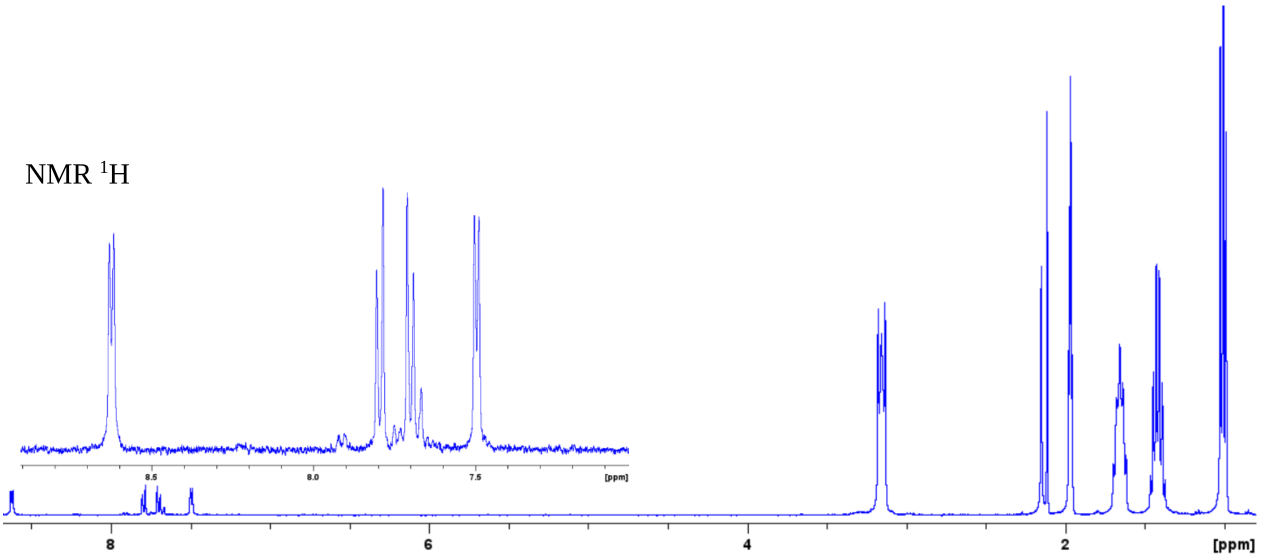

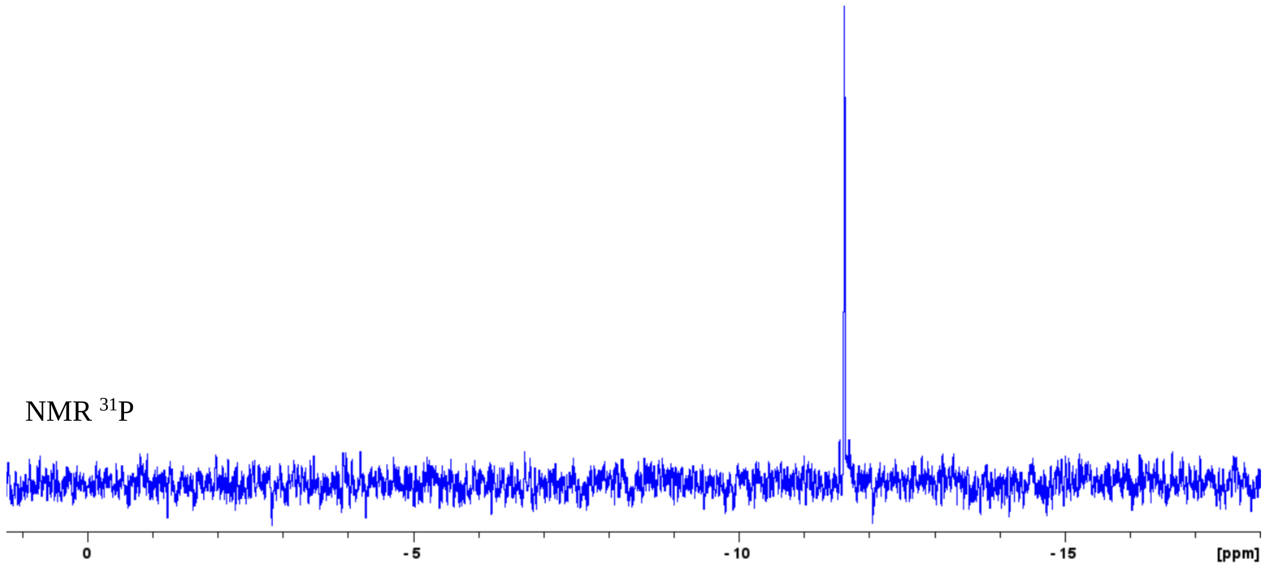

I.9 – Synthesis of $TOA_4[PW_{11}O_{39}\{Sn(C_{13}H_8N)\}]$

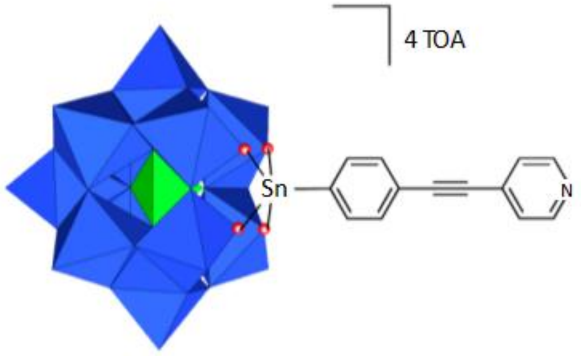

W = 4842.09 g/mol

TOA[K^W(pyr)]

250 mg of $TBA_4[PW_{11}O_{39}\{Sn(C_{13}H_8N)\}]$ (0.063 mmol, 1eq) are solubilized in 5 ml of acetonitrile, 138.6 mg of tetraoctylammonium bromide (0.253 mmol, 4.01 eq) are added to the solution and stirred during 5 min. 35 ml of distilled water slightly basified with 45 µl of KOH are added to the mixture to precipitate the POM. After centrifugation, the viscous brown product is solubilized in 5 ml of toluene and stirred, then 20 ml of cyclohexane are added to the mixture and the POM precipitate. The viscous product obtained after centrifugation is dried under static vacuum overnight. A brownish powder is obtained (189 mg, yield = 61.9%).

Analysis

1H NMR (400 MHz, CD3CN, ppm): δ 8.62 (d+dd, J = 5.82 Hz, 2H, Ar-H), δ 7.8 (d+dd, J = 8.2 Hz, 2H, Ar-H), δ 7.69 (d, J = 8.2 Hz, 2H, Ar-H), δ 7.48 (d, J = 5.82 Hz, 2H, Ar-H), δ 3.14 (m, 32H, N-CH2-CH2-CH2-CH3, CH2), δ 1.65 (m, 32H, N-CH2-CH2-CH2-CH3), δ 1.41-1.29 (m, 160H, TOA), δ 0.93 (t, J = 7.03 Hz, 48H, N-CH2-CH2-CH2-CH3).

31P NMR (162 MHz, CD3CN, ppm): δ = -11.63 (s, $J_{Sn,P}$ = 23 Hz)

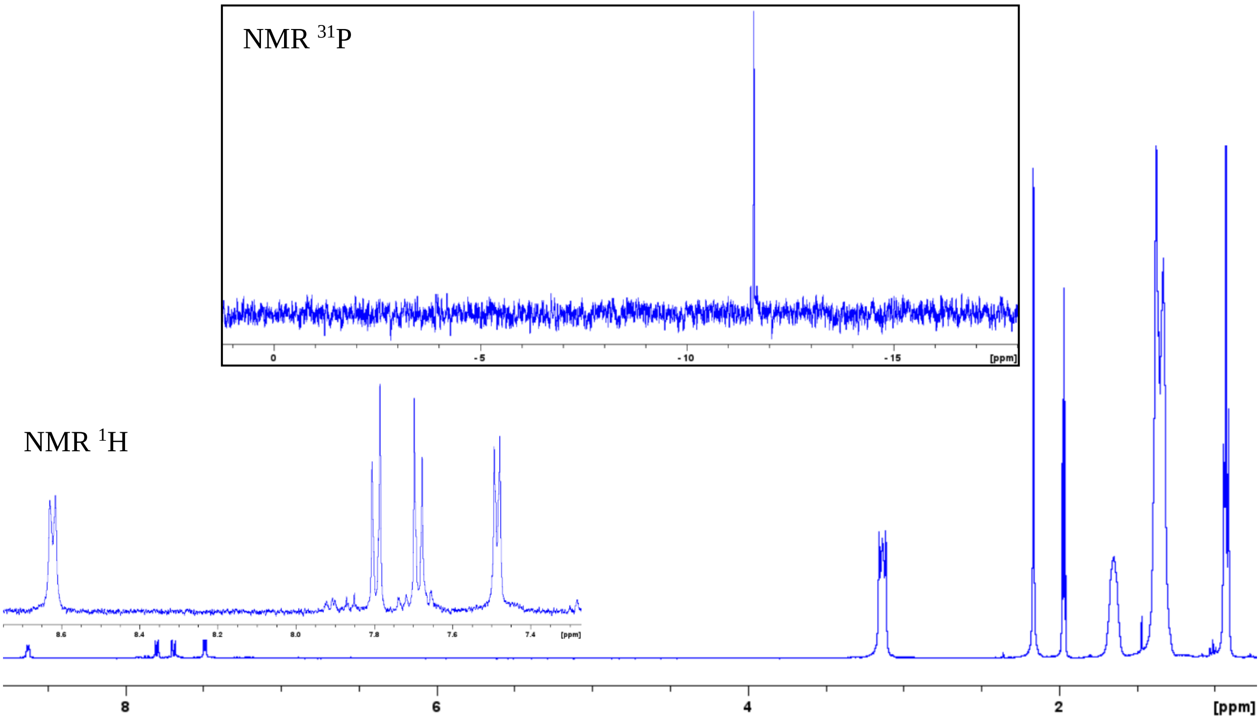

I.10 – Synthesis of ethyl acetimidate hydrochloride $CH_3C(=NH)OC_2H_5 \cdot HCl$[258]

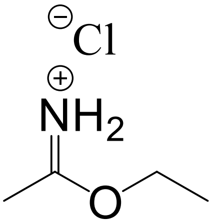

W = 123.58 g/mol

26.11 mL (0.5 mol, 1 eq.) of dry acetonitrile, 29.18 mL (0.5 mol, 1eq.) of absolute ethanol dried on a molecular sieve and 40 mL of toluene were introduced in a 200 mL round bottom flask. 1.1 equivalent of HCl was bubbled in the solution during two hours. The temperature was held below 45 °C using an ice bath. The mixture was then stirred overnight. The product was obtained as a white powder (yield 94%).

Analysis

1H NMR (400 MHz, $CDCl_3$, ppm): δ 12.45 (s, 1H, $=NH_2^+$), δ 11.52 (s, 1H, $=NH_2^+$), δ 4.65 (q, J = 7.1 Hz, 2H, O-CH_2-CH_3), δ 2.49 (s, 3H, CH_3C), δ 1.5 (t, J = 7.05 Hz, 3H, CH_3CH_2)

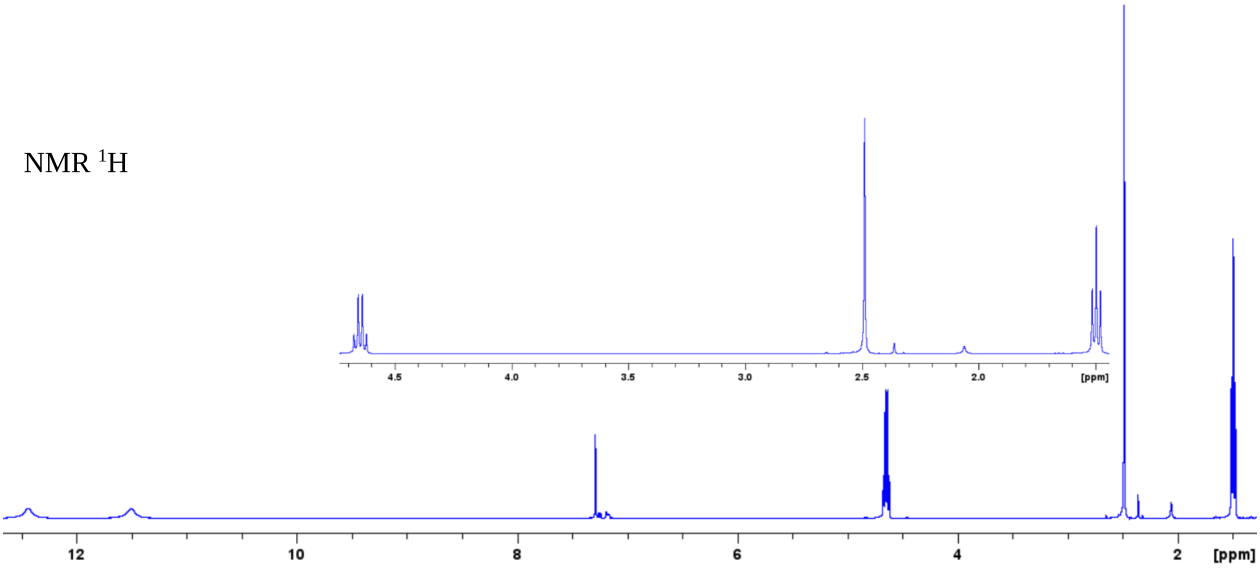

I.11 – Synthesis of ethyl acetimidate C_4H_9NO[258]

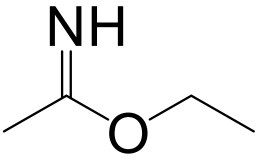

W = 87.12 g/mol

43.2g (0.35 mol, 1 eq.) of ethyl acetimidate hydrochloride were added to a vigorously stirred solution of dichloromethane (89 mL) and 72 g of potassium carbonate dissolved in 250 mL of water. After 10 min stirring the organic phase was separated and the aqueous phase was extracted with 50 ml fresh CH_2Cl_2 for another 20 min. The organic phases were assembled and dried on potassium carbonate overnight in a refrigerator. The product was obtained as a colorless liquid after filtration and solvent evaporation (yield 83%).

Analysis

1H NMR (400 MHz, $CDCl_3$, ppm): δ 6.8 (s, 1H, $=NH_1$), δ 4.12 (q, 2H, O-CH_2-CH_3), δ 2.01 (s, 3H, CH_3C), δ 1.29 (t, J = 7.10 Hz, 3H, CH_3CH_2)

** CH_2Cl_2 δ 5.3 ppm

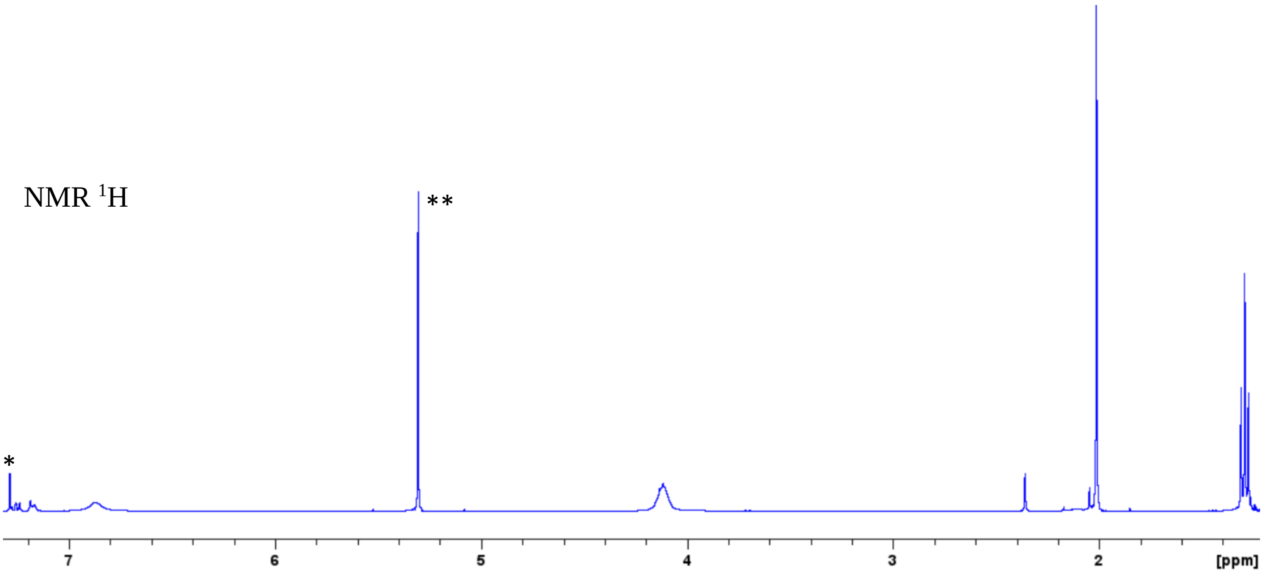

* $CHCl_3$ δ 7.29 ppm

I.12 – Synthesis of 2,4,6-Trimethyl-1,3,5-triazine $C_6H_9N_3$[258]

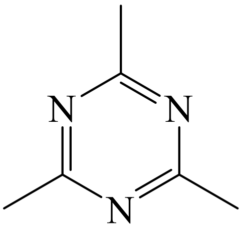

W = 123.16 g/mol

16 mL (0.164 mol, 1 eq.) of ethyl acetimidate free base were placed into a round bottom flask and stirred, 0.75 mL (0.0131 mol, 0.08 eq.) of glacial acetic acid were added dropwise and the

mixture was left under stirring overnight, in a water bath at 30 °C. The mixture was allowed to stand for 16 hours. The ethanol formed was eliminated using a rotary evaporator and the rest of the solution was diluted with 3 volumes of CH_2Cl_2 and the solution was filtered to eliminate the powder that crystalized and then washed with a solution of K2CO3 to remove the residual acetic acid. The organic phase was dried on Na2SO4 and the solvent evaporated. The product obtained was then purified by distillation (yield 79%).

Analysis

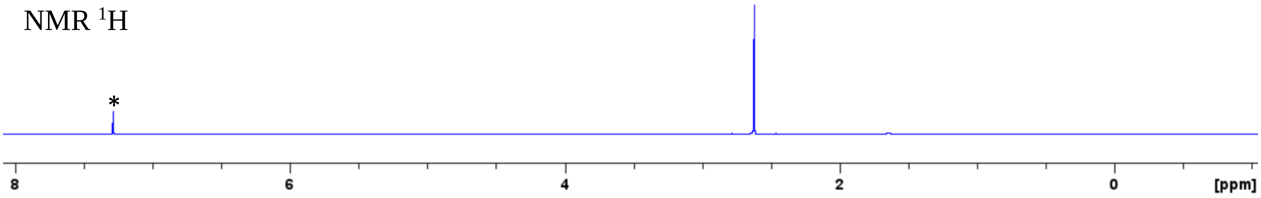

1H NMR (400 MHz, $CDCl_3$, ppm): δ 2.62 (s, 9H, 3 CH_3 of the triazine ring). *$CHCl_3$

I.13 – Synthesis of 3,5-bis(dodecyloxy)benzaldehyde

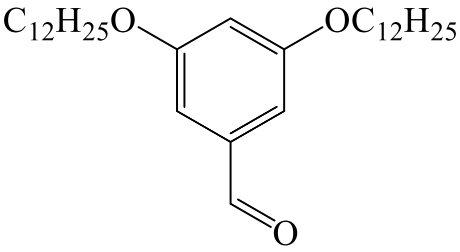

W = 123.16 g/mol

1g (7.44 mmol, 1 eq.) of 3,5-dihydroxybenzaldehyde and 6.16 g (44.6 mmol, 6 eq.) of potassium carbonate were mixed in 30 mL of DMF. 4.5 mL (18.62 mmol, 2.5 eq.) of 1-

bromododecane were added to the stirring solution and the mixture was refluxed during one night. The K2CO3 was filtered and 30 mL of dichloromethane were added to the solution, the organic phase was extracted five times with 70 ml of water, dried on Na2SO4 and the solvent was evaporated. The product was purified by flash chromatography (cyclohexane/dichloromethane) to obtain a white powder (yield 81%).

Analysis

1H NMR (400 MHz, $CDCl_3$, ppm): δ 9.91 (s, 1H, HCO), δ 7.01 (d, j = 2.25 Hz, 2H, Ar-H), δ 6.72 (t, j = 2.25 Hz, 1H, O-CH_2CH_2), δ 1.81 (sex, j = 6.93 Hz, 4H, $CH_2C\mathbf{H_2}CH_3$), δ 1.41-1.25 (m, 36H, alkyl), δ 0.90 (t, j = 6.93 Hz, 6H, CH_3CH_2).

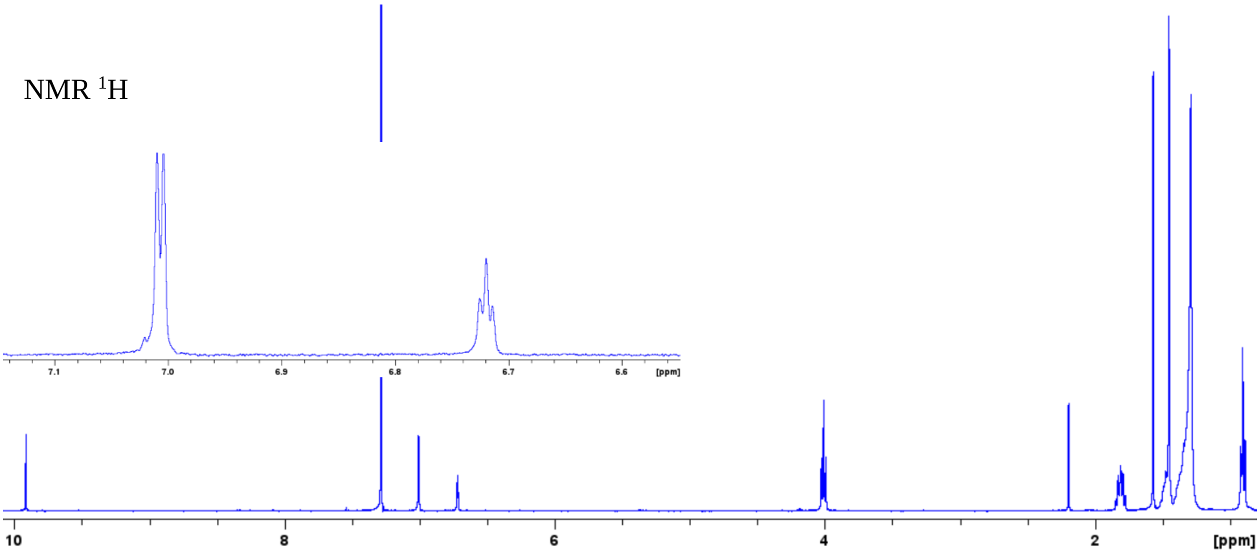

I.14 – Synthesis of 2,4,6-tris((E)-3,5-bis(dodecyloxy)styryl)-1,3,5-triazine (Tz-C12)

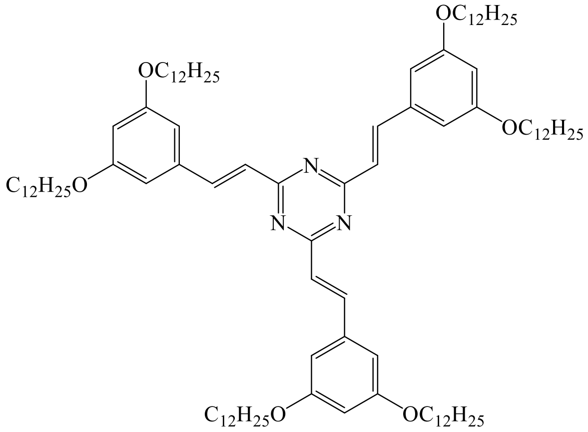

W = 1493.43 g/mol

Tz-C12

100 mg (0.81 mmol) of 2,4,6-trimethyl-s-triazine (1) and 1.54 g (3.25 mmol) of 3,5-(tridecyloxy)benzaldehyde (2) were solubilized in 22 mL of freshly distilled dry THF, 273 mg (2.44 mmol) of t BuOK are added and the solution was refluxed during 16 hours. The mixture was allowed to cool down to room temperature and 100 mL of cold ethanol were added. The product was filtrated and the solid washed with cold ethanol. The product was purified by flash chromatography (cyclohexane/dichloromethane) and a white powder was obtained (yield 73%).

Analysis

1H NMR (400 MHz, $CDCl_3$, ppm): δ 8.21 (d, J = 15.84 Hz, 3H, **H**C=CH-tz trans), δ 7.14 (d, j = 15.84 Hz, 3H, HC=C**H**-tz trans), δ 6.85 (d, j = 2.00 Hz, 6H, Ar-H), δ 6.53 (t, j = 2.00 Hz, 3H, Ar-H), δ 4.02 (t, j = 6.54 Hz, 12H, OCH_2), δ 1.83 (quint, J = 6.98 Hz,12H, OCH_2-C**H_2**-CH_2), δ 1.5 (m, 12H, CH_2C**H_2**CH_2), δ 1.43-1.25 (m, 96H, Alkyl-H), δ 0.90 (t, j = 7 Hz, 18H, CH_3CH_2). * H_2O ** $CHCl_3$

13C NMR (100 MHz, $CDCl_3$, ppm): δ (ppm) 171.34 ppm (N=C-N), 160.64 ppm (O-C=C), 141.94 ppm (Tz-CH=CH-C), 137.26 ppm (Ph), 126.56 ppm (Tz-CH=CH-C), 106.51 ppm (Ph), 103.58 ppm (Ph), 68.23 ppm (CH2-O), 31.9 ppm (-CH2-), 29.7 ppm (-CH2-), 29.65 ppm (-CH2-), 29.62 ppm (-CH2-), 29.60 ppm (-CH2-), 29.40 ppm (-CH2-), 29.36 ppm (-CH2-), 29.27 ppm (-CH2-), 26.08 ppm (-CH2-), 22.74 ppm (-CH2-)

HRMS (ESI), m/z (%) calculated for $C_{99}H_{165}N_3O_6H$: 1493.2771 $[M + H]^+$; found : 1493.277

NMR ^{1}H

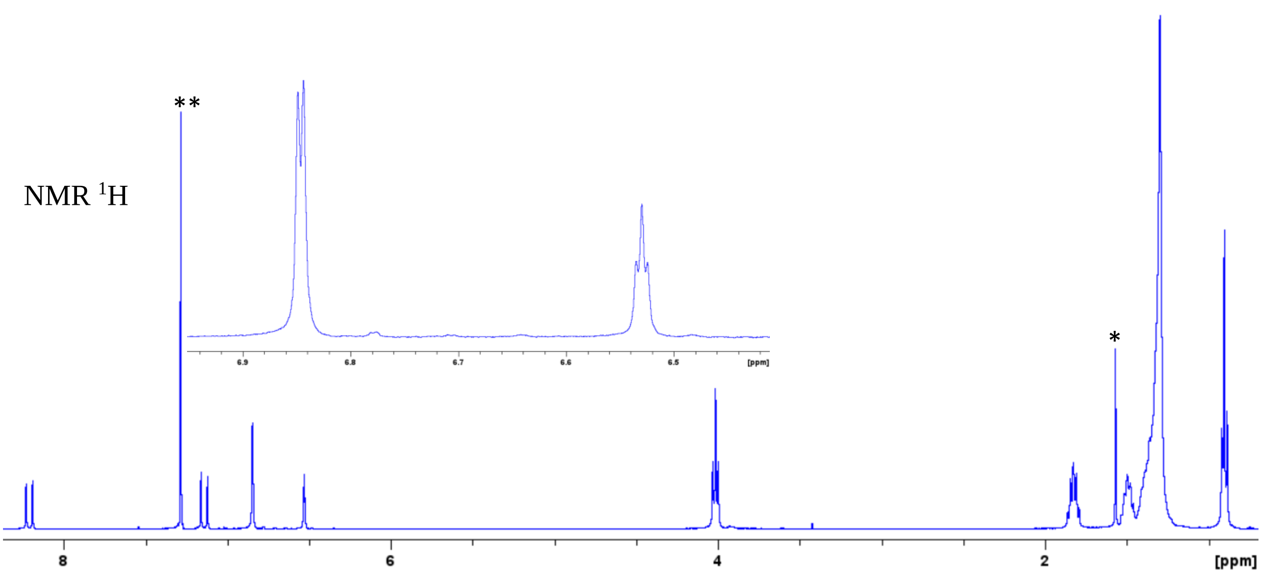

NMR ^{13}C jmod

HRMS

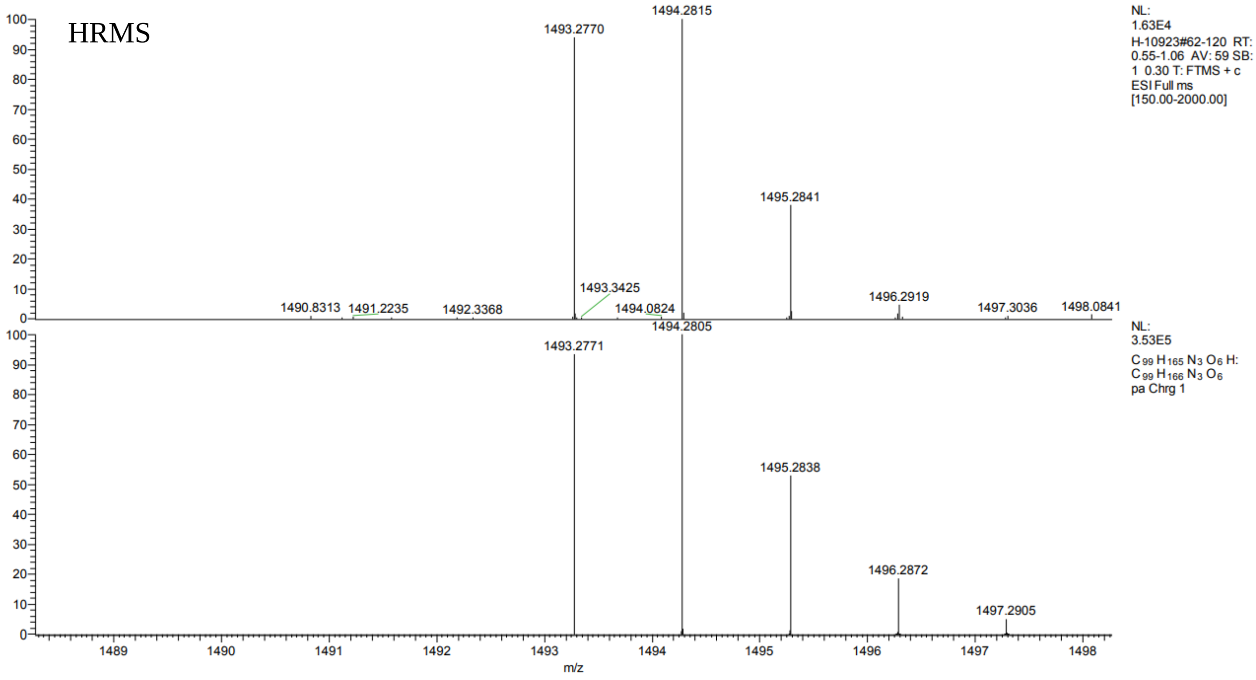

I.15 – Synthesis of 2,6-Dibromoisonicotinic acid

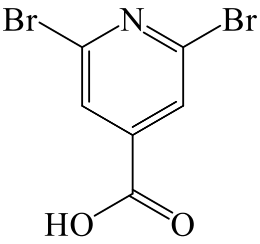

W = 280.90 g/mol

3.78 g (0.024 mol, 1 eq) of citrazinic acid are placed in a round bottom flask with 21 g (0.073 mol, 3.04 eq) of $POBr_3$. The products are heated at 140 °C and HBr vapors are released. After 16 hours, the reaction is quenched with deionized water (strongly exothermic). The solid phase is thoroughly washed with deionized water then placed in 100 ml of methanol and heated at 65°C. The solution is cooled to room temperature, filtered and the solvent evaporated. The brown powder obtained is washed with water and dried. 6.67 g of the product are obtained (yield = 99%).

Analysis

1H NMR (400 MHz, $CDCl_3$, ppm): δ 8.09 (s, Ar-H). * methanol, **$CHCl_3$

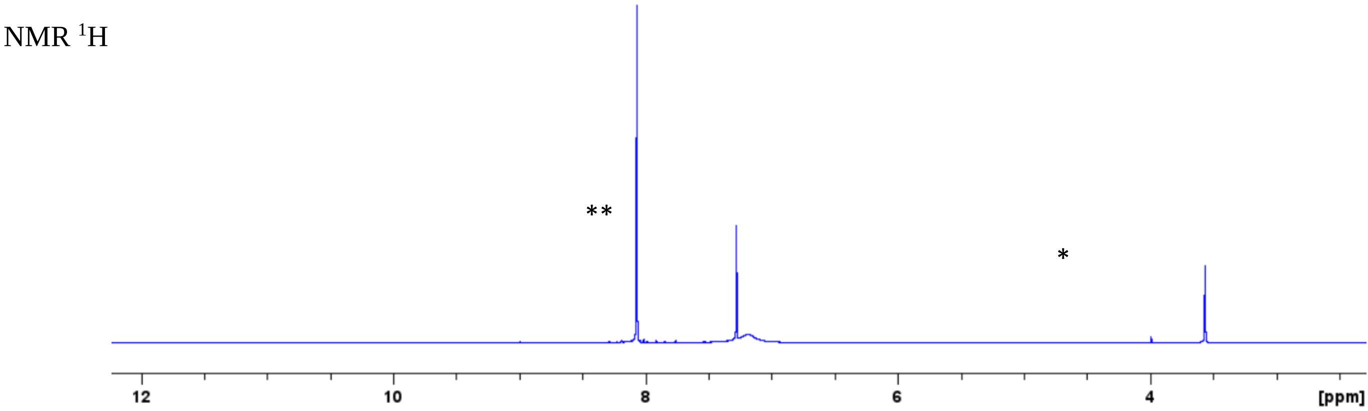

I.16 – Synthesis of 2,6-Dibromo-4-pyridinemethanol

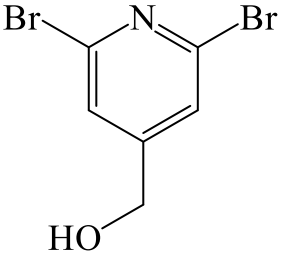

W = 266.92 g/mol

2.81 g (0.01 mol, 1 eq) of 2,6-Dibromoisonicotinic acid are placed in a round bottom flask under argon atmosphere and dissolved in 15 ml of freshly distilled THF. The solution is cooled at 0°C and 15 ml of BH_3THF solution (1M, 1.5 eq) are added slowly. The mixture is allowed to return to room temperature and stirred overnight. The reaction is quenched by a slow addition of deionized water, and the pH is adjusted to 9 using saturated solution of K_2CO_3. The mixture is extracted with 3 x 50 ml of dichloromethane, the organic phase is dried over Na_2SO_4 and the solvent is evaporated. 2.19 g of powder are obtained (yield = 82%).

Analysis

1H NMR (400 MHz, $CDCl_3$, ppm): δ 7.48 (s, 2H, Ar-H), δ 4.74 (s, 2H, CH_2), δ 2.22 (s, 1H, OH). *$CHCl_3$

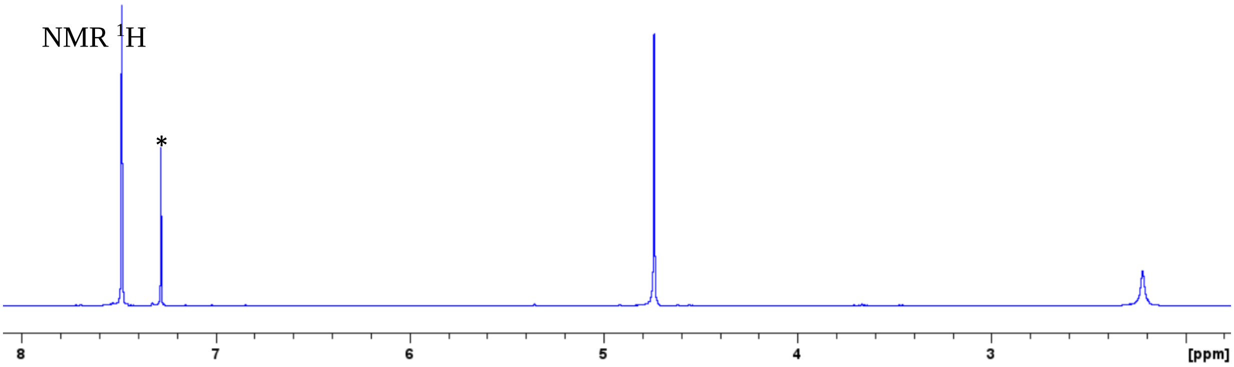

I.17 – Synthesis of (2,6-di(dodec-1-yn-1-yl)pyridin-4-yl)methanol

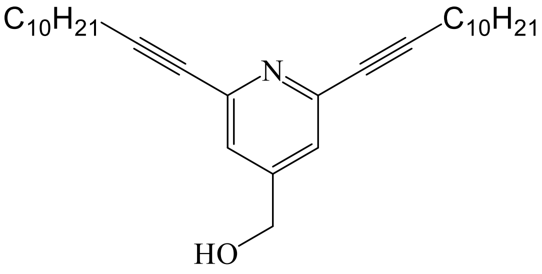

W = 437.71 g/mol

1 g (3.75 mmol, 1 eq) of 2,6-Dibromo-4-pyridinemethanol, 2.4 ml (11.23 mmol, 3 eq) of 1-dodecyne, 140 mg (5% mol) of $Pd(PPh_3)_2Cl_2$ and 37 mg (5% mol) of CuI are placed in a schlenk flask under argon atmosphere. 5 ml dry and degassed DMF and 5 ml of freshly distilled Et_3N are added and the mixture is stirred during 12h. 30 ml of deionized water are added and the solution is extracted with 3 x 30 ml of pentane; The organic phase is washed with water 2 x 40 ml, dried over Na_2SO_4 and the solvent is evaporated. The oily orange solid obtained is purified by flash chromatography (cyclohexane/AcOEt 100/0 – 100/20). 1.28 g of product are obtained (yield = 78%).

Analysis

1H NMR (400 MHz, $CDCl_3$, ppm): δ 7.28 (s, 2H, Ar-H), δ 4.70 (d, j = 6.05 Hz, 2H, CH_2), δ 2.43 (t, j = 7.10 Hz, 4H, 2CH_2-C≡C), δ 1.86 (t, j = 6.05 Hz, 1H, O**H**-CH_2), δ 1.63 (quint, j = 7.34 Hz, 4H, $CH_2\text{-}C\mathbf{H_2}\text{-}CH_2$), δ 1.45 (m, 4H, $CH_2\text{-}C\mathbf{H_2}\text{-}CH_2$), δ 1.35-1.26 (m, 24H, Alkyl-H), δ 0.90 (t, j = 7 Hz, 6H, 2CH_3CH_2).

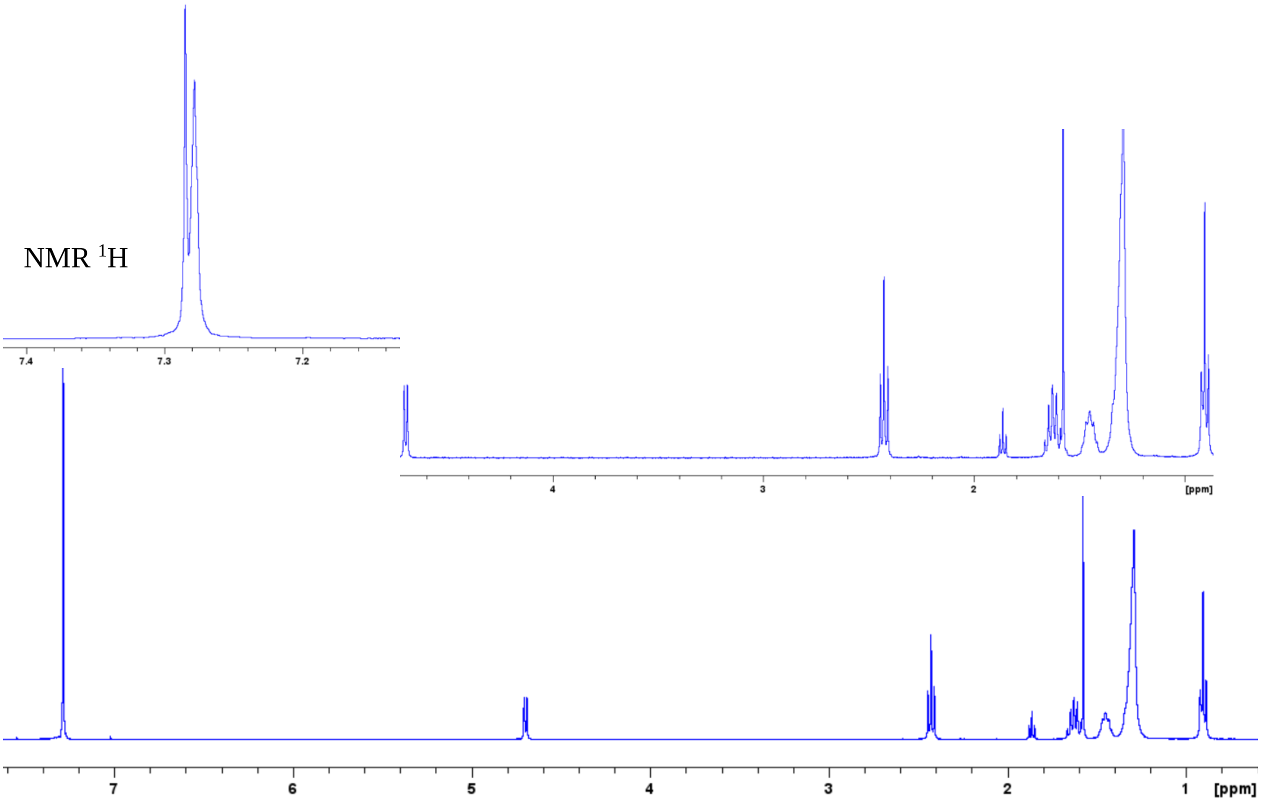

I.18 – Synthesis of (2,6-didodecylpyridin-4-yl)methanol

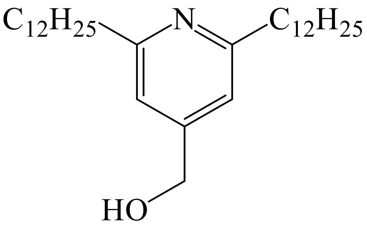

W = 445.78 g/mol

2.02 g (4.62 mmol, 1eq) of (2,6-di(dodec-1-yn-1-yl)pyridin-4-yl)methanol and 483 mg of Pd/C (10% W) (5% mol of Pd) are placed in a round bottom flask under argon atmosphere. 14 ml of dried and degassed methanol and 14 ml of freshly distilled THF are added. H_2 gas is introduced through a syringe and the mixture is stirred during 18h. 50 ml of dichloromethane are added and the solution is filtered on celite. The solvent is evaporated and an orange oily solid is obtained. (2.05 g, yield 99.5%).

Analysis

1H NMR (400 MHz, CDCl$_3$, ppm): δ 6.97 (s, 2H, Ar-H), δ 4.71 (s, 2H, CH$_2$), δ 2.77 (t, j = 7.86 Hz, 4H, 2C$\mathbf{H_2}$-CH$_2$), δ 1.71 (m, 4H, 2CH$_2$-C$\mathbf{H_2}$-CH$_2$), δ 1.41-1.25 (m, 36H, Alkyl-H), δ 0.90 (t, j = 7.02 Hz, 6H, 2CH$_3$CH$_2$).

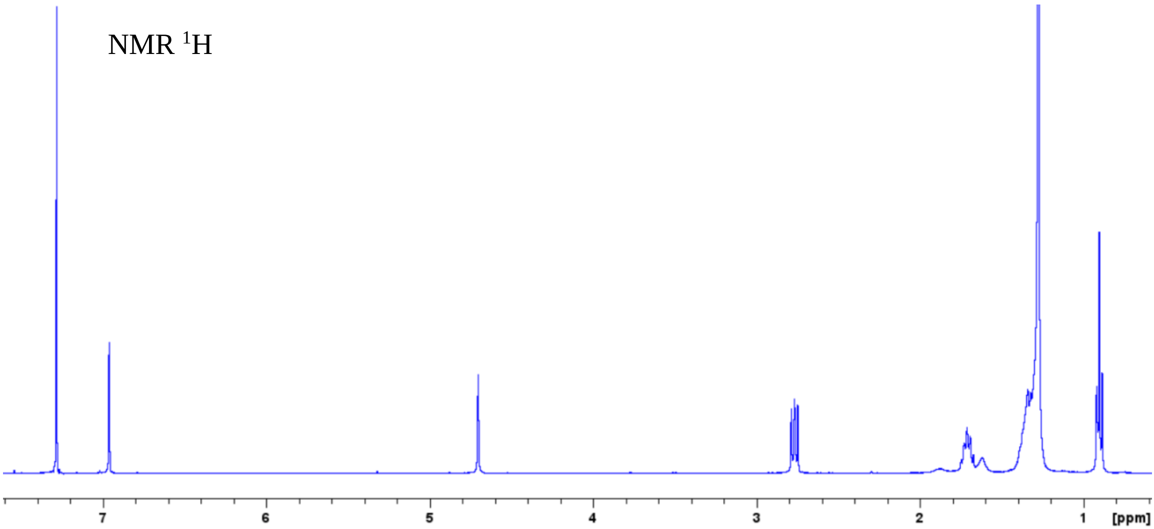

I.19 – Synthesis of 2,6-didodecynepyridine-4-methanal

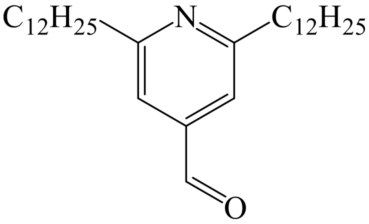

W = 443.76 g/mol

15 ml of dichloromethane are placed in a round bottom flask and cooled to -78 °C and 1 ml of $(COCl)_2$ (11.3 mmol, 5 eq) are introduced. 1.7 ml of dry DMSO (22.5 mmol, 10 eq) in 3 ml of dry dichloromethane are added slowly to the solution. The mixture is stirred during 15 min, and a solution containing 1 g of (2,6-didodecylpyridin-4-yl)methanol (2.25 mmol, 1 eq) in 50 ml of dry dichloromethane are added slowly. The mixture is stirred during 30 min, 5 ml of freshly distilled Et_3N (15 eq) are added and the mixture is stirred for 30 more minutes at -78°C. The solution is allowed to return to room temperature and 100 ml of water are slowly added, the organic phase is separated and the aqueous phase extracted with 2 x 40 ml of CH_2Cl_2. The reassembled organic phases are dried with Na_2SO_4 and the solvent evaporated. The product is purified by flash chromatography (cyclohexane/AcOEt 85/15). 720 mg of pure product are obtained (yield = 72.1%).

Analysis

1H NMR (400 MHz, $CDCl_3$, ppm): δ 10.05 (s, 1H, HCO), δ 7.37 (s, 2H, Ar-H), δ 2.88 (t, j = 7.83 Hz, 4H, 2C**H_2**-CH_2), δ 1.75 (m, 4H, 2CH_2-C**H_2**-CH_2), δ 1.42-1.24 (m, 36H, Alkyl-H), δ 0.90 (t, j = 7.02 Hz, 6H, CH_3CH_2).

NMR ^1H

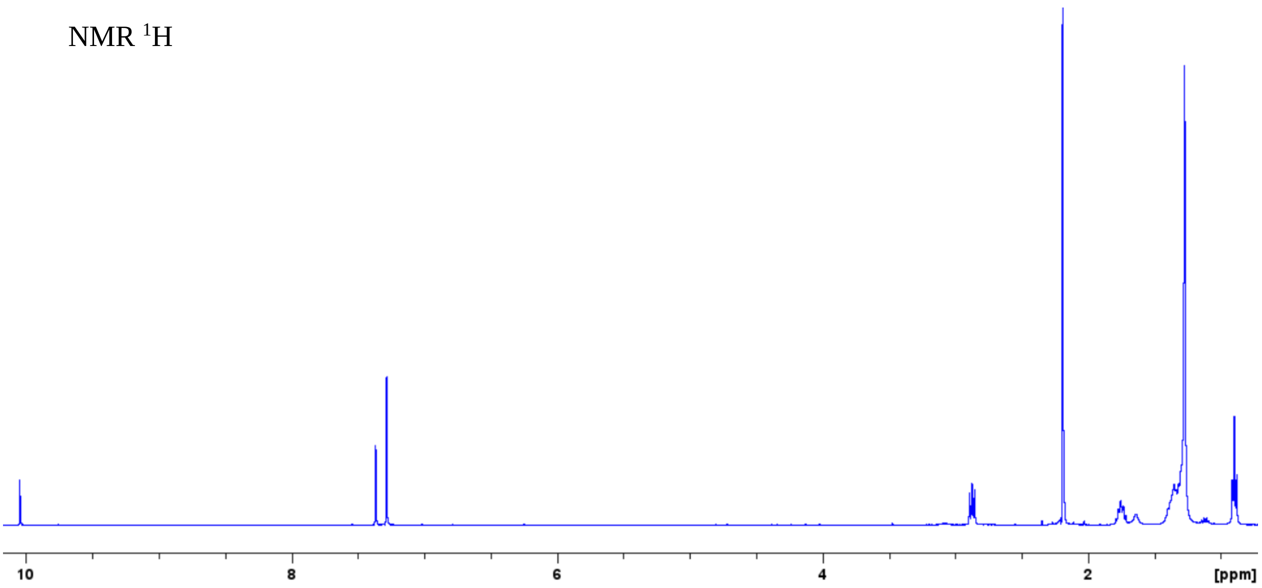

I.20 – Synthesis of Hexaethyl (s-phenenyltrimethylene)triphosphonate

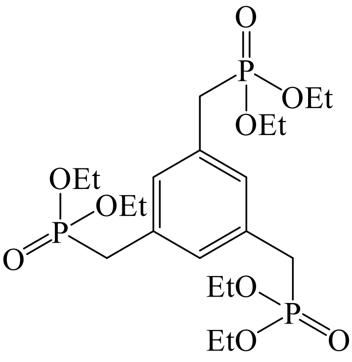

W = 528.45 g/mol

1g of 1,3,5-Tri(bromomethyl)benzene (2.8 mmol, 1eq) and 2.5 ml of triethyl phosphite (14.4 mmol, 5.1 eq) are placed in a round bottom flask. The mixture is heated at 140 °C and stirred during 12h. The product is purified by distillation under vacuum in a Kugelrohr (T=130 °C) to eliminate the triethyl phosphite. A colorless liquid is obtained (1.48 g, yield 100%).

Analysis

1H NMR (400 MHz, $CDCl_3$, ppm): δ 7.11 (m, 5H, Ar-H), δ 4.00 (m, 12H, CH_2), δ 3.09 (d, j = 21.75 Hz, CH_2), δ 1.23 (t, j = 6.98 Hz, 18H, CH_3CH_2).

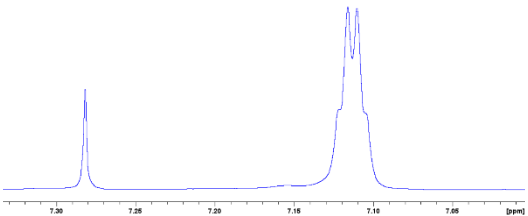

NMR ^{1}H

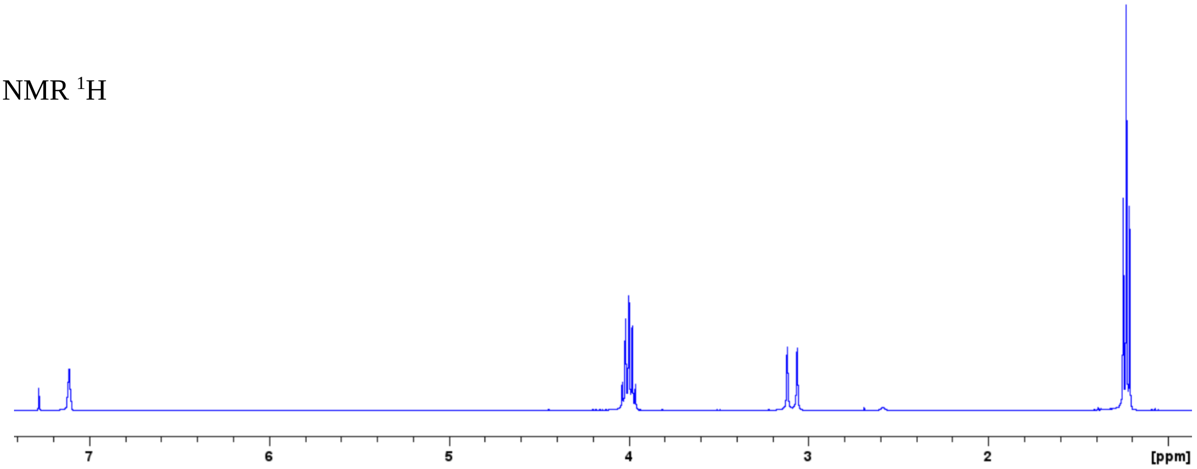

I.21 – Synthesis of 1,3,5-tris((E)-2-(2,6-didodecylpyridin-4-yl)vinyl)benzene

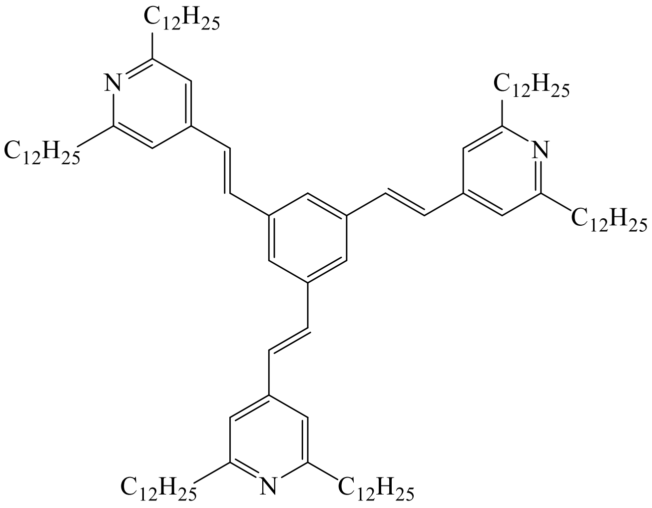

W = 1397.43 g/mol

100 mg of Hexaethyl (s-phenenyltrimethylene)triphosphonate (0.189 mmol, 1 eq) and 260 mg of 2,6-didodecynepyridine-4-methanal (587 mmol, 3.1 eq) are placed in a round bottom flask under argon atmosphere and solubilized in 5 ml of freshly distilled THF. The mixture is cooled to 0°C and a solution of NaH (15.7 mg, 0.657 mmol) with 5% mol of 15-Crown-5 in 3 ml of THF is added slowly and the mixture is stirred overnight. 25 ml of CH_2Cl_2 are added to the solution and the organic

phase is washed with 3 x 40 ml of water, dried over Na_2SO_4 and the solvent evaporated. The product is purified by a recrystallization in absolute ethanol.

Analysis

1H NMR (400 MHz, $CDCl_3$, ppm): δ 7.64 (s, 3H, Ar-H), δ 7.33 (d, j = 16.28 Hz, 3H, **H**C=CH-tz), δ 7.11 (d, j = 16.28 Hz, HC=C**H**-tz), δ 7.08 (s, 6H, Py-H), δ 2.81 (t, j = 7.75 Hz, 12H, Py-CH_2-), δ 1.76 (m, 12H, Alkyl-H), δ 1.45 – 1.22 (m, 98H, Alkyl-H), δ 0.88 (t, j = 7.00 Hz, 12H, CH_3-CH_2).

13C NMR (100 MHz, $CDCl_3$, ppm): δ 162.6 ppm (C=C benz), 144.80 ppm (C=C Py), δ 137.6 ppm (C=**C**-alkyl Py), 131.5 ppm (HC=CH benz), 128.04 ppm (Py-CH=**CH**-benz), 125.04 ppm (Py-**CH**=CH-benz), 117.11 ppm (HC=CH Py), 38.7 ppm (Py-CH_2), 31.9 ppm (Py-CH_2-**CH_2**), 30.3 – 29.5 ppm (alkyl CH_2), 22.8 ppm (**CH_2**-CH_3), 14.1 ppm (CH_3)

NMR ^{1}H

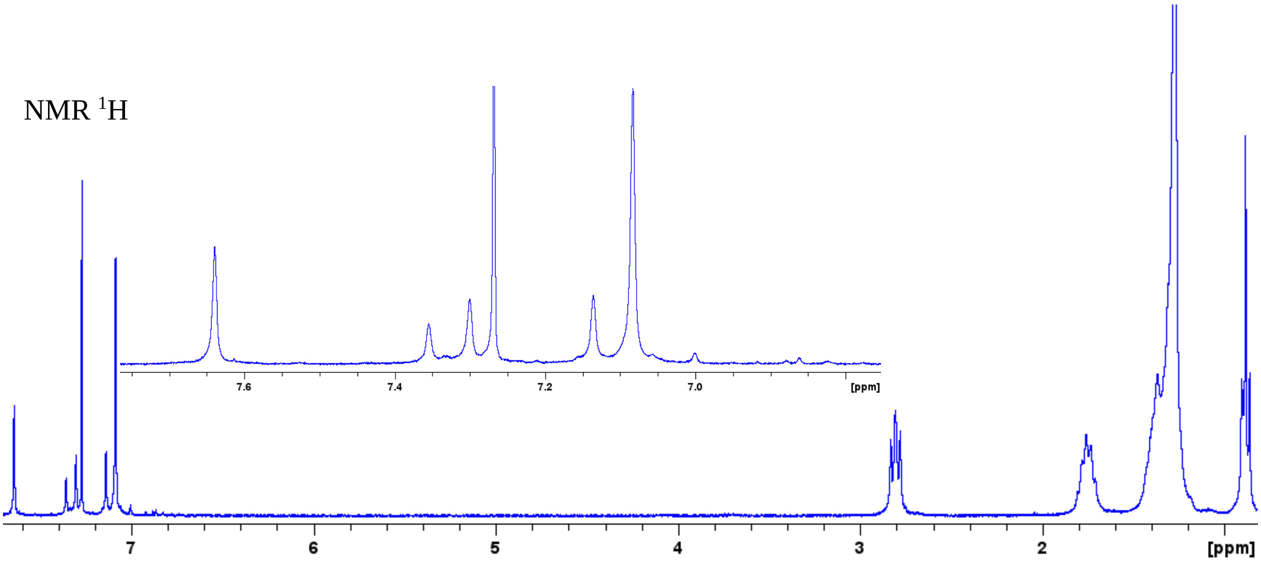

NMR ^{13}C jmod

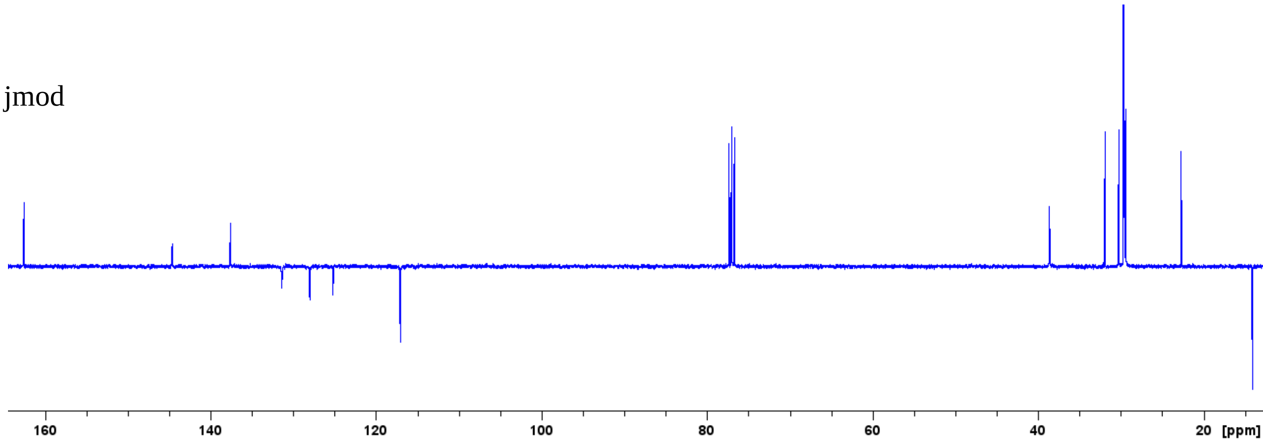

II – Materials and methods

II.1 – Materials

II.1.1 – NMR spectroscopy

^1H and ^{13}C spectra were recorded on a Bruker Avance III Nanobay 400 MHz spectrometer equipped with a BBFO probehead and using 5 mm diameter NMR tubes. Chemical shifts were quoted as parts per million (ppm) relative to tetramethylsilane using the solvent signals as secondary standard. For 31P NMR, the reference is 85% phosphoric acid, measured using the substitution method.

Saturation transfer difference NMR spectroscopy was recorded on a Bruker 600 MHz

II.1.2 – IR spectrometry

The infrared spectra for powders are recorded for solid compounds diluted to approximately 2% by weight in KBr pellets. The recording range is from 4000 to 250 cm^{-1} using a JASCO FT/IR – 4100 spectrometer. The number of acquisitions for each spectrum is 32.

AFM-IR spectra are recorded on a Bruker IconIR spectrometer with a recording range from 900 to 1900 cm^{-1}. The frequency used for topography imaging is the tapping mode at 1.7 MHz, and the mode at 280 kHz is used for detecting the IR signal.[272]

II.1.3 – UV-visible spectroscopy

UV visible spectra of all molecules were recorded on an Agilent Cary 5000 apparatus from 400 to 800 nm.

II.1.4 – X-ray photoelectron spectroscopy (XPS)

XPS analyses were performed using an Omicron Argus X-ray photoelectron spectrometer, equipped with a monochromated AlKα radiation source (hν = 1486.6 eV) and a 280 W electron beam power. The emission of photoelectrons from the sample was analyzed at a takeoff angle of 45° under ultra-high vacuum conditions (≤10−9 mBar). Spectra were carried out with a 100 eV pass energy for the survey scan and 20 eV pass energy for the C 1s, O 1s, N 1s, Si 2p, Mo 3d, W 4f, P 2p, P 2s regions. The spectra were fitted using Casa XPS v.2.3.18PR1.0 software (Casa Software Ltd, U.K.).

II.1.5 – Scanning tunneling microscopy (STM) and atomic force microscopy (AFM)

Scanning tunneling microscopy and atomic force microscopy were used to study the deposition of the different molecules on HOPG substrate (Mateck, Germany). All experiments were performed using 5100 AFM/SPM microscope system equipped with Keysight 1 µm STM scanner and Agilent 90 µm AFM. STM images were recorded in constant current mode, at air-solid interface and room temperature using mechanically cut Pt/Ir (80 / 20) tips (GoodFellow, UK). The tip-sample bias voltage was kept between - 1700 and - 1000 mV and the tunneling current setpoint between 10 and 16 pA.

AFM tips were purchased from Mikromasch Inc. The spring constant of the AFM cantilever was around 40 N/m. All experiments were repeated several times with different tips, at different spots on the sample, and the results presented in this article are representative and consistent with the more comprehensive data set. The information obtained by STM or AFM is not directly presented as a visually understandable image. The data treatment consists of image processing to optimize the visual appearance. STM and AFM images were treated and analysed using the WSxM software.[273]

AFM-IR images were performed on Bruker IconIR using coated commercial AFM tips PointProbe® Plus (PPP) coated with gold or platine and with a radius of curvature of 25 nm. All AFM-AR images are made with taping mode.

II.1.6 – Field emission scanning electron microscope

Sample surfaces morphologies were evaluated through Scanning Electron Microscope, thanks to a Hitachi SU-70 FESEM (Field Effect Scanning Electron Microscope - Schottky type gun). Images were obtained with this microscope at 5 kV high voltage electron beam and were acquired by an SE detector located inside the electronic column (called Upper detector by Hitachi). Low voltage condition (5 kV) was selected in order to prevent in depth penetration of electrons so that contribution of fine features at the surface would be enhanced in the image while preserving the best limit of separation for the SEM. Note that the upper detector is devoted to pure secondary electrons detection. Image contrast in that case is a mix of local electric conductivity, average atomic number and morphology.

II.2 – Methods

II.2.1 – Calculation of the TSB-C12 and ZnPc required to form a monolayer on 1 x 1 cm^2 HOPG substrate

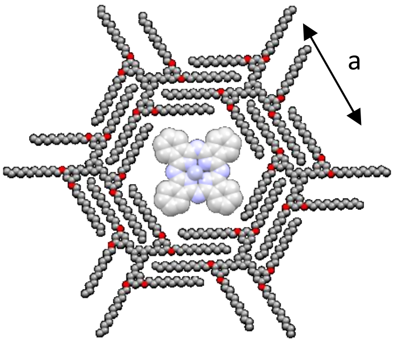

Area of hexagonal cell unit : $A = \frac{3\sqrt{3}}{2}a^2$

Where a ≈ 1.5 nm => A = 5.85 nm^2 ($5.85\text{x}10^{-14}$ cm^2)

There are 6 molecules of TSB in $5.85\text{x}10^{-14}$ cm^2

1 cm^2 = $1.026\text{x}10^{14}$ molecules and 1 mol = $6.02285\text{x}10^{23}$ molecules

$1.026\text{x}10^{14}$ molecules = 1.7 $\text{x}10^{-10}$ mol and $V_{deposition}$ = $5\text{x}10^{-6}$ L

so:

$C = \frac{1.70\times10^{-10}\text{mol}}{5\times10^{-6}L}$ = 3.4 x 10^{-5} mol/L

and **1.7 x 10^{-5} mol/L for V = 10 µL**

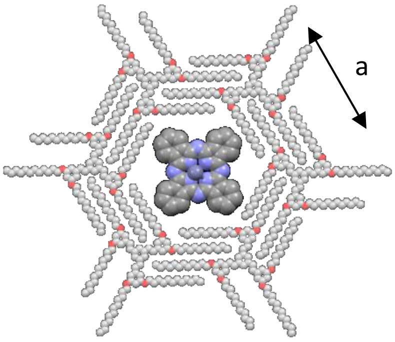

Same area as before. A = 5.85 nm^2 ($5.85\text{x}10^{-14}cm^2$)

There is 1 molecule of ZnPc in $5.85\text{x}10^{-14}cm^2$

1 cm^2 = $1.71\text{x}10^{13}$ molecules and 1 mol = $6.02285\text{x}10^{23}$ molecules

$1.71\text{x}10^{13}$ molecules - 2.84 $\text{x}10^{-11}$ mol and $V_{deposition}$ = $2\text{x}10^{-6}$ L

so:

$C = \frac{2.84\times10^{-11}\text{mol}}{2\times10^{-6}L}$ = 1.4 x 10^{-5} mol/L

and **1.96 x 10^{-6} mol/L for V = 15 µL**

II.2.2 – Calculation method of the complexation constant K of TBA[KMo(pyr)]-ZnPc with the Hill equation

An approximation is made by stating that the saturation of the solution is reached after the addition of 20 equivalents of TBA[K^{Mo}(pyr)] to the ZnPc solution => all ZnPc are complexed.

The method is detailed below:

For an equilibrium [ZnPc] + [TBA[K^{Mo}(pyr)] = [TBA[K^{Mo}(pyr)]-ZnPc]

$$\mathrm{K} = \frac{[\mathrm{TBA[KMo(pyr)]} - \mathrm{ZnPc}]}{[\mathrm{ZnPc}][\mathrm{TBA[KMo(pyr)]}]}$$

A constant Y = coordinated species fraction is defined

For a total coordination of [ZnPc] => Y = 1

For no coordination Y = 0

Thus, $\mathrm{Y} = \frac{K[\mathrm{ZnPc}][\mathrm{TBA[KMo(pyr)]}}{[ZnPc]+K[\mathrm{ZnPc}][\mathrm{TBA[KMo(pyr)]}}$ = $\mathrm{Y} = \frac{K[\mathrm{TBA[KMo(pyr)]}}{1+K[\mathrm{TBA[KMo(pyr)]}}$

⇨ $K[\mathrm{TBA[KMo(pyr)]} = \frac{Y}{1-Y}$

For [ZnPc] + n TBA[K^{Mo}(pyr)] = [TBA[K^{Mo}(pyr)]-ZnPc]

=> $\mathrm{K} = \frac{[\mathrm{TBA[KMo(pyr)]-ZnPc}]}{[\mathrm{ZnPc}]+[\mathrm{TBA[KMo(pyr)]}]^{n}}$ and $K[\mathrm{TBA[KMo(pyr)]}^{n} = \frac{Y}{1-Y}$

=> $\ln\left(\frac{Y}{1-Y}\right) = lnK + nln[\mathrm{TBA[KMo(pyr)]}]$ we plot the line $ln\left(\frac{Y}{1-Y}\right)$ as a function of ln[TBA[K^{Mo}(pyr)]

if n = 1 complex formed with one TBA[K^{Mo}(pyr) and one ZnPc, if n = 2 the complex is formed with 2 TBA[K^{Mo}(pyr)] and one ZnPc

⇨ In the case of UV-visible $\frac{Y}{1-Y}$ => $\frac{\Delta A}{\Delta A_{\infty}-\Delta A}$

With:

$\Delta A = A - A_0$

$\Delta A_{\infty} = A_{\infty} - A_0$

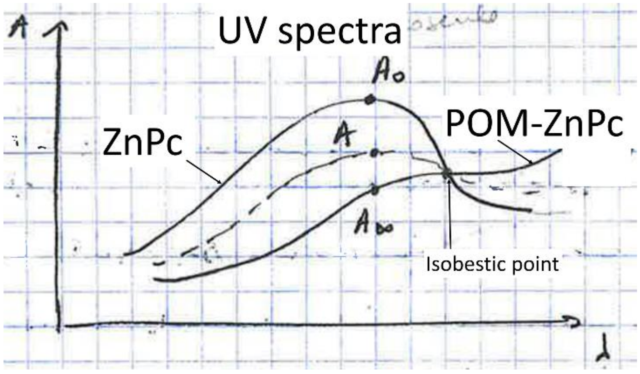

Figure 115 : Figure 1 : Schema of the the A, A0 and A∞

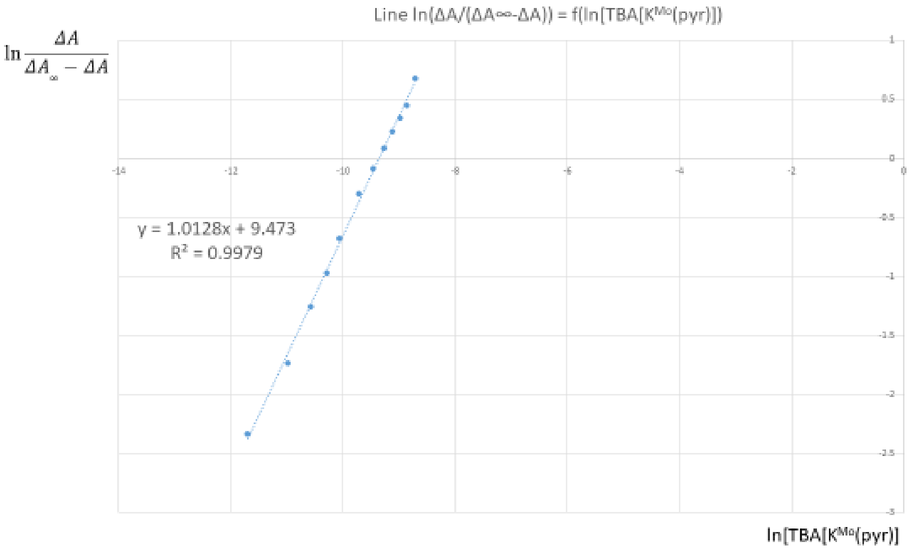

Figure 116: Line ln(ΔA/(ΔA∞-ΔA)) = f(ln[TBA[KMo(pyr)])

II.2.3 – Sample preparation for AFM and STM

The deposition of the TSB-like molecules is made in toluene, except for the last AFM-IR experiment (cf. Chapter II. I.3.3.5), and exclusively with a volume of 10 µL and a concentration of 10^{-4} mol.L^{-1}. For ZnPc, the deposition is made in chloroform with a volume of 15 µL and a concentration of 1.47×10^{-6} mol.L^{-1}. For the POMs-ZnPc complex the deposition the deposition is made in a binary solvent $CH_3CN/CHCl_3$ (30/70 in volume) with a varying concentration relatively of the POM to the ZnPc molecule.

The depositions are made under ambient conditions with the posed substrate vertically. After the deposition the sample is covered with a glass cup tow slow down the evaporation of the solvent and allows the molecules to self-assemble.

For the deposition of the Keggin heteropolyacide H_3K^{Mo}, a Tz-C12/HOPG sample is immersed vertically in a solution of 1 mM of H_3K^{Mo} in acetonitrile during approximately one minute and removed very slowly Figure.

References

(1) Anžel, A.; Heider, D.; Hattab, G. The Visual Story of Data Storage: From Storage Properties to User Interfaces. *Comput. Struct. Biotechnol. J.* **2021**, *19*, 4904–4918. https://doi.org/10.1016/j.csbj.2021.08.031.

(2) *Handbook of Microlithography, Micromachining, and Microfabrication*; Rai-Choudhury, P., Ed.; IEE materials and devices series; SPIE Optical Engineering Press ; Institution of Electrical Engineers: Bellingham, Wash., USA : London, UK, 1997.

(3) Li, S.; Chu, D. A Review of Thin-Film Transistors/Circuits Fabrication with 3D Self-Aligned Imprint Lithography. *Flex. Print. Electron.* **2017**, *2* (1), 013002. https://doi.org/10.1088/2058-8585/aa5c6d.

(4) Koo, N.; Schmidt, M.; Mollenhauer, T.; Moormann, C.; Schlachter, F.; Kurz, H. Fabrication of MOSFETs by 3D Soft UV-Nanoimprint. *Microelectron. Eng.* **2012**, *97*, 85–88. https://doi.org/10.1016/j.mee.2012.05.015.

(5) *Samsung Electronics Starts Producing Industry’s First 16-Gigabit GDDR6 for Advanced Graphics Systems*. https://news.samsung.com/global/samsung-electronics-starts-producing-industrys-first-16-gigabit-gddr6-for-advanced-graphics-systems (accessed 2023-05-01).

(6) Sze, S. M.; Lee, M. K. *Semiconductor Devices, Physics and Technology*, 3rd ed.; Wiley: Hoboken, N.J, 2012.

(7) Siu, C. Introduction to MOSFETs. In *Electronic Devices, Circuits, and Applications*; Springer International Publishing: Cham, 2022; pp 65–84. https://doi.org/10.1007/978-3-030-80538-8_5.

(8) Adams, J. *Mastering Electronics Workbench*, Version 5 and Multisim version 6.; McGraw-Hill: New York, 2001.

(9) Neamen, D. A. *Semiconductor Physics and Devices: Basic Principles*, 4th ed.; McGraw-Hill: New York, NY, 2012.

(10) *What are Enhancement-mode MOSFETs? - Technical Articles*. https://eepower.com/technical-articles/what-are-enhancement-mode-mosfets/ (accessed 2023-08-22).

(11) Cavin, R. K.; Lugli, P.; Zhirnov, V. V. Science and Engineering Beyond Moore’s Law. *Proc. IEEE* **2012**, *100* (Special Centennial Issue), 1720–1749. https://doi.org/10.1109/JPROC.2012.2190155.

(12) *3nm Technology - Taiwan Semiconductor Manufacturing Company Limited*. http://www.tsmc.com/english/dedicatedFoundry/technology/logic/l_3nm (accessed 2023-05-24).

(13) Moore, G. E. Cramming More Components Onto Integrated Circuits. *Proc. IEEE* **1998**, *86* (1), 82–85. https://doi.org/10.1109/JPROC.1998.658762.

(14) *What is Moore’s Law? – Is Moore’s Law Finally Ending? | Synopsys*. https://www.synopsys.com/glossary/what-is-moores-law.html (accessed 2023-08-22).

(15) Salahuddin, S.; Ni, K.; Datta, S. The Era of Hyper-Scaling in Electronics. *Nat. Electron.* **2018**, *1* (8), 442–450. https://doi.org/10.1038/s41928-018-0117-x.

(16) *The future of data storage must handle heavy volume | TechTarget*. Storage. https://www.techtarget.com/searchstorage/feature/The-future-of-data-storage-must-handle-heavy-volume (accessed 2023-05-01).

(17) Kargar, S.; Nawab, F. Challenges and Future Directions for Energy, Latency, and Lifetime Improvements in NVMs. *Distrib. Parallel Databases* **2022**. https://doi.org/10.1007/s10619-022-07421-x.

(18) *Data Centres and Data Transmission Networks – Analysis*. IEA. https://www.iea.org/reports/data-centres-and-data-transmission-networks (accessed 2023-05-28).

(19) *3D NAND fash and FeFET in the data storage roadmap | imec*. https://www.imec-int.com/en/articles/role-3d-nand-flash-and-fefet-data-storage-roadmap (accessed 2023-05-27).

(20) Liao, F.; Guo, Z.; Wang, Y.; Xie, Y.; Zhang, S.; Sheng, Y.; Tang, H.; Xu, Z.; Riaud, A.; Zhou, P.; Wan, J.; Fuhrer, M. S.; Jiang, X.; Zhang, D. W.; Chai, Y.; Bao, W. High-Performance Logic and Memory Devices Based on a Dual-Gated MoS2 Architecture. *ACS Appl. Electron. Mater.* **2020**, *2* (1), 111–119. https://doi.org/10.1021/acsaelm.9b00628.

(21) Huang, X.; Liu, C.; Zhou, P. 2D Semiconductors for Specific Electronic Applications: From Device to System. *Npj 2D Mater. Appl.* **2022**, *6* (1), 1–19. https://doi.org/10.1038/s41699-022-00327-3.

(22) Naqi, M.; Kwon, N.; Jung, S. H.; Pujar, P.; Cho, H. W.; Cho, Y. I.; Cho, H. K.; Lim, B.; Kim, S. High-Performance Non-Volatile InGaZnO Based Flash Memory Device Embedded with a Monolayer Au Nanoparticles. *Nanomaterials* **2021**, *11* (5), 1101. https://doi.org/10.3390/nano11051101.

(23) Doricchi, A.; Platnich, C. M.; Gimpel, A.; Horn, F.; Earle, M.; Lanzavecchia, G.; Cortajarena, A. L.; Liz-Marzán, L. M.; Liu, N.; Heckel, R.; Grass, R. N.; Krahne, R.; Keyser, U. F.; Garoli, D. Emerging Approaches to DNA Data Storage: Challenges and Prospects. *ACS Nano* **2022**, *16* (11), 17552–17571. https://doi.org/10.1021/acsnano.2c06748.

(24) Cafferty, B. J.; Ten, A. S.; Fink, M. J.; Morey, S.; Preston, D. J.; Mrksich, M.; Whitesides, G. M. Storage of Information Using Small Organic Molecules. *ACS Cent. Sci.* **2019**, *5* (5), 911–916. https://doi.org/10.1021/acscentsci.9b00210.

(25) *Single-molecule magnet breaks performance records*. Chemical & Engineering News. https://cen.acs.org/articles/95/i35/Single-molecule-magnet-breaks-performance.html (accessed 2023-05-30).

(26) Li, C.; Fan, W.; Lei, B.; Zhang, D.; Han, S.; Tang, T.; Liu, X.; Liu, Z.; Asano, S.; Meyyappan, M.; Han, J.; Zhou, C. Multilevel Memory Based on Molecular Devices. *Appl. Phys. Lett.* **2004**, *84* (11), 1949–1951. https://doi.org/10.1063/1.1667615.

(27) Gaita-Ariño, A.; Luis, F.; Hill, S.; Coronado, E. Molecular Spins for Quantum Computation. *Nat. Chem.* **2019**, *11* (4), 301–309. https://doi.org/10.1038/s41557-019-0232-y.

(28) *Molecular Memory: Small Molecules Could Be the Future of Data Storage*. Informatics from Technology Networks. http://www.technologynetworks.com/informatics/news/molecular-memory-small-molecules-could-be-the-future-of-data-storage-318986 (accessed 2023-05-28).

(29) Lörtscher, E. Wiring Molecules into Circuits. *Nat. Nanotechnol.* **2013**, *8* (6), 381–384. https://doi.org/10.1038/nnano.2013.105.

(30) Peurifoy, S. R. Organic Electronics Enhanced via Molecular Contortion, Columbia University, 2020. https://doi.org/10.7916/d8-v1cz-6v61.

(31) Fairlamb, I. J. S.; Dickinson, J. M. 1.22 - Ions, Radicals, Carbenes, and Other Monocoordinated Systems. In *Comprehensive Organic Functional Group Transformations II*; Katritzky, A. R., Taylor, R. J. K., Eds.; Elsevier: Oxford, 2005; pp 1177–1259. https://doi.org/10.1016/B0-08-044655-8/00022-2.

(32) Katsonis, N.; Lubomska, M.; Pollard, M. M.; Feringa, B. L.; Rudolf, P. Synthetic Light-Activated Molecular Switches and Motors on Surfaces. *Prog. Surf. Sci.* **2007**, *82* (7), 407–434. https://doi.org/10.1016/j.progsurf.2007.03.011.

(33) Fu, H.; Zhu, X.; Li, P.; Li, M.; Yang, L.; Jia, C.; Guo, X. Recent Progress in Single-Molecule Transistors: Their Designs, Mechanisms and Applications. *J. Mater. Chem. C* **2022**, *10* (7), 2375–2389. https://doi.org/10.1039/D1TC04079K.

(34) Quan, L. N.; Kang, J.; Ning, C.-Z.; Yang, P. Nanowires for Photonics. *Chem. Rev.* **2019**, *119* (15), 9153–9169. https://doi.org/10.1021/acs.chemrev.9b00240.

(35) Sukegawa, J.; Schubert, C.; Zhu, X.; Tsuji, H.; Guldi, D. M.; Nakamura, E. Electron Transfer through Rigid Organic Molecular Wires Enhanced by Electronic and Electron–Vibration Coupling. *Nat. Chem.* **2014**, *6* (10), 899–905. https://doi.org/10.1038/nchem.2026.

(36) Irie, M. Photochromism: Memories and SwitchesIntroduction. *Chem. Rev.* **2000**, *100* (5), 1683–1684. https://doi.org/10.1021/cr980068l.
(37) Sekkat, Z.; Knoll, W. *Photoreactive Organic Thin Films*; Elsevier, 2002.
(38) Wu, P.; Dharmadhikari, B.; Patra, P.; Xiong, X. Rotaxane Nanomachines in Future Molecular Electronics. *Nanoscale Adv.* **2022**, *4* (17), 3418–3461. https://doi.org/10.1039/D2NA00057A.
(39) Bailey, B. *Product Lifecycle Management For Semiconductors*. Semiconductor Engineering. https://semiengineering.com/product-lifecycle-management-for-semiconductors/ (accessed 2023-05-25).
(40) Ohtake, T. Bottom-up Approaches for Material and Device Designing Using Practical Aspects of Self-Assembled Molecular Architectures. *Mol. Syst. Des. Eng.* **2018**, *3* (5), 804–818. https://doi.org/10.1039/C8ME00020D.
(41) Jung, W.-B.; Jang, S.; Cho, S.-Y.; Jeon, H.-J.; Jung, H.-T. Recent Progress in Simple and Cost-Effective Top-Down Lithography for ≈10 Nm Scale Nanopatterns: From Edge Lithography to Secondary Sputtering Lithography. *Adv. Mater.* **2020**, *32* (35), 1907101. https://doi.org/10.1002/adma.201907101.
(42) Mayer, J. W.; Lau, S. S. *Electronic Materials Science: For Integrated Circuits in Si and GaAs*; Macmillan, 1990.
(43) Madou, M. J. *Fundamentals of Microfabrication: The Science of Miniaturization, Second Edition*, 2nd ed.; CRC Press: Boca Raton, 2017. https://doi.org/10.1201/9781482274004.
(44) Arora, V. K. *Nanoelectronics: Quantum Engineering of Low-Dimensional Nanoensembles*; 2015; p 401. https://doi.org/10.1201/b18131.
(45) *ASML EUV lithography systems*. https://www.asml.com/en/products/euv-lithography-systems (accessed 2023-04-13).
(46) Stan, M. R.; Franzon, P. D.; Goldstein, S. C.; Lach, J. C.; Ziegler, M. M. Molecular Electronics: From Devices and Interconnect to Circuits and Architecture. *Proc. IEEE* **2003**, *91* (11), 1940–1957. https://doi.org/10.1109/JPROC.2003.818327.
(47) Nánai, L.; Benk?, Z. I.; Letfullin, R. R.; George, T. F. Laser-Matter Interactions: Nanostructures, Fabrication and Characterization. In *Computational Studies of New Materials II*; WORLD SCIENTIFIC, 2011; pp 1–36. https://doi.org/10.1142/9789814287197_0001.
(48) Teo, B. K.; Sun, X. H. From Top-Down to Bottom-Up to Hybrid Nanotechnologies: Road to Nanodevices. *J. Clust. Sci.* **2006**, *17* (4), 529–540. https://doi.org/10.1007/s10876-006-0086-5.
(49) Characterization Techniques for Molecular Electronics. In *Molecular-Scale Electronics*; Guo, X., Xiang, D., Li, Y., Eds.; Wiley, 2020; pp 157–207. https://doi.org/10.1002/9783527818914.ch7.
(50) SCHEER, E.; CUEVAS, J. C. *Molecular Electronics: An Introduction to Theory and Experiment*, 2nd edition.; WSPC: New Jersey, 2017.
(51) Petty, M. C.; Nagase, T.; Suzuki, H.; Naito, H. Molecular Electronics. In *Springer Handbook of Electronic and Photonic Materials*; Kasap, S., Capper, P., Eds.; Springer Handbooks; Springer International Publishing: Cham, 2017; pp 1–1. https://doi.org/10.1007/978-3-319-48933-9_51.
(52) Griffiths, R.-R.; L. Greenfield, J.; R. Thawani, A.; R. Jamasb, A.; B. Moss, H.; Bourached, A.; Jones, P.; McCorkindale, W.; A. Aldrick, A.; J. Fuchter, M.; A. Lee, A. Data-Driven Discovery of Molecular Photoswitches with Multioutput Gaussian Processes. *Chem. Sci.* **2022**, *13* (45), 13541–13551. https://doi.org/10.1039/D2SC04306H.
(53) Amar, A.; Savel, P.; Akdas-Kilig, H.; Katan, C.; Meghezzi, H.; Boucekkine, A.; Malval, J.-P.; Fillaut, J.-L. Photoisomerisation in Aminoazobenzene-Substituted Ruthenium(II) Tris(Bipyridine) Complexes: Influence of the Conjugation Pathway. *Chem. – Eur. J.* **2015**, *21* (22), 8262–8270. https://doi.org/10.1002/chem.201406002.
(54) Jensen, P. W. K.; Kristensen, L. B.; Lavigne, C.; Aspuru-Guzik, A. Toward Quantum Computing with Molecular Electronics. *J. Chem. Theory Comput.* **2022**, *18* (6), 3318–3326. https://doi.org/10.1021/acs.jctc.2c00162.
(55) Sessoli, R. Toward the Quantum Computer: Magnetic Molecules Back in the Race. *ACS Cent. Sci.* **2015**, *1* (9), 473–474. https://doi.org/10.1021/acscentsci.5b00384.

(56) Moreno-Pineda, E.; Godfrin, C.; Balestro, F.; Wernsdorfer, W.; Ruben, M. Molecular Spin Qudits for Quantum Algorithms. *Chem. Soc. Rev.* **2018**, *47* (2), 501–513. https://doi.org/10.1039/C5CS00933B.

(57) Moseley, D. H.; Stavretis, S. E.; Thirunavukkuarasu, K.; Ozerov, M.; Cheng, Y.; Daemen, L. L.; Ludwig, J.; Lu, Z.; Smirnov, D.; Brown, C. M.; Pandey, A.; Ramirez-Cuesta, A. J.; Lamb, A. C.; Atanasov, M.; Bill, E.; Neese, F.; Xue, Z.-L. Spin–Phonon Couplings in Transition Metal Complexes with Slow Magnetic Relaxation. *Nat. Commun.* **2018**, *9* (1), 2572. https://doi.org/10.1038/s41467-018-04896-0.

(58) Dorn, M.; Hunger, D.; Förster, C.; Naumann, R.; van Slageren, J.; Heinze, K. Towards Luminescent Vanadium(II) Complexes with Slow Magnetic Relaxation and Quantum Coherence. *Chem. – Eur. J.* **2023**, *29* (9), e202202898. https://doi.org/10.1002/chem.202202898.

(59) Govia, L. C. G.; Lingenfelter, A.; Clerk, A. A. Stabilizing Two-Qubit Entanglement by Mimicking a Squeezed Environment. *Phys. Rev. Res.* **2022**, *4* (2), 023010. https://doi.org/10.1103/PhysRevResearch.4.023010.

(60) Loft, N. J. S.; Kjaergaard, M.; Kristensen, L. B.; Andersen, C. K.; Larsen, T. W.; Gustavsson, S.; Oliver, W. D.; Zinner, N. T. Quantum Interference Device for Controlled Two-Qubit Operations. *Npj Quantum Inf.* **2020**, *6* (1), 1–9. https://doi.org/10.1038/s41534-020-0275-3.

(61) RAJARAMAN, V.; ADABALA, N. *FUNDAMENTALS OF COMPUTERS*; PHI Learning Pvt. Ltd., 2014.

(62) Mandviwalla, A.; Ohshiro, K.; Ji, B. Implementing Grover's Algorithm on the IBM Quantum Computers. In *2018 IEEE International Conference on Big Data (Big Data)*; 2018; pp 2531–2537. https://doi.org/10.1109/BigData.2018.8622457.

(63) Tanttu, T.; Lim, W. H.; Huang, J. Y.; Stuyck, N. D.; Gilbert, W.; Su, R. Y.; Feng, M.; Cifuentes, J. D.; Seedhouse, A. E.; Seritan, S. K.; Ostrove, C. I.; Rudinger, K. M.; Leon, R. C. C.; Huang, W.; Escott, C. C.; Itoh, K. M.; Abrosimov, N. V.; Pohl, H.-J.; Thewalt, M. L. W.; Hudson, F. E.; Blume-Kohout, R.; Bartlett, S. D.; Morello, A.; Laucht, A.; Yang, C. H.; Saraiva, A.; Dzurak, A. S. Stability of High-Fidelity Two-Qubit Operations in Silicon. arXiv March 7, 2023. https://doi.org/10.48550/arXiv.2303.04090.

(64) Soe, W.-H.; Manzano, C.; Renaud, N.; de Mendoza, P.; De Sarkar, A.; Ample, F.; Hliwa, M.; Echavarren, A. M.; Chandrasekhar, N.; Joachim, C. Manipulating Molecular Quantum States with Classical Metal Atom Inputs: Demonstration of a Single Molecule NOR Logic Gate. *ACS Nano* **2011**, *5* (2), 1436–1440. https://doi.org/10.1021/nn1033899.

(65) Lavroff, R. H.; Pennington, D. L.; Hua, A. S.; Li, B. Y.; Williams, J. A.; Alexandrova, A. N. Recent Innovations in Solid-State and Molecular Qubits for Quantum Information Applications. *J. Phys. Chem. Lett.* **2021**, *12* (44), 10742–10745. https://doi.org/10.1021/acs.jpclett.1c03269.

(66) Zadrozny, J. M.; Niklas, J.; Poluektov, O. G.; Freedman, D. E. Millisecond Coherence Time in a Tunable Molecular Electronic Spin Qubit. *ACS Cent. Sci.* **2015**, *1* (9), 488–492. https://doi.org/10.1021/acscentsci.5b00338.

(67) Baldoví, J. J.; Cardona-Serra, S.; Clemente-Juan, J. M.; Coronado, E.; Gaita-Ariño, A.; Prima-García, H. Coherent Manipulation of Spin Qubits Based on Polyoxometalates: The Case of the Single Ion Magnet [GdW30P5O110]14−. *Chem. Commun.* **2013**, *49* (79), 8922. https://doi.org/10.1039/c3cc44838j.

(68) Liu, Z.; Wang, Y.-X.; Fang, Y.-H.; Qin, S.-X.; Wang, Z.-M.; Jiang, S.-D.; Gao, S. Electric Field Manipulation Enhanced by Strong Spin-Orbit Coupling: Promoting Rare-Earth Ions as Qubits. *Natl. Sci. Rev.* **2020**, *7* (10), 1557–1563. https://doi.org/10.1093/nsr/nwaa148.

(69) Reddy, I. R.; Oppeneer, P. M.; Tarafder, K. Interfacial Spin Manipulation of Nickel-Quinonoid Complex Adsorbed on Co(001) Substrate. *Magnetochemistry* **2019**, *5* (1), 2. https://doi.org/10.3390/magnetochemistry5010002.

(70) Ariciu, A.-M.; Woen, D. H.; Huh, D. N.; Nodaraki, L. E.; Kostopoulos, A. K.; Goodwin, C. A. P.; Chilton, N. F.; McInnes, E. J. L.; Winpenny, R. E. P.; Evans, W. J.; Tuna, F. Engineering Electronic Structure to Prolong Relaxation Times in Molecular Qubits by Minimising Orbital Angular Momentum. *Nat. Commun.* **2019**, *10* (1), 3330. https://doi.org/10.1038/s41467-019-11309-3.

(71) Bertaina, S.; Gambarelli, S.; Mitra, T.; Tsukerblat, B.; Müller, A.; Barbara, B. Quantum Oscillations in a Molecular Magnet. *Nature* **2008**, *453* (7192), 203–206. https://doi.org/10.1038/nature06962.

(72) Amoza, M.; Gómez-Coca, S.; Ruiz, E. Magnetic Anisotropy in Yb $^{\text{III}}$ Complex Candidates for Molecular Qubits: A Theoretical Analysis. *Phys. Chem. Chem. Phys.* **2021**, *23* (3), 1976–1983. https://doi.org/10.1039/D0CP05422D.

(73) Zhu, H.; Li, Q. Novel Molecular Non-Volatile Memory: Application of Redox-Active Molecules. *Appl. Sci.* **2016**, *6* (1), 7. https://doi.org/10.3390/app6010007.

(74) Dixon, I. M.; Rat, S.; Sournia-Saquet, A.; Molnár, G.; Salmon, L.; Bousseksou, A. On the Spin-State Dependence of Redox Potentials of Spin Crossover Complexes. *Inorg. Chem.* **2020**, *59* (24), 18402–18406. https://doi.org/10.1021/acs.inorgchem.0c03043.

(75) Watanabe, E.; Zhao, W.; Sugahara, A.; Mortemard de Boisse, B.; Lander, L.; Asakura, D.; Okamoto, Y.; Mizokawa, T.; Okubo, M.; Yamada, A. Redox-Driven Spin Transition in a Layered Battery Cathode Material. *Chem. Mater.* **2019**, *31* (7), 2358–2365. https://doi.org/10.1021/acs.chemmater.8b04775.

(76) Busche, C.; Vilà-Nadal, L.; Yan, J.; Miras, H. N.; Long, D.-L.; Georgiev, V. P.; Asenov, A.; Pedersen, R. H.; Gadegaard, N.; Mirza, M. M.; Paul, D. J.; Poblet, J. M.; Cronin, L. Design and Fabrication of Memory Devices Based on Nanoscale Polyoxometalate Clusters. *Nature* **2014**, *515* (7528), 545–549. https://doi.org/10.1038/nature13951.

(77) Zhu, C.; Ji, X.; You, D.; Chen, T. L.; Mu, A. U.; Barker, K. P.; Klivansky, L. M.; Liu, Y.; Fang, L. Extraordinary Redox Activities in Ladder-Type Conjugated Molecules Enabled by B ← N Coordination-Promoted Delocalization and Hyperconjugation. *J. Am. Chem. Soc.* **2018**, *140* (51), 18173–18182. https://doi.org/10.1021/jacs.8b11337.

(78) Lindsey, J. S.; Bocian, D. F. Molecules for Charge-Based Information Storage. *Acc. Chem. Res.* **2011**, *44* (8), 638–650. https://doi.org/10.1021/ar200107x.

(79) Espinoza, E. M.; Clark, J. A.; Soliman, J.; Derr, J. B.; Morales, M.; Vullev, V. I. Practical Aspects of Cyclic Voltammetry: How to Estimate Reduction Potentials When Irreversibility Prevails. *J. Electrochem. Soc.* **2019**, *166* (5), H3175–H3187. https://doi.org/10.1149/2.0241905jes.

(80) Dai, Y.; Xie, Z.; Bao, M.; Liu, C.; Su, Y. Multiple Stable Redox States and Tunable Ground States *via* the Marriage of Viologens and Chichibabin's Hydrocarbon. *Chem. Sci.* **2023**, *14* (13), 3548–3553. https://doi.org/10.1039/D3SC00102D.

(81) Zhu, H.; Li, Q.; Zhu, H.; Li, Q. *Redox-Active Molecules for Novel Nonvolatile Memory Applications*; IntechOpen, 2017. https://doi.org/10.5772/intechopen.68726.

(82) Yan, Y.; Robinson, S. G.; Vaid, T. P.; Sigman, M. S.; Sanford, M. S. Simultaneously Enhancing the Redox Potential and Stability of Multi-Redox Organic Catholytes by Incorporating Cyclopropenium Substituents. *J. Am. Chem. Soc.* **2021**, *143* (33), 13450–13459. https://doi.org/10.1021/jacs.1c07237.

(83) Casañ-Pastor, N.; Gómez-Romero, P. Polyoxometalates: From Inorganic Chemistry to Materials Science. *Front. Biosci.-Landmark* **2004**, *9* (2), 1759–1770. https://doi.org/10.2741/1365.

(84) Yang, L.; Lei, J.; Fan, J.; Yuan, R.; Zheng, M.; Chen, J.; Dong, Q. The Intrinsic Charge Carrier Behaviors and Applications of Polyoxometalate Clusters Based Materials. *Adv. Mater.* **2021**, *33* (50), 2005019. https://doi.org/10.1002/adma.202005019.

(85) Baldoví, J. J.; Cardona-Serra, S.; Gaita-Ariño, A.; Coronado, E. Design of Magnetic Polyoxometalates for Molecular Spintronics and as Spin Qubits. In *Advances in Inorganic Chemistry*; Elsevier, 2017; Vol. 69, pp 213–249. https://doi.org/10.1016/bs.adioch.2016.12.003.

(86) Huez, C.; Guérin, D.; Lenfant, S.; Volatron, F.; Calame, M.; Perrin, M. L.; Proust, A.; Vuillaume, D. Correction: Redox-Controlled Conductance of Polyoxometalate Molecular Junctions. *Nanoscale* **2023**, *15* (1), 387–387. https://doi.org/10.1039/D2NR90231A.

(87) Gumerova, N. I.; Rompel, A. Synthesis, Structures and Applications of Electron-Rich Polyoxometalates. *Nat. Rev. Chem.* **2018**, *2* (2), 1–20. https://doi.org/10.1038/s41570-018-0112.

(88) Rathee, B.; Wati, M.; Sindhu, R.; Sindhu, S. Review of Some Applications of Polyoxometalates. *Orient. J. Chem.* **2022**, *38* (2), 327–335.
(89) d, R. S. B. de los A. *Extractos De Las Juntas Generales Celebradas Por La Real Sociedad Bascongada De Los Amigos Del País En La Villa De Vergara Por Septiembre De 1773*; Nabu Press, 2011.
(90) Berzelius, J. J. Beitrag Zur Näheren Kenntniss Des Molybdäns. *Ann. Phys.* **1826**, *82* (4), 369–392. https://doi.org/10.1002/andp.18260820402.
(91) Keggin, J. F. Structure of the Molecule of 12-Phosphotungstic Acid. *Nature* **1933**, *131* (3321), 908–909. https://doi.org/10.1038/131908b0.
(92) Keggin, J. F.; Bragg, W. L. The Structure and Formula of 12-Phosphotungstic Acid. *Proc. R. Soc. Lond. Ser. Contain. Pap. Math. Phys. Character* **1934**, *144* (851), 75–100. https://doi.org/10.1098/rspa.1934.0035.
(93) Misra, A.; Kozma, K.; Streb, C.; Nyman, M. Beyond Charge Balance: Counter-Cations in Polyoxometalate Chemistry. *Angew. Chem. Int. Ed.* **2020**, *59* (2), 596–612. https://doi.org/10.1002/anie.201905600.
(94) Anderson, J. S. Constitution of the Poly-Acids. *Nature* **1937**, *140* (3550), 850–850. https://doi.org/10.1038/140850a0.
(95) Evans, H. T. Jr. THE CRYSTAL STRUCTURES OF AMMONIUM AND POTASSIUM MOLYBDOTELLURATES. *J. Am. Chem. Soc.* **1948**, *70* (3), 1291–1292. https://doi.org/10.1021/ja01183a521.
(96) Wang, X.-S.; Huang, Y.-B.; Lin, Z.-J.; Cao, R. Phosphotungstic Acid Encapsulated in the Mesocages of Amine-Functionalized Metal–Organic Frameworks for Catalytic Oxidative Desulfurization. *Dalton Trans.* **2014**, *43* (31), 11950–11958. https://doi.org/10.1039/C4DT01043D.
(97) Sun, J.; Abednatanzi, S.; Van Der Voort, P.; Liu, Y.-Y.; Leus, K. POM@MOF Hybrids: Synthesis and Applications. *Catalysts* **2020**, *10* (5), 578. https://doi.org/10.3390/catal10050578.
(98) Hervé, G.; Tézé, A.; Contant, R. General Principles of The Synthesis of Polyoxometalates in Aqueous Solution. In *Polyoxometalate Molecular Science*; Borrás-Almenar, J. J., Coronado, E., Müller, A., Pope, M., Eds.; NATO Science Series; Springer Netherlands: Dordrecht, 2003; pp 33–54. https://doi.org/10.1007/978-94-010-0091-8_2.
(99) *De la solution à l'oxyde - 2e ED: Chimie aqueuse des cations métalliques - synthèse de nanostructures chimie aqueuse des cations métalliques synthèse de nanostructures (Savoirs actuels) eBook : Jolivet Jean-Pierre: Amazon.fr: Boutique Kindle*. https://www.amazon.fr/solution-%C3%A0-loxyde-2e-ED-ebook/dp/B01HOLSG2Q (accessed 2023-04-17).
(100) Rubio, L. R.; Vilela, J. L. V.; Artetxe, B.; Gutiérrez-Zorrilla, J. M. *Polyoxometalates: Advances, Properties, and Applications*; Jenny Stanford Publishing, 2022.
(101) Ni, Z.; Lv, H.; Yang, G. Recent Advances of Ti/Zr-Substituted Polyoxometalates: From Structural Diversity to Functional Applications. *Molecules* **2022**, *27* (24), 8799. https://doi.org/10.3390/molecules27248799.
(102) Dolbecq, A.; Dumas, E.; Mayer, C. R.; Mialane, P. Hybrid Organic–Inorganic Polyoxometalate Compounds: From Structural Diversity to Applications. *Chem. Rev.* **2010**, *110* (10), 6009–6048. https://doi.org/10.1021/cr1000578.
(103) Ding, Y.-X.; Zheng, Q.-H.; Peng, M.-T.; Liu, W.-L.; Teng, Y.-L. A New Ɛ-Keggin Polyoxometalate-Based Metal-Organic Framework: From Design and Synthesis to Electrochemical Hydrogen Evolution. *Catal. Commun.* **2021**, *161*, 106367. https://doi.org/10.1016/j.catcom.2021.106367.
(104) Chen, X.; Huang, P.; Zhu, X.; Zhuang, S.; Zhu, H.; Fu, J.; Nissimagoudar, A. S.; Li, W.; Zhang, X.; Zhou, L.; Wang, Y.; Lv, Z.; Zhou, Y.; Han, S.-T. Keggin-Type Polyoxometalate Cluster as an Active Component for Redox-Based Nonvolatile Memory. *Nanoscale Horiz.* **2019**, *4* (3), 697–704. https://doi.org/10.1039/C8NH00366A.
(105) Laurans, M.; Mattera, M.; Salles, R.; K'Bidi, L.; Gouzerh, P.; Renaudineau, S.; Volatron, F.; Guillemot, G.; Blanchard, S.; Izzet, G.; Solé-Daura, A.; Poblet, J. M.; Proust, A. When

Identification of the Reduction Sites in Mixed Molybdenum/Tungsten Keggin-Type Polyoxometalate Hybrids Turns Out Tricky. *Inorg. Chem.* **2022**, *61* (20), 7700–7709. https://doi.org/10.1021/acs.inorgchem.2c00866.

(106) Wang, S.-M.; Liu, L.; Huang, Z.-Y.; Han, Z.-B. Vanadium Substituted Keggin-Type POM-Based Electrochromic Films Showing High Performance in a Li+-Based Neutral Non-Aqueous Electrolyte. *RSC Adv.* **2016**, *6* (45), 38782–38789. https://doi.org/10.1039/C6RA03037H.

(107) Li, Q.; Zhang, L.; Dai, J.; Tang, H.; Li, Q.; Xue, H.; Pang, H. Polyoxometalate-Based Materials for Advanced Electrochemical Energy Conversion and Storage. *Chem. Eng. J.* **2018**, *351*, 441–461. https://doi.org/10.1016/j.cej.2018.06.074.

(108) Macht, J.; Janik, M. J.; Neurock, M.; Iglesia, E. Mechanistic Consequences of Composition in Acid Catalysis by Polyoxometalate Keggin Clusters. *J. Am. Chem. Soc.* **2008**, *130* (31), 10369–10379. https://doi.org/10.1021/ja803114r.

(109) Zhang, D.; Zhang, W.; Lin, Z.; Dong, J.; Zhen, N.; Chi, Y.; Hu, C. Mono- and Di-Sc-Substituted Keggin Polyoxometalates: Effective Lewis Acid Catalysts for Nerve Agent Simulant Hydrolysis and Mechanistic Insights. *Inorg. Chem.* **2020**, *59* (14), 9756–9764. https://doi.org/10.1021/acs.inorgchem.0c00976.

(110) Bardin, B. B.; Bordawekar, S. V.; Neurock, M.; Davis, R. J. Acidity of Keggin-Type Heteropolycompounds Evaluated by Catalytic Probe Reactions, Sorption Microcalorimetry, and Density Functional Quantum Chemical Calculations. *J. Phys. Chem. B* **1998**, *102* (52), 10817–10825. https://doi.org/10.1021/jp982345y.

(111) Malmir, M.; Heravi, M. M.; Yekke-Ghasemi, Z.; Mirzaei, M. Incorporating Heterogeneous Lacunary Keggin Anions as Efficient Catalysts for Solvent-Free Cyanosilylation of Aldehydes and Ketones. *Sci. Rep.* **2022**, *12* (1), 11573. https://doi.org/10.1038/s41598-022-15831-1.

(112) Kortz, U.; Müller, A.; van Slageren, J.; Schnack, J.; Dalal, N. S.; Dressel, M. Polyoxometalates: Fascinating Structures, Unique Magnetic Properties. *Coord. Chem. Rev.* **2009**, *253* (19–20), 2315–2327. https://doi.org/10.1016/j.ccr.2009.01.014.

(113) Rong, C. C.; So, H.; Pope, M. T. Electron Paramagnetic Resonance Investigation of Some 11-Tungstoruthenate(III) Polyoxoanions. *Eur. J. Inorg. Chem.* **2009**, *2009* (34), 5211–5214. https://doi.org/10.1002/ejic.200900578.

(114) Gumerova, N. I.; Roller, A.; Giester, G.; Krzystek, J.; Cano, J.; Rompel, A. Incorporation of Cr^{III} into a Keggin Polyoxometalate as a Chemical Strategy to Stabilize a Labile $\{Cr^{III}O_4\}$ Tetrahedral Conformation and Promote Unattended Single-Ion Magnet Properties. *J. Am. Chem. Soc.* **2020**, *142* (7), 3336–3339. https://doi.org/10.1021/jacs.9b12797.

(115) Shi, Z.; Peng, J.; Gómez-García, C. J.; Benmansour, S.; Gu, X. Influence of Metal Ions on the Structures of Keggin Polyoxometalate-Based Solids: Hydrothermal Syntheses, Crystal Structures and Magnetic Properties. *J. Solid State Chem.* **2006**, *179* (1), 253–265. https://doi.org/10.1016/j.jssc.2005.09.051.

(116) Kuramochi, S.; Shiga, T.; Cameron, J.; Newton, G.; Oshio, H. Synthesis, Crystal Structures and Magnetic Properties of Composites Incorporating an Fe(II) Spin Crossover Complex and Polyoxometalates. *Inorganics* **2017**, *5* (3), 48. https://doi.org/10.3390/inorganics5030048.

(117) Laurans, M.; Trinh, K.; Dalla Francesca, K.; Izzet, G.; Alves, S.; Derat, E.; Humblot, V.; Pluchery, O.; Vuillaume, D.; Lenfant, S.; Volatron, F.; Proust, A. Covalent Grafting of Polyoxometalate Hybrids onto Flat Silicon/Silicon Oxide: Insights from POMs Layers on Oxides. *ACS Appl. Mater. Interfaces* **2020**, *12* (42), 48109–48123. https://doi.org/10.1021/acsami.0c12300.

(118) Yi, X.; Izarova, N. V.; Stuckart, M.; Guérin, D.; Thomas, L.; Lenfant, S.; Vuillaume, D.; van Leusen, J.; Duchoň, T.; Nemšák, S.; Bourone, S. D. M.; Schmitz, S.; Kögerler, P. Probing Frontier Orbital Energies of $\{Co_9(P_2W_{15})_3\}$ Polyoxometalate Clusters at Molecule–Metal and Molecule–Water Interfaces. *J. Am. Chem. Soc.* **2017**, *139* (41), 14501–14510. https://doi.org/10.1021/jacs.7b07034.

(119) Amin, S. S.; Cameron, J. M.; Cousins, R. B.; Wrigley, J.; Liirò-Peluso, L.; Sans, V.; Walsh, D. A.; Newton, G. N. Redox-Active Hierarchical Assemblies of Hybrid Polyoxometalate Nanostructures

at Carbon Surfaces. *Inorg. Chem. Front.* **2022**, *9* (8), 1777–1784. https://doi.org/10.1039/D2QI00174H.

(120) Clemente-León, M.; Agricole, B.; Mingotaud, C.; Gómez-García, C. J.; Coronado, E.; Delhaes, P. Toward New Organic/Inorganic Superlattices: Keggin Polyoxometalates in Langmuir and Langmuir−Blodgett Films. *Langmuir* **1997**, *13* (8), 2340–2347. https://doi.org/10.1021/la960576v.

(121) Clemente-León, M.; Coronado, E.; Gómez-García, C. J.; Mingotaud, C.; Ravaine, S.; Romualdo-Torres, G.; Delhaès, P. Polyoxometalate Monolayers in Langmuir–Blodgett Films. *Chem. – Eur. J.* **2005**, *11* (13), 3979–3987. https://doi.org/10.1002/chem.200401063.

(122) Clemente-Leon, M.; Mingotaud, C.; Gomez-Garcia, C. J.; Coronado, E.; Delhaes, P. Polyoxometalates in Langmuir–Blodgett Films: Toward New Magnetic Materials. *Thin Solid Films* **1998**, *327–329*, 439–442. https://doi.org/10.1016/S0040-6090(98)00681-6.

(123) Li, H.; Pang, S.; Wu, S.; Feng, X.; Müllen, K.; Bubeck, C. Layer-by-Layer Assembly and UV Photoreduction of Graphene–Polyoxometalate Composite Films for Electronics. *J. Am. Chem. Soc.* **2011**, *133* (24), 9423–9429. https://doi.org/10.1021/ja201594k.

(124) Gam Derouich, S.; Rinfray, C.; Izzet, G.; Pinson, J.; Gallet, J.-J.; Kanoufi, F.; Proust, A.; Combellas, C. Control of the Grafting of Hybrid Polyoxometalates on Metal and Carbon Surfaces: Toward Submonolayers. *Langmuir* **2014**, *30* (8), 2287–2296. https://doi.org/10.1021/la500067e.

(125) Volatron, F.; Noël, J.-M.; Rinfray, C.; Decorse, P.; Combellas, C.; Kanoufi, F.; Proust, A. Electron Transfer Properties of a Monolayer of Hybrid Polyoxometalates on Silicon. *J. Mater. Chem. C* **2015**, *3* (24), 6266–6275. https://doi.org/10.1039/C5TC00074B.

(126) Rinfray, C.; Brasiliense, V.; Izzet, G.; Volatron, F.; Alves, S.; Combellas, C.; Kanoufi, F.; Proust, A. Electron Transfer to a Phosphomolybdate Monolayer on Glassy Carbon: Ambivalent Effect of Protonation. *Inorg. Chem.* **2016**, *55* (14), 6929–6937. https://doi.org/10.1021/acs.inorgchem.6b00485.

(127) Tang, Z.; Liu, S.; Wang, E.; Dong, S. Self-Assembled Monolayer of Polyoxometalate on Gold Surfaces: Quartz Crystal Microbalance, Electrochemistry, and in-Situ Scanning Tunneling Microscopy Study. *Langmuir* **2000**, *16* (11), 4946–4952. https://doi.org/10.1021/la9907127.

(128) Velessiotis, D.; Douvas, A. M.; Athanasiou, S.; Nilsson, B.; Petersson, G.; Södervall, U.; Alestig, G.; Argitis, P.; Glezos, N. Molecular Junctions Made of Tungsten-Polyoxometalate Self-Assembled Monolayers: Towards Polyoxometalate-Based Molecular Electronics Devices. *Microelectron. Eng.* **2011**, *88* (8), 2775–2777. https://doi.org/10.1016/j.mee.2011.01.039.

(129) Huez, C.; Guérin, D.; Lenfant, S.; Volatron, F.; Calame, M.; Perrin, M. L.; Proust, A.; Vuillaume, D. Redox-Controlled Conductance of Polyoxometalate Molecular Junctions. *Nanoscale* **2022**, *14* (37), 13790–13800. https://doi.org/10.1039/D2NR03457C.

(130) De Luca, G.; Bisignano, F.; Figoli, A.; Galiano, F.; Furia, E.; Mancuso, R.; Saoncella, O.; Carraro, M.; Bonchio, M.; Gabriele, B. Bromide Ion Exchange with a Keggin Polyoxometalate on Functionalized Polymeric Membranes: A Theoretical and Experimental Study. *J. Phys. Chem. B* **2014**, *118* (9), 2396–2404. https://doi.org/10.1021/jp411401v.

(131) Kasem, K. K.; Schultz, F. A. Electrochemistry of Polyoxometalates Immobilized in Ion Exchange Polymer Films. *Can. J. Chem.* **1995**, *73* (6), 858–864. https://doi.org/10.1139/v95-107.

(132) Francesca, K. D.; Lenfant, S.; Laurans, M.; Volatron, F.; Izzet, G.; Humblot, V.; Methivier, C.; Guerin, D.; Proust, A.; Vuillaume, D. Charge Transport through Redox Active [H7P8W48O184]33− Polyoxometalates Self-Assembled onto Gold Surfaces and Gold Nanodots. *Nanoscale* **2019**, *11* (4), 1863–1878. https://doi.org/10.1039/C8NR09377F.

(133) Vergnani, L.; Barra, A.-L.; Neugebauer, P.; Rodriguez-Douton, M. J.; Sessoli, R.; Sorace, L.; Wernsdorfer, W.; Cornia, A. Magnetic Bistability of Isolated Giant-Spin Centers in a Diamagnetic Crystalline Matrix. *Chem. - Eur. J.* **2012**, *18* (11), 3390–3398. https://doi.org/10.1002/chem.201103251.

(134) Llanos, L.; Aravena, D. Relaxation Time Enhancement by Magnetic Dilution in Single-Molecule Magnets: An Ab Initio Study. *J. Magn. Magn. Mater.* **2019**, *489*, 165456. https://doi.org/10.1016/j.jmmm.2019.165456.

(135) McElhinny, K. M.; Park, J.; Ahn, Y.; Huang, P.; Joo, Y.; Lakkham, A.; Pateras, A.; Wen, H.; Gopalan, P.; Evans, P. G. Photoisomerization Dynamics in a Densely Packed Optically Transformable Azobenzene Monolayer. *Langmuir* **2018**, *34* (37), 10828–10836. https://doi.org/10.1021/acs.langmuir.8b01524.

(136) Linnenberg, O.; Moors, M.; Solé-Daura, A.; López, X.; Bäumer, C.; Kentzinger, E.; Pyckhout-Hintzen, W.; Monakhov, K. Yu. Molecular Characteristics of a Mixed-Valence Polyoxovanadate {VIV/V18O42} in Solution and at the Liquid–Surface Interface. *J. Phys. Chem. C* **2017**, *121* (19), 10419–10429. https://doi.org/10.1021/acs.jpcc.7b02138.

(137) de Bruijckere, J.; Gehring, P.; Palacios-Corella, M.; Clemente-León, M.; Coronado, E.; Paaske, J.; Hedegård, P.; van der Zant, H. S. J. Ground-State Spin Blockade in a Single-Molecule Junction. *Phys. Rev. Lett.* **2019**, *122* (19), 197701. https://doi.org/10.1103/PhysRevLett.122.197701.

(138) Tessonnier, J.-P.; Goubert-Renaudin, S.; Alia, S.; Yan, Y.; Barteau, M. A. Structure, Stability, and Electronic Interactions of Polyoxometalates on Functionalized Graphene Sheets. *Langmuir* **2013**, *29* (1), 393–402. https://doi.org/10.1021/la303408j.

(139) Linnenberg, O.; Moors, M.; Notario-Estévez, A.; López, X.; de Graaf, C.; Peter, S.; Baeumer, C.; Waser, R.; Monakhov, K. Yu. Addressing Multiple Resistive States of Polyoxovanadates: Conductivity as a Function of Individual Molecular Redox States. *J. Am. Chem. Soc.* **2018**, *140* (48), 16635–16640. https://doi.org/10.1021/jacs.8b08780.

(140) Lombana, A.; Rinfray, C.; Volatron, F.; Izzet, G.; Battaglini, N.; Alves, S.; Decorse, P.; Lang, P.; Proust, A. Surface Organization of Polyoxometalate Hybrids Steered by a 2D Supramolecular PTCDI/Melamine Network. *J. Phys. Chem. C* **2016**, *120* (5), 2837–2845. https://doi.org/10.1021/acs.jpcc.5b11945.

(141) Di, A.; Xu, J.; Zinn, T.; Sztucki, M.; Deng, W.; Ashok, A.; Lian, C.; Bergström, L. Tunable Ordered Nanostructured Phases by Co-Assembly of Amphiphilic Polyoxometalates and Pluronic Block Copolymers. *Nano Lett.* **2023**, *23* (5), 1645–1651. https://doi.org/10.1021/acs.nanolett.2c03068.

(142) Zhang, J.; Chang, S.; Suryanto, B. H. R.; Gong, C.; Zeng, X.; Zhao, C.; Zeng, Q.; Xie, J. Efficient Synthesis of Ir-Polyoxometalate Cluster Using a Continuous Flow Apparatus and STM Investigation of Its Coassembly Behavior on HOPG Surface. *Inorg. Chem.* **2016**, *55* (11), 5585–5591. https://doi.org/10.1021/acs.inorgchem.6b00670.

(143) Prashar, D. Self Assembled Monolayers -A Review. *Int. J. ChemTech Res.* **2012**, *4*.

(144) Casalini, S.; Bortolotti, C. A.; Leonardi, F.; Biscarini, F. Self-Assembled Monolayers in Organic Electronics. *Chem. Soc. Rev.* **2017**, *46* (1), 40–71. https://doi.org/10.1039/C6CS00509H.

(145) Mirkin, C. A.; Letsinger, R. L.; Mucic, R. C.; Storhoff, J. J. A DNA-Based Method for Rationally Assembling Nanoparticles into Macroscopic Materials. *Nature* **1996**, *382* (6592), 607–609. https://doi.org/10.1038/382607a0.

(146) Decher, G. Fuzzy Nanoassemblies: Toward Layered Polymeric Multicomposites. *Science* **1997**, *277* (5330), 1232–1237. https://doi.org/10.1126/science.277.5330.1232.

(147) Wang, L.; Gong, C.; Yuan, X.; Wei, G. Controlling the Self-Assembly of Biomolecules into Functional Nanomaterials through Internal Interactions and External Stimulations: A Review. *Nanomaterials* **2019**, *9* (2), 285. https://doi.org/10.3390/nano9020285.

(148) Cengiz, B.; Gevrek, T. N.; Chambre, L.; Sanyal, A. Self-Assembly of Cyclodextrin-Coated Nanoparticles:Fabrication of Functional Nanostructures for Sensing and Delivery. *Molecules* **2023**, *28* (3), 1076. https://doi.org/10.3390/molecules28031076.

(149) Brisse, R.; Guianvarc'h, D.; Mansuy, C.; Sagan, S.; Kreher, D.; Sosa-Vargas, L.; Hamitouche, L.; Humblot, V.; Arfaoui, I.; Labet, V.; Paris, C.; Petit, C.; Attias, A.-J. Probing the In-Air Growth of Large Area of 3D Functional Structures into a 2D Supramolecular Nanoporous Network. *Chem. Commun.* **2018**, *54* (72), 10068–10071. https://doi.org/10.1039/C8CC06125D.

(150) Fernez, Q.; Moradmand, S.; Mattera, M.; Djampa-Tapi, W.; Fiorini, C.; Charra, F.; Mathevet, F.; David, K.; Arfaoui, I.; Sosa Vargas, L. From Molecules in Solution to Molecules on Surfaces – Using Supramolecular Dyads to Form Functional Self-Assembled Networks on Graphene. *J. Mater. Chem. C* **2022**, *10*. https://doi.org/10.1039/D2TC01331B.

(151) Famili, M.; Jia, C.; Liu, X.; Wang, P.; Grace, I. M.; Guo, J.; Liu, Y.; Feng, Z.; Wang, Y.; Zhao, Z.; Decurtins, S.; Häner, R.; Huang, Y.; Liu, S.-X.; Lambert, C. J.; Duan, X. Self-Assembled Molecular-Electronic Films Controlled by Room Temperature Quantum Interference. *Chem* **2019**, *5* (2), 474–484. https://doi.org/10.1016/j.chempr.2018.12.008.

(152) Wang, P.; Jia, C.; Huang, Y.; Duan, X. Van Der Waals Heterostructures by Design: From 1D and 2D to 3D. *Matter* **2021**, *4* (2), 552–581. https://doi.org/10.1016/j.matt.2020.12.015.

(153) Lemme, M. C.; Akinwande, D.; Huyghebaert, C.; Stampfer, C. 2D Materials for Future Heterogeneous Electronics. *Nat. Commun.* **2022**, *13* (1), 1392. https://doi.org/10.1038/s41467-022-29001-4.

(154) Naydenov, B.; Torsney, S.; Bonilla, A. S.; El Garah, M.; Ciesielski, A.; Gualandi, A.; Mengozzi, L.; Cozzi, P. G.; Gutierrez, R.; Samorì, P.; Cuniberti, G.; Boland, J. J. Self-Assembled Two-Dimensional Supramolecular Networks Characterized by Scanning Tunneling Microscopy and Spectroscopy in Air and under Vacuum. *Langmuir* **2018**, *34* (26), 7698–7707. https://doi.org/10.1021/acs.langmuir.8b01374.

(155) Uemura, S.; Tanoue, R.; Yilmaz, N.; Ohira, A.; Kunitake, M. Molecular Dynamics in Two-Dimensional Supramolecular Systems Observed by STM. *Materials* **2010**, *3* (8), 4252–4276. https://doi.org/10.3390/ma3084252.

(156) Zhang, Z.; Li, Y.; Song, B.; Zhang, Y.; Jiang, X.; Wang, M.; Tumbleson, R.; Liu, C.; Wang, P.; Hao, X.-Q.; Rojas, T.; Ngo, A. T.; Sessler, J. L.; Newkome, G. R.; Hla, S. W.; Li, X. Intra- and Intermolecular Self-Assembly of a 20-Nm-Wide Supramolecular Hexagonal Grid. *Nat. Chem.* **2020**, *12* (5), 468–474. https://doi.org/10.1038/s41557-020-0454-z.

(157) Fung, S. Y.; Hong, Y.; Keyes-baig, C.; Chen, P. 12 - Self-Assembly of Peptides and Its Potential Applications. In *Molecular Interfacial Phenomena of Polymers and Biopolymers*; Chen, P., Ed.; Woodhead Publishing Series in Biomaterials; Woodhead Publishing, 2005; pp 421–474. https://doi.org/10.1533/9781845690830.3.421.

(158) Li, W.; Leng, X.; Xu, C.; Liu, N. Formation of Hydrogen Bond-Based 2D Two-Component Supramolecular Networks at Liquid-Solid Surface. *Phys. E Low-Dimens. Syst. Nanostructures* **2018**, *101*, 197–200. https://doi.org/10.1016/j.physe.2018.04.013.

(159) Xu, L.; Miao, X.; Ying, X.; Deng, W. Two-Dimensional Self-Assembled Molecular Structures Formed by the Competition of van Der Waals Forces and Dipole–Dipole Interactions. *J. Phys. Chem. C* **2012**, *116* (1), 1061–1069. https://doi.org/10.1021/jp210000e.

(160) Gerbelli, B. B.; Vassiliades, S. V.; Rojas, J. E. U.; Pelin, J. N. B. D.; Mancini, R. S. N.; Pereira, W. S. G.; Aguilar, A. M.; Venanzi, M.; Cavalieri, F.; Giuntini, F.; Alves, W. A. Hierarchical Self-Assembly of Peptides and Its Applications in Bionanotechnology. *Macromol. Chem. Phys.* **2019**, *220* (14), 1970027. https://doi.org/10.1002/macp.201970027.

(161) Wang, Y.; Miao, X.; Deng, W.; Brisse, R.; Jousselme, B.; Silly, F. Coronene and Phthalocyanine Trapping Efficiency of a Two-Dimensional Kagomé Host-Nanoarchitecture. *Nanomaterials* **2022**, *12* (5), 775. https://doi.org/10.3390/nano12050775.

(162) Velpula, G.; Takeda, T.; Adisoejoso, J.; Inukai, K.; Tahara, K.; Mali, K. S.; Tobe, Y.; Feyter, S. D. On the Formation of Concentric 2D Multicomponent Assemblies at the Solution–Solid Interface. *Chem. Commun.* **2017**, *53* (6), 1108–1111. https://doi.org/10.1039/C6CC09188A.

(163) Lee, S.-L.; Fang, Y.; Velpula, G.; Cometto, F. P.; Lingenfelder, M.; Müllen, K.; Mali, K. S.; De Feyter, S. Reversible Local and Global Switching in Multicomponent Supramolecular Networks: Controlled Guest Release and Capture at the Solution/Solid Interface. *ACS Nano* **2015**, *9* (12), 11608–11617. https://doi.org/10.1021/acsnano.5b06081.

(164) Schull, G.; Douillard, L.; Fiorini-Debuisschert, C.; Charra, F.; Mathevet, F.; Kreher, D.; Attias, A.-J. Selectivity of Single-Molecule Dynamics in 2D Molecular Sieves. *Adv. Mater.* **2006**, *18* (22), 2954–2957. https://doi.org/10.1002/adma.200600683.

(165) Schull, G.; Douillard, L.; Fiorini-Debuisschert, C.; Charra, F.; Mathevet, F.; Kreher, D.; Attias, A.-J. Single-Molecule Dynamics in a Self-Assembled 2D Molecular Sieve. *Nano Lett.* **2006**, *6* (7), 1360–1363. https://doi.org/10.1021/nl060292n.

(166) Li, Y.; Cheng, L.; Liu, C.; Liu, W.; Fan, Y.; Fan, X.; Zeng, Q. On-Surface Observation of the Formation of Organometallic Complex in a Supramolecular Network. *Sci. Rep.* **2015**, *5* (1), 10972. https://doi.org/10.1038/srep10972.

(167) Brom, C. R. van den; Rudolf, P.; Palstra, T. T. M.; Hessen, B. Selective Co-Aggregation of Gold Nanoparticles Functionalised with Complementary Hydrogen-Bonding Groups. *Chem. Commun.* **2007**, No. 46, 4922–4924. https://doi.org/10.1039/B711435D.

(168) van den Brom, C. R.; Arfaoui, I.; Cren, T.; Hessen, B.; Palstra, T. T. M.; De Hosson, J. T. M.; Rudolf, P. Selective Immobilization of Nanoparticles on Surfaces by Molecular Recognition Using Simple Multiple H-Bonding Functionalities. *Adv. Funct. Mater.* **2007**, *17* (13), 2045–2052. https://doi.org/10.1002/adfm.200600497.

(169) *Hydrogen bonding in life - Labster Theory*. https://theory.labster.com/h-bonding-life-vdw/ (accessed 2023-08-22).

(170) Hunter, C. A.; Sanders, J. K. M. The Nature of .Pi.-.Pi. Interactions. *J. Am. Chem. Soc.* **1990**, *112* (14), 5525–5534. https://doi.org/10.1021/ja00170a016.

(171) *6.5.1: Química Host-Invitado e Interacciones de apilamiento π-π*. LibreTexts Español. https://espanol.libretexts.org/Quimica/Qu%C3%ADmica_Inorg%C3%A1nica/Mapa%3A_Qu%C3%ADmica_Inorg%C3%A1nica_(LibreTextos)/06%3A_Qu%C3%ADmica_%C3%A1cido-base_y_donador-aceptor/6.05%3A_Fuerzas_intermoleculares/6.5.01%3A_Qu%C3%ADmica_Host-Invitado_e_Interacciones_de_apilamiento_%CF%80-%CF%80 (accessed 2023-08-22).

(172) Georgakilas, V.; Tiwari, J. N.; Kemp, K. C.; Perman, J. A.; Bourlinos, A. B.; Kim, K. S.; Zboril, R. Noncovalent Functionalization of Graphene and Graphene Oxide for Energy Materials, Biosensing, Catalytic, and Biomedical Applications. *Chem. Rev.* **2016**, *116* (9), 5464–5519. https://doi.org/10.1021/acs.chemrev.5b00620.

(173) Dhotel, A.; Chen, Z.; Delbreilh, L.; Youssef, B.; Saiter, J.-M.; Tan, L. Molecular Motions in Functional Self-Assembled Nanostructures. *Int. J. Mol. Sci.* **2013**, *14* (2), 2303–2333. https://doi.org/10.3390/ijms14022303.

(174) Gao, H.-Y.; Wagner, H.; Held, P. A.; Du, S.; Gao, H.-J.; Studer, A.; Fuchs, H. In-Plane Van Der Waals Interactions of Molecular Self-Assembly Monolayer. *Appl. Phys. Lett.* **2015**, *106* (8), 081606. https://doi.org/10.1063/1.4907777.

(175) Altman, M.; Lee, P.; Rich, A.; Zhang, S. Conformational Behavior of Ionic Self-Complementary Peptides. *Protein Sci.* **2000**, *9* (6), 1095–1105. https://doi.org/10.1110/ps.9.6.1095.

(176) Zhao, X. Design of Self-Assembling Surfactant-like Peptides and Their Applications. *Curr. Opin. Colloid Interface Sci.* **2009**, *14* (5), 340–348. https://doi.org/10.1016/j.cocis.2009.07.002.

(177) Decher, G.; Hong, J. D.; Schmitt, J. Buildup of Ultrathin Multilayer Films by a Self-Assembly Process: III. Consecutively Alternating Adsorption of Anionic and Cationic Polyelectrolytes on Charged Surfaces. *Thin Solid Films* **1992**, *210–211*, 831–835. https://doi.org/10.1016/0040-6090(92)90417-A.

(178) Cherevan, A. S.; Nandan, S. P.; Roger, I.; Liu, R.; Streb, C.; Eder, D. Polyoxometalates on Functional Substrates: Concepts, Synergies, and Future Perspectives. *Adv. Sci.* **2020**, *7* (8), 1903511. https://doi.org/10.1002/advs.201903511.

(179) Cook, T. R.; Zheng, Y.-R.; Stang, P. J. Metal–Organic Frameworks and Self-Assembled Supramolecular Coordination Complexes: Comparing and Contrasting the Design, Synthesis, and Functionality of Metal–Organic Materials. *Chem. Rev.* **2013**, *113* (1), 734–777. https://doi.org/10.1021/cr3002824.

(180) Burnett, B. J.; Choe, W. Sequential Self-Assembly in Metal–Organic Frameworks. *Dalton Trans.* **2012**, *41* (14), 3889–3894. https://doi.org/10.1039/C2DT12103D.

(181) Kim, B.; Cho, C.; Arfaoui, I.; Paris, C.; Petit, C.; Bahers, T. L.; Kim, E.; Attias, A.-J. 2D Host–Guest Supramolecular Chemistry for an on-Monolayer Graphene Emitting Platform. *Mater. Horiz.* **2020**, *7* (10), 2741–2748. https://doi.org/10.1039/D0MH00950D.

(182) Teyssandier, J.; De Feyter, S.; S. Mali, K. Host–Guest Chemistry in Two-Dimensional Supramolecular Networks. *Chem. Commun.* **2016**, *52* (77), 11465–11487. https://doi.org/10.1039/C6CC05256H.

(183) Tahara, K.; Lei, S.; Adisoejoso, J.; Feyter, S. D.; Tobe, Y. Supramolecular Surface-Confined Architectures Created by Self-Assembly of Triangular Phenylene–Ethynylene Macrocycles via van Der Waals Interaction. *Chem. Commun.* **2010**, *46* (45), 8507–8525. https://doi.org/10.1039/C0CC02780D.

(184) Griessl, S.; Lackinger, M.; Edelwirth, M.; Hietschold, M.; Heckl, W. M. Self-Assembled Two-Dimensional Molecular Host-Guest Architectures From Trimesic Acid. *Single Mol.* **2002**, *3* (1), 25–31. https://doi.org/10.1002/1438-5171(200204)3:1<25::AID-SIMO25>3.0.CO;2-K.

(185) Bléger, D.; Kreher, D.; Mathevet, F.; Attias, A.-J.; Schull, G.; Huard, A.; Douillard, L.; Fiorini-Debuischert, C.; Charra, F. Surface Noncovalent Bonding for Rational Design of Hierarchical Molecular Self-Assemblies. *Angew. Chem.* **2007**, *119* (39), 7548–7551. https://doi.org/10.1002/ange.200702376.

(186) Plas, J.; Ivasenko, O.; Martsinovich, N.; Lackinger, M.; Feyter, S. D. Nanopatterning of a Covalent Organic Framework Host–Guest System. *Chem. Commun.* **2015**, *52* (1), 68–71. https://doi.org/10.1039/C5CC07557B.

(187) Bellamy-Carter, A.; Roche, C.; Anderson, H. L.; Saywell, A. Self-Assembly of a Strapped Linear Porphyrin Oligomer on HOPG. *Sci. Rep.* **2021**, *11* (1), 20388. https://doi.org/10.1038/s41598-021-99881-x.

(188) Qin, Y.; Yang, Y.; Yao, M.; Xue, X.; Wang, X.; Huang, H.; Chen, T.; Wang, D.; Wan, L. Self-Assembly of an Oligo(p -Phenylenevinylene)-Based Molecule on an HOPG Surface: Insights from Multi-Scale Simulation and STM Observation. *RSC Adv.* **2018**, *8* (56), 31868–31873. https://doi.org/10.1039/C8RA05477K.

(189) Jaroch, T.; Maranda-Niedbala, A.; Kotwica, K.; Wamil, D.; Bujak, P.; Pron, A.; Nowakowski, R. Self-Assembly of Tetraalkoxydinaphthophenazines in Monolayers on HOPG by Scanning Tunneling Microscopy. *Surf. Sci.* **2015**, *641*, 252–259. https://doi.org/10.1016/j.susc.2015.04.016.

(190) Gurdumov, K.; Mazur, U.; Hipps, K. W. Self-Assembly Dynamics and Stability through Concentration Control at the Solution/HOPG Interface. *J. Phys. Chem. C* **2022**, *126* (30), 12916–12927. https://doi.org/10.1021/acs.jpcc.2c03766.

(191) Moore, A. W. Pyrolytic Carbon and Graphite. In *Encyclopedia of Materials: Science and Technology*; Buschow, K. H. J., Cahn, R. W., Flemings, M. C., Ilschner, B., Kramer, E. J., Mahajan, S., Veyssière, P., Eds.; Elsevier: Oxford, 2001; pp 7933–7937. https://doi.org/10.1016/B0-08-043152-6/01428-5.

(192) Bashir, A. Growth and Structural Characterization of Self-Assembled Monolayers (SAMs) on Gold Made from Functionalized Thiols and Selenols. *Httpwww-Brsubruhr-Uni-BochumdenetahtmlHSSDissBashirAsifdisspdf* **2023**.

(193) Wang, Z.; Xu, F.; Lu, C.; Zhang, H.; Xu, Q.; Zhu, J. Electronic Conductivity Upturn of HOPG Contrast to Transport Properties of Polycrystal Graphite. arXiv January 21, 2008. https://doi.org/10.48550/arXiv.0801.3298.

(194) Yan, H.-J.; Liu, J.; Wang, D.; Wan, L.-J. Two-Dimensional Self-Assemblies of Telechelic Organic Compounds: Structure and Surface Host–Guest Chemistry. *Philos. Trans. R. Soc. Math. Phys. Eng. Sci.* **2013**, *371* (2000), 20120302. https://doi.org/10.1098/rsta.2012.0302.

(195) Otero, R.; Gallego, J. M.; de Parga, A. L. V.; Martín, N.; Miranda, R. Molecular Self-Assembly at Solid Surfaces. *Adv. Mater. Deerfield Beach Fla* **2011**, *23* (44), 5148–5176. https://doi.org/10.1002/adma.201102022.

(196) Rosei, F. Nanostructured Surfaces: Challenges and Frontiers in Nanotechnology. *J. Phys. Condens. Matter* **2004**, *16* (17), S1373. https://doi.org/10.1088/0953-8984/16/17/001.

(197) Feyter, S. D.; Schryver, F. C. D. Two-Dimensional Supramolecular Self-Assembly Probed by Scanning Tunneling Microscopy. *Chem. Soc. Rev.* **2003**, *32* (3), 139–150. https://doi.org/10.1039/B206566P.

(198) De Feyter, S.; De Schryver, F. C. Self-Assembly at the Liquid/Solid Interface: STM Reveals. *J. Phys. Chem. B* **2005**, *109* (10), 4290–4302. https://doi.org/10.1021/jp045298k.

(199) Xiao, Y.; Tao, J.; Peng, X.; Song, Y.; Lei, P.; Xu, H.; Xiao, X.; Tu, B.; Zeng, Q. Two-Dimensional Molecular Network Built from Hierarchy Self-Assembly of Perylene Bisimide Derivatives. *ACS Appl. Mater. Interfaces* **2021**, *13* (14), 17129–17138. https://doi.org/10.1021/acsami.1c03201.

(200) Bellec, A.; Arrigoni, C.; Schull, G.; Douillard, L.; Fiorini-Debuisschert, C.; Mathevet, F.; Kreher, D.; Attias, A.-J.; Charra, F. Solution-Growth Kinetics and Thermodynamics of Nanoporous Self-Assembled Molecular Monolayers. *J. Chem. Phys.* **2011**, *134* (12), 124702. https://doi.org/10.1063/1.3569132.

(201) Gutzler, R.; Cardenas, L.; Rosei, F. Kinetics and Thermodynamics in Surface-Confined Molecular Self-Assembly. *Chem. Sci.* **2011**, *2* (12), 2290–2300. https://doi.org/10.1039/C1SC00531F.

(202) Kalashnyk, N.; Gouesmel, A.; Kim, E.; Attias, A.-J.; Charra, F. Functional Hybrid Multilayered van Der Waals Heterostructures from Graphene and Self-Assembled Supramolecular 2D Crystals. *2D Mater.* **2019**, *6* (4), 045016. https://doi.org/10.1088/2053-1583/ab2ba7.

(203) Kalashnyk, N.; Jaouen, M.; Fiorini-Debuisschert, C.; Douillard, L.; Attias, A.-J.; Charra, F. Electronic Effects of the Bernal Stacking of Graphite on Self-Assembled Aromatic Adsorbates. *Chem. Commun.* **2018**, *54* (69), 9607–9610. https://doi.org/10.1039/C8CC05806G.

(204) Schull, G. Dynamique d'auto-assemblages moléculaires bidimensionnels. phdthesis, École normale supérieure de Cachan - ENS Cachan, 2006. https://theses.hal.science/tel-00143236 (accessed 2023-04-28).

(205) Xu, S.; Zeng, Q.; Lu, J.; Wang, C.; Wan, L.; Bai, C.-L. The Two-Dimensional Self-Assembled n-Alkoxy-Substituted Stilbenoid Compounds and Triphenylenes Studied by Scanning Tunneling Microscopy. *Surf. Sci.* **2003**, *538* (1), L451–L459. https://doi.org/10.1016/S0039-6028(03)00698-8.

(206) Laurans, M.; Mattera, M.; Salles, R.; K'Bidi, L.; Gouzerh, P.; Renaudineau, S.; Volatron, F.; Guillemot, G.; Blanchard, S.; Izzet, G.; Solé-Daura, A.; Poblet, J. M.; Proust, A. When Identification of the Reduction Sites in Mixed Molybdenum/Tungsten Keggin-Type Polyoxometalate Hybrids Turns Out Tricky. *Inorg. Chem.* **2022**, *61* (20), 7700–7709. https://doi.org/10.1021/acs.inorgchem.2c00866.

(207) K/Bidi, L.; Desjonquères, A.; Izzet, G.; Guillemot, G. H2 Evolution at a Reduced Hybrid Polyoxometalate and Its Vanadium-Oxo Derivative Used as Molecular Models for Reducible Metal Oxides. *Inorg. Chem.* **2023**, *62* (5), 1935–1941. https://doi.org/10.1021/acs.inorgchem.2c01741.

(208) Himeno, S.; Takamoto, M. Difference in Voltammetric Properties between the Keggin-Type [XW12O40]N− and [XMo12O40]N− Complexes. *J. Electroanal. Chem.* **2002**, *528* (1–2), 170–174. https://doi.org/10.1016/S0022-0728(02)00901-4.

(209) *Zinc phthalocyanine, [ZnPc]*. https://omlc.org/spectra/PhotochemCAD/html/026.html (accessed 2023-09-14).

(210) Salhi, J.; Calupitan, J. P.; Mattera, M.; Montero, D.; Miche, A.; Maruchenko, R.; Proust, A.; Izzet, G.; Kreher, D.; Arfaoui, I.; Volatron, F. Ready-to-Be-Addressed Oxo-Clusters: Individualized, Periodically Organized and Separated from the Substrate. *Nanoscale* **2023**, *15* (32), 13233–13238. https://doi.org/10.1039/D3NR02649C.

(211) Hammiche, A.; Pollock, H. M.; Reading, M.; Claybourn, M.; Turner, P. H.; Jewkes, K. Photothermal FT-IR Spectroscopy: A Step towards FT-IR Microscopy at a Resolution Better Than the Diffraction Limit. *Appl. Spectrosc.* **1999**, *53* (7), 810–815. https://doi.org/10.1366/0003702991947379.

(212) Bozec, L.; Hammiche, A.; Pollock, H. M.; Conroy, M.; Chalmers, J. M.; Everall, N. J.; Turin, L. Localized Photothermal Infrared Spectroscopy Using a Proximal Probe. *J. Appl. Phys.* **2001**, *90* (10), 5159–5165. https://doi.org/10.1063/1.1403671.

(213) Dazzi, A.; Prazeres, R.; Glotin, F.; Ortega, J. M. Local Infrared Microspectroscopy with Subwavelength Spatial Resolution with an Atomic Force Microscope Tip Used as a

Photothermal Sensor. *Opt. Lett.* **2005**, *30* (18), 2388–2390. https://doi.org/10.1364/OL.30.002388.

(214) Dazzi, A.; Glotin, F.; Carminati, R. Theory of Infrared Nanospectroscopy by Photothermal Induced Resonance. *J. Appl. Phys.* **2010**, *107* (12), 124519. https://doi.org/10.1063/1.3429214.

(215) Katzenmeyer, A. M.; Aksyuk, V.; Centrone, A. Nanoscale Infrared Spectroscopy: Improving the Spectral Range of the Photothermal Induced Resonance Technique. *Anal. Chem.* **2013**, *85* (4), 1972–1979. https://doi.org/10.1021/ac303620y.

(216) Lahiri, B.; Holland, G.; Centrone, A. Chemical Imaging Beyond the Diffraction Limit: Experimental Validation of the PTIR Technique. *Small* **2013**, *9* (3), 439–445. https://doi.org/10.1002/smll.201200788.

(217) Pollock, H. M.; Kazarian, S. G. Microspectroscopy in the Mid-Infrared. In *Encyclopedia of Analytical Chemistry*; John Wiley & Sons, Ltd, 2014; pp 1–26. https://doi.org/10.1002/9780470027318.a5609.pub2.

(218) Lu, F.; Jin, M.; Belkin, M. A. Tip-Enhanced Infrared Nanospectroscopy via Molecular Expansion Force Detection. *Nat. Photonics* **2014**, *8* (4), 307–312. https://doi.org/10.1038/nphoton.2013.373.

(219) Dazzi, A.; Prater, C. B. AFM-IR: Technology and Applications in Nanoscale Infrared Spectroscopy and Chemical Imaging. *Chem. Rev.* **2017**, *117* (7), 5146–5173. https://doi.org/10.1021/acs.chemrev.6b00448.

(220) *IR: alkenes*. https://orgchemboulder.com/Spectroscopy/irtutor/alkenesir.shtml (accessed 2023-09-21).

(221) Hamouni, S.; Arous, O.; Abdessemed, D.; Nezzal, G.; Van der Bruggen, B. Alcohol and Alkane Organic Extraction Using Pervaporation Process. *Macromol. Symp.* **2019**, *386* (1), 1800247. https://doi.org/10.1002/masy.201800247.

(222) Preketes, N. K.; Biggs, J. D.; Ren, H.; Andricioaei, I.; Mukamel, S. Simulations of Two-Dimensional Infrared and Stimulated Resonance Raman Spectra of Photoactive Yellow Protein. *Chem. Phys.* **2013**, *422*, 10.1016/j.chemphys.2012.09.002. https://doi.org/10.1016/j.chemphys.2012.09.002.

(223) Kalisz, G.; Gieroba, B.; Chrobak, O.; Suchora, M.; Starosta, A. L.; Sroka-Bartnicka, A. Vibrational Spectroscopic Analyses and Imaging of the Early Middle Ages Hemp Bast Fibres Recovered from Lake Sediments. *Molecules* **2021**, *26* (5), 1314. https://doi.org/10.3390/molecules26051314.

(224) Meier, H.; Lehmann, M.; Kolb, U. Stilbenoid Dendrimers. *Chem. – Eur. J.* **2000**, *6* (13), 2462–2469. https://doi.org/10.1002/1521-3765(20000703)6:13<2462::AID-CHEM2462>3.0.CO;2-A.

(225) Skoog, D. A.; Crouch, S. R.; Holler, F. J. *Principles of Instrumental Analysis*, 6th ed.; Thomson Brooks/Cole: Belmont, CA, 2007.

(226) G.D. christan. *Analytical Chemistry By Gary D. Christian*; 2018.

(227) Drago, R. S. *Physical Methods for Chemists*; Saunders College Pub., 1992.

(228) Blinder, S. M. *Introduction to Quantum Mechanics*, 2nd edition.; Academic Press: London ; San Diego, CA, 2020.

(229) Lv, F.; Cao, B.; Cui, Y.; Liu, T. Zinc Phthalocyanine Labelled Polyethylene Glycol: Preparation, Characterization, Interaction with Bovine Serum Albumin and Near Infrared Fluorescence Imaging in Vivo. *Molecules* **2012**, *17* (6), 6348–6361. https://doi.org/10.3390/molecules17066348.

(230) Keshipour, S.; Mohammad-Alizadeh, S. Nickel Phthalocyanine@graphene Oxide/TiO2 as an Efficient Degradation Catalyst of Formic Acid toward Hydrogen Production. *Sci. Rep.* **2021**, *11* (1), 16148. https://doi.org/10.1038/s41598-021-95382-z.

(231) Díaz, J.; Pizzio, L. R.; Pecchi, G.; Campos, C. H.; Azócar, L.; Briones, R.; Romero, R.; Henríquez, A.; Gaigneaux, E. M.; Contreras, D. Tetrabutyl Ammonium Salts of Keggin-Type Vanadium-Substituted Phosphomolybdates and Phosphotungstates for Selective Aerobic Catalytic Oxidation of Benzyl Alcohol. *Catalysts* **2022**, *12* (5), 507. https://doi.org/10.3390/catal12050507.

(232) Coronel, N. C.; da Silva, M. J. Lacunar Keggin Heteropolyacid Salts: Soluble, Solid and Solid-Supported Catalysts. *J. Clust. Sci.* **2018**, *29* (2), 195–205. https://doi.org/10.1007/s10876-018-1343-0.

(233) Yang, L.; May, P. W.; Yin, L.; Smith, J. A.; Rosser, K. N. Ultra Fine Carbon Nitride Nanocrystals Synthesized by Laser Ablation in Liquid Solution. *J. Nanoparticle Res.* **2007**, *9* (6), 1181–1185. https://doi.org/10.1007/s11051-006-9192-4.

(234) Yoon, S. H.; Chamot-Rooke, J.; Perkins, B. R.; Hilderbrand, A. E.; Poutsma, J. C.; Wysocki, V. H. IRMPD Spectroscopy Shows That AGG Forms an Oxazolone B2+ Ion. *J. Am. Chem. Soc.* **2008**, *130* (52), 17644–17645. https://doi.org/10.1021/ja8067929.

(235) Dvoryaninova, O. P.; Sokolov, A. V.; Peregonchaya, O. V.; Solovyeva, E. A.; Syanov, D. A. Identification of Composition and Structure of Functional Groups of Ferment Lysates Based on IR Spectroscopy. *IOP Conf. Ser. Earth Environ. Sci.* **2021**, *640* (3), 032062. https://doi.org/10.1088/1755-1315/640/3/032062.

(236) Rathjens, G. W. Jr.; Freeman, N. K.; Gwinn, W. D.; Pitzer, K. S. Infrared Absorption Spectra, Structure and Thermodynamic Properties of Cyclobutane1. *J. Am. Chem. Soc.* **1953**, *75* (22), 5634–5642. https://doi.org/10.1021/ja01118a048.

(237) Rohman, A.; Musfiroh, A.; Wijaya, E. G.; Mada, G. Quantitative Determination of Simethicone in Antacid Suspension and Chewable Tablet Using FTIR Spectroscopy; 2013.

(238) Poiana, M.-A.; Alexa, E.; Munteanu, M.-F.; Gligor, R.; Moigradean, D.; Mateescu, C. Use of ATR-FTIR Spectroscopy to Detect the Changes in Extra Virgin Olive Oil by Adulteration with Soybean Oil and High Temperature Heat Treatment. *Open Chem.* **2015**, *13* (1). https://doi.org/10.1515/chem-2015-0110.

(239) Guo, Y.-C.; Cai, C.; Zhang, Y.-H. Observation of Conformational Changes in Ethylene Glycol–Water Complexes by FTIR–ATR Spectroscopy and Computational Studies. *AIP Adv.* **2018**, *8* (5), 055308. https://doi.org/10.1063/1.4995975.

(240) Kumar, T.; Umamaheswari, S. FTIR, FTR and UV-Vis Analysis of Carbamazepine. *Res. J. Pharm. Biol. Chem. Sci.* **2011**, *2*, 685–693.

(241) Zhu, J.; Cao, X.; Li, J. Ethanol-Induced Aggregation of Nonpolar Nanoparticles in Water/Ethanol Mixed Solvents. *Langmuir* **2022**, *38* (45), 13910–13915. https://doi.org/10.1021/acs.langmuir.2c02126.

(242) Zhao, H.; Zhang, S.; Li, S.; Song, X.; Liu, W.; Liu, B.; Dong, M. Investigation of the Non-Covalent Interactions of Molecular Self-Assembly by Scanning Tunneling Microscopy Using the Association of Aromatic Structures in Pyrene-4,5,9,10-Tetraone and Phenanthrene-9,10-Dione Molecules. *RSC Adv.* **2015**, *5* (125), 103316–103320. https://doi.org/10.1039/C5RA20316C.

(243) Camerman, A.; Trotter, J. The Crystal and Molecular Structure of Pyrene. *Acta Crystallogr.* **1965**, *18* (4), 636–643. https://doi.org/10.1107/S0365110X65001494.

(244) Sau, S. P.; Hrdlicka, P. J. C2′-Pyrene-Functionalized Triazole-Linked DNA: Universal DNA/RNA Hybridization Probes. *J. Org. Chem.* **2012**, *77* (1), 5–16. https://doi.org/10.1021/jo201845z.

(245) Kozhevnikov, I. V. Catalysis by Heteropoly Acids and Multicomponent Polyoxometalates in Liquid-Phase Reactions. *Chem. Rev.* **1998**, *98* (1), 171–198. https://doi.org/10.1021/cr960400y.

(246) Arrigoni, C. Monocouches Nanoporeuses Auto-Assemblées Sur Graphite : Contrôle et Modulation Des Propriétés de Tamis Moléculaire. These de doctorat, Paris 6, 2010. https://www.theses.fr/2010PA066681 (accessed 2023-08-28).

(247) Bellec, A.; Arrigoni, C.; Douillard, L.; Fiorini-Debuisschert, C.; Mathevet, F.; Kreher, D.; Attias, A.-J.; Charra, F. Formation of Hydroxyl-Functionalized Stilbenoid Molecular Sieves at the Liquid/Solid Interface on Top of a 1-Decanol Monolayer. *Nanotechnology* **2014**, *25* (43), 435604. https://doi.org/10.1088/0957-4484/25/43/435604.

(248) Schull, G.; Ness, H.; Douillard, L.; Fiorini-Debuisschert, C.; Charra, F.; Mathevet, F.; Kreher, D.; Attias, A.-J. Single Atom Substitution for Marking and Motion Tracking of Individual Molecules by Scanning Tunneling Microscopy. *J. Phys. Chem. C* **2008**, *112* (36), 14058–14063. https://doi.org/10.1021/jp8030013.

(249) Li, S.; Gong, C.; Zhang, Y.; Fu, S.; Wang, Z.; Lu, Y.; Gu, S.; Liu, X.; Wang, L. Transformation of the Coordination Nanostructures of 4,4′,4″-(1,3,5-Triazine-2,4,6-Triyl) Tribenzoic Acid Molecules on HOPG Triggered by the Change in the Concentration of Metal Ions. *RSC Adv.* **2022**, *12* (7), 3892–3896. https://doi.org/10.1039/D1RA09073A.

(250) Liu, C.; Yang, L.; Wang, Y.; Lei, S.; Hu, W. Substrate Effects in the Supramolecular Self-Assembly of 2,4,6-Tris(4-Bromophenyl)-1,3,5-Triazine on Graphite and Graphene. *J. Phys. Chem. C* **2018**, *122* (23), 12307–12314. https://doi.org/10.1021/acs.jpcc.8b02979.

(251) Qiao, Y.; Zeng, Q.; Tan, Z.; Xu, S.; Wang, C.; Bai, C. STM Observation of 1,3,5-Triazines Bearing Rod-like Benzeneazonaphthalene Moieties Monolayers Self-Assembled on Graphite Surface. *J. Mater. Chem.* **2002**, *12* (5), 1239–1241. https://doi.org/10.1039/B200043C.

(252) Gatti, R.; MacLeod, J. M.; Lipton-Duffin, J. A.; Moiseev, A. G.; Perepichka, D. F.; Rosei, F. Substrate, Molecular Structure, and Solvent Effects in 2D Self-Assembly via Hydrogen and Halogen Bonding. *J. Phys. Chem. C* **2014**, *118* (44), 25505–25516. https://doi.org/10.1021/jp507729w.

(253) Silly, F. Elucidating the Intramolecular Contrast in the STM Images of 2,4,6-Tris(4′,4″,4‴-Trimethylphenyl)-1,3,5-Triazine Molecules Recorded at Room-Temperature and at the Liquid-Solid Interface. *RSC Adv.* **2020**, *10* (10), 5742–5746. https://doi.org/10.1039/C9RA09681G.

(254) *Baran, Richter Essentials of Heterocyclic Chemistry-I ... / baran-richter-essentials-of-heterocyclic-chemistry-i.pdf / PDF4PRO*. PDF4PRO. https://pdf4pro.com/amp/view/baran-richter-essentials-of-heterocyclic-chemistry-i-1b5f0.html (accessed 2023-09-25).

(255) Duraimurugan, K.; Dhanamoorthy, V.; Madhavan, J.; Siva, A. Synthesis and Photophysical Investigations of C3-Triazine Based Star-like Conjugated Molecules. *J. Photochem. Photobiol. Chem.* **2018**, *359*, 164–171. https://doi.org/10.1016/j.jphotochem.2018.04.016.

(256) *eBook: CRC Handbook of Chemistry and Physics von William M. Haynes | ISBN 978-1-4987-5429-3 | Sofort-Download kaufen - Lehmanns.de*. https://www.lehmanns.de/shop/technik/39568473-9781498754293-crc-handbook-of-chemistry-and-physics (accessed 2023-08-29).

(257) Heravi, M. M.; Vazin Fard, M.; Faghihi, Z. Heteropoly Acids-Catalyzed Organic Reactions in Water: Doubly Green Reactions. *Green Chem. Lett. Rev.* **2013**, *6* (4), 282–300. https://doi.org/10.1080/17518253.2013.846415.

(258) SCHAEFER, F. C.; PETERS, G. A. Synthesis of the S-Triazine System. III.1 Trimerization of Imidates. *J. Org. Chem.* **1961**, *26* (8), 2778–2784. https://doi.org/10.1021/jo01066a036.

(259) Meier, H.; Holst, H. C.; Oehlhof, A. Star-Shaped Compounds Having 1,3,5-Triazine Cores. *Eur. J. Org. Chem.* **2003**, *2003* (21), 4173–4180. https://doi.org/10.1002/ejoc.200300132.

(260) Wu, H.; Lian, K. The Development of Pseudocapacitive Molybdenum Oxynitride Electrodes for Supercapacitors. *ECS Trans.* **2014**, *58* (25), 67. https://doi.org/10.1149/05825.0067ecst.

(261) Chen, R.; Li, T.; Zhang, Q.; Ding, Z.; Ma, P.; Zhang, S.; Chen, M.; Dong, W.; Ming, W. Design of Polyurethane Acrylic Antimicrobial Films via One-Step UV Curing. *New J. Chem.* **2017**, *41* (18), 9762–9768. https://doi.org/10.1039/C7NJ02023F.

(262) Song, X.; Ma, Y.; Wang, C.; Dietrich, P. M.; Unger, W. E. S.; Luo, Y. Effects of Protonation, Hydrogen Bonding, and Photodamaging on X-Ray Spectroscopy of the Amine Terminal Group in Aminothiolate Monolayers. *J. Phys. Chem. C* **2012**, *116* (23), 12649–12654. https://doi.org/10.1021/jp302716w.

(263) Bryant, M. A.; Crooks, R. M. Determination of Surface pKa Values of Surface-Confined Molecules Derivatized with pH-Sensitive Pendant Groups. *Langmuir* **1993**, *9* (2), 385–387. https://doi.org/10.1021/la00026a005.

(264) Vysotsky, Y. B.; Kartashynska, E. S.; Vollhardt, D.; Fainerman, V. B. Surface pKa of Saturated Carboxylic Acids at the Air/Water Interface: A Quantum Chemical Approach. *J. Phys. Chem. C* **2020**, *124* (25), 13809–13818. https://doi.org/10.1021/acs.jpcc.0c03785.

(265) Wellen, B. A.; Lach, E. A.; Allen, H. C. Surface pKa of Octanoic, Nonanoic, and Decanoic Fatty Acids at the Air–Water Interface: Applications to Atmospheric Aerosol Chemistry. *Phys. Chem. Chem. Phys.* **2017**, *19* (39), 26551–26558. https://doi.org/10.1039/C7CP04527A.

(266) Sharma, A.; Sharma, N.; Kumar, R.; Shard, A.; Sinha, A. K. Direct Olefination of Benzaldehydes into Hydroxy Functionalized Oligo (p-Phenylenevinylene)s via Pd-Catalyzed Heterodomino Knoevenagel-Decarboxylation-Heck Sequence and Its Application for Fluoride Sensing π-Conjugated Units. *Chem. Commun.* **2010**, *46* (19), 3283–3285. https://doi.org/10.1039/C001980A.
(267) Matt, B.; Moussa, J.; Chamoreau, L.-M.; Afonso, C.; Proust, A.; Amouri, H.; Izzet, G. Elegant Approach to the Synthesis of a Unique Heteroleptic Cyclometalated Iridium(III)-Polyoxometalate Conjugate. *Organometallics* **2012**, *31* (1), 35–38. https://doi.org/10.1021/om200910p.
(268) Laurans, M. Synthèse d'hybrides de Polyoxométallates: Greffage Contrôlé Sur Électrodes Pour l'étude de Jonctions Moléculaires. 320.
(269) Combs-Walker, L. A.; Hill, C. L. Stabilization of the Defect ("lacunary") Complex Polymolybdophosphate, PMo11O397-. Isolation, Purification, Stability Characteristics, and Metalation Chemistry. *Inorg. Chem.* **1991**, *30* (21), 4016–4026. https://doi.org/10.1021/ic00021a010.
(270) Rinfray, C. Greffage de polyoxométallates hybrides sur surfaces planes. 199.
(271) Piot, M. Auto-assemblages d'hybrides de polyoxométallates par coordination dirigée. phdthesis, Sorbonne Université, 2018. https://theses.hal.science/tel-02865498 (accessed 2023-10-01).
(272) Mathurin, J.; Deniset-Besseau, A.; Bazin, D.; Dartois, E.; Wagner, M.; Dazzi, A. Photothermal AFM-IR Spectroscopy and Imaging: Status, Challenges, and Trends. *J. Appl. Phys.* **2022**, *131* (1), 010901. https://doi.org/10.1063/5.0063902.
(273) Horcas, I.; Fernández, R.; Gómez-Rodríguez, J. M.; Colchero, J.; Gómez-Herrero, J.; Baro, A. M. WSXM: A Software for Scanning Probe Microscopy and a Tool for Nanotechnology. *Rev. Sci. Instrum.* **2007**, *78* (1), 013705. https://doi.org/10.1063/1.2432410.